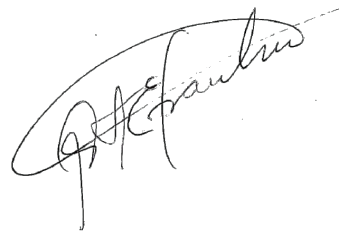


Universidade de São Paulo
Instituto de Física

O papel do tempo em fenômenos fora do
equilíbrio: coarse-graining por transições,
transições de fase e máquinas térmicas

Pedro Eduardo Harunari



Orientador: Prof. Dr. Carlos E. Fiore dos Santos

Tese de doutorado apresentada ao Instituto de Física
da Universidade de São Paulo, como requisito parcial
para a obtenção do título de Doutor(a) em Ciências.

Banca Examinadora:

Prof. Dr. Carlos Eduardo Fiore dos Santos (Orientador) - IFUSP

Prof. Dr. André de Pinho Vieira - IFUSP

Prof. Dr. Marcus Vinicius Segantini Bonança - UNICAMP

Prof. Dr. Ronald Dickman - UFMG

Prof. Dr. Domingos Sávio Pereira Salazar - UFRPE

São Paulo

2022

FICHA CATALOGRÁFICA
Preparada pelo Serviço de Biblioteca e Informação
do Instituto de Física da Universidade de São Paulo

Harunari, Pedro Eduardo

O papel do tempo em fenômenos fora do equilíbrio: coarse-graining por transições, transições de fase e máquinas térmicas. São Paulo, 2022.

Tese (Doutorado) – Universidade de São Paulo. Instituto de Física. Depto. de Física Geral

Orientador: Prof. Dr. Carlos Eduardo Fiore dos Santos.

Área de Concentração: Física Estatística.

Unitermos: 1. Termodinâmica; 2. Processos estocásticos; 3. Máquinas térmicas.

USP/IF/SBI-63/2022

University of São Paulo
Physics Institute

The role of time in nonequilibrium:
transition-based coarse-graining, phase
transitions and heat engines

Pedro E. Harunari

Supervisor: Prof. Dr. Carlos E. Fiore dos Santos

Thesis submitted to the Physics Institute of the University of São Paulo
in partial fulfillment of the requirements for the degree of Doctor of
Science.

Examining Committee:

Prof. Dr. Carlos Eduardo Fiore dos Santos (Supervisor) - IFUSP

Prof. Dr. André de Pinho Vieira - IFUSP

Prof. Dr. Marcus Vinicius Segantini Bonança - UNICAMP

Prof. Dr. Ronald Dickman - UFMG

Prof. Dr. Domingos Sávio Pereira Salazar - UFRPE

São Paulo

2022

Acknowledgements

This thesis and all the work done during my Ph.D. would not be possible without the academic and non-academic contribution of many people I was lucky enough to come across.

First and foremost, my wife **Maria Angélica**, with whom I grew up together in every possible sense, for the mutual and timely attractive forces, and for emphasizing the lyricism of the world. You are a constant smile in the best memories and a shoulder in the worst, your kind heart and beautiful mind are inspiring. I hope you experience immeasurable happiness in your life. Prepare for our many adventures to come.

A bit of Portuguese now: *meus incríveis pais **Eduardo e Cecília**, vó e **bachan**, cujos generosos e incessantes esforços foram fundamentais. Sempre que sentirem orgulho de mim, sintam de vocês também. Meus irmãos **Fábio e Paulo**, tios, primos, sogros, cunhadas, sobrinhos, cachorras e todo o resto da família, por todas as relações de apoio, carinho e muita diversão.*

My supervisor **Fiore**, for his always sincere advice that contributed to my development in several aspects, including learning how to study, research, and behave as a physicist should. **Matteo**, who fortuitously became something of a mentor to me, for the unexpected amount of trust and the large amount of shared knowledge. **Mário de Oliveira**, for inspiring and introducing me to physics research. And **Landi**, for getting me back on track when I got the closest to quitting.

With my friends I shared several discussions about physics and science, but all the fun moments were very important to keep up with the studies. **Pedro** and **Luís**, for our rare and constant friendship, in which we always try and improve each other with companionship, honesty, and rationality. During this period I was also fortunate enough to have **Ariel**, **Isa** and **Gülce** as best friends, three brilliant and inspiring human beings. And the list goes on with Mayhara, Irem, Rongrong, Lufê, Mari, Lefundes, Gustavo, and definitely many more.

In the meantime, I greatly benefitted from scientific visits, and for that I am thankful to

Massimiliano, his excellent group at the University of Luxembourg, **Édgar**, and **Jukka**.

The life at the **University of São Paulo**, the department, the research group, all professors, colleagues and employees, meals at *bandejão*, coffees, parties, Tubatuque presentations, classes, discussions, and time spent at the campus will be fondly remembered. **Fundação Antônio e Helena Zerrenner**, ETWB teachers and staff, for providing me with high-quality free-of-cost education, without which I would not be able to enroll in such a prestigious university.

I acknowledge the São Paulo Research Foundation (**FAPESP**) for the financial support through grants #2017/24567-0 and #2020/03708-8 and, above all, for giving the most stable grants in Brazil, even in difficult times; the foundation approach to scientific funding is exemplary. I am thankful to the **examining committee**, a set of physicists that I greatly admire that contributed with comments and insightful discussions. Lastly, I have to cite **Milton Nascimento**, for all the hours I spent listening to his masterpieces, and **Julia Galef**, for transforming boring commuting into opportunities to improve thinking skills.

*A todos que nos deixaram devido à escassez de racionalidade
no enfrentamento da pandemia de COVID-19.*

Resumo

O desafio de estender a termodinâmica para o regime fora do equilíbrio é um problema fundamental na física estatística que recentemente obteve muito progresso. Neste contexto surge a termodinâmica estocástica, que descreve transformações de energia a partir da matemática dos processos de Markov, formando um relevante ferramental na física estatística moderna. Uma das suas principais grandezas, a produção de entropia, estende a segunda lei e quantifica irreversibilidade temporal. Na presente tese de doutorado, estudamos diferentes problemas de termodinâmica fora do equilíbrio como a inferência da produção de entropia a partir de informação parcial e seu uso como um indicador de transições de fase. Mais especificamente, na primeira parte, desenvolvemos um método para analisar a estatística de sistemas a partir da observação de algumas transições visíveis e suas implicações em termodinâmica e biofísica. Provamos um limite inferior para a produção de entropia superior a outras desigualdades conhecidas na literatura e estudamos como ele é saturado, também recuperamos um teorema de flutuação para dinâmicas parcialmente observadas. Na segunda parte mostramos que a produção de entropia localiza e identifica transições de fase contínuas e de primeira ordem. Flutuações de correntes integradas na vizinhança de transições de fase de primeira ordem são consideradas, e particularmente a competição entre tempo de observação e o tempo de tunelamento interfases. Por último, abordamos a termodinâmica de máquinas térmicas a tempo finito e suas otimizações, em particular pelo controle do tempo de interação entre sistema e reservatórios e a interação entre partículas.

Palavras-chave: Termodinâmica estocástica; transições de fase fora do equilíbrio; máquinas térmicas; mecânica estatística.

Abstract

The challenge of extending thermodynamics to the nonequilibrium regime is a fundamental problem in statistical physics that has witnessed many developments in recent years. Stochastic thermodynamics was developed in this context, it describes energy transformations from the mathematics of Markov process, constituting a relevant toolbox in modern statistical physics. One of its main quantities, entropy production, extends the second law and quantifies time irreversibility. In the present doctoral thesis, we study distinct nonequilibrium thermodynamics problems such as the inference of entropy production from partial information and its usage as a phase transition indicator. More specifically, in the first part, we develop a framework to assess the statistics of systems through the observation of a set of visible transitions and its implications to thermodynamics and biophysics. We prove a lower bound for the entropy production tighter than other known inequalities and study its saturation, and we also recover a fluctuation theorem for partially observed dynamics. In the second part, we show that entropy production locates and distinguishes continuous and first-order phase transitions. Fluctuations of integrated currents in the vicinity of first-order phase transitions are addressed, in particular the key interplay between observation time and inter-phase tunneling times. Lastly, we address the thermodynamics of finite-time heat engines and their optimization, in particular through the control of interaction time between system and reservoirs and interaction between particles.

Keywords: Stochastic thermodynamics; nonequilibrium phase transitions; heat engines; statistical mechanics.

List of publications

- [I] Jesus M Encinas et al. “Fundamental ingredients for discontinuous phase transitions in the inertial majority vote model”. In: *Scientific reports* 8.1 (2018), pp. 1–9.
- [II] C. E. Fernández Noa et al. “Entropy production as a tool for characterizing nonequilibrium phase transitions”. In: *Phys. Rev. E* 100 (1 July 2019), p. 012104.
- [III] Pedro E Harunari, Carlos E Fiore, and Karel Proesmans. “Exact statistics and thermodynamic uncertainty relations for a periodically driven electron pump”. In: *Journal of Physics A: Mathematical and Theoretical* 53.37 (2020), p. 374001.
- [IV] Pedro E. Harunari et al. “Maximal power for heat engines: Role of asymmetric interaction times”. In: *Phys. Rev. Research* 3 (2 June 2021), p. 023194.
- [V] C. E. Fiore et al. “Current fluctuations in nonequilibrium discontinuous phase transitions”. In: *Phys. Rev. E* 104 (6 Dec. 2021), p. 064123.
- [VI] Iago N. Mamede et al. “Obtaining efficient thermal engines from interacting Brownian particles under time-periodic drivings”. In: *Phys. Rev. E* 105 (2 Feb. 2022), p. 024106.
- [VII] Pedro E Harunari et al. “What to learn from few visible transitions’ statistics?” In: *arXiv preprint arXiv:2203.07427 [accepted for publication in Physical Review X]* (2022).
- [VIII] Pedro E Harunari, Alberto Garilli, and Matteo Polettini. “The beat of a current”. In: *arXiv preprint arXiv:2205.05060* (2022).

Contents

1	Introduction	10
2	Setting the stage	13
2.1	Mesoscopic stochastic dynamics	13
2.1.1	Discrete state space	13
2.1.2	Continuous state space	16
2.2	Stochastic Thermodynamics	18
2.3	Fluctuation and uncertainty relations	22
3	Transition-based coarse graining	26
3.1	First-passage time	29
3.1.1	Mapping and solving the problem	29
3.1.2	Developing the results	34
3.2	Entropy production inference	39
3.2.1	Definition and lower bound	39
3.2.2	Inter-transition time revealing the arrow of time	40
3.2.3	Visible irreversibility	42
3.2.4	Single current observation	45
3.2.5	Kullback-Leibler estimation	48
3.2.6	Ring networks	49
3.3	Markov chain in visible transition space	52
3.4	Fluctuation relations	53
3.5	Biophysical applications	58
3.5.1	Molecular motors	59
3.5.2	Disorder on a track	65

<i>CONTENTS</i>	8
3.6 Chapter summary	67
4 Nonequilibrium Phase transitions	69
4.1 What is a phase transition	69
4.2 Systems with up-down symmetry	71
4.2.1 Mean-field description	71
4.2.2 Mean-field description - Majority vote model with inertia	76
4.2.3 Beyond the mean-field theory	84
4.2.4 Beyond mean-field - Majority vote model with inertia	87
4.3 Two-state coarse graining of phase transitions	96
4.3.1 Large deviation theory	97
4.3.2 Finite-time large deviation theory	101
4.3.3 Conditional cumulants	103
4.3.4 Lumping of phases	105
4.3.5 Schlögl's model	110
4.4 Chapter's summary	115
5 Heat engines	117
5.1 Asymmetric interaction in a collisional model	119
5.1.1 Collisional two-level system	119
5.1.2 The role of asymmetric switching	122
5.2 Interacting Brownian engine	129
5.2.1 Dynamic and thermodynamic description	129
5.2.2 Harmonic potentials and periodic driving	131
5.2.3 Efficiency as a work-to-work converter	134
5.2.4 Different temperatures	138
5.3 Chapter summary	139
6 Conclusions and Discussions	141
Front page of the papers	163

Preface

This thesis is based on the works [I, II, III, IV, V, VI, VII, VIII], and adjacent results. Some excerpts from the original papers are transcribed here.

“Our primary interest is frequently in processes rather than in states. It is the life process that captures our imagination, rather than the eventual equilibrium state to which each organism inevitably proceeds.”

Herbert B. Callen [1]

Chapter 1

Introduction

From the atomic to cosmological scale, the celebrated theory of thermodynamics unifies the description of phenomena involving an ensemble of particles at thermal equilibrium. It describes how equilibrium macroscopic systems are affected by macroscopic properties, such as temperature, that emerge from the behavior of microscopic constituents. However, many relevant systems in nature operate out of equilibrium and present fluxes; they are present across all scales, such as the constant heat flow from the Sun causing life on Earth, the transport of hormones from endocrine glands to target cells, and the movement of electrons along wires.

Typically, the macroscopic limit is characterized by a suppression of fluctuations of physical quantities, in and out of equilibrium. However, these fluctuations are crucial to understanding systems on smaller scales, thus the need for a stochastic treatment. The mathematics of stochastic dynamics, Markovian or not, combined to thermodynamics, gave rise to the field of stochastic thermodynamics. It enables modeling mesoscopic systems under the assumption that environmental degrees of freedom are considered to be in equilibrium and coarse-grained. Nonequilibrium is captured by stochastic thermodynamics and manifested via the break of detailed balance and the emergence of fluxes. These fluxes are amenable to a thermodynamical description, and their fluctuations are accounted for. Even further, many results involving fluctuations are unique to stochastic thermodynamics.

Recent years have witnessed many experimental validations of stochastic thermodynamics' results, and the development of techniques to control small systems leverage its relevance to technological applications. Many systems that were once restricted to *Gedankenexperiments* are now real and more controllable, such as Maxwell demons and single-particle heat engines. Apart from further developing stochastic thermodynamics results, a major challenge lies in ex-

tending its range of application; for instance, to systems with hidden degrees of freedom. When the observer is only sensitive to partial information, coarse-graining schemes based on mesoscopic state occupancy are usually employed. However, the whole theory of thermodynamics is based on transformations rather than sojourns. Numerous systems of interest only provide partial information through the occurrence of transitions, for example, electronic devices and fermionic chains connected to monitored reservoirs, and molecular motors such as ribosomes translocating along RNA. Here, we provide an alternative coarse-graining framework based on transitions that reveals the dynamical and thermodynamical properties of the observation of transformations.

A stochastic treatment also extends the prosperous field of phase transitions, in particular nonequilibrium phase transitions. We study how relevant fluxes behave during continuous and first-order phase transitions; not only their averages, but also higher-order moments. The behavior of entropy production rate proves to constitute a powerful tool for localizing and characterizing phase transitions. A finite-time version of large deviation theory is employed to study the statistics of fluxes in the vicinity of first-order phase transitions. For so, a notion of conditional quantities is explored based on a two-state coarse-graining based on phases. These results are applied to distinct nonequilibrium models that present phase transitions: majority vote, Schlögl, and Potts. Despite the last being an iconic equilibrium model, its nonequilibrium versions have attracted some attention.

Lastly, we explore the field of nonequilibrium heat engines. At all scales, useful transformations of energy are of utmost importance, and many experimental realizations of small heat engines are being developed recently. Power and efficiency are two relevant figures of merit for heat engines, and optimizing both at the same time is in general not feasible. Maximum power operation often leads to the Curzon-Ahblorn efficiency, while maximum efficiency leads to vanishing power. We explore the interplay between power and efficiency when the physical parameters and the protocol are controlled in a collisional heat engine and an interacting two-particle Brownian engine. We observed the relevance of asymmetric times in the first model and how the interaction intensity affects the performance in the second.

As stated by Ludwig von Bertalanffy in 1949 [2], following Prigogine's works, "the consideration of irreversible phenomena leads to the conception of a thermodynamical, as opposed to astronomical, time." This notion of time is the common denominator of the works discussed throughout this thesis. The physicality of timescales that arise in systems of thermodynamic in-

terest, in particular systems out of equilibrium, is discussed. We dissect the emerging rhythms, both internal and external. Internal rhythms arise in systems that, given some conditions such as temperature and state space, are free to evolve. They can be assessed by modeling the dynamics or by inference schemes. Conversely, external rhythms need not be modeled since they are not emerging, they are imposed through e.g. time-periodic forces exerted by external agents; the reaction to such has fundamental thermodynamic consequences.

This thesis is organized as follows: Chapter 2 is a brief summary of the basics, Chap. 3 introduces the transition-based coarse-graining framework and its results, Chap. 4 addresses nonequilibrium phase transitions, and Chap. 5 the study of heat engines. Conclusions and discussions are drawn in the final Chap. 6. The front page of all published/submitted articles can be found in the Appendix.

Chapter 2

Setting the stage

2.1 Mesoscopic stochastic dynamics

In contrast to the deterministic character of macroscopic thermodynamics, we resort to Markovian stochastic processes to describe how the probability of mesoscopic states evolves in time. A mesoscopic state is a coarse-grained version of the microscopic configurations based on their energy and irrespective of the microscopic evolution, which can be described by mechanics. For instance, the Brownian motion of pollen grains suspended in water is described by random forces rather than individual molecule collisions.

These mesoscopic states will be used to model systems of interest, and the evolution of probability distributions describe the behavior of relevant physical quantities, such as currents, average velocities, efficiency, and entropy production. We consider continuous-time, autonomous chains, Markovian evolution, and split the dynamics into two cases, discrete and continuous state space.

2.1.1 Discrete state space

The case of discrete state space is known as a continuous-time Markov chain, or simply CTMC, and sometimes known as jump processes. The time evolution of the probability mass function follows a partial equation known as the master equation.

Setting the *tempo*, transition rates define exponential distributions that are followed by the random variable known as the sojourn time, the time spent in a state before the next transition. While the states of a Markov chain are constrained by possible system configurations, values of transition rates are affected by external parameters since they coarse-grain environmental de-

degrees of freedom. In CTMCs the transitions are instantaneous, which can be seen as a timescale separation; therefore, time is rather spent in states.

The state space is rendered by a network whose vertices represent states and edges represent transitions. Lastly, the network is assumed to be *irreducible*: There exists a path with positive probability connecting each to every pair of states. This property ensures, via Perron-Frobenius theorem, the existence of a stationary probability mass function towards which the system relaxes to. Possible “reducible” networks are composed of the combination of disconnected irreducible networks, networks with absorbing states or with absorbing cycles.

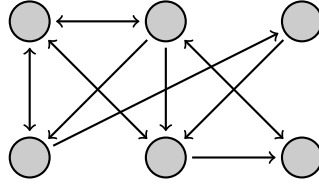


Figure 2.1: Example of an irreducible network.

The Markov chain over the N states network is defined by a set of $N \times N$ time-independent transition rates. A transition rate W_{ij} is the mean number of jumps from state j to state i per unit of time, given that the system is occupying j . The Markov property states that the probabilities related to the next jump only depend on the current state; thus, the chain has no memory.

Let $p(j, t)$ be the fraction of paths from a large ensemble that occupy state j at time t , viz. the occupation probability, hence the mean number of transitions $j \rightarrow i$ per unit time is $W_{ij}p(j, t)$ at t . Therefore, at a given time t , the total flux towards i is given by $\sum_{j \neq i} W_{ij}p(j, t)$ and outwards by $\sum_{j \neq i} W_{ji}p(i, t)$, the mismatch between them is the flux of probability per unit of time of state i , comprising the so-called master equation

$$\frac{d}{dt}p(i, t) = \sum_{j \neq i} W_{ij}p(j, t) - W_{ji}p(i, t). \quad (2.1)$$

Alternatively, it can be expressed in matrix form¹ as

$$\frac{d}{dt}|p(t)\rangle = \mathbf{W}|p(t)\rangle, \quad (2.2)$$

where \mathbf{W} is the *stochastic matrix* (sometimes rate matrix, evolution matrix and \mathbb{W} -matrix), with

¹Using Dirac’s notation, $|p(t)\rangle$ is a column vector with elements $p(i, t)$, for every state i with arbitrary order. Its transpose is the row vector $\langle p(t)|$. Also, $|i\rangle$ is used as a notation for the column vector with elements δ_{ij} to make reference to state i .

transition rates as off-diagonal elements W_{ij} and diagonal elements are defined as the negative of exit rates $W_{ii} := -\sum_{j \neq i} W_{ji}$. As a consequence, the elements in every column add up to zero, which is a property of Markovian stochastic matrices.

The Perron-Frobenius ensures the existence of a unique stationary distribution given by the right eigenvector of \mathbf{W} whose eigenvalue is zero,

$$\mathbf{W} |p_\infty\rangle = 0, \quad (2.3)$$

towards which the system is evolving to, and is known as stationary distribution or steady-state². Its solution can be obtained by different approaches; a general and common approach involves using Cramer's rule, which provides the solution

$$p_\infty(i) = \langle i | p_\infty \rangle \propto (-1)^{i+j} \det[\mathbf{W}_{\setminus(j,i)}] \quad \forall j, \quad (2.4)$$

where $\mathbf{W}_{\setminus(j,i)}$ is the result after removing row j and column i from matrix \mathbf{W} . Another common general solution for the master equation is obtained using Hill's diagram method [3], and distinct solutions can appear for particular structures of \mathbf{W} .

The stationary distribution can be of equilibrium or out of equilibrium, where the former is achieved when the *detailed balance* condition is met: $W_{ij}p_\infty(j) = W_{ji}p_\infty(i) \quad \forall i, j$. This condition implies that every probability current stalls, and Eq. (2.1) vanishes term by term. It is important to notice that the stationary distribution is a property of the stochastic matrix, as shown in Eq. (2.4), thus the notion of equilibrium lies in the transition rates and the topology of the CTMC.

The formal solution of the master equation (2.2) is given by the product of a propagator and the initial state

$$|p(t)\rangle = \exp(t\mathbf{W}) |p(0)\rangle. \quad (2.5)$$

A spectral decomposition of the propagator leads to $p(t) = \sum_{i=1}^N c_i e^{\lambda_i t} |v_i\rangle$, where coefficients c_i depend on the initial state $|p(0)\rangle$ and $|v_i\rangle$ are the eigenvectors related to eigenvalues λ_i . Assuming that the eigenvectors are non-degenerate and, since \mathbf{W} is a stochastic matrix, all eigenvalues have a negative real part while the dominant one is zero, therefore, the long-time limit of the occupation probability vector approaches the stationary distribution as a linear combination

²Steady-state can create confusion since the word "state" is also used for the network vertices, however it is the most widespread nomenclature.

of exponentials:

$$\lim_{t \rightarrow \infty} |p(t)\rangle = \lim_{t \rightarrow \infty} e^{t\mathbf{W}} |p(0)\rangle = \lim_{t \rightarrow \infty} \sum_{i=1}^N c_i e^{\lambda_i t} |v_i\rangle = |p_\infty\rangle, \quad (2.6)$$

where in the last equality the coefficients were dropped due to the normalization of probabilities.

This framework also fits time-dependent transition rates, in particular the case of periodic rates is important to the study of driven systems such as heat engines. In ergodic systems, these distributions become time-dependent and periodic in the long-time limit.

Several systems of interest are modelled by master equations, but they often are too complicated to be analytically dealt with, raising the necessity of a numerical simulation framework for CTMCs. This framework is provided by the Gillespie algorithm [4], which draws the next transition proportionally to the respective transition rate

$$P[i|j] = \frac{W_{ij}}{\sum_{k \neq j} W_{kj}} \quad (2.7)$$

and the time interval before the next jump is exponentially distributed

$$P[t|j, i] = \left(\sum_{k \neq j} W_{kj} \right) \exp\left(-t \sum_{k \neq j} W_{kj} \right), \quad (2.8)$$

which is referred to as a Poisson process. The Gillespie algorithm produces trajectories accordingly, it is a powerful tool in particular for treating the sojourn times as random variables.

2.1.2 Continuous state space

For simplicity, we start with the one-dimensional case. The motion of a particle performing Brownian motion along the line subject to a position-dependent force is described by a differential equation involving three forces, dissipative, external, and random:

$$m \frac{d^2 x}{dt^2} = -\alpha \frac{dx}{dt} + f_{\text{ext}}(x) + f_T(t), \quad (2.9)$$

where m is the mass, and α the friction coefficient ($-\alpha v$ is the dissipative force, also known as drift). $f_{\text{ext}}(x)$ is the external force applied to the particle; it depends on the position and usually originates from a potential that, for example, can trap the particle. f_T is the random force stemming from the environment with temperature T , its average is zero since there is no

preferential direction for the environment

$$\langle f_T(t) \rangle = 0. \quad (2.10)$$

The fluctuation of the random force is related to the temperature and it is not correlated over time since the model assumes independent contributions (white noise), therefore

$$\langle f_T(t) f_T(t') \rangle \propto T \delta(t - t'). \quad (2.11)$$

When the mass is negligible, Eq. (2.9) arrives at the overdamped Langevin equation for a general external force

$$\frac{dx}{dt} = \frac{1}{\alpha} [f_{\text{ext}}(x) + f_T(t)]. \quad (2.12)$$

Notice how the friction coefficient α acts as a scale for the forces, thus we will set it to unity for clarity and the Langevin equation is expressed as

$$\frac{dx}{dt} = f_{\text{ext}}(x) + f_T(t). \quad (2.13)$$

An important property of the Langevin equation is that the net displacement is due only to the external force, since the random force does not have preferential directions. However, higher-order moments of the position are also related to the temperature, and thus the diffusion depends on it.

Expanding the characteristic function of a discretized version of Eq. (2.13) [5], it is possible to derive the evolution for the probability density, the Fokker-Planck equation

$$\frac{\partial}{\partial t} P(x, t) = -\frac{\partial}{\partial x} [f_{\text{ext}}(x) P(x, t)] + \frac{\Gamma}{2} \frac{\partial^2}{\partial x^2} P(x, t), \quad (2.14)$$

where $P(x, t)$ is the probability density function of a particle following a Langevin equation, and Γ is related to the temperature through the evaluation of Eq. (2.11), $\langle f_T(t) f_T(t') \rangle = \Gamma \delta(t - t')$.

Equation (2.14) is conveniently expressed as a continuity equation, in terms of probability currents $\mathcal{J}(x, t)$:

$$\frac{\partial}{\partial t} P(x, t) = -\frac{\partial}{\partial x} \mathcal{J}(x, t), \quad (2.15)$$

where

$$\mathcal{J}(x, t) = f_{\text{ext}}(x)P(x, t) - \frac{\Gamma}{2} \frac{\partial}{\partial x} P(x, t). \quad (2.16)$$

The first term represents the currents due to drift and external forces, and the second term is due to diffusion.

To solve the Fokker-Planck equation, it is necessary to consider boundary conditions, which are usually periodic or of vanishing probabilities and probability currents at the boundaries. In the stationary distribution, the current $\mathcal{J}(x, t)$ does not depend on position,

$$\frac{\partial}{\partial x} \mathcal{J}_{\infty}(x, t) = 0. \quad (2.17)$$

When ever the probability currents vanish the equation above is satisfied and the stationary distribution is known as equilibrium, $\mathcal{J}_{\infty}(x, t) = 0$ is the detailed balance condition for continuous state-space. To obtain the equilibrium stationary probability density one has to find the zero of Eq. (2.16).

The present description can be extended for an arbitrary number of particles by considering a family of Langevin equations with uncorrelated noise functions. The joint probability density $P(x_1, x_2, \dots, t)$ will follow a multi-variate Fokker Planck equation that has can be written as

$$\frac{\partial}{\partial t} P(\vec{x}, t) = - \sum_i \frac{\partial}{\partial x_i} \mathcal{J}_i(\vec{x}, t), \quad (2.18)$$

where each current J_i has its own force $f_{\text{ext},i}$ and temperature T_i .

2.2 Stochastic Thermodynamics

The identification of thermodynamic quantities and transformations in the mesoscopic dynamics constitutes the field of stochastic thermodynamics. Importantly, quantities can be defined at the trajectory level, therefore they fluctuate. In traditional thermodynamics the systems are macroscopic and fluctuations get suppressed, while in stochastic thermodynamics the fluctuations are relevant and results about their behavior have been largely explored, such as fluctuation relations.

In the framework stochastic thermodynamics, we assume that the system is in contact with an equilibrium reservoir of temperature T whose properties are not affected by the system. It

means that all removed degrees of freedom are assumed to relax in a much faster timescale. This assumption is reasonable in many applications of the framework such as colloidal particles and biological motors.

The identification of energetics in stochastic dynamics was performed by Sekimoto in Ref. [6], and consequently the establishment of a fluctuating *first law* at the trajectory level. Consider a system that obeys a Langevin equation, with external force stemming to a potential $V(x, a)$, which depends on the position and one external parameter. Following Ref. [6], Equation (2.13) multiplied by a infinitesimal displacement can be expressed as

$$0 = - \left(-\alpha \frac{dx}{dt} + f_T \right) dx - f_{\text{ext}} dx. \quad (2.19)$$

We make some identifications, $-\alpha \frac{dx}{dt} + f_T$ is the force applied by the bath on the system and $f_{\text{ext}} = -\partial V/\partial x$. Multiplied by dx , the former is the differential heat exchange from the bath to the system $-dQ$. The latter is one of the terms in the differential potential energy change $dV = (\partial V/\partial x)dx + (\partial V/\partial a)da$, while $(\partial V/\partial a)da$ is identified as the infinitesimal work $dW = (\partial V/\partial a)da$ performed by the manipulation of external parameter a . Together, the first law reads³

$$dW = dQ + dV. \quad (2.20)$$

For the study of entropic quantities, we start with the Gibbs entropy

$$S(t) = -k_B \int P(\vec{x}, t) \ln P(\vec{x}, t) d\vec{x}, \quad (2.21)$$

where we set $k_B = 1$, and whose time derivative reads

$$\frac{d}{dt} S(t) = - \int \frac{\partial}{\partial t} P(\vec{x}, t) \ln P(\vec{x}, t) d\vec{x} \quad (2.22)$$

$$= - \int [\ln P(\vec{x}, t) + 1] \frac{\partial P(\vec{x}, t)}{\partial t} d\vec{x} \quad (2.23)$$

This expression can be specialized in terms of the Fokker-Planck equation (2.14). As shown in Ref. [7] (see Ref. [8] for the underdamped regime), integrating by parts, using the definition of

³This is not a proof or verification of the first law, the energetic quantities are defined in order to always satisfy this equality.

\mathcal{J}_i , and the assumption that $\lim_{x_i \rightarrow \pm\infty} \mathcal{J}_i = 0$,

$$\frac{d}{dt}S(t) = \sum_i \frac{2}{\Gamma_i} \int \frac{\mathcal{J}_i^2}{P} d\vec{x} - \sum_i \frac{2}{\Gamma_i} \int f_{\text{ext},i} \mathcal{J}_i d\vec{x}, \quad (2.24)$$

where the first term is always non-negative and identified as the entropy production rate

$$\sigma := \sum_i \frac{2}{\Gamma_i} \int \frac{\mathcal{J}_i^2}{P} d\vec{x}, \quad (2.25)$$

and the second is the entropy flux rate from the system to the environment

$$\phi := \sum_i \frac{2}{\Gamma_i} \int f_{\text{ext},i} \mathcal{J}_i d\vec{x}. \quad (2.26)$$

The discrete state-space version of the entropic balance is given by transition rates and occupation probabilities [9, 10]. In terms of the probability flux from state j to i , $J_{ij}(t) = W_{ij}p(j, t) - W_{ji}p(i, t)$, the entropy production reads

$$\sigma(t) = \frac{1}{2} \sum_{ij} J_{ij}(t) \log \frac{W_{ij}p(j, t)}{W_{ji}p(i, t)}, \quad (2.27)$$

that is also known as the Schnakenberg expression, and the entropy flux

$$\phi(t) = \frac{1}{2} \sum_{ij} J_{ij}(t) \log \frac{W_{ij}}{W_{ji}}. \quad (2.28)$$

The mismatch between entropy production and entropy flux rates is, as the names suggest, the increase in entropy of the system:

$$\frac{d}{dt}S(t) = \sigma(t) - \phi(t) = \frac{1}{2} \sum_{ij} J_{ij}(t) \log \frac{p(j, t)}{p(i, t)}. \quad (2.29)$$

In the steady-state, Eqs. (2.29) and (2.24) vanish. Therefore, the entropy production rate equals the entropy flux rate: All the entropy produced is dumped into the thermal reservoirs. When detailed balance is satisfied, $J_{ij} = 0$ and $\mathcal{J}_i = 0$, therefore all fluxes stall and there is no entropy production. Here, the importance of entropy production rate starts to emerge, as a quantity that probes the distance to equilibrium.

Since the transition rates are consequences of the established coarse-graining, they convey

the notion of temperature. The connection is given by the local detailed balance condition [11] that ensures thermodynamic consistency: In the absence of external forces, the system will relax to a Gibbs equilibrium distribution. The local detailed balance states that the ratio between opposite transition rates equals the exponential of the entropy flux exchanged between system and reservoir at the event of such transition,

$$\frac{W_{ij}}{W_{ji}} = \exp(-\phi_{ij}). \quad (2.30)$$

The entropy flux ϕ_{ij} can have different expressions, depending on the parameters changing between states i and j . For instance, when the only difference between them are the energies, the entropy flux is given by the heat exchange between system and reservoir over the temperature: $\phi_{ij} = \exp[-(E_i - E_j)/k_B T]$.

In some models more than one equilibrium bath is in contact with the system of interest, which is very common in heat engines. There exists a set of transition rates related to each reservoir, and every set has to satisfy local detailed balance by itself to ensure thermodynamic consistency. The total transition rate of a transition will be given by the sum of every reservoir contribution.

Immediately, a challenge to stochastic thermodynamic becomes evident. When a transition is not reversible, in the sense that it cannot be performed in the opposite direction, the flux of entropy diverges. For this reason, many works assume *microreversibility*: The inverse of a transition can be performed if and only if said transition can.

Lastly, Eq. (2.28) for the entropy flux has a bilinear form in terms of fluxes and the log-ratio of directly involved transition rates. The last term is identified as the microscopic affinity or thermodynamic force between two states [10],

$$A_{ij} = \log \frac{W_{ij}}{W_{ji}}. \quad (2.31)$$

The notion of macroscopic affinities is of key importance in the thermodynamic analysis of systems with Markovian dynamics, and it is defined as the sum of all A_{ij} 's involved in an oriented cycle of the network [10].

2.3 Fluctuation and uncertainty relations

Fluctuation relations: Compared with the celebrated theory of (equilibrium) thermodynamics, little is known about nonequilibrium. Recent years have witnessed great development in the study of nonequilibrium thermodynamics, including stochastic thermodynamics' first milestone known as fluctuation relations [12–14]. Strikingly, they bridge nonequilibrium to equilibrium processes. For instance, the Crooks fluctuation theorem [14] leads to the Jarzynski equality [15], which states that the nonequilibrium work W involved in taking a system from one equilibrium state to another can be related to the difference in equilibrium free energy ΔF between them, $\langle \exp(-\beta W) \rangle = \exp(-\beta \Delta F)$, with β denoting the inverse temperature of the reservoir. This equality can be employed in many small-scale experiments, in particular the folding and unfolding of RNA hairpins through optical tweezers⁴ [16]. A plethora of experiments verified or applied stochastic thermodynamics results to small-scale systems, classical and quantum, arbitrarily far from equilibrium; for examples, see Ref. [17].

Whereas fluctuation relations are properties of numerous observables, we focus in particular on fluctuation relations for the entropy production rate. Let γ_τ be a trajectory over the state space, i.e. the time series of occupied states in $t \in \{0, \tau\}$; its time-reversed trajectory $\bar{\gamma}_\tau$ is such a sequence after transformation $t \rightarrow \tau - t$. The fluctuating entropy production over a steady state trajectory can be expressed as the distinguishability between the probability of a trajectory and its time reversal [18–20],

$$\Sigma_\tau[\gamma_\tau] = \log \frac{P[\gamma_\tau]}{P[\bar{\gamma}_\tau]}, \quad (2.32)$$

where we remind that $k_B = 1$. Its average value, simply dubbed the entropy production rate, is given by

$$\sigma = \lim_{\tau \rightarrow \infty} \frac{1}{\tau} \sum_{\gamma_\tau} P[\gamma_\tau] \log \frac{P[\gamma_\tau]}{P[\bar{\gamma}_\tau]} = \lim_{\tau \rightarrow \infty} \frac{1}{\tau} D(P[\gamma_\tau] || P[\bar{\gamma}_\tau]). \quad (2.33)$$

Here, we observe the connection between entropy production and irreversibility, σ quantitatively estimates the probabilistic difference between forward and backward trajectories, revealing the arrow of time. In equilibrium the trajectories and their reverse share the same probability since there is no preferential time direction $P[\gamma_\tau] = P[\bar{\gamma}_\tau]$, hence watching a video of an equilibrium system in reverse is indistinguishable from the original. Therefore, entropy production vanishes, so it is also considered a quantitative distance to equilibrium.

Entropy production is a time-asymmetric functional of the trajectory, i.e. odd under time-

⁴Optical tweezers are stochastic thermodynamics' own piston.

reversal transformation, it acquires an opposite sign when the trajectory is time reversed. From this property and definition (2.32), a fluctuation relation can be derived for the fluctuating entropy production of a steady-state trajectory, known as the detailed (steady-state) fluctuation theorem:

$$\frac{P[\Sigma_\tau]}{P[-\Sigma_\tau]} = \exp\{\Sigma_\tau\}, \quad (2.34)$$

where $P[\Sigma_\tau] = \sum_{\gamma_\tau} P[\gamma_\tau] \delta_{\Sigma_\tau[\gamma_\tau], \Sigma_\tau}$. Equation (2.34) holds beyond the stationary distribution. For instance, it has a conjugate probability $\bar{P}[-\Sigma_\tau]$ in the denominator when the evolution is not time-symmetric, e.g. in the presence of time-dependent driving, and it has explicit mentions to the heat involved between system initially at distinct temperatures in exchange fluctuation theorems [21]

Consequence of the detailed fluctuation theorem is the integral fluctuation theorem, that, as the name suggests, is obtained from the integral of Eq. (2.34). The integral fluctuation theorem of a trajectory's entropy production is

$$\langle \exp(-\Sigma_\tau) \rangle = 1. \quad (2.35)$$

With no further assumptions, Jensen's inequality leads to

$$\langle \Sigma_\tau \rangle \geq 0, \quad (2.36)$$

which is known as the second law in stochastic thermodynamics⁵.

Negative entropy production values have been related to “violations” of the second law of thermodynamics, they are feasible in microscopic systems due to the fluctuating character of the quantities involved. However, Eq. (2.34) shows that the probability of negative entropy production values is exponentially suppressed by the probability of those that are positive, leading to a non-negative average value in Eq. (2.36), which is the result observed in macroscopic thermodynamics. Therefore, negative entropy production values are possible, but come from mere fluctuations.

Lastly, when the nonequilibrium process starts and ends in equilibrium states, the entropy production can be related to the Helmholtz free energy by $\Sigma_\tau = -\beta\Delta F + \beta\mathcal{W}$. Usually τ has to be infinitely large, that way the system naturally evolves towards an equilibrium state after the nonequilibrium process. Plugging this result into the integral fluctuation theorem Eq. (2.35)

⁵It is not a proof of the second law, this property is engraved in the stochastic dynamics' assumptions [22].

we obtain the famous Jarzynski equality [15]

$$\langle \exp(-\beta \mathcal{W}) \rangle = \exp(-\beta \Delta F), \quad (2.37)$$

which relates the statistics of fluctuating work \mathcal{W} and equilibrium free energy differences.

Uncertainty relations: Ilya Prigogine, Nobel laureate “for his contributions to non-equilibrium thermodynamics, particularly the theory of dissipative structures” [23], has noted and explored the inseparable role of time in out of equilibrium systems. In his Nobel lecture he stated that “we cannot propagate signals with arbitrary speed, we cannot construct a perpetuum mobile forbidden by the second law” [24]. Prigogine compared forbidden thermodynamics phenomena to speed bounds in relativity.

Recently, a lot of effort has been concentrated into bounds that are exclusive to nonequilibrium processes. These bounds relate dissipation to fluctuations [25, 26], the speed at which tasks can be performed [27], and the indirect observation of dissipation estimators [III, 28–30]. The usefulness of such bounds goes beyond the understanding of insurmountable limits, they can be used for inference schemes: If it is known that at least some amount A of a resource has to be spent for a process to be observed, the observation of such a process logically leads to the inference that A or more was spent. The fact that a lower/upper bound is established is key for indirect observations of a physical quantity, it creates a clear connection between the inferred and the real values when only partial information is available. Interestingly, any fluctuation relation leads to the existence of a thermodynamic uncertainty relation [31, 32].

A second milestone in stochastic thermodynamics is the establishment of (original) thermodynamic uncertainty relation, that was proposed for biomolecular systems described by Markov dynamics [25]. They were rigorously proved, and many extensions followed [26, 33–43]. It shows for steady-state Markov systems that the signal-to-noise ratio of any thermodynamic flux is bounded by half the entropy production rate

$$\frac{\langle J \rangle^2}{\text{Var}(J)} \leq \frac{\Sigma}{2}, \quad (2.38)$$

where J is an arbitrary current and Σ the average entropy production. This relation shows that thermodynamics, through its celebrated entropy production, bounds nonequilibrium dynamics. For precise and strong currents, there is an unavoidable production of entropy.

There are many other relevant aspects of stochastic thermodynamics that were not covered

in this introductory Chapter, such as Maxwell demons, implications of time-dependent drivings, decompositions of entropy production, fluctuating efficiency, active matter, computation, quantum stochastic thermodynamics, and more. The field is still very active, and we expect more milestones and applications to come.

As a final comment, we highlight the role of entropy production rate in stochastic thermodynamics, supporting its regular presence throughout this thesis: It generalizes the second law for nonequilibrium processes, measures irreversibility, distance to equilibrium and energy dissipation, has particular symmetries in its probability distribution, and is connected to Lyapunov stability of Markov processes [44]. Entropy production rate is a quantity of theoretical and experimental interest, and it will be analyzed in distinct scenarios.

“Que metro serve para medir-nos? Que forma é
nossa e que conteúdo?”

Carlos Drummond de Andrade, “Perguntas em
forma de cavalo-marinho” [67]

Chapter 3

Transition-based coarse graining

Whenever a hydrogen atom emits a photon, a molecular motor moves along a microtubule, an electron tunnels inside a junction, or a ribosome translates a mRNA molecule to synthesize spike proteins, the observed phenomena arise from transitions between different states. In numerous systems of interest, a particular subset of transitions emit signals that are significantly easier to observe through the experimental apparatus, we call them *visible transitions*. For instance, despite experimental results suggesting the existence of distinct transitions to which the apparatus is insensitive, the rotation of a bacterial motor’s flagella can be observed in terms of the switch of its orientation, the only two visible transitions [45]. Moreover, another example is the directed transport of organelles by molecular motors inside cells. They are fundamental for, e.g., neuronal function and diverse cellular activities; their motion can be tracked and studied by imaging techniques, while the internal ATP-ADP metabolic cycle is experimentally unavailable due to requiring very refined resolutions [46–48].

Such systems where only partial information available pose a challenge for Markov modelling. Describing stochastic processes by the mathematics of Markov processes is successful across fields: physics [49], chemistry [50–52], biology [53–55], computation [56], and others. The Markovian description, as discussed in Chapter 2, thrives when all mesostates are known and can be monitored, allowing for detailed thermodynamic analysis even out of equilibrium [6, 57–60]. To address the challenge of analyzing experiments/simulations while being aware of the absence of some data in the collected time-series, different procedures of coarse-graining have been explored in recent years. Coarse-graining is so fundamental in equilibrium thermodynamics that its name is scarcely mentioned, the macroscopic description of gases can be viewed as a coarse-graining of the mechanical description of particles. These procedures

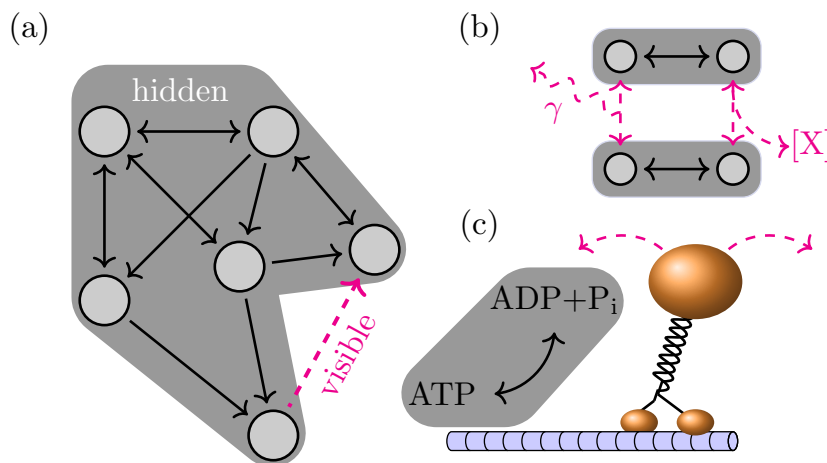


Figure 3.1: Examples of systems that emit partial information through the occurrence of a few particular transitions. (a) General scheme of a discrete state space with transitions with all states (circles) and some transitions (black arrows) hidden, while some transitions (dashed magenta arrows) visible to the observer. Examples of how this scenario can emerge in models that include (b) emission/absorption of photons γ or chemical species X , and (c) a molecular motor performing steps along a track and transitions related to displacement are detected by the cargo's position.

imply in reducing the degrees of freedom and can be done in many ways that will be non-exhaustively listed here. Lumping is a procedure where two or more states are considered as just one mesostate, the occupation of states within each mesostate are indistinguishable and the internal transitions are hidden [11, 61]. Decimation procedures record the arrival in some particular states [28, 62, 63]. Multiplex networks have replicas of the states in different layers, and they are used to model systems which often have the layer indicator as a hidden variable [64]. Also the removal of information based on the velocity of phenomena is addressed, founded by the idea that the finite apparatus resolution will be insensitive to fast changes, giving rise to the notion of timescale separation [65, 66], which is of particular interest to phase transitions [V], as discussed in Chapter 2.

Unlike previously mentioned procedures, we propose a transition-based coarse graining [VII], in touch with physical systems that only leave “footprints” at the incidence of visible transitions. As illustrated in Fig. 3.1, the underlying dynamics takes place in a discrete state space and some transitions (in dashed magenta) can be observed. In panel (a) a general scheme is presented to show that states and some transitions are hidden, panel (b) illustrates the emission of a photon γ and a chemical species X , and panel (c) represents a common model for molecular motor in which some transitions are related to mechanical motion.

Given that the visible transitions are a subset \mathcal{L} of all possible transitions, the object of

study is a trajectory comprised of sequences of transitions and the time elapsed between them, which we dub *inter-transition time*. We consider the experimenter as an observer with the ability to collect the visible phenomena and time them with an external clock. The output of an experiment is therefore a time-series that can be expressed as

$$\Gamma_T^{\mathcal{L}} : \quad \begin{array}{c} t_0 \\ \text{---} \\ \ell_0 \end{array} \text{---} \begin{array}{c} t_1 \\ \text{---} \\ \ell_1 \end{array} \text{---} \begin{array}{c} t_2 \\ \text{---} \\ \dots \end{array} \text{---} \begin{array}{c} t_{n+1} \\ \text{---} \\ \end{array} \quad (3.1)$$

where t_i denotes the inter-transition time between two successive transitions $\ell_{i-1}, \ell_i \in \mathcal{L}$, and the experiment's duration is $\sum_i t_i = T$.

The trajectory over the state-space γ_T leading to a coarse-grained observation of transitions and inter-transition times $\Gamma_T^{\mathcal{L}} = \Gamma_T^{\mathcal{L}}[\gamma_T]$ is illustrated in Fig. 3.2 below. Over a state space $\Omega = \{1, 2, 3\}$ a trajectory (black lines) takes place, but since the observer is only sensitive to visible transitions $\mathcal{L} = \{1 \rightarrow 2, 2 \rightarrow 1\}$ the collected trajectory $\Gamma_T^{\mathcal{L}}$ is limited to their occurrence (blue and magenta arrows).

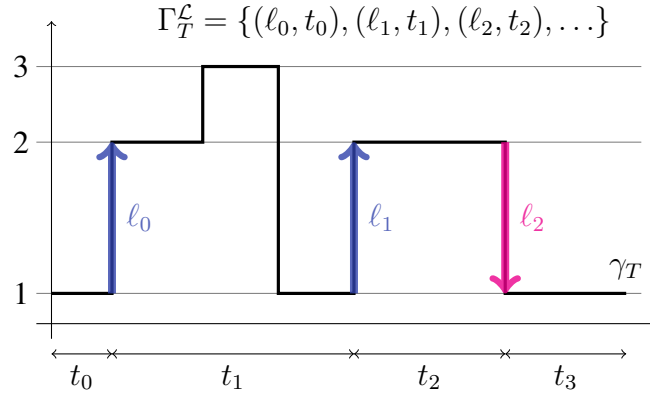


Figure 3.2: Illustration of an underlying dynamics γ_T (black lines) over state space $\Omega = \{1, 2, 3\}$ with visible transitions $\mathcal{L} = \{1 \rightarrow 2, 2 \rightarrow 1\}$, and the subsequent coarse-grained trajectory $\Gamma_T^{\mathcal{L}}$.

Statistical properties of such trajectories are characterized from three points of view. (i) *statistical*: What can be said about output probabilities from the partial information provided by the subset of visible transitions; (ii) *thermodynamical*: How and to what extent thermodynamic quantities can be inferred from the collected trajectories; (iii) *biophysical*: The formalism is applied to usual biophysical models and we study how properties such as force load and disorder show up in the measurements.

It is worth mentioning that up to this point we do not assume that all transitions are reversible, nor that there exists only one direct transition from one state to the other, however the

latter case is left out of the illustrations and its implications are only explored in the discussions Chapter 6.

3.1 First-passage time

3.1.1 Mapping and solving the problem

To study the statistics of trajectories under transition-based coarse-graining it is necessary to assess the probabilities of sequences of jumps and inter-transition times, which is done in terms of the conditional probability of the next transition $\ell_{i+1} \in \mathcal{L}$ given the previous $\ell_i \in \mathcal{L}$,

$$P(\ell_{i+1}|\ell_i), \quad (3.2)$$

and the probability¹ that the inter-transition time between them falls within $[t, t + dt)$,

$$P(t|\ell_i, \ell_{i+1})dt. \quad (3.3)$$

Notice that since these results are based on conditional probabilities, the state space distribution is not playing a role, therefore stationary and transient states are encompassed.

In words, the question being asked is: *Given the occurrence of ℓ_i , what is the probability that the first performed visible transition is ℓ_{i+1} , and that it happens after time $[t, t + dt)$?* Put like that, it is evident that it is a first-passage time problem, we do not care about the long and winding road the system might take, we are only interested in the next visible transition and the time it took.

To map the problem of first-passage time of transitions onto a usual first-passage time problem we use a technique that includes redirecting every visible transitions into auxiliary absorbing states. These states are introduced into the original state space and the problem is to find the first-passage time that one of them will be reached, and which auxiliary state will be reached first. Notice that performing a visible transition and arriving at its auxiliary state are linked events that occur simultaneously. This technique was already used in problems of first-passage time [68, 69]². It is also similar to the manipulation of networks to obtain current statistics by

¹We use the same notation for probability mass-function and probability density, each case can be deduced from the domains of the variables at hand.

²This trick was suggested by Ken Sekimoto during blackboard discussions, events that are key for the progress of theoretical physics

creating copies of some states introduced by Hill [70, 71].

Starting from a discrete state space Ω indexed as $\{1, 2, \dots, N\}$, connected by an irreducible network from which a subset of visible transitions \mathcal{L} is drawn, we introduce $|\mathcal{L}|$ auxiliary states $\{s_i\}$. In the auxiliary Markov chain, each visible transition \mathcal{L}_i is directed towards s_i (cf. Fig. 3.3) while the hidden transitions are unchanged. Since no transitions emerge from auxiliary states they are sinks (absorbing states). Whenever the evolution reaches sink s_i the dynamics stalls, at this very instant we are sure that visible transition \mathcal{L}_i occurred and, importantly, no other visible transition took place since the start of the evolution. Thus, by construction, the first-passage of a sink in the auxiliary system is equivalent to the first-passage of the respective visible transition in the original system.

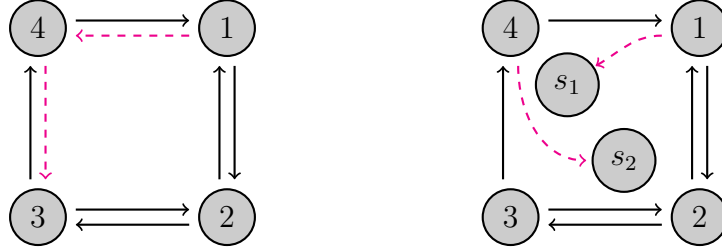


Figure 3.3: Left: Example of a 4 states network with hidden transitions (black arrows) and visible transitions $\mathcal{L} = \{1 \rightarrow 4, 4 \rightarrow 3\}$ (dashed magenta arrows). Right: Network of the auxiliary dynamics, where visible transitions are redirected to sinks s_1 and s_2 .

The auxiliary state space is $\{1, 2, \dots, |\Omega|\} \cup \{s_1, s_2, \dots, s_{|\mathcal{L}|}\}$ and the resulting auxiliary stochastic matrix \mathbf{W}_s , with dimensions $(|\Omega| + |\mathcal{L}|)^2$, has elements

$$[\mathbf{W}_s]_{ij} = \begin{cases} 0 & \text{if } i = \langle \mathcal{L}_k \rangle \text{ and } j = \langle \mathcal{L}_k \rangle, \text{ for some } 1 \leq k \leq |\mathcal{L}| \\ [\mathbf{W}]_{|\mathcal{L}_k\rangle, \langle \mathcal{L}_k \rangle} & \text{if } i = s_k, \text{ for some } 1 \leq k \leq |\mathcal{L}| \\ [\mathbf{W}]_{ij} & \text{otherwise} \end{cases} \quad (3.4)$$

The first line in Eq. (3.4) represents the exclusion of visible transitions, second line is the redirection of them, and the third line comprises the hidden transitions, that are left the same.

The auxiliary stochastic matrix \mathbf{W}_s is composed of four blocks. The top-left is the *survival matrix*, a matrix that will improve to be important to express further results,

$$\mathbf{S} := \mathbf{W} - \sum_{\ell \in \mathcal{L}} |\ell\rangle \langle \ell| \mathbf{W}^\top |\ell\rangle \langle \ell|. \quad (3.5)$$

Notice that $\langle \ell | \mathbf{W}^\top | \ell \rangle$ is the rate of transition ℓ and \mathbf{S} has dimensions $|\Omega|^2$. The survival matrix corresponds to the original stochastic matrix subtracted of every visible transitions, and it represents the evolution constrained to the absence of visible transitions, thus the name survival, borrowed from first-passage time theory.

As a consequence of the auxiliary dynamics construction, the bottom-left matrix is

$$\mathbf{L} := \sum_{i=1}^{|\mathcal{L}|} \langle \mathcal{L}_i | \mathbf{W}^\top | \mathcal{L}_i \rangle |s_i\rangle \langle \mathcal{L}_i|, \quad (3.6)$$

a $|\mathcal{L}| \times |\Omega|$ matrix comprised of the transitions redirected to the sinks. In other words, the visible transitions are removed from the stochastic matrix, and the remainder is \mathbf{S} , and they are reconstructed in the direction of sinks, unraveling \mathbf{L} .

Lastly, the rightmost blocks are zero matrices. The top one has dimensions $|\Omega| \times |\mathcal{L}|$ and represents that no transitions emerge from a sink to the original states, while the bottom one has dimensions $|\mathcal{L}| \times |\mathcal{L}|$ and represents that there are no connection between sinks. Together they display the sinks' absorbing nature.

As an illustration, the auxiliary dynamics depicted in the right-hand-side of Fig. 3.3 admits auxiliary stochastic matrices of the form

$$\mathbf{W}_s = \left(\begin{array}{cccc|cc} 1 & 2 & 3 & 4 & s_1 & s_2 \\ \hline [\mathbf{W}]_{11} & [\mathbf{W}]_{12} & [\mathbf{W}]_{13} & [\mathbf{W}]_{14} & 0 & 0 \\ [\mathbf{W}]_{21} & [\mathbf{W}]_{22} & [\mathbf{W}]_{23} & [\mathbf{W}]_{24} & 0 & 0 \\ [\mathbf{W}]_{31} & [\mathbf{W}]_{32} & [\mathbf{W}]_{33} & 0 & 0 & 0 \\ 0 & [\mathbf{W}]_{42} & [\mathbf{W}]_{43} & [\mathbf{W}]_{44} & 0 & 0 \\ \hline [\mathbf{W}]_{41} & 0 & 0 & 0 & 0 & 0 \\ 0 & 0 & 0 & [\mathbf{W}]_{34} & 0 & 0 \end{array} \right) = \left(\begin{array}{c|c} \mathbf{S} & \mathbf{0} \\ \hline \mathbf{L} & \mathbf{0} \end{array} \right) \quad (3.7)$$

From first-passage time theory [72], the cumulative probability density of not occupying an absorbing state j at time t in a Markov process starting from state i is given by the survival function

$$\mathbb{S}(t, j|i) = \sum_{k \neq j} \langle k | \exp(t\mathbf{W}_s) | i \rangle = 1 - \langle j | \exp(t\mathbf{W}_s) | i \rangle, \quad (3.8)$$

where, as discussed in Section 2, $\exp(t\mathbf{W}_s)$ is the propagator obtained from the master equa-

tion's solution. In words, Eq. (3.8) is the probability that the system is in any state other than j , during time interval $[t, t + dt)$, after being propagated from i by a master equation with stochastic matrix \mathbf{W}_s .

Let $\mathbb{F}(t, j|i)$ be the first-passage distribution, the probability density of hitting state j for the first time by time t , i.e. it hasn't been reached since the start of the evolution. The survival probability at time t is equivalent to the first-passage being greater than t :

$$\mathbb{S}(t, j|i) = \int_t^\infty ds \mathbb{F}(s, j|i) = 1 - \int_0^t ds \mathbb{F}(s, j|i), \quad (3.9)$$

where the second equality comes from the fact that \mathbb{F} is defined over the positive real numbers and is normalized. Differentiating both sides we obtain from Leibniz's integral rule and Eq. (3.8) that

$$\mathbb{F}(t, j|i) = -\frac{\partial}{\partial t} \mathbb{S}(t, j|i) = \frac{\partial}{\partial t} \langle j | \exp(t\mathbf{W}_s) | i \rangle, \quad (3.10)$$

where the first equality is a known relation between a probability measure and its cumulative.

Next, we show that the evolution between visible transitions, only comprised of visible phenomena, can be obtained in terms of the survival matrix. We start with the matrix exponential $\exp(t\mathbf{W}_s) = \sum_{n=0}^\infty t^n \mathbf{W}_s^n / n!$, and notice that a positive power $n \geq 1$ of \mathbf{W}_s can be expressed in terms of an index that runs over state space Ω and the sinks:

$$\begin{aligned} [\mathbf{W}_s^n]_{i,j} &= \sum_{k=1}^{|\Omega|} [\mathbf{W}_s]_{i,k} [\mathbf{W}_s^{n-1}]_{k,j} + \sum_{k'=s_1}^{s_{|\mathcal{L}|}} [\mathbf{W}_s]_{i,k'} [\mathbf{W}_s^{n-1}]_{k',j} \\ &= \sum_{k=1}^{|\Omega|} [\mathbf{W}_s]_{i,k} [\mathbf{W}_s^{n-1}]_{k,j}. \end{aligned} \quad (3.11)$$

For a top-left block's element, $i, j \in \{1, 2, \dots, \Omega\}$, both $[\mathbf{W}_s]_{i,k}$ and $[\mathbf{W}_s^{n-1}]_{k,j}$ in Eq. (3.11) belong to the top-left block, therefore

$$[\mathbf{W}_s^n]_{i,j} = \sum_{k=1}^{|\Omega|} [\mathbf{S}]_{i,k} [\mathbf{W}_s^{n-1}]_{k,j} = \sum_{k=1}^{|\Omega|} [\mathbf{S}]_{i,k} [\mathbf{S}^{n-1}]_{k,j} = [\mathbf{S}^n]_{i,j}, \quad (3.12)$$

where the second equality comes from the fact that positive powers can be built from $n = 1$, where the first matrix will be \mathbf{S} while the second is the identity. Bottom-left block's elements can also be worked out from Eq. (3.11) by noting that the first and second factors are respectively

elements of \mathbf{L} and \mathbf{S} . For $i, j \in \{s_1, s_2, \dots, s_{|\mathcal{L}|}\}$ and $j \in \{1, 2, \dots, \Omega\}$, it follows that

$$[\mathbf{W}_s^n]_{i,j} = \sum_{k=1}^{|\Omega|} [\mathbf{L}]_{i,k} [\mathbf{S}^{n-1}]_{k,j} = [\mathbf{L}\mathbf{S}^{n-1}]_{i,j}. \quad (3.13)$$

Also, the top and bottom-right blocks are found to be zero matrices. For $j \in \{s_1, s_2, \dots, s_{|\mathcal{L}|}\}$

$$[\mathbf{W}_s^n]_{i,j} = \sum_{k=1}^{|\Omega|} [\mathbf{W}_s^{n-1}]_{i,k} [\mathbf{W}_s]_{k,j} + \sum_{k'=s_1}^{s_{|\mathcal{L}|}} [\mathbf{W}_s^{n-1}]_{i,k'} [\mathbf{W}_s]_{k',j} = 0. \quad (3.14)$$

Using Eqs. (3.12), (3.13) and (3.14), the matrix exponential is

$$\begin{aligned} \exp(t\mathbf{W}_s) &= \sum_{n=0}^{\infty} \frac{1}{n!} t^n \mathbf{W}_s^n \\ &= \mathbf{1} + \sum_{n=1}^{\infty} \frac{1}{n!} t^n \begin{pmatrix} \mathbf{S}^n & \mathbf{0} \\ \mathbf{L}\mathbf{S}^{n-1} & \mathbf{0} \end{pmatrix} \\ &= \begin{pmatrix} \exp(t\mathbf{S}) & \mathbf{0} \\ \mathbf{L}\mathbf{S}^{-1}[\exp(t\mathbf{S}) - \mathbf{1}] & \mathbf{1} \end{pmatrix}, \end{aligned}$$

where $\mathbf{1}$ is the identity matrix with appropriate dimensions.

Plugging this result into Eq. (3.10) to obtain the first-passage time probability density to reach a sink s_j by time within $[t, t + dt)$ we obtain

$$\begin{aligned} \mathbb{F}(t, s_j | i) &= \frac{\partial}{\partial t} \langle s_j | \exp(t\mathbf{W}_s) | i \rangle = \frac{\partial}{\partial t} \langle s_j | \mathbf{L}\mathbf{S}^{-1}[\exp(t\mathbf{S}) - \mathbf{1}] | i \rangle \\ &= \langle s_j | \mathbf{L} \exp(t\mathbf{S}) | i \rangle \\ &= \langle s_j | \left[\sum_{k=1}^{|\mathcal{L}|} \langle \mathcal{L}_k | \mathbf{W}^\top | \mathcal{L}_k \rangle | s_k \rangle \langle \mathcal{L}_k | \right] \exp(t\mathbf{S}) | i \rangle \\ &= \langle \mathcal{L}_j | \mathbf{W}^\top | \mathcal{L}_j \rangle \langle \mathcal{L}_j | \exp(t\mathbf{S}) | i \rangle \end{aligned} \quad (3.15)$$

where we used the definition of \mathbf{L} , Eq. (3.6), which result in the replacement of sink s_j by its respective visible transition \mathcal{L}_j .

Now we frame the problem in terms of the inter-transition observation: Let i be the target of the last observed transition ℓ_i and the sink be related to the next observed transition ℓ_{i+1} . Then,

in terms of the notation introduced in Ref. [VII], the above equation can be expressed as

$$P(t, \ell_{i+1} | \ell_i) = \langle \ell_{i+1} | \mathbf{W}^\top | \ell_{i+1} \rangle \langle \ell_{i+1} | \exp(t\mathbf{S}) | \ell_i \rangle. \quad (3.16)$$

Equation (3.16) is a major result of this chapter and will be used to obtain further results. $P(t, \ell_{i+1} | \ell_i)$ is the probability density that the next visible transition is $\ell_{i+1} \in \mathcal{L}$, and it occurs after time $[t, t + dt)$, given that the previous visible transition $\ell_i \in \mathcal{L}$ occurred at time zero, and no other visible transitions occurred in between. The physical interpretation of such an expression is that $\langle \ell_{i+1} | \exp(t\mathbf{S}) | \ell_i \rangle$ is a probability accounting for the propagation of initial state $|\ell_i\rangle$ onto $\langle \ell_{i+1} |$, which is the initial state of the next consecutive visible transition, and it is multiplied by the rate at which transition ℓ_{i+1} occurs. Eq. (3.16) reads: $P(t, \ell_{i+1} | \ell_i)$ is given by the probability of, starting from state $|\ell_i\rangle$, reaching $\langle \ell_{i+1} |$ without the performance of any visible transition, times the rate of transition ℓ_{i+1} .

Lastly, it is also worth noting that survival propagator $\exp(t\mathbf{S})$ rules the original continuous-time Markov chain when the visible transitions are removed. However, their values are present in the exit rates $[\mathbf{W}]_{ii} = -\sum_j [\mathbf{W}]_{ji}$, therefore columns of \mathbf{S} do not add up to zero, which means that this matrix does not conserve probability. It can be interpreted as a transition matrix of a process with probability leakages: Every time a visible transition is performed the considered trajectory “dies”. Its spectrum is negative, which means

$$\lim_{t \rightarrow \infty} \exp(t\mathbf{S}) = 0 \quad (3.17)$$

and Eq. (3.10) vanishes for large times, which is a necessary property of first-passage time functions.

3.1.2 Developing the results

The result in Equation (3.16) is enough to describe the statistics of trajectories that are coarse-grained in view of a few visible transitions since it encompasses sequences of transitions and inter-transition times. Confronting analytical and experimental results of such nature can be performed with the quantities listed below.

(i) *Sequence of visible transitions*: the occurrence probability of a pair of consecutive transitions can be obtained by marginalizing the inter-transition time in Equation (3.16). Let $\ell_i, \ell_{i+1} \in \mathcal{L}$ be such a pair, the probability that ℓ_{i+1} occurs, given that the previous visible

transition was l_i , is then

$$\begin{aligned}
P(l_{i+1}|l_i) &= \int_0^\infty dt P(t, l_{i+1}|l_i) \\
&= \langle l_{i+1} | \mathbf{W}^\top | l_{i+1} \rangle \langle l_{i+1} | \int_0^\infty dt \exp(t\mathbf{S}) | l_i \rangle \\
&= \langle l_{i+1} | \mathbf{W}^\top | l_{i+1} \rangle \langle l_{i+1} | \mathbf{S}^{-1} \exp(t\mathbf{S}) \Big|_0^\infty | l_i \rangle \\
&= -\langle l_{i+1} | \mathbf{W}^\top | l_{i+1} \rangle \langle l_{i+1} | \mathbf{S}^{-1} | l_i \rangle,
\end{aligned} \tag{3.18}$$

where in the last equality we used the fact that \mathbf{S} is a negative matrix, all of its eigenvalues have negative real part, therefore $\lim_{t \rightarrow \infty} \exp(t\mathbf{S}) = 0$ and $\det(\mathbf{S}) = \prod_i \lambda_i \neq 0$, which ensures the existence of \mathbf{S}^{-1} . The second factor in Equation (3.18) represents, for any inter-transition time, the propagation from the target of the first transition to the source of the next one, $-\langle l_{i+1} | \mathbf{S}^{-1} | l_i \rangle$, while the first $\langle l_{i+1} | \mathbf{W}^\top | l_{i+1} \rangle$ is precisely the transition rate of the next transition. Since the process is ergodic, the first passage time of performing any of the visible transitions at any given time (i.e. with marginalized time) is normalized

$$\sum_{l_{i+1} \in \mathcal{L}} \mathbb{F}(l_{i+1}|l_i) = - \sum_{l_{i+1} \in \mathcal{L}} \langle l_{i+1} | \mathbf{W}^\top | l_{i+1} \rangle \langle l_{i+1} | \mathbf{S}^{-1} | l_i \rangle = 1, \tag{3.19}$$

hence probabilities $P(l_{i+q}|l_i)$ are also normalized.

From an experiment performed up until time τ , the analysis of a collected time-series leads to the construction of the empirical frequency for a sequence of visible transitions

$$F_\tau(l_{i+1}|l_i) \equiv \frac{\#_\tau(l_i \rightarrow l_{i+1})}{\sum_{j=1}^{|\mathcal{L}|} \#_\tau(l_i \rightarrow l_j)}, \tag{3.20}$$

where $\#_\tau(\bullet)$ counts the occurrence of an event in the recorded time-series. Due to ergodicity, the long-time value and the ensemble average of this frequency equals to the probability in Equation (3.18), in fact it will happen for every empirical frequency studied here: $P(\bullet) = \langle F_\tau(\bullet) \rangle = \lim_{\tau \rightarrow \infty} F_\tau(\bullet)$.

(ii) *Inter-transition times*: with no further assumptions, the inter-transition time probability

density can be obtained from Equations (3.16) and (3.18) as a property of joint probabilities

$$P(t|\ell_i, \ell_{i+1}) = \frac{P(t, \ell_{i+1}|\ell_i)}{P(\ell_{i+1}|\ell_i)} = -\frac{\langle \ell_{i+1} | \exp(t\mathbf{S}) | \ell_i \rangle}{\langle \ell_{i+1} | \mathbf{S}^{-1} | \ell_i \rangle}, \quad (3.21)$$

for the inter-transition time between a pair $\ell_i, \ell_{i+1} \in \mathcal{L}$.

Experimentally, such quantity is built by recording the inter-transition times taking place when the desired pair of transitions occur

$$F_\tau(t|\ell_i, \ell_{i+1})dt \sim \text{histogram}(t|\ell_i, \ell_{i+1}), \quad (3.22)$$

which is asymptotically and on average approaching Equation (3.21).

Inter-transition time densities provide some hints about the transitions in question. For instance, if one transition ends where the next starts, $|\ell_i\rangle = \langle \ell_{i+1}|$, the inter-transition time might be infinitesimally small. This can be seen from Equation (3.21), at $t = 0$ $\partial_t P(t|\ell_i, \ell_{i+1})$ and $\langle \ell_{i+1} | \mathbf{S} | \ell_i \rangle$ share the same sign. The latter is always negative at its diagonal elements, thus the probability value has to be positive at zero time, yielding the largest likelihood of null times between a transition that ends where the next is rooted.

Conversely, any pair of transitions that do not satisfy above property will have an increasing inter-transition time density at the origin. The shape of such densities contain information about the relation between the addressed transitions, which represents a candidate for topology inferences from measured inter-transition times.

Figure 3.4 contains inter-transition time probability densities for a system inspired by molecular motors [73]. In this kind of motors the chemical transformations and state occupancy is hidden, only two transitions are visible: forward and backward mechanical motion. Let + and – denote transitions that cause opposite displacement of such molecular motor. Alternated pairs of transitions +- and -+ satisfy the property $|\ell_i\rangle = \langle \ell_{i+1}|$, leading to an always decreasing density that has its peak at null time, which does not happen for repeated transitions. This property is observed in Figure 3.4.

Assuming that the survival matrix \mathbf{S} has a non-degenerate spectrum [74] and *hidden irreducibility*, i.e. that the state space is still irreducible after the removal of every visible transitions, Equation (3.21)'s numerator can be expressed in terms of eigenvalues of \mathbf{S} by $\langle \ell_{i+1} | \exp(t\mathbf{S}) | \ell_i \rangle = \sum_{k=1}^N c_k e^{ts_k}$, where s_k are the eigenvalues, with negative real part, and c_k real-valued coefficients that can be obtained by projecting the expression onto the survival matrix's eigenbasis.

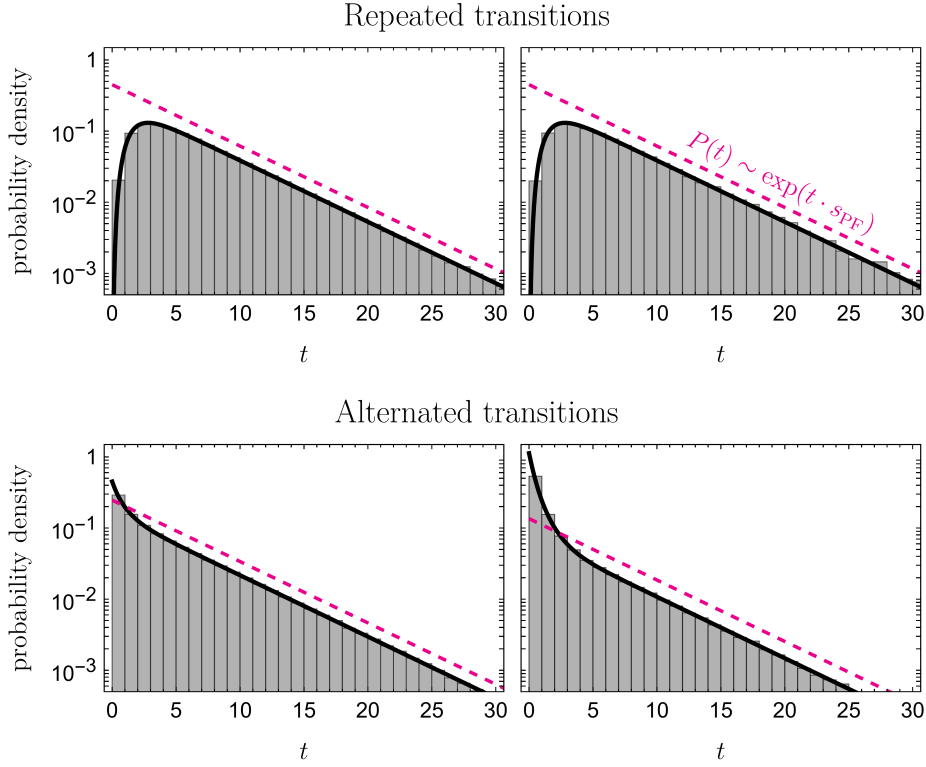


Figure 3.4: Simulation and analytical results for inter-transition time probability densities of a molecular motor model with visible transitions between a pair of states. Histograms for the empirical frequency (grey bars) and analytical probabilities from Equation (3.21) (black curve) are shown for repeated and alternated pairs of transitions. Dashed magenta lines have \mathbf{S} 's largest eigenvalue as slope and are arbitrarily placed for illustration purposes.

In the long-time limit the expressions asymptotically converge to the same exponential irrespective of the transitions considered, i.e.

$$\lim_{t \rightarrow \infty} \frac{1}{t} \ln [\langle \ell_{i+1} | \exp(t\mathbf{S}) | \ell_i \rangle] \asymp s_{\text{PF}}. \quad (3.23)$$

where s_{PF} is the dominant Perron-Frobenius root. Hence, all possible inter-transition time probability densities share the same tail, an exponential decay with the largest eigenvalue of the survival matrix. This can be observed by the dashed magenta lines in Figure 3.4.

Usually, first-passage time problems aim at evaluating mean first passage times (MFPT). From the present results, they are of straightforward calculation, since the full probability density is at hand. It suffices to integrate it as the definition of statistical moments:

$$\text{MFPT}(l_i, l_{i+1}) = \int_0^\infty dt t P(t | l_i, l_{i+1}) = - \frac{\langle \ell_{i+1} | (\mathbf{S}^{-1})^2 | \ell_i \rangle}{\langle \ell_{i+1} | \mathbf{S}^{-1} | \ell_i \rangle}, \quad (3.24)$$

and its fluctuations can be obtained by evaluation of higher-order moments. Notice how the

value is once again obtained from matrix elements of survival matrix's inverse.

Thus far, no assumptions on the distribution over state space were made, which is an advantage of conditional probabilities. The state space is collapsed at the target of the last visible transition, where we root the observation. Hence all results presented until this point hold for any state space distribution, at any given time. For the next statistical entity we have to make the use of state space distribution.

(iii) *Unconditional probabilities*: assuming stationarity, the distribution over states satisfying $\mathbf{W} |p_\infty\rangle = 0$, the probability that a transition from a time-series is ℓ can be expressed as

$$P(\ell) = \frac{1}{\langle K \rangle} \langle \ell | \mathbf{W}^\top | \ell \rangle \langle \ell | p_\infty \rangle, \quad (3.25)$$

where the pre-factor ensures normalization and is the expected *visible traffic rate*, the mean number of visible transition per unit of time at stationarity

$$\langle K \rangle := \sum_{\ell} \langle \ell | \mathbf{W}^\top | \ell \rangle \langle \ell | p_\infty \rangle. \quad (3.26)$$

The visible traffic rate is a value that is symmetric under time-reversal and equivalent to other quantities that are relevant for the description of nonequilibrium stochastic systems [75], sometimes referred to as dynamical activity [76] and frenesy [77–79].

Before proceeding, two additional remarks are worth mentioning. First, part of the formalism can be alternatively derived from Large Deviation Theory [80]. Let \mathbf{W}_λ be the tilted generating matrix, it has the values of \mathbf{W} under transformation $[\mathbf{W}]_{|\ell\rangle, \langle \ell|} \mapsto [\mathbf{W}]_{|\ell\rangle, \langle \ell|} e^\lambda$, for every $\ell \in \mathcal{L}$, and λ is a counting field. The moment generating function for a current that “clicks” every time a visible transition is performed can be calculated as $\sum_y \langle y | \exp(t\mathbf{W}_\lambda) | x \rangle$ [81]. In the limit of $\lambda \rightarrow \infty$ it counts 1 all the trajectories where ϕ is zero (survival) and zero for trajectories where visible transitions were performed, and the tilted matrix recover the survival matrix \mathbf{S} .

Second, the first-passage time of transitions developed herein generalizes the well established result of first-passage time of a state. Consider a state i of a network and the set of all transitions leading to it $\mathcal{L}_i = \{i' \rightarrow i : \forall i' \neq i\}$. The first-passage time that any transition in \mathcal{L}_i is performed is equivalent to the first-passage time of reaching i , which can be obtained from

Equation (3.16),

$$P(t|j, i)dt = \sum_{\ell \in \mathcal{L}_i} P(t, \ell|j)dt = \sum_{\ell \in \mathcal{L}_i} \langle \ell | \mathbf{W}^\top | \ell \rangle \langle \ell | \exp(t\mathbf{S}) | j \rangle dt, \quad (3.27)$$

where the evolution starts in state j .

3.2 Entropy production inference

A central quantity to be measured in system out of equilibrium is the entropy production, as discussed in Section 2, but of difficult accessibility in many systems. In particular coarse-grained systems miss many contributions to the entropy production, therefore inference schemes are necessary to assess dissipation and irreversibility of systems that only emit partial information.

From Schnakenberg's expression for the entropy production rate at stationarity [10, 30],

$$\sigma = \lim_{T \rightarrow \infty} \sum_{i < j} J_{ij}(T) \ln \frac{W_{ij}}{W_{ji}}, \quad (3.28)$$

it gets evident that entropy production depends only on the statistics of the number of transitions per unit of time $J_{ij}(T)$ between every pairs of states $j \rightarrow i$ up to a time T that is taken to infinity. Inter-transition times do not contribute to the total entropy production rate. Jumps are weighted by the log-ratio $\ln W_{ij}/W_{ji}$, which in thermodynamically consistent systems is related to energy exchanges by local detailed balance.

The fact that transitions reveal information about entropy production and that complete monitoring of systems is often not feasible has led to the development of works that estimate entropy production by the transitions between a subset of visible states [28, 82, 83]. Here we introduce a scheme that need not be supported by the visibility of states, instead, transitions are the visible phenomena.

3.2.1 Definition and lower bound

Entropy production can be quantitatively defined as the distinguishability between the probability of a trajectory and its time reverse [19, 20], which is done in terms of the Kullback-Leibler divergence: $D[P(x)||Q(x)] = \sum_x P(x) \ln[P(x)/Q(x)] \geq 0$, a non-negative quantity that only vanishes when $P(x) = Q(x) \forall x$ [84]. For a trajectory $\gamma(t)$ defined in $t \in [0, T]$, the steady-state

entropy production rate is

$$\sigma = \lim_{T \rightarrow \infty} \frac{1}{T} k_B D[P(\gamma) || \bar{P}(\bar{\gamma})], \quad (3.29)$$

where k_B is Boltzmann's constant, $P(\gamma)$ is the probability that the trajectory takes value γ at the time of evaluation. $\bar{P}(\bar{\gamma})$ is the probability of its time-reversed version, where \bar{P} also carries a hat since the protocol is also reversed when considering time-reversed dynamics.

Through Eq. (3.29), it gets evident why entropy production rate is a measure of irreversibility. It only vanishes when the probability of a process and its time-reverse exactly coincide, and it increases the larger the difference between distributions of forward and backward processes.

When a system only allows for the collection of coarse-grained data, non-negative contributions for the entropy production are missed, leading to a smaller measurement of its value. This is highlighted as a property of the Kullback-Leibler divergence [19, 85]: Given two random-variables with well-defined probability distributions, the divergence between the joint and non-joint probabilities satisfy $D[P_1(x, y) || P_2(x, y)] \geq D[P_1(x) || P_2(x)]$. Thus, washing away the hidden data implies in a *visible entropy production* $\sigma_{\mathcal{L}}$ that is smaller than the total one:

$$\sigma_{\mathcal{L}} := \lim_{T \rightarrow \infty} \frac{1}{T} k_B D \left(P[\Gamma_T^{\mathcal{L}}] || P[\bar{\Gamma}_T^{\mathcal{L}}] \right) \leq \lim_{T \rightarrow \infty} \frac{1}{T} k_B D \left(P[\gamma_T] || P[\bar{\gamma}_T] \right) = \sigma. \quad (3.30)$$

The above inequality is valid beyond the stationary state and, since it is a way of writing the data processing inequality, establishes the entropy production rate as an information-theoretic measure of the distance to equilibrium. It can be written in terms of relative entropies to assess the thermodynamics of quantum systems.

It is really useful that an inequality is established between the measured and desired quantities, otherwise the measurement would have blurred meaning. An observed can always be sure that the entropy production rate is, at least, $\sigma_{\mathcal{L}}$.

3.2.2 Inter-transition time revealing the arrow of time

Entropy production is a measure of the distance to equilibrium. Whenever a system satisfies detailed-balance its entropy production vanishes, as so do heat and particle net currents. Monitoring a single current of a system means that it will stall at scenarios that might or might not be in equilibrium, since parameters can be tuned to stall one current even when other currents have finite net values. Therefore, using one current to infer entropy production, as in the thermodynamic uncertainty relation, can mislead to the conclusion of equilibrium states.

Using solely the sequence of transitions within a trajectory, as in the case of single integrated current monitoring, hinders the irreversible character of inter-transitions times. As discussed, the coarse-grained trajectory presents information about the occurrence of transitions and the interval between them, both can be explored to infer quantities. While the first has been extensively explored, the second recently proved to entail information about irreversibility [28].

In some cases the system can be irreversible, even though the sequence of observed phenomena leads to a vanishing net current. Consider the following example [illustrated in Fig. 3.5]: A boy named Ludwig is asked to collect a parcel for his mom Katharina, as soon as he leaves the house he tells her goodbye and goes to a post office at walking distance. Immediately after getting there, he texts his mom saying he arrived, collected the parcel right away, and will be heading home. After some time, the boy, struggling with such a heavy load, arrives at home and opens the door to find the grateful mom.



Figure 3.5: Ludwig on his way to the post office and his way back home carrying a heavy parcel. The first takes a time t_M and the second a usually larger time t_H .

Consider the mom as an experimenter. She is unaware of all the details of Ludwig's path, the only collected information is that he left home, after some time t_M he arrived at the post office, and after some time t_H he got back home. At the end of the day, the son is back home. If the mom is a regular online shopper, she will be able to ask Ludwig to collect many parcels and gather good statistics of the process. The statistics related to the sequence of events is the following: Every occurrence of the process involves Ludwig going out and getting back, there's no net movement, if Katharina interprets it as a current she will come to the conclusion that its net value vanishes and therefore the system might be in equilibrium. However, if Katharina have read some papers like [VII, 28, 29, 86], she knows that inter-transition times' statistics has to be considered as well. She then proceeds to observe that the distribution of times t_M and t_H differ, precisely because the process of coming back from the post office is slower due to the cost of carrying parcels. Thus, Katharina concludes that the process is not reversible and she can even find a non-zero lower bound for the entropy production from inter-transition time

measurements.

3.2.3 Visible irreversibility

Having discussed the reasoning behind asymmetry of inter-transition times contributing to irreversibility, we dissect the inferred entropy production and pinpoint its contribution.

To study irreversibility quantification through entropy production it is necessary to establish the definition of a time-reversed trajectory, both for the underlying process in state [Equation (3.29)] and transition spaces [right-hand-side of Equation (3.30)]. The time-reversal of a visible trajectory is not a naive inversion of its recorded phenomena. For both cases, the underlying process, taking place in state space, ought to be reversed. The observable trajectory, depending on available apparatus, is a consequence of such.

Let γ_τ be a state-space trajectory comprised of visited states, arrival times, and with no hidden information. Reversing a physical process leads to trajectory $\bar{\gamma}_\tau$, which has the same states of γ_τ but in the opposite order and time goes under transformation $t \rightarrow \tau - t$.

For $\Gamma_\tau^\mathcal{L}$, the coarse-grained version of γ_τ when only transitions in \mathcal{L} are visible, not only the order of transitions have to be reversed but also their directions. ‘‘Arriving at state i ’’ is a time-symmetric phenomena, whereas ‘‘transition $j \rightarrow i$ ’’ is not. It gets evident the need for another assumption when dealing with entropy production inference: The existence and visibility of every visible transition’s reverse, i.e. $(i \rightarrow j) \in \mathcal{L} \Rightarrow (j \rightarrow i) \in \mathcal{L}$.

Further, since inter-transition times are measured as the time preceding a visible transition, in the time-reversed scheme they will be translated because they will now succeed that transition. A transition-based coarse-grained trajectory and its time-reversed are thus

$$\Gamma_\tau^\mathcal{L} = \{(\ell_0, t_0), (\ell_1, t_1), \dots, (\ell_n, t_n)\} \quad (3.31)$$

and

$$\bar{\Gamma}_\tau^\mathcal{L} = \{(\bar{\ell}_n, t_{n+1}), (\bar{\ell}_{n-1}, t_n), \dots, (\bar{\ell}_0, t_1)\}. \quad (3.32)$$

See Figure 3.6 for an example of state space trajectory and its coarse-grained version, and the time reversal of both.

Notice that the last inter-transition time t_{n+1} is not present in Equation (3.31), as well as t_0 in Equation (3.32). In both observations, they are an immediate consequence of previously recorded inter-transition times through $\sum_{i=0}^{n+1} t_i = \tau$.

$$\Gamma_\tau^\mathcal{L} = \{(1 \rightarrow 2, t_0), (1 \rightarrow 2, t_1), (2 \rightarrow 1, t_2)\}$$

$$\bar{\Gamma}_\tau^\mathcal{L} = \{(1 \rightarrow 2, t_3), (2 \rightarrow 1, t_2), (2 \rightarrow 1, t_1)\}$$

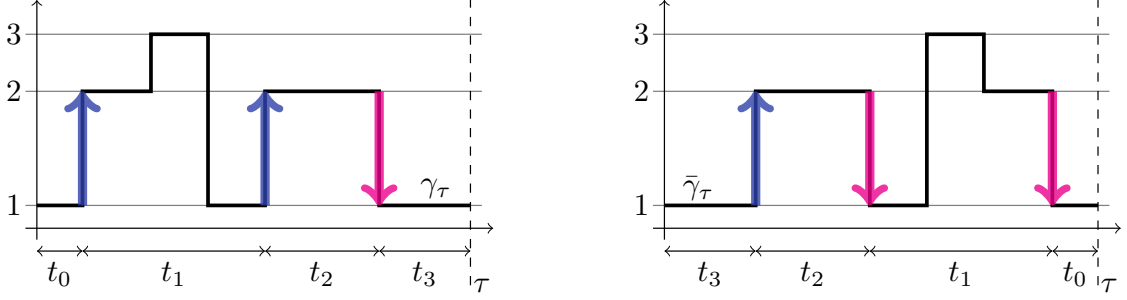


Figure 3.6: *Time reversal of a trajectory.* Left: A trajectory $\Gamma_\tau^\mathcal{L}$ collected from a process over states $\{1, 2, 3\}$ (black line) with visible transitions (highlighted arrows) in $\mathcal{L} = \{1 \rightarrow 2, 2 \rightarrow 1\}$, t_i are inter-transition times. Right: The time-reversed process and consequent reversed trajectory $\bar{\Gamma}_\tau^\mathcal{L}$.

Irreversibility is a property related to the statistics of trajectories, and it quantifies the relative entropy between forward and backward trajectories. For that, we study probabilities $P[\Gamma_\tau^\mathcal{L}]$. We adopt the notation

$$P[\Gamma_\tau^\mathcal{L}] \equiv P(\vec{t}|\vec{\ell})P(\vec{\ell}), \quad (3.33)$$

where \vec{t} is the sequence of inter-transition times between all the visible transitions $\vec{\ell}$. From probability theory $P[\Gamma_\tau^\mathcal{L}] = P(\vec{\ell})P(\vec{t}|\vec{\ell})$.

Assuming Markovianity of the sequence $\vec{\ell}$, which is later proved on Section 3.3, notice that

$$P(\vec{\ell}) = P(\ell_0) \prod_{i=1}^n P(\ell_i|\ell_{i-1}) \quad (3.34)$$

is the path probability of such a sequence, while inter-transition times follow

$$P(\vec{t}|\vec{\ell}) = P(t_0) \prod_{i=1}^n P(t_i|\ell_{i-1}, \ell_i). \quad (3.35)$$

The boundary terms $P(\ell_0)$ and $P(t_0)$ depend on events previous to the observation, however for the long-time statistical behavior their contribution will wane.

Standard manipulations over the inferred entropy production equation yield

$$\begin{aligned}
\sigma_{\mathcal{L}} &= \lim_{\tau \rightarrow \infty} \frac{1}{\tau} \sum_{\Gamma_{\tau}^{\mathcal{L}}} P[\Gamma_{\tau}^{\mathcal{L}}] \ln \frac{P[\Gamma_{\tau}^{\mathcal{L}}]}{P[\bar{\Gamma}_{\tau}^{\mathcal{L}}]} \\
&= \lim_{\tau \rightarrow \infty} \frac{1}{\tau} \sum_{\vec{\ell}} \int d\vec{t} P(\vec{t}|\vec{\ell}) P(\vec{\ell}) \ln \frac{P(\vec{t}|\vec{\ell}) P(\vec{\ell})}{P(\vec{t}|\vec{\bar{\ell}}) P(\vec{\bar{\ell}})} \\
&= \lim_{\tau \rightarrow \infty} \frac{1}{\tau} \sum_{\vec{\ell}} \int d\vec{t} P(\vec{t}|\vec{\ell}) P(\vec{\ell}) \left\{ \ln \frac{P(\vec{t}|\vec{\ell})}{P(\vec{t}|\vec{\bar{\ell}})} + \ln \frac{P(\vec{\ell})}{P(\vec{\bar{\ell}})} \right\} \quad (3.36)
\end{aligned}$$

Due to the autonomous character of the process, there is no dependence on the instantaneous time, leading to a time-translational symmetry. Therefore, using Equations (3.34) and (3.35), the sum above asymptotically goes to the typical term multiplied by the traffic rate,

$$\begin{aligned}
\sigma_{\mathcal{L}} &= \lim_{\tau \rightarrow \infty} \frac{1}{\tau} \sum_{\vec{\ell}} \int d\vec{t} P(\vec{t}|\vec{\ell}) P(\vec{\ell}) \left\{ \dots + \ln \frac{P(t_i|\ell_i, \ell_{i+1})}{P(t_i|\bar{\ell}_{i+1}, \bar{\ell}_i)} + \ln \frac{P(\ell_i)}{P(\bar{\ell}_i)} + \dots \right\} \\
&= \lim_{\tau \rightarrow \infty} \frac{1}{\tau} \sum_{\vec{\ell}} P(\vec{\ell}) \left\{ \dots \int dt_i P(t_i|\vec{\ell}) \ln \frac{P(t_i|\ell_i, \ell_{i+1})}{P(t_i|\bar{\ell}_{i+1}, \bar{\ell}_i)} + \ln \frac{P(\ell_i)}{P(\bar{\ell}_i)} + \dots \right\} \\
&= \langle K \rangle \sum_{\ell, \ell' \in \mathcal{L}} P(\ell|\ell') P(\ell') \left\{ \ln \frac{P(\ell|\ell')}{P(\bar{\ell}'|\bar{\ell})} + D[P(t|\ell', \ell) || P(t|\bar{\ell}, \bar{\ell}')] \right\}, \quad (3.37)
\end{aligned}$$

which leads to the definition of entropy production rate due to transitions sequence

$$\sigma_{\ell} := \langle K \rangle \sum_{\ell, \ell' \in \mathcal{L}} P(\ell|\ell') P(\ell') \ln \frac{P(\ell|\ell')}{P(\bar{\ell}'|\bar{\ell})} \quad (3.38)$$

and to inter-transition times

$$\sigma_t := \langle K \rangle \sum_{\ell, \ell' \in \mathcal{L}} P(\ell|\ell') P(\ell') D[P(t|\ell', \ell) || P(t|\bar{\ell}, \bar{\ell}')] \quad (3.39)$$

for any visible set \mathcal{L} of reversible transitions. Notice that the sum runs over all possible pairs of visible transitions in \mathcal{L} , which is very natural since the sequence contribution comprises of conditional probabilities and the inter-transition times contribution of time span between such pairs. At equilibrium both vanish; thus, no irreversibility can be erroneously detected. Out of equilibrium, they can vanish in different scenarios, which become evident for the case of observing a single pair of transitions: σ_{ℓ} vanishes when no net current is present and σ_t vanishes in ring structures. Furthermore, as proven in Ref. [87], when the hidden network either has no

cycles or satisfies detailed balance, σ_t vanishes and $\sigma_{\mathcal{L}} = \sigma$

3.2.4 Single current observation

A paradigmatic example of few visible transitions observation is the monitoring of a single current. The displacement of a molecular motor, the charge flow through a junction and the exchange of chemical species with a reservoir are some examples of systems where a single current is being measured over time. See Figure 3.7.

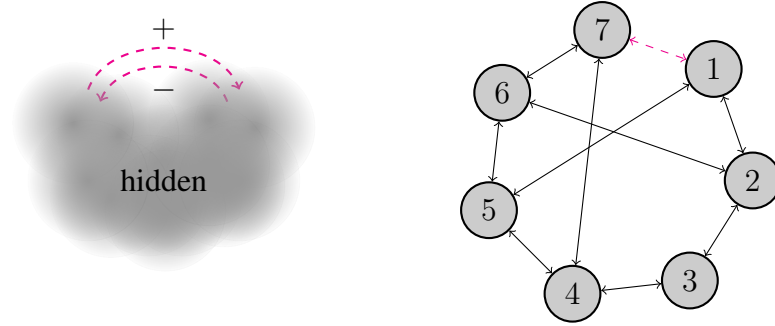


Figure 3.7: Examples of single current observation schemes, two transitions in opposite directions emerge from a hidden system (left), such a system can have any topology e.g. seven states with many transitions and a visible transition pair between two states (right).

The current is defined as the number of times the system jumps from a given state to another one, without going through any other states in between, minus the number of opposite jumps. We adopt the notation $\mathcal{L} = \{+, -\}$, and the integrated value of the monitored current is

$$J_{\tau} = \frac{\#\tau(+)-\#\tau(-)}{\tau}. \quad (3.40)$$

Expressions for entropy production inference get substantially simplified when dealing with a single current and, further, reveal new physical properties. First, let's study the transition sequence's contribution [Equation (3.39)]. The sum $\sum_{\ell, \ell' \in \mathcal{L}}$ leads to four terms, but two of them vanish,

$$\begin{aligned} \sigma_{\ell} &= \langle K \rangle \left\{ P(+|+)P(+)\ln \frac{P(+|+)}{P(-|-)} + P(+|-)P(-)\ln \frac{P(+|-)}{P(+|-)} \right. \\ &\quad \left. + P(-|+)P(+)\ln \frac{P(-|+)}{P(-|+)} + P(-|-)P(-)\ln \frac{P(-|-)}{P(+|+)} \right\} \\ &= \langle K \rangle \left\{ P(+|+)P(+)-P(-|-)P(-) \right\} \ln \frac{P(+|+)}{P(-|-)}. \end{aligned} \quad (3.41)$$

The same happens for inter-transition times' contribution [Equation (3.39)],

$$\begin{aligned}
\sigma_t &= \langle K \rangle \left\{ P(+|+)P(+)\cancel{D[P(t|+, +)||P(t|-, -)]} \right. \\
&\quad + P(+|-)P(-)\cancel{D[P(t|-, +)||P(t|-, +)]} \\
&\quad + P(-|+)P(+)\cancel{D[P(t|+, -)||P(t|+, -)]} \\
&\quad \left. + P(-|-)P(-)D[P(t|-, -)||P(t|+, +)] \right\} \\
&= \langle K \rangle \sum_{\ell=\{+,-\}} P(\ell|\ell)P(\ell)D[P(t|\ell, \ell)||P(t|\bar{\ell}, \bar{\ell})]. \tag{3.42}
\end{aligned}$$

The two vanishing terms are the contribution of sequences $(+, -)$ and $(-, +)$, and their inter-transition time. We dub these as *alternated transitions*, and they do not contribute since they do not change under time reversal, remember that the order has to be reversed as well as the directions. Meanwhile *repeated transitions* $(+, +)$ and $(-, -)$ account for all of the irreversibility.

A recent important result is the thermodynamic uncertainty relation, an inequality relation moments of any current to the entropy production of a system. It is strikingly general for steady-state systems and describes a trade-off between precision and dissipation. It has also been used as a tool for entropy production inference when only partial information is available. Using the statistics of an empirical time-integrated current, the thermodynamic uncertainty relation reads

$$\sigma_{\text{TUR}} := \frac{2\langle J \rangle^2}{\text{Var}(J)} \leq \sigma, \tag{3.43}$$

which states that the entropy production rate is lower bounded by the average and variance of any stationary current $J = \lim_{t \rightarrow \infty} \langle \sum_{i < j} d_{ij} n_{ij}^{\text{stat}}(t) \rangle / t$ flowing over the system [25, 26], with d_{ij} being the asymmetric current increment related to transition $j \rightarrow i$ and $n_{ij}^{\text{stat}}(t)$ the number of such transitions in a time interval t . For each trajectory, the stochastic time-integrated current J depends on the number of transitions in each direction, hence the full statistics of sequence of transitions should contain at least the same amount of information as the statistics of J , therefore we conjecture $\sigma_{\text{TUR}} \leq \sigma_\ell$. Moreover the inter-transition times contribute to the entropy production rate and goes unnoticed by $\langle J \rangle$ and $\text{Var}(J)$, therefore the contribution σ_t contains additional information such as the detection of irreversibility in the absence of net currents.

Fig. 3.8 illustrates how the entropy production inference is obtained using empirical esti-

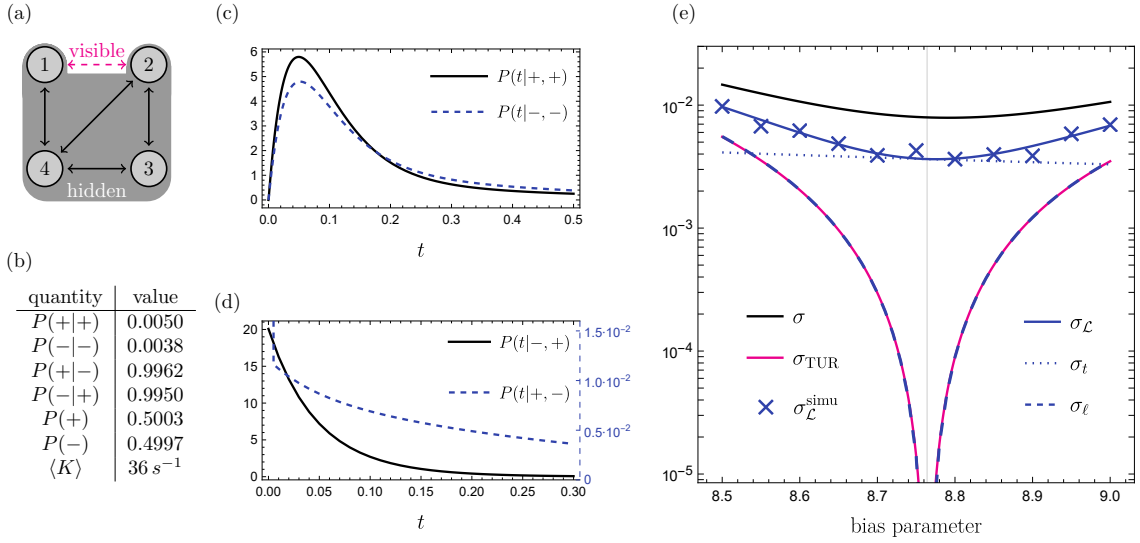


Figure 3.8: *Estimating entropy production rate (k_B/s) from repeated transition statistics:* Illustration of the inference scheme for a network depicted in (a) with the observation of transitions $+ = 1 \rightarrow 2$ and $- = 2 \rightarrow 1$. From the analytical equations, we show (b) conditional and unconditional probabilities of transitions, and the value of traffic rate, inter-transition time probability densities for (c) repeated and (d) alternated transitions. (e) In terms of a bias parameter, entropy production σ in a solid black curve, thermodynamic uncertainty relation's lower bound σ_{TUR} in a magenta solid curve, results from a Gillespie simulation $\sigma_{\mathcal{L}}^{\text{simu}}$ are shown in blue dots with error bars; followed by the present results of inferred entropy production rate $\sigma_{\mathcal{L}}$ in solid blue, and its decomposition in inter-transition times σ_t in dotted blue and sequence of transitions σ_{ℓ} in dashed blue. The vertical line is the value of the (dimensionless) bias parameter for which the visible current vanishes. More details: Transition rates are $W_{24} = W_{34} = W_{41} = W_{43} = 1$, $W_{14} = W_{21} = W_{32} = W_{42} = 20$ and W_{12} equals the exponential of the bias parameter; in (b)-(e) the bias parameter is fixed to 8.5; simulations were performed with a Gillespie algorithm for 2×10^6 s, the Kullback-Leibler divergence of inter-transition times was obtained with an unbiased estimation scheme.

mates of $P(\pm|\pm)$ and $P(t|\pm, \pm)$ as a function of a bias parameter, a value present in transition rates that controls the bias towards a given orientation. In a four-state multicyclic network, panel (e) shows the entropy production rate σ (solid black line) that is indeed larger than its discussed lower bounds. The contribution from sequence of transitions σ_{ℓ} (dashed blue) coincides with the thermodynamic uncertainty relation σ_{TUR} (solid magenta) and they vanish for a value of bias parameter that stalls the current between $1 \leftrightarrow 2$, which is known as stalling force. The inter-transition time contribution is less sensitive to the bias parameter in this region. It does not vanish at the stalling force, leading to the detection of irreversibility when no net current is visible.

Lastly, for different values of bias parameter, a single trajectory of visible transitions and inter-transition times from Gillespie simulations was analyzed in view of Eqs. (3.38) and (3.39) to obtain the inferred entropy production rate $\sigma_{\mathcal{L}}^{\text{simu}}$ (blue crosses), in good agreement with the

analytical $\sigma_{\mathcal{L}}$. Due to the Kullback-Leibler divergence in σ_t we employed an unbiased method to the simulated data.

3.2.5 Kullback-Leibler estimation

Estimating entropic functionals such as the Kullback-Leibler divergence of two distributions from finite data is known to be a non-straightforward task that often leads to systematic errors, it constitutes a field in itself [19, 88, 89]. It is of particular importance in nonequilibrium thermodynamics since entropy production, one of the most studied quantities, is the relative entropy between forward and backward trajectories [19]. Consider data regarding a system in equilibrium, biased convergence of the estimator might lead to the erroneous conclusion that the system is out of equilibrium. Furthermore, inference schemes to deal with finite data have been largely explored in the analytical sense, as discussed in this paper, hence the need for accurate estimators.

The Kullback-Leibler divergence is present in Eq. (3.39) and poses a problem for the inference from a time-series. The most intuitive approach involves estimating the probability distribution from data collected from an experiment or simulation, and later evaluating the integral $D[P||Q] = \int P \ln P/Q$, however it leads to a biased estimation. A method developed in Ref. [90] explores the comparison between the cumulative distributions of two independent data sets to obtain an unbiased estimation of the Kullback-Leibler divergence. This method was applied to the analysis of simulated results present in Fig. 3.8.

The code is available and ready to use in Ref. [91] with further details and illustrations of generating visible transitions' time-series, and evaluating Kullback-Leibler divergences and $\sigma_{\mathcal{L}}$. It can be of particular importance to the application of the present results, in particular entropy production estimation from time-series, but also to any other application that involves comparing two empirical probability distributions.

Briefly, the method consists of taking two finite data sets sampled from two independent processes with distributions $P(x)$ and $Q(x)$. Linear interpolations $P_c(x)$ and $Q_c(x)$ are rendered from the empirical cumulative distributions and for small enough ϵ the estimator converges to the Kullback-Leibler divergence

$$\frac{1}{n} \sum_{i=1}^n \ln \frac{P_c(X_i) - P_c(X_i - \epsilon)}{Q_c(X_i) - Q_c(X_i - \epsilon)} - 1 \rightarrow D[P(x)||Q(x)], \quad (3.44)$$

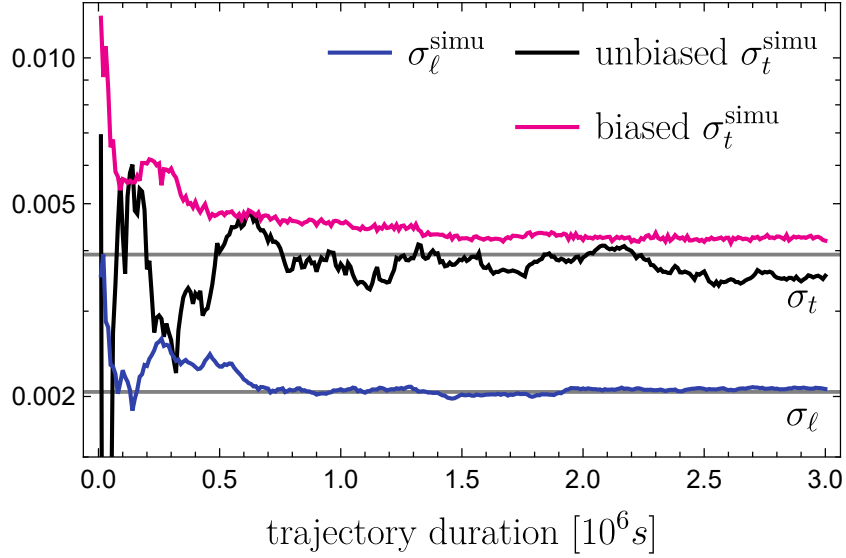


Figure 3.9: Convergence of both contributions to the entropy production rate inferred from simulations $\sigma_{\mathcal{L}}^{\text{simu}}$ [cf. Fig. 3.8] with bias parameter 8.6. The top curve (magenta) σ_t^{simu} is the inter-transition times' contribution evaluated by the biased method of first inferring the distributions, middle curve (black) is the same but with the unbiased method [90, 91]. The bottom curve (blue) stems from the sequence of transitions contribution from the simulated data $\sigma_{\ell}^{\text{simu}}$. The analytical values of both σ_t and σ_{ℓ} are shown in horizontal gray lines.

where n is the number of points X_i from the data with distribution $P(x)$.

Figure 3.9 shows the converge of σ_{ℓ} and σ_t estimates. The value of $\sigma_{\ell}^{\text{simu}}$ has a fast convergence using the empirical frequencies of transition occurrences. The top curve (biased σ_t^{simu}) was evaluated by estimating the probability distributions with kernel density estimations methods and numerically evaluating Kullback-Leibler divergence's integral, leading to a clear bias above the expected value. Using Eq. (3.44) through the resources in Ref. [91], the middle curve (unbiased σ_t^{simu}) indeed shows no evident sign of bias in the estimation.

3.2.6 Ring networks

A ring network has the specific topology in which states i are only connected to both $i \pm 1$, consequently there is a single cycle and a single affinity [10]. See Figure 3.10 below for an illustration. Networks with ring topology are an important particular case for the inference of irreversibility as will be shown in the present section.

At the stationary distribution, the unique macroscopic flux can be measured from any edge of the network since the current will be the same between any two states, i.e. $[\mathbf{W}]_{i+1,i}p_{\infty}(i) - [\mathbf{W}]_{i,i+1}p_{\infty}(i+1)$ for any i . To the best of our knowledge, there was no analogous result for the macroscopic affinity, until recently [VII]. Its value is usually assessed by the log-ratio of

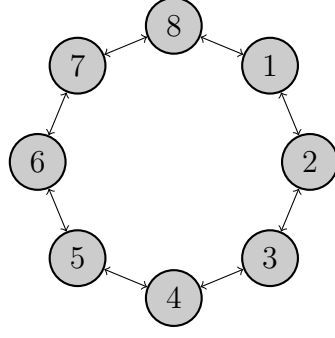


Figure 3.10: Example of a ring network with 8 states and transitions in both directions.

every transition rate along the ring $\ln \prod_i (W_{i+1,i}/W_{i,i+1})$, it turns out that it can be obtained by the sequence of transitions' statistics over a single edge.

The stochastic matrix of a ring has a tridiagonal structure, plus two terms on its corners, W_{1N} and W_{N1} . The probabilities of repeated transitions benefit from this form, using the relation between inverse and adjugate of a matrix, and the Laplace expansion for the determinant, we obtain that the effective affinity is exactly the real affinity A ,

$$A_{\text{eff}} = \ln \frac{P(+|+)}{P(-|-)} = \ln \prod_i \frac{W_{i+1,i}}{W_{i,i+1}} = A, \quad (3.45)$$

leading to a novel interpretation of the affinity on a ring in terms of conditional probabilities of sequence of visible transitions. In this case $\sigma_{\mathcal{L}} = J_{\mathcal{L}}A$, which is the definition of entropy production σ in a cycle, therefore $\sigma_{\mathcal{L}}$ equals the system's entropy production from the observation of any single pair of opposite transitions:

$$\sigma_{\mathcal{L}} = \sigma_{\ell} = \sigma. \quad (3.46)$$

The full entropy production of a ring network can be assessed by a single experiment in which a marginal observer collects statistics of a single pair of transitions over the same edge, ruling out the necessity of assessing all the microscopic details of stationary probabilities, transition rates, and even inter-transition times. In fact, $\sigma_{\mathcal{L}}$ uses the same information employed to the thermodynamic uncertainty relation.

In addition, ring structures present a symmetry in their inter-transition time densities, proven in Refs. [VII] and [87]. It is reminiscent of the Haldane equality [92–94] and reads: The inter-transition time probability densities between a sequence of repeated transitions are exactly the

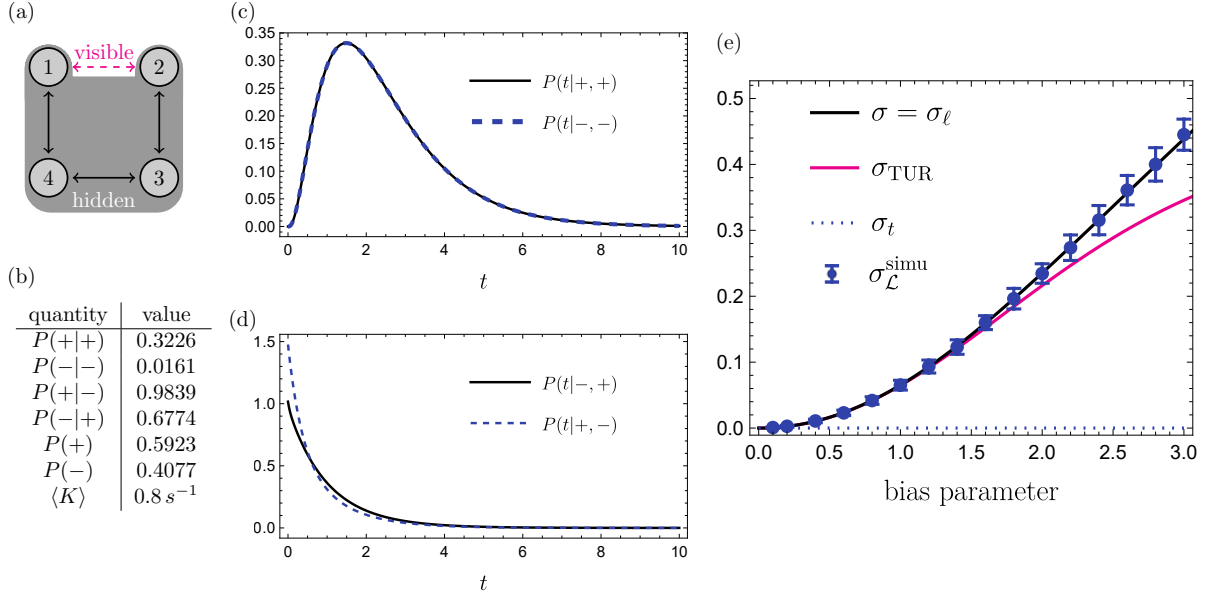


Figure 3.11: For a ring with four states, ring network, and visible transitions $+ = 1 \rightarrow 2$ and $- = 2 \rightarrow 1$, as illustrated in (a), we show in (b) the conditional and unconditional probabilities of transitions and the visible traffic rate. (c) is the coinciding inter-transition time densities for repeated transitions and (d) for alternated. (e) is a summary of the entropy production rate inference scheme: Entropy production σ and the sequence of transitions contribution σ_{ℓ} coincide, both in solid black; inter-transition time contribution σ_t in dotted blue is shown to vanish; the thermodynamic uncertainty relation σ_{TUR} is depicted in solid magenta and simulations $\sigma_{\mathcal{L}}^{\text{simu}}$ in blue dots with error bars. All transitions rates are equal to 1 apart from W_{14} that is the exponential of the dimensionless bias parameter, and entropy production rate dimensions are k_{B}/s .

same³,

$$P(t|+, +) = P(t|-, -). \quad (3.47)$$

This symmetry implies $\sigma_t = 0$, which is consistent with the facts that $\sigma_{\ell} = \sigma$ and $\sigma_{\ell} + \sigma_t = \sigma$.

Fig. 3.11 shows the entropy production inference scheme for a ring network of four states. The contribution σ_t vanishes for any value of bias parameter due to the equality of inter-transition time densities for repeated transitions shown in panel (c). The values of σ and σ_{ℓ} are precisely the same (solid black) as discussed in Eq. (3.46). Meanwhile, σ_{TUR} provides a lower bound that is approximately saturated for vanishing values of bias parameter, which represents the close to equilibrium regime.

³This property might look counter-intuitive, in particular for rings with a bias towards one direction. Notice that the orientation is given and the random variable is only the cycle duration. The time between transitions is only ruled by the exit rates of the visited nodes, which are the same in a ring regardless of the direction performed

3.3 Markov chain in visible transition space

We have split visible entropy production rate into its contributions from transition sequences and inter-transition times, and the notion of time proves to be particularly important in the absence of net fluxes. Conversely, inter-transition times play no role in integrated currents: To evaluate an integrated current, the only quantities required are the number of each visible transition and the total time.

We introduce the idea of transition space, where each mesoscopic “state” represents the visible transition last performed. When delving into transition space, details of hidden jumps and sojourn times are coarse-grained away, and inter-transition times are also lost. Delving deeper, we can establish a process with discrete-time where a new visible transition is performed at each step. For integrated currents, together with the notion of number of transitions per unit of time, this will suffice. In summary, from the underlying continuous-time Markov-chain in state space and a given set of visible transitions, a Markov chain is established in the space of transitions, and we dub the jumps in transition space as “trans-transitions”.

Such a process has an evolution matrix \mathbf{M} with elements $P(\ell'|\ell)$, that can be obtained from Equation (3.18). Notice that any survival function $\mathbb{S}(\bullet) = 1 - \int \mathbb{F}(\bullet)$ [Equation (3.8)] has to vanish for $t \rightarrow \infty$ since ergodic systems will eventually perform any transition. Consequently, the first-passage function $\mathbb{F}(\bullet)$ is normalized. In view of the developed first-passage time of performing a visible transition, the first-passage function is given by $\sum_{\ell_{i+1} \in \mathcal{L}} P(t, \ell_{i+1}|\ell_i)$, thus

$$1 = \int_0^{\infty} dt \sum_{\ell_{i+1} \in \mathcal{L}} P(t, \ell_{i+1}|\ell_i) = - \sum_{\ell_{i+1} \in \mathcal{L}} \langle \ell_{i+1} | \mathbf{W}^T | \ell_{i+1} \rangle \langle \ell_{i+1} | \mathbf{S}^{-1} | \ell_i \rangle = \sum_{\ell_{i+1} \in \mathcal{L}} P(\ell_{i+1}|\ell_i), \quad (3.48)$$

which means that the columns of \mathbf{M} add up to unity and the process on visible transitions space \mathcal{L} is Markovian.

Markovianity of the sequence of visible transitions is not an obvious property, other coarse-graining procedures lead to non-Markovian processes unless some time-scale separation is considered [11, 28, 62].

Ergodicity in state space means that there is always a path with positive probability connecting the target of a transition to the source of another, which means that there will always be a path in space \mathcal{L} connecting one visible transition to the other. Hence, the Markov chain defined by \mathbf{M} is also ergodic. Further, we assume and introduce the concept of *hidden irreducibility*:

After removing transitions \mathcal{L} from the state space, the resulting network is still irreducible. In other words, there is always a path with positive probability connecting any states solely formed by hidden transitions, which leads to a fully connected Markov chain in space \mathcal{L} .

3.4 Fluctuation relations

The fluctuation relation (FR), one of the most encompassing result about nonequilibrium systems, states that, for a set of integrated currents $\vec{c} = \tau \vec{J}$ cumulated up to some stopping time τ , the log-ratio of their positive to negative probabilities is linear

$$\log \frac{p_\tau(\vec{c})}{p_\tau(-\vec{c})} = \vec{f} \cdot \vec{c}. \quad (3.49)$$

The above relation holds at times τ beaten by an external clock (upon a proper choice of initial distribution [95], or asymptotically) only if the observer has access to (fundamentally) all currents and forces in the system's state space, up to boundary contributions. Instead, it does not generally hold if some of the currents are not visible.

The state space can be depicted as a graph with states as nodes and transitions as directed links, for example



Notice that not all transitions need be reversible. We will instead focus on the statistics of a single current, as described in Section 3.2.4. Without loss of generality we take $\uparrow = 1 \leftarrow 2$ and $\downarrow = 2 \leftarrow 1$ as our visible transitions, on the assumption that there are no other mechanisms connecting 1 and 2 directly. We further assume *hidden irreducibility*, i.e. the existence of a non-zero probability path between any pair of states not containing visible transitions.

For a physical picture, these transitions could be associated with measurable emission and absorption of photons of frequency ω with a thermal bath at inverse temperature β . Local

detailed balance then implies in the equality

$$\frac{W_{1,2}}{W_{2,1}} = \exp \hbar\beta\omega. \quad (3.51)$$

We assume non-degeneracy, that is $1 \leftrightarrow 2$ is the only transition exchanging photons of that energy (from now on $\hbar\omega = 1$), and that the temperature can be regulated.

From the transition space Markov chain 3.3 we can arrange trans-transition probabilities in a trans-transition matrix

$$P := \begin{pmatrix} p(\uparrow | \uparrow) & p(\uparrow | \downarrow) \\ p(\downarrow | \uparrow) & p(\downarrow | \downarrow) \end{pmatrix}, \quad (3.52)$$

which is a discrete-time transition matrix in the following space of transitions:



Thus, the sequence of visible transitions is a Markov chain in transition space, which by hidden irreducibility is fully connected. This result also holds for a larger number of visible transitions. Notice that here the Markov property is preserved by lifting the observable process into a different space. Other decimation procedures anchored on states typically break markovianity, which is only recovered in the limit of time-scale separation [11, 62].

The probability of transition path $\vec{\ell} = \{\ell_0, \ell_1, \dots\}$ is

$$p(\vec{\ell}) = p_1(\ell_1) \prod_{k=1}^{n-1} p(\ell_{k+1} | \ell_k), \quad (3.54)$$

where $p_1(\bullet)$ is the probability that the first recorded transition. We now compare it to that of its time-reversed, both sampled from the same initial distribution, by taking their ratio. The time-reversed of $p(\ell | \vec{\ell})$ is itself, therefore all such terms cancel out and we are left with

$$\frac{p(\vec{\ell})}{p(\vec{\ell})} = \frac{p_1(\ell_1)}{p_1(\vec{\ell}_n)} \left[\frac{p(\uparrow | \uparrow)}{p(\downarrow | \downarrow)} \right]^{n_{\uparrow\uparrow}(\vec{\ell}) - n_{\downarrow\downarrow}(\vec{\ell})} \quad (3.55)$$

where $n_{\ell\ell'}(\vec{\ell})$ is the number of times trans-transition $\ell \rightarrow \ell'$ occurs along the path.

Letting $j(\ell) := \delta_{\ell,\uparrow} - \delta_{\ell,\downarrow}$ be the instantaneous current, signaling when a transition occurs,

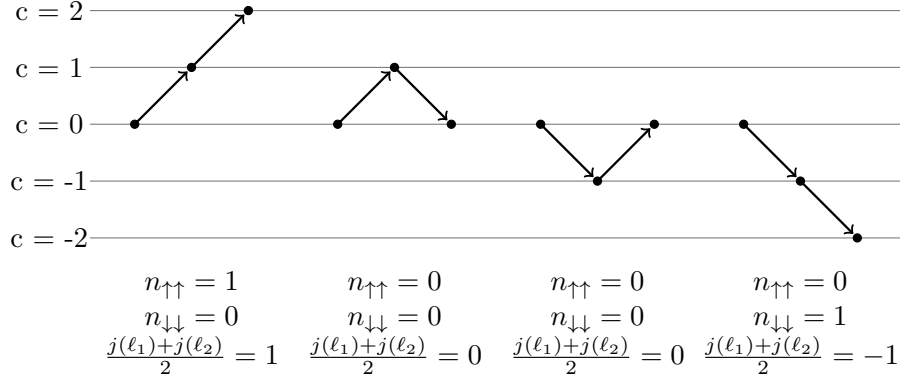


Figure 3.12: Counting of the current as per Eq. (3.57)

we focus on the integrated current

$$c(\vec{\ell}) := \sum_{k=1}^n j(\ell_k) = n_{\uparrow}(\vec{\ell}) - n_{\downarrow}(\vec{\ell}). \quad (3.56)$$

where n_{ℓ} is the number of times transition ℓ has been performed along the process. Notice that, it can only take values $\{-n, -n+2, \dots, n-2, n\}$, and that it is anti-symmetric by time reversal, $c(\vec{\ell}) = -c(\vec{\ell})$. Importantly, we can also express it in terms of the trans-transition numbers $n_{\ell\ell}$ as

$$c(\vec{\ell}) = n_{\uparrow\uparrow}(\vec{\ell}) - n_{\downarrow\downarrow}(\vec{\ell}) + \frac{j(\ell_1) + j(\ell_n)}{2}. \quad (3.57)$$

The first term is due to the fact that occurrences of $\uparrow\downarrow$ and $\downarrow\uparrow$ always reset the current to its initial value, and therefore only self-loops contribute to it. The second boundary term is less intuitive, and is explained in Fig. 3.12.

From the probability of a path in transition-space $p(\vec{\ell})$ we can introduce the joint probability of a path and the value of its current

$$p(c, \vec{\ell}) = \delta_{c, c(\vec{\ell})} p(\vec{\ell}), \quad (3.58)$$

which is normalized since $\sum_{c, \vec{\ell}} p(c, \vec{\ell}) = \sum_{\vec{\ell}} p(\vec{\ell}) = 1$.

The probability of a path can be expressed in terms of the probability of the number of its pairs of transitions. Marginalizing over the bulk transitions, all the transitions apart from the

first and last, we obtain

$$\begin{aligned}
p(c, \ell_1, \ell_n) &= \sum_{\ell_2, \dots, \ell_{n-1}} p(c, \vec{\ell}) = \sum_{\ell_2, \dots, \ell_{n-1}} \delta_{c, c(\vec{\ell})} p(\vec{\ell}) \\
&= \sum_{\ell_2, \dots, \ell_{n-1}} \delta_{c, c(\vec{\ell})} p_1(\ell_1) \prod_{m=2}^n p(\ell_m | \ell_{m-1}) \\
&= p_1(\ell_1) \sum_{\ell_2, \dots, \ell_{n-1}} \delta_{c, c(\vec{\ell})} [p(\uparrow | \uparrow)]^{n_{\uparrow\uparrow}(\vec{\ell})} [p(\downarrow | \downarrow)]^{n_{\downarrow\downarrow}(\vec{\ell})} \\
&\quad \times [p(\uparrow | \downarrow)]^{n_{\uparrow\downarrow}(\vec{\ell})} [p(\downarrow | \uparrow)]^{n_{\downarrow\uparrow}(\vec{\ell})}
\end{aligned} \tag{3.59}$$

whereas for the time-reversed the effective force A_{eff} can be cast to express pairs of transitions of $\vec{\bar{\ell}}$ in terms of $\vec{\ell}$'s pairs:

$$\begin{aligned}
p(-c, \bar{\ell}_1, \bar{\ell}_{n-1}) &= \sum_{\bar{\ell}_2, \dots, \bar{\ell}_{n-1}} p(-c, \vec{\bar{\ell}}) = \sum_{\ell_2, \dots, \ell_{n-1}} \delta_{-c, c(\vec{\bar{\ell}})} p(\vec{\bar{\ell}}) \\
&= \sum_{\ell_2, \dots, \ell_{n-1}} \delta_{c, c(\vec{\bar{\ell}})} p_1(\bar{\ell}_n) \prod_{m=2}^n p(\bar{\ell}_{m-1} | \bar{\ell}_m) \\
&= p_1(\bar{\ell}_n) \sum_{\ell_2, \dots, \ell_{n-1}} \delta_{c, c(\vec{\bar{\ell}})} [p(\uparrow | \uparrow)]^{n_{\uparrow\uparrow}(\vec{\bar{\ell}})} [p(\downarrow | \downarrow)]^{n_{\downarrow\downarrow}(\vec{\bar{\ell}})} \\
&\quad \times [p(\uparrow | \downarrow)]^{n_{\uparrow\downarrow}(\vec{\bar{\ell}})} [p(\downarrow | \uparrow)]^{n_{\downarrow\uparrow}(\vec{\bar{\ell}})} \\
&= p_1(\bar{\ell}_n) \sum_{\ell_2, \dots, \ell_{n-1}} \delta_{c, c(\vec{\bar{\ell}})} [p(\downarrow | \downarrow) e^{A_{\text{eff}}}]^{n_{\downarrow\downarrow}(\vec{\bar{\ell}})} [p(\uparrow | \uparrow) e^{-A_{\text{eff}}}]^{n_{\uparrow\uparrow}(\vec{\bar{\ell}})} \\
&\quad [p(\uparrow | \downarrow)]^{n_{\uparrow\downarrow}(\vec{\bar{\ell}})} [p(\downarrow | \uparrow)]^{n_{\downarrow\uparrow}(\vec{\bar{\ell}})} \\
&= p_1(\bar{\ell}_n) e^{-A_{\text{eff}}(c - [j(\ell_1) + j(\ell_n)]/2)} \frac{p(c, \ell_1, \ell_n)}{p_1(\ell_1)}.
\end{aligned} \tag{3.60}$$

To obtain the expression above, we used the following properties: The sum over all possible paths is the same for the time-reversed paths $\sum_{\ell_m} = \sum_{\bar{\ell}_m}$; reversing the path changes the sign of the charge $\delta_{c, c(\ell)} = \delta_{-c, c(\bar{\ell})}$; pairs of repeated transitions change, $n_{\uparrow\uparrow}(\bar{\ell}) = n_{\downarrow\downarrow}(\ell)$ and $n_{\downarrow\downarrow}(\bar{\ell}) = n_{\uparrow\uparrow}(\ell)$, while alternated do not, $n_{\uparrow\downarrow}(\bar{\ell}) = n_{\uparrow\downarrow}(\ell)$ and $n_{\downarrow\uparrow}(\bar{\ell}) = n_{\downarrow\uparrow}(\ell)$; the effective affinity yields $e^{A_{\text{eff}}} = p(\uparrow | \uparrow)/p(\downarrow | \downarrow)$; lastly, we also use Equation (3.57) $c(\ell) = n_{\uparrow\uparrow}(\ell) - n_{\downarrow\downarrow}(\ell) + [j(\ell_1) + j(\ell_n)]/2$.

Notice that $j(\ell_n) = -j(\bar{\ell}_n)$ and, introducing the potential

$$u(\ell) := A_{\text{eff}}j(\ell)/2 - \log p_1(\ell), \quad (3.61)$$

above expression simplifies to the joint fluctuation relation of charge and boundary transitions

$$\frac{p(c, \ell_1, \ell_n)}{p(-c, \bar{\ell}_1, \bar{\ell}_n)} = \exp\{A_{\text{eff}}c + u(\bar{\ell}_n) - u(\ell_1)\}. \quad (3.62)$$

This result can acquire the fluctuation theorem form in all its glory, i.e. a pure exponential of the current, in three different scenarios. When satisfied, the equation reads

$$\frac{p_n(c)}{p_n(-c)} = \exp A_{\text{eff}}c, \quad (3.63)$$

which is the recovery of a fluctuation relation for partial information.

The first and most obvious case is for large currents $c \gg 1$, where the contribution is suppressed. Therefore, one should expect to see the exponential behavior for large fluctuations of c . Secondly, the potential vanish when $\ell_1 = \bar{\ell}_n$. From the collected ensemble of trajectories, a filtering procedure of post-selecting trajectories satisfying this property will give rise to the fluctuation relation. Lastly, the potential difference can be vanished by selecting as the initial distribution

$$p_1(\ell) \propto p(\ell|\ell), \quad (3.64)$$

dubbed preferential distribution. This particular initial distribution ensures that the potential difference vanishes for every combination of first and final transitions of a trajectory, as can be seen from Eq. (3.61) and the table below.

ℓ_1, ℓ_n	$u(\bar{\ell}_n) - u(\ell_1)$, with $p_1(\ell) \propto p(\ell \ell)$
\uparrow, \uparrow	$-A_{\text{eff}} - \ln[p(\downarrow \downarrow)/p(\uparrow \uparrow)] = 0$
\uparrow, \downarrow	$-\ln[p(\uparrow \uparrow)/p(\uparrow \uparrow)] = 0$
\downarrow, \uparrow	$-\ln[p(\downarrow \downarrow)/p(\downarrow \downarrow)] = 0$
\downarrow, \downarrow	$A_{\text{eff}} - \ln[p(\uparrow \uparrow)/p(\downarrow \downarrow)] = 0$

The statistics of a current can also be entailed in the cumulant generating function, and the same stands for the fluctuation relation. For large values of $n \rightarrow \infty$ the contribution from the

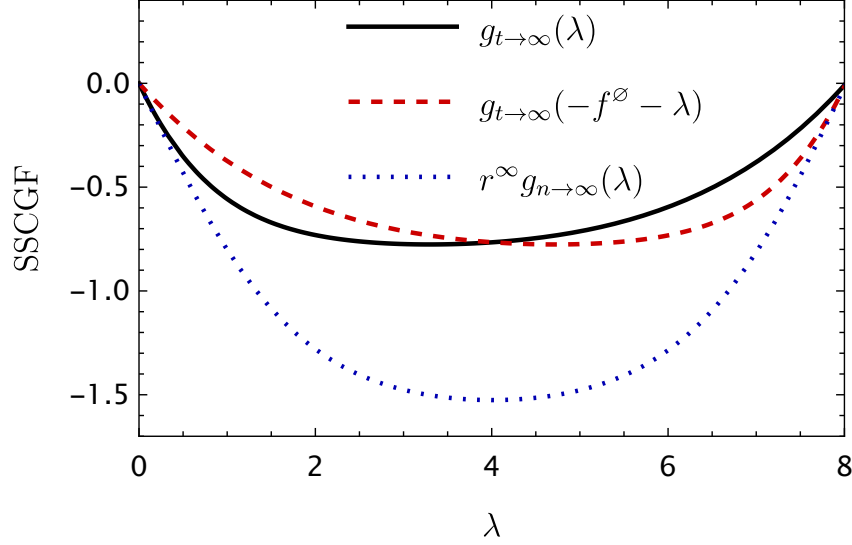


Figure 3.13: The charge's scaled cumulant generating function at long time (dominant eigenvalue of the tilted rate matrix obtained by $R_\ell \rightarrow R_\ell e^{\lambda j(\ell)}$) and at large number of transitions (logarithm of the dominant eigenvalue of the tilted trans-transition matrix, obtained by tilting $p(\ell|\ell') \rightarrow p(\ell|\ell') e^{\lambda j(\ell)}$). Only the second displays the fluctuation symmetry $\lambda \rightarrow -A_{\text{eff}} - \lambda$.

potential term is suppressed and, letting $g_{\tau \rightarrow \infty} = \lim_{\tau \rightarrow \infty} \tau^{-1} \log \langle e^{\lambda c} \rangle$ for $\tau = t, n$ (stopping time and stopping number of transitions) be the generating functions of the cumulants of the stationary charge at long times/large number of transitions, the FR can be cast as the symmetry

$$g_{n \rightarrow \infty}(\lambda) = g_{n \rightarrow \infty}(-A_{\text{eff}} - \lambda) \quad (3.65)$$

uniquely in terms of the effective force, which is known to be operationally determined by $A_{\text{eff}} = \beta - \beta^\varnothing$ in terms of the inverse temperature β^\varnothing that causes the current to stall [82]. Fig. 3.13 shows that the symmetry is typically not satisfied at large times for stopping time, but only when the observation is taken at the beat of the current.

3.5 Biophysical applications

Here we apply our theoretical framework to bio-molecular machines where partial information, stemming from the observation of few transitions, is experimentally accessible. For example, DNA polymerase [96], data obtained from single-molecule FRET microscopy [97, 98] and optical tweezers [99, 100] to resolve the displacement of a motor along a track, yet most of the structural and chemical degrees of freedom are hidden. Inspired by these experimental limitations, we first focus on two examples of biologically-relevant molecular machines in which we

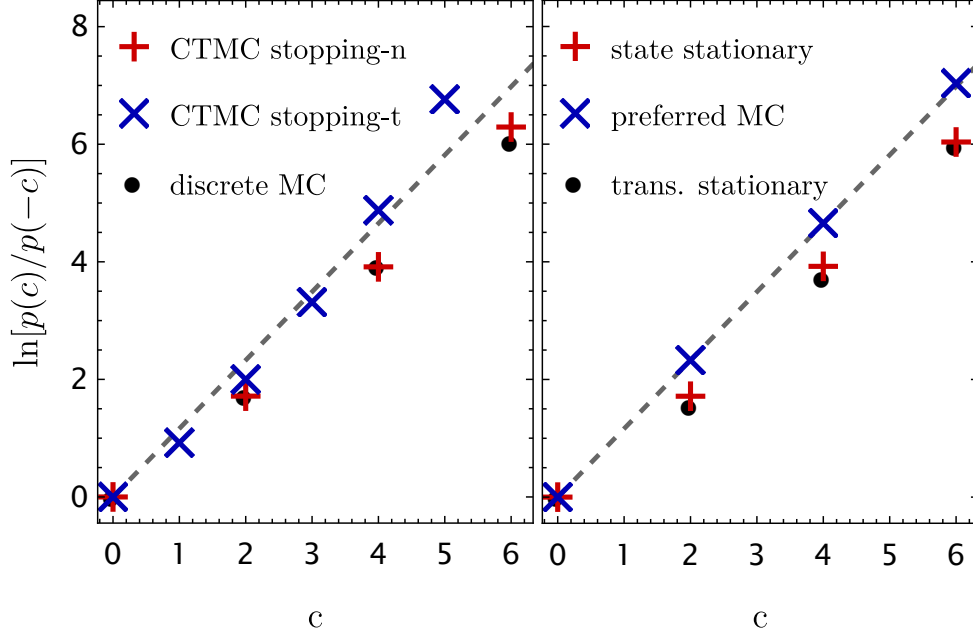


Figure 3.14: Plots of $\log p_{\tau}(+c)/p_{\tau}(-c)$, $c \geq 0$ for different stopping times and processes, for the four-state system in Eq. (3.50), current along $1 \leftrightarrow 2$, a suitable choice of rates, equal number of samples. *Left*: Sampling from the stationary distribution, comparison of CTMC at clock time t , at stopping time the total number of visible transitions n , and of transition-space Markov chain at discrete clock time n . *Right*: CTMC at stopping time n sampled from different initial distributions: transition-space stationary, state-space stationary, preferential distribution, showing that this latter lie on the the line with slope $A_{\text{eff}}c$ (dashed line).

assume that one can only resolve mechanical transitions involving spatial displacements dynein and kinesin, which serve as case studies of ring and multicyclic networks, respectively. Next, we extend our study to motors that move in heterogeneous tracks, and study the effect of the degree of disorder in the statistics of transitions.

3.5.1 Molecular motors

Dyneins are cytoskeletal nano-scale motors that move along microtubules inside cells and perform varied range of functions, like intracellular cargo transport and beating of flagella [101, 102]. Dyneins transduce chemical energy from ATP hydrolysis into mechanical work done by displacing loads along the microtubule.

Here, we study a unicyclic seven-state kinetic model of dynein stepping (cf. Fig. 3.15) that has a ring topology and is described in [103, 104]. During every forward stepping cycle, one ATP molecule binds to the dynein (D) ($1 \rightarrow 2$), thereby triggering the release of the dynein from the microtubule (MT) ($2 \rightarrow 3$). This is followed by the hydrolysis of ATP that induces a conformational change of the dynein (D^*) ($3 \rightarrow 4$) and consequently leads to microtubule binding

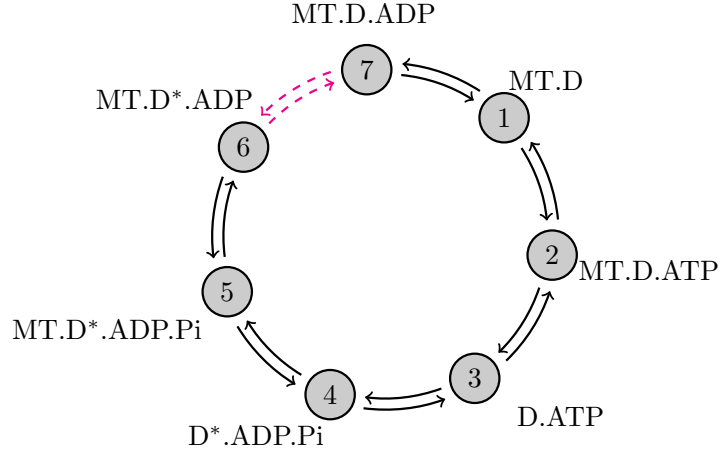


Figure 3.15: Sketch of the chemo-mechanical ring network for dynein with visible transitions $6 \leftrightarrow 7$. The meaning of the transitions between each states and the experimentally inferred values of the transition rates are listed in Table. 3.1.

(4→5). In the next step, release of one phosphate group Pi (5→6) is followed by a power stroke (6→7), and release of one adenosine diphosphate molecule ADP (7→1). The different transition rates between these discrete states and their description are listed in the Table 3.1.

We consider the setting where single molecule experiments can follow the cargo displacement and therefore observe only transitions $6 \leftrightarrow 7$. As discussed in Section 3.2.6 the inferred entropy production rate for this model is exactly given by $\sigma = \sigma_\ell$. From the network topology and transition rates we evaluate σ_ℓ analytically for different values of parameters such as the concentrations of ATP and ADP. The probabilities of a sequence of two transitions $P(\pm|\pm)$ and $P(\pm|\mp)$ are given analytically from our framework by Eq. (3.18), and the probability of a single transition is given by Eq. (3.25).

In Fig. 3.16, we observe that entropy production rate increases as the concentration of ATP is raised and decrease the concentration of ADP. This implies that the forward step of dynein is associated with high dissipation compared to the backwards step. The typical dissipation rate for biophysical systems of nanometer to micrometer size ranges between 10-1000 $k_B T/s$ [105]. Some examples are of kinesin with dissipation rate 250 $k_B T/s$ and single RNA hairpin with dissipation rate between 10-250 $k_B T/s$.

We now study a stochastic model for kinesin motion [106] validated in single-molecule experimental studies [48, 107], see Fig. 3.17 for an illustration. The model is described by a chemo-mechanical network comprising six discrete states which describe the mechanism of movement of kinesin on the microtubule. Notice that it has two independent cycles: “F” cycle [(1) →(2) → (5) → (6) → (1)] corresponding to the forward motion of kinesin by one step, and

Parameter	Description	Value
W_{17}	ADP release	160
W_{71}	ADP binding	$2.7 \times [\text{ADP}]$
W_{21}	ATP binding	$2 \times [\text{ATP}]$
W_{12}	ATP release	50
W_{32}	MT release in poststroke state	500
W_{23}	MT binding in poststroke state	100
W_{43}	linker swing to prestroke	1000
W_{34}	linker swing to poststroke	100
W_{54}	MT binding in prestroke state	10000
W_{45}	MT release in prestroke state	500
W_{65}	Pi release	5000
W_{56}	Pi binding	$0.01 \times [\text{Pi}]$
W_{76}	Power stroke	5000
W_{67}	Reverse stroke	10

Table 3.1: Transition rates for the chemo-mechanical cycle for the dynein model in Fig. 3.15 (see [103, 104]). All the rate constants W_{ij} (except W_{12} , W_{32} and W_{67} which are in $s^{-1}\mu\text{M}^{-1}$) are given in units of s^{-1} , and the concentrations in μM . Here MT refers to the microtubule.

“B” cycle $[(4) \rightarrow (5)F \rightarrow (2) \rightarrow (3) \rightarrow (4)]$ resulting in a step backwards. The dynamics along one F cycle is as follows: After ATP binding ($1 \rightarrow 2$), kinesin makes a step forward ($2 \rightarrow 5$) in the filament, followed by ATP hydrolysis that results in the release of one ADP molecule ($5 \rightarrow 6$) and inorganic phosphate Pi ($6 \rightarrow 1$). The backward B cycle proceeds similarly, with the only difference that after the binding of ATP to kinesin a backward step along the filament ($5 \rightarrow 2$) occurs. Notice that, in contrast to the model example of dynein, here forward and backward movements are driven by the hydrolysis of one molecule of ATP. The transition rate values are listed in the Table 3.5.1. An external load force f biases the transition rates W_{25} and W_{52} involving spatial motion:

$$\begin{aligned}
 W_{52}(f) &= W_{52}^0 e^{-\theta f d_0 / k_B T} \\
 W_{25}(f) &= W_{25}^0 e^{(1-\theta) f d_0 / k_B T},
 \end{aligned} \tag{3.66}$$

where θ is the load distribution factor, d_0 is the step size and f is the load force. On the other hand, for the chemical transitions we have

$$W_{ij}(f) = 2W_{ij}^0 (1 + e^{\chi_{ij} f d_0 / k_B T})^{-1} \mathcal{I}_{ij}, \tag{3.67}$$

where χ_{ij} represents the mechanical strain on catalytic domains with $\chi_{ij} = \chi_{ji} > 0$ where $i, j \neq 2, 5$ and \mathcal{I}_{ij} is the concentration of the molecular species involved in the transition $j \rightarrow i$.

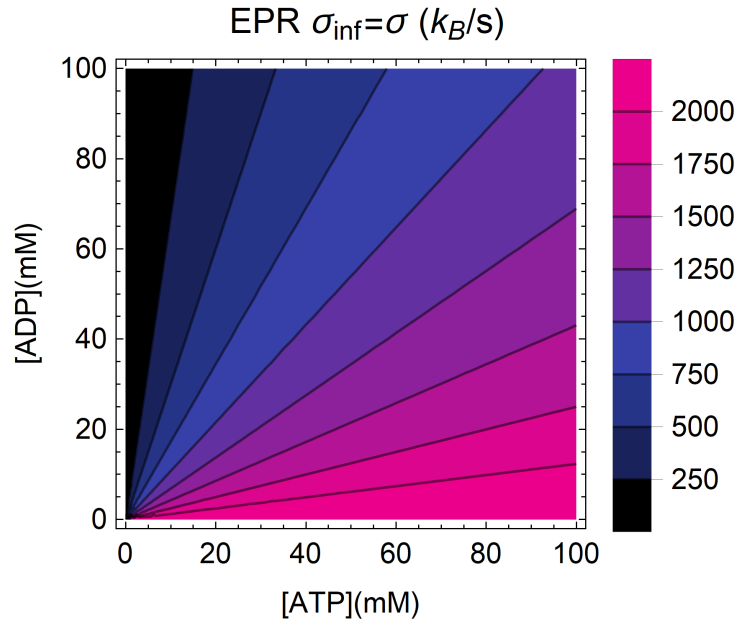


Figure 3.16: Entropy production rate in k_B/s for the dynein with visible transitions $6 \leftrightarrow 7$, using rates from Table 3.1 and $[P_i]=1\text{mM}$, in terms of $[ATP]$ and $[ADP]$.

We now focus on the statistics of the transitions associated with the mechanical movement of kinesin i.e. $2 \leftrightarrow 5$, which are the only ones that can be observed experimentally. For our calculations, we have considered the concentration for ADP to be $[ADP]=70\mu\text{M}$ and $[P_i]=1\text{mM}$, the load distribution factor $\theta = 0.65$, $d_0 = 2k_B T$, $\chi_{12} = 0.25$ and $\chi_{56} = \chi_{61} = 0.15$.

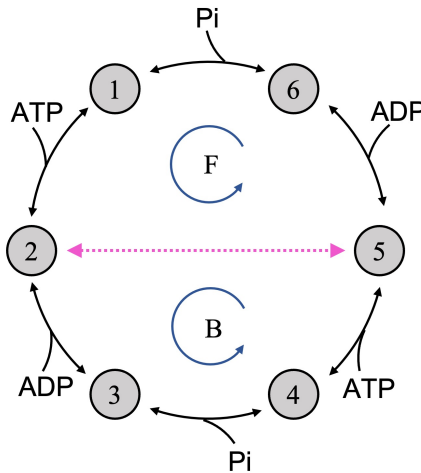


Figure 3.17: Sketch of the chemo-mechanical network model used to describe kinesin motion. The only visible transitions $2 \leftrightarrow 5$ are marked in dotted magenta. Here F and B denote the cycle corresponding to the forward and backward movement of kinesin, respectively.

Figure 3.18 shows the inter-transition statistics of this model obtained from the analytical

Parameter	Description	Value
$W_{21}^0 = W_{54}^0$	ATP binding	$2.0 \times [\text{ATP}]$
W_{12}^0	Release of ATP	100
$W_{32}^0 = W_{65}^0$	ADP release	100
$W_{23}^0 = W_{56}^0$	ADP binding	$0.02 \times [\text{ADP}]$
W_{25}^0	ATP binding	0.24
W_{52}^0	Mechanical step	3×10^5
$W_{43}^0 = W_{16}^0$	Hydrolysis of ATP	100
$W_{34}^0 = W_{61}^0$	Pi binding	$0.02 \times [\text{Pi}]$
W_{45}^0	Release of ATP	$R_{12}^0 (R_{25}^0 / R_{52}^0)^2$

Table 3.2: Transition rates for the chemo-mechanical cycle for kinesin model in Fig. 3.17 [106]. All the rate constants W_{ij} (except W_{21} , W_{23} , W_{34} , W_{54} , W_{56} and W_{61} , which are in $\text{s}^{-1} \mu\text{M}^{-1}$) are given in units of s^{-1} , and the concentrations in μM .

expressions in Eq. (3.21), which displays a rich structure due to the multicyclic structure of the model. Our results show that apart from being defined in a network with two cycles, Fig. 3.18(a) shows that densities for repeated transitions are the same $P(t|+, +) = P(t|-, -)$, which in general is not true for multicyclic networks. However, in this particular case both cycles have the same sequence of transition rates, leading to a similar inter-transition time for the performance of each cycle. This symmetry implies that σ_t for the present kinesin model.

As can be seen in Fig. 3.18 (b), the alternated transitions in general have different inter-transition time densities, but for the stall force $P(t|+, -)$ and $P(t|-, +)$ become similar, as can be seen by minima in $D[P(t|+, -)||P(t|-, +)]$. Both for the force and the concentrations of ATP [cf. Fig. 3.18 (c)] we observe regions of decreasing divergence, however the entropy production rate is increasing in these regions, this is an evidence of the finding that inter-transition times between alternated transitions do not contribute to the dissipation.

Fig. 3.19 shows entropy production rate σ and the values inferred from our approach of observing the forward and backward mechanical transition and the thermodynamic uncertainty relation. Fig. 3.19(a) is in terms of the external force f with a zoomed-in view around the stalling force, for which both $\sigma_{\mathcal{L}}$ and σ_{TUR} vanish since there is no flux and no inter-transition time asymmetry between repeated transitions. Fig. 3.19(b) is depicted in terms of the concentration of ATP and (c) of ADP, from them we observe a monotonic increase of dissipation with $[\text{ATP}]$ while it is almost independent of $[\text{ADP}]$. In this model $\sigma_{\mathcal{L}}$ obtained from Eq. (3.37) in general provides a good estimate for σ , in general overperforming the thermodynamic uncertainty relation σ_{TUR} . Due to the absence of σ_t no dissipation is detected when no net current is present (at stalling force).

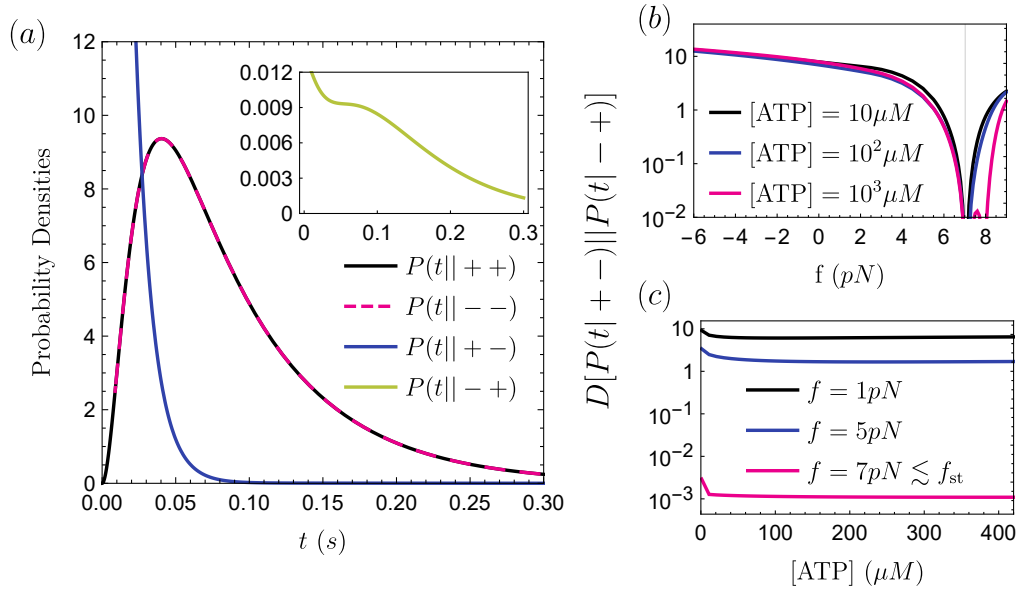


Figure 3.18: Exact inter-transition time statistics for the kinesin model in Fig. 3.17 with visible transitions $2 \leftrightarrow 5$. (a) Inter-transition time densities for every possible pair of transitions. (b) Kullback-Leibler divergence for alternated transitions in terms of the external force f with vertical line corresponding to the stalling force of $f_{st} \sim 7.02$ pN, (c) and in terms of the ATP concentration. The rates are displayed Table 3.5.1 and $[ADP] = [P] = 5\mu M$.

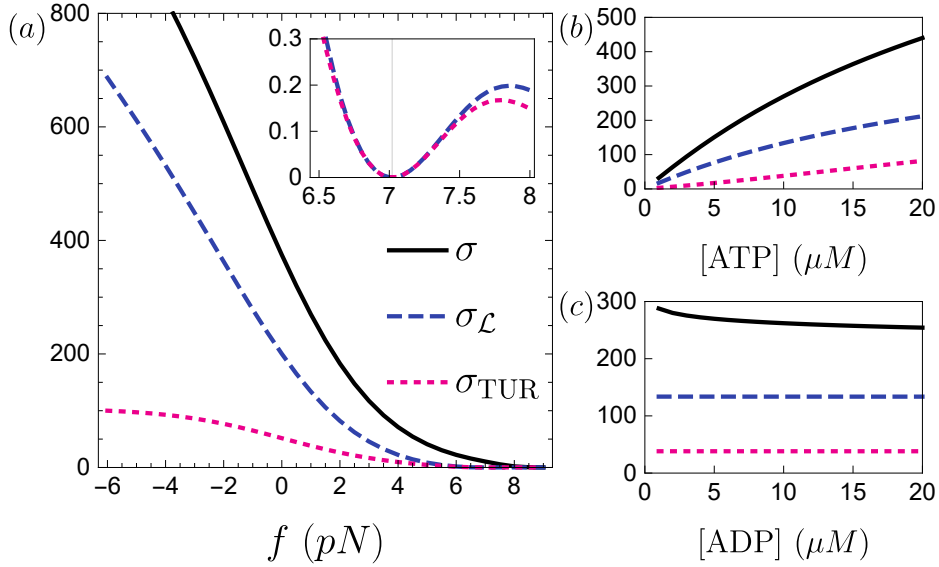


Figure 3.19: Exact analytical values for the rate of entropy production for the kinesin model in Fig. 3.17 with visible transitions $2 \leftrightarrow 5$: entropy production σ of the underlying Markov chain (black curves), inferred entropy production from transition statistics $\sigma_{\mathcal{L}}$ (blue dashed line) and estimate from the thermodynamic uncertainty relation lower bound σ_{TUR} (magenta dotted line). (a) Values in terms of the external load force f and a zoomed-in view around the stalling force in the inset, for this case $[ATP] = 10\mu M$, and $[ADP] = [P] = 5\mu M$. (b) In terms of the concentration of ATP, with $f = 1pN$, and $[ADP] = [P] = 5\mu M$. (c) In terms of the concentration of ADP, with $f = 1pN$, $[ATP] = 10\mu M$, and $[P] = 5\mu M$.

3.5.2 Disorder on a track

In many instances, the stochastic motion of molecular machines display a disordered behavior due to the heterogeneity of the track. For example, template-copying machines like DNA and RNA polymerases [108] and ribosomes [109] are modelled as machines whose motion is dependent on the sequence constituting the track [110, 111]. In this section, we study the effects of track disorder during the movement of a molecular machine.

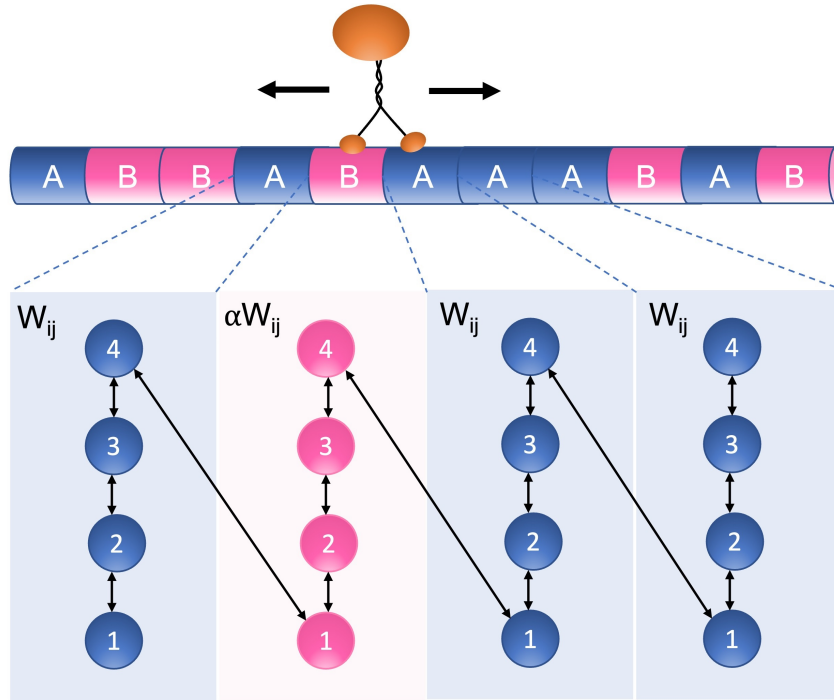


Figure 3.20: Schematic representation of our minimal stochastic model of molecular motor motion with disorder in the composition of the track. The track comprises of two types of sequences: A and B that appear with probabilities p and $1 - p$ respectively. For both types, the motor follows the same kinetic scheme but for blue-labeled position on the track, it has a given set of rates W_{ij} , and for magenta-labeled position, its transition rates are multiplied by the disorder factor, i.e., αW_{ij} . The only visible transitions are the related to translocation to the right $+ = 4 \rightarrow 1$ and to the left $- = 1 \rightarrow 4$.

We consider a minimal stochastic model of a molecular machine that moves along a track by burning fuel (i.e. by hydrolysis of ATP). The machine undergoes a series of conformational changes and translocates on a linear heterogeneous track (a polymer) composed of two types of monomers, labeled A and B . We assume that the track is infinite (i.e. we effectively have **annealed** disorder), and that the generation of the template $q_n \in \{A, B\}$, $n = \{1, 2, \dots\}$, is an i.i.d. process such with prescribed probabilities $P(q_n = A) = p$ and $P(q_n = B) = 1 - p$ for the occurrence of A and B type monomers, respectively. For our numerical study, we generate the template before running the simulations and use the same template for every run.

Figure 3.20 sketches the disordered nature of a track along the motion of the molecular machine. We also assume that the motor moves following a unicyclic enzymatic reaction composed of four internal configurational states and that only two transitions are visible $4 \rightarrow 1 = +$ and $1 \rightarrow 4 = -$ corresponding to forward and backward steps along the track, respectively. The template disorder is implemented in the stochastic model as follows: When the motor reaches a monomer of type q_n , its internal configurational states within one periodicity cell are connected by rates

$$W_{ij}^{(q_n)} = \begin{cases} W_{ij} & \text{if } q_n = A \text{ and } i, j \neq 4, 1 \\ \alpha W_{ij} & \text{if } q_n = B \text{ and } i, j \neq 4, 1 \\ W_{41} & \text{if } q_{n-1} = A \text{ and } i, j = 4, 1 \\ \alpha W_{41} & \text{if } q_{n-1} = B \text{ and } i, j = 4, 1 \end{cases} \quad (3.68)$$

where $\alpha \in (0, 1]$ is the disorder factor. This factor scales the transition rates, effectively slowing or accelerating the transitions depending on the track position. As a convention, we have set the transition rate related to a back step $W_{41}^{(q_n)}$ to be defined in terms of the previous monomer's type q_{n-1} . Apart from specific choices of the parameters, this motor has a nonequilibrium dynamics, evidenced by a net drift along the track. In ring topologies, we have observed that inter-transition times do not contain irreversibility traces, which is not necessarily true for the disordered case.

We now study how the disorder parameters α and p of this minimal model affect the inter-transition time probability densities between pairs of repeated transitions $++$ and $+ -$, and alternated transitions $- +$ and $--$. From the simulation of a molecular motor on a disordered track with four internal states, we observe in Fig. 3.21 that only the inter-transition time between alternated transitions is affected by different levels of disorder.

Symmetry $D[P(t|+, +)||P(t|-, -)] = 0$ is preserved by changes in disorder, which is already expected for the homogeneous case ($\alpha = 1, p = 0$ or $p = 1$) and it is interesting to note that it holds for different scenarios. Conversely, $D[P(t|+, -)||P(t|-, +)]$ changes with values of α and p . Asymmetry in inter-transition times of repeated transitions is insensitive to the degree of disorder while the asymmetry for alternated transitions proves to be a meaningful quantity to the study of molecular machines on disordered tracks. Remarkably, unlike in the study of entropy production, only alternated transitions entail information to study levels of disorder.

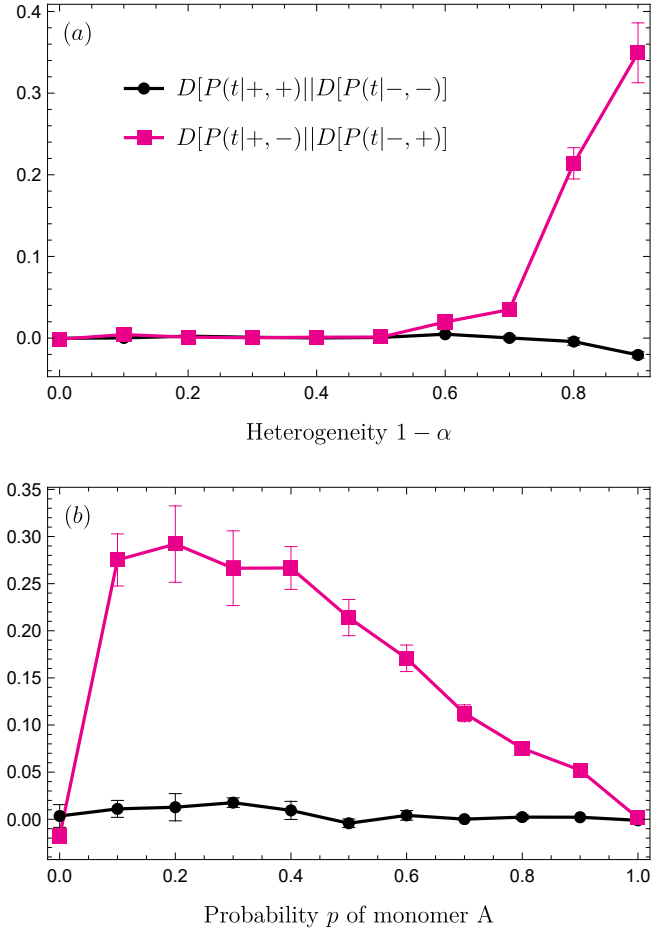


Figure 3.21: Kullback-Leibler Divergences of the inter-transition time densities for repeated (black circles) and alternated (magenta squares) pairs of transitions. (a) in terms of heterogeneity $1 - \alpha$ with fixed monomer probability $p = 0.5$. (b) in terms of probability p of monomer A, with fixed $\alpha = 0.2$. The rates used for Gillespie simulations are $W_{12} = W_{43} = 1 \text{ s}^{-1}$, $W_{21} = W_{23} = W_{34} = 5 \text{ s}^{-1}$ and $W_{32} = W_{14} = W_{41} = 4 \text{ s}^{-1}$, and visible transitions are the ones involving translocation along the track, i.e. transitions $1 \rightarrow 4$ and $4 \rightarrow 1$.

3.6 Chapter summary

In this chapter we developed the proposal of a transition-based coarse-graining scheme to describe stochastic processes with discrete state-space. The role of time is highlighted for entropy production inference and fluctuation relations.

Mapping the problem of visible transition statistics onto a first-passage time one, analytic expressions are obtained and analyzed for sequence of transitions and inter-transition times. The introduced survival matrix proves to be a powerful tool to obtain such properties and a notation for transition space is developed. Consequently, the entropy production inferred from a few visible transitions can be assessed and split into two contribution, from the sequence and

the time. The sequence of transitions contain the full entropy production in ring networks, the inter-transition times detect nonequilibrium even when no net flux is observed.

Delving into transition space, a Markov chain can be established using the previous results. From such, a fluctuation relation is recovered when the current is observed at “its own beat”, which rules out inter-transition times and establishes an inner notion of time.

Lastly, the framework of transition-based coarse-graining is applied to biophysical models, illustrating it can be used as an inference tool to the common scenario of from partial information from both sequence of transitions and inter-transitions times. The time between repeated transitions also carry information about disorder, probing its intensity.

“More is different.”

P. W. Anderson [115]

“More is the same.”

Leo P. Kadanoff [116]

Chapter 4

Nonequilibrium Phase transitions

4.1 What is a phase transition

The broadness of how phase transition concepts are defined may come as a surprise for the unwary physicist, but so is the range of applicability of the theory. They are evidenced by sharp changes in the properties of a system and come in all flavors. There are obvious examples such as the boiling of water and a change in magnetization direction. There are more convoluted phase transitions such as the superfluidity of helium, the suppression of superconductivity in thin films, the critical opalescence of carbon dioxide, and others. Also, there are phase transitions of clear relevance such as emergence of political consensus, epidemic outbreaks and the melting of polar ice caps.

In equilibrium systems, phase transitions are defined by singularities in the free energy derivatives [112], which give rise to sharp changes in several physical quantities¹. Similar phenomena occur even out of equilibrium, they are marked by a sudden change in the non-equilibrium steady state [114].

In a more precise way the study of phase transitions describes such phenomena with the introduction of two key concepts: control and order parameter. The former is a parameter that can be tuned and affect the system's behavior or structure, examples are temperature, magnetic field and presence of disorder. The order parameter is an indicator of phases, vanishing when the system is in one phase and presenting a non-zero value in the other phase, as examples we cite the density of fluids, magnetization of magnetic systems and a tensor describing order in

¹An interesting and ongoing discussion arises from the mathematical definition of phase transitions as divergences in physical quantities. These divergences are only achieved in the limit of infinitely many particles, whereas finite real systems go through phase transitions all around us [113].

liquid crystals. Therefore, in a generic way, a phase transition occurs at the crossover of distinct phases through the change of well defined values of a control parameter, it is marked by the order parameter vanishing in one of the phases.

The modern classification embraces two types:

- (i) *First-order phase transitions*: Also known as discontinuous phase transitions, they present a discontinuity in the order parameter. In equilibrium, they are marked by a discontinuity in the first derivative of the free-energy, thus their name. A particular feature is the presence of a phase coexistence region. One common example is the boiling of water, whose control parameter is the temperature and order parameter is the density.
- (ii) *Continuous phase transitions*: They go through a continuous vanishing in the order parameter, but not in its derivative. In equilibrium, they present a discontinuity in the second or higher derivative of the free energy, or a divergence in one of them. The location of continuous phase transitions is known as a critical point, and its vicinity as the criticality. At criticality, the correlation length gets infinite and correlations present a power law decay, characterized by critical exponents that give rise to universality classes. For example, the ferromagnetic-paramagnetic Ising model phase transition is continuous.

There is a well-established theory to characterize equilibrium phase transitions, however for systems out of equilibrium the lack of free energies poses a problem. Leveraged by the recent success and developments of stochastic thermodynamics, the most common thermodynamic distance to equilibrium—entropy production—has been studied in terms of how well it can typify non-equilibrium phase transitions [II, 117–125]. As an advantage, the entropy production rate captures important nonequilibrium traits and, depending on the system, might be easier to obtain than the order parameter itself. Whereas a widespread and unified theory for out of equilibrium systems is not yet established.

Nonequilibrium phase transitions encompass transitions between equilibrium phases. However, we aim for a theory of transitions between phases that are genuinely out of equilibrium, thus equilibrium can be recovered as a particular case. Furthermore, nonequilibrium phases are not defined as simply as in equilibrium; for instance, the coexisting phases along a first-order phase transition have to be characterized in terms of the interactions (e.g. energy exchanges) between them rather than only in terms of intrinsic properties [126].

The goal of this chapter is to provide a further step in this direction, characterizing nonequilibrium phase transitions in terms of entropy production signatures and studying how coexisting nonequilibrium phases affect the statistics of generic fluxes.

4.2 Systems with \mathbb{Z}_2 symmetry

An important class of system are those presenting \mathbb{Z}_2 symmetry, also known as “up-down” and “inversion” symmetry. The dynamics do not change under the change of the sign of all degrees of freedom. An example is a spin system that presents the same dynamics if all spins are flipped, as is the case for many Ising-like Hamiltonians, with the Ising model itself standing out as the most important example.

Many systems with \mathbb{Z}_2 symmetry yield continuous and/or discontinuous phase transitions between ordered and disordered phases. One example is the transition between ferromagnetic (ordered) and paramagnetic (disordered) phases due to spontaneous symmetry breaking, in which the ferromagnetic presents two distinct non-zero values of magnetization.

4.2.1 Mean-field description

Heuristically, a continuous phase transition in such class of models is described by the general logistic order parameter equation:

$$\frac{d}{dt}m = a(q_c - q)m - bm^3, \quad (4.1)$$

where q denotes the control parameter, t is the time, and a and b are positive constants. It has two steady solutions, the disordered phase magnetization $m^{(D)} = 0$ (for all values of a and b) that is stable for large values of q , and the ordered phase magnetization $m^{(S)} = \pm\sqrt{a(q_c - q)/b}$, stable for small q . The phase transition follows the mean-field exponent $\beta_{mf} = 1/2$ as m vanishes. Also, Eq (4.1) behaves as $m \sim \exp[a(q - q_c)t]$ for $q < q_c$ when $m \ll 1$.

The simplest description of first-order phase transitions requires an additional term cm^5 in order to admit phase coexistence, leading to [I]

$$\frac{d}{dt}m = a(q_b - q)m + bm^3 - cm^5, \quad (4.2)$$

where $c > 0$. As before, $m^{(D)} = 0$ is always a solution, which is stable for values of $q >$

q_b . However, along the hysteretic branch there are two additional solutions, the unstable $m^{(U)}$ and stable $m^{(S)}$. The existence of a hysteretic branch containing three distinct solutions is a trademark of (mean-field) discontinuous phase transitions, rendering the phase coexistence.

Starting from a positive and small value of the control parameter q , the single stable solution is the magnetized $m^{(S)}$. Increasing q leads to a phase transition at $q = q_f = q_b + (b^2/4ac)$, where the magnetization m abruptly jumps from the magnetized stable state $m^{(S)}(q_f)$ to the non-magnetic solution $m^{(D)} = 0$. On the other hand, starting from a larger $q > q_f$ and decreasing its value leads to a phase transition at q_b from $m^{(D)}$ to $m^{(S)}(q_b)$. This difference between the location of “forward” and “backward” phase transitions forms a hysteresis located at $q_f < q < q_b$.

Inside the hysteresis, the unstable solution $m^{(U)}$ splits the order parameter convergence. For a value of q inside the hysteresis, a system with initial magnetization greater than $m^{(U)}$ will converge to $m^{(S)}$, whereas the opposite leads to a convergence towards $m^{(D)}$. Outside such a region, the evolution of the magnetization is $m \sim \exp[a(q_b - q)t]$ for initial values $m_0 \ll 1$ when $q > q_f$, and it also exponentially approaches $m^{(S)}$ at its vicinity when $q < q_b$.

Figure 4.1 illustrates the mean-field description discussed above. The steady-state solutions $m^{(S)}$, $m^{(U)}$ and $m^{(D)}$ are shown in red curves in terms of the control parameter q . The critical point q_c is shown as a dot in the left panel and the hysteresis is located between q_b and q_f in the right panel. The curves dm/dt from Eqs. (4.1) and (4.2) are shown in the insets for different regimes; notice that the zeroes of such a function locate the steady-state solutions and the slope at these zeroes, d^2m/dt^2 , provide the stability. Negative slopes refer to stable solutions (e.g. in the left panel, the non-zero solutions for $q < q_c$ and zero for $q > q_c$), while positive slopes are present in unstable solutions (e.g. in the right panel, the first non-zero solutions for $q_b < q < q_f$).

Above phenomenological relation hides the irreversible character of non-equilibrium phase transitions, and it does not provide any information about the entropy production at the phase transition. Therefore, we derive a general expression for the entropy production taking into account a generic dynamics with \mathbb{Z}_2 symmetry. Based on Markovian dynamics, we deal with systems defined over a lattice that undergo a phase transition induced by parameter q . The starting point consists of assigning to each site i of an arbitrary lattice topology a spin variable s_i that assumes values ± 1 . The transition rate for the spin flip is given by $w(s_i) = [1 - qs_i g[X]]/2$, with $g[X]$ expressing a generic dependence on a local neighborhood of spins, where $-k \leq X \leq k$ is bounded between the number of neighbours of the local spin s_i .

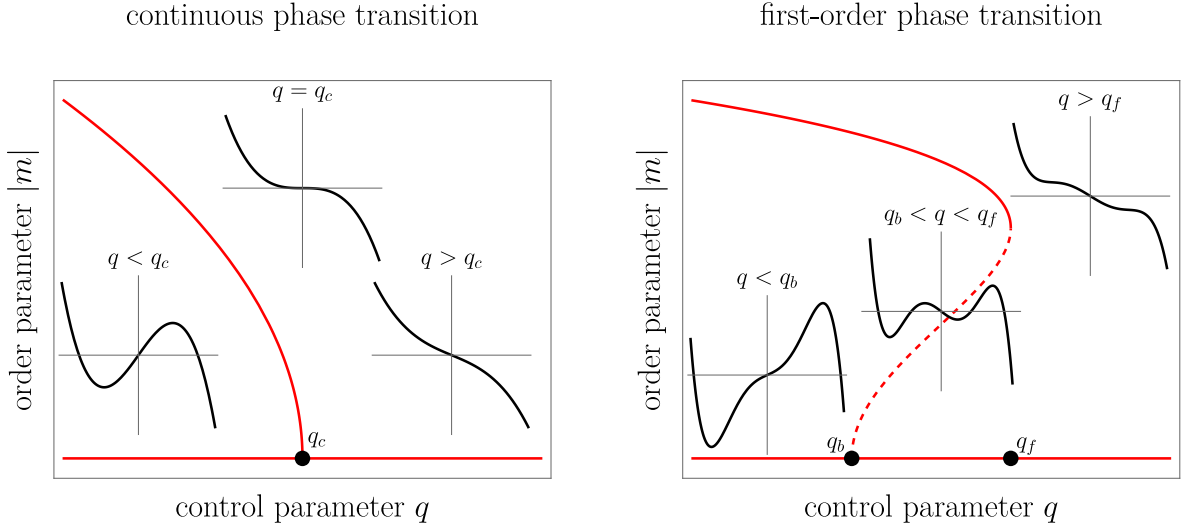


Figure 4.1: Mean-field description of a continuous (left) and first-order (right) phase transitions. Solutions for $m(q)$ are shown in red lines. Insets are dm/dt versus m for different values of q [Eq. (4.1) for the left panel and Eq. (4.2) for the right one], whose zeroes represent the steady-state solutions $m(q)$.

Only two assumptions regarding $g[X]$ are required. The first is that, due to the \mathbb{Z}_2 symmetry, it is an odd function on the sign of the local spin neighborhood, $g[X] = -g[-X]$. Also, taking into account that $w(s_i)$ is constrained between 0 and 1, the product $|qg[X]| \leq 1$ for all values of X . These assumptions allow us to rewrite $g[X]$ as $g[X] = |g[X]|\text{sgn}[X]$, where $\text{sgn}[X]$ is the sign function.

The order parameter is the expected magnetization of a spin $m = \langle s_i \rangle$, and from the master equation its evolution is described by [5]

$$\frac{d}{dt} \langle s_i \rangle = -2 \langle s_i w(s_i) \rangle. \quad (4.3)$$

By inserting the transition rate and noticing that $s_i^2 = 1$, the steady-state solution is given by $m = q \langle |g[X]| \text{sgn}[X] \rangle$ since. The steady state entropy production rate is given by $\sigma = \sum_i \langle w(s_i) \ln[w(s_i)/w(-s_i)] \rangle$. In this case of spin-half dynamics it simplifies since there are only two possible values:

$$\ln \frac{w(s_i)}{w(-s_i)} = \begin{cases} \ln \frac{1-q|g[X]|}{1+q|g[X]|} & \text{if } s_i \text{sgn}[X] = 1 \\ \ln \frac{1+q|g[X]|}{1-q|g[X]|} & \text{if } s_i \text{sgn}[X] = -1 \end{cases} \quad (4.4)$$

Hence, σ reads

$$\sigma = \sum_i \left\langle \frac{1}{2} [s_i \text{sgn}[X] - q |g[X]| \text{sgn}[X]^2] \ln \frac{1 - q |g[X]|}{1 + q |g[X]|} \right\rangle. \quad (4.5)$$

The one-site mean-field theory consists of rewriting the joint probability $P(s_i, \dots, s_k)$ as a product of one-site probabilities $P(s_i) \cdots P(s_k)$, from which one derives closed relations for the correlations as function of the control parameters. Since the main marks of critical and discontinuous phase transitions are not expected to depend on the particularities of $g[X]$, it is reasonable, within the mean-field theory, to replace the averages in terms of an effective value \bar{g} given by

$$m = q \langle |g[X]| \text{sgn}[X] \rangle \rightarrow q \bar{g} \langle \text{sgn}[X] \rangle, \quad (4.6)$$

$$\frac{1}{2} \left\langle s_i \text{sgn}[X] \ln \frac{1 - q |g[X]|}{1 + q |g[X]|} \right\rangle \rightarrow \frac{1}{2} \ln \frac{1 - q \bar{g}}{1 + q \bar{g}} \langle s_i \text{sgn}[X] \rangle, \quad (4.7)$$

and

$$\frac{1}{2} \left\langle |g[X]| S^2[X] \ln \frac{1 - q |g[X]|}{1 + q |g[X]|} \right\rangle \rightarrow \frac{\bar{g}}{2} \ln \frac{1 - q \bar{g}}{1 + q \bar{g}} \langle S^2[X] \rangle. \quad (4.8)$$

At this level of approximation, the steady entropy production per site then reads

$$\frac{\sigma}{N} = \frac{1}{2} q \bar{g} \ln \frac{1 + q \bar{g}}{1 - q \bar{g}} \text{Var}[\text{sgn}[X]], \quad (4.9)$$

which is a non-negative quantity depending on the variance of the neighborhood sign $\text{Var}[\text{sgn}[X]] = \langle \text{sgn}[X]^2 \rangle - \langle \text{sgn}[X] \rangle^2$.

The above averages are calculated by the probabilities of having a positive or negative neighborhood

$$P[\text{sgn}[X] = \pm 1] = \sum_{n=\lceil k/2 \rceil}^k C_n^k p_{\pm}^n p_{\mp}^{k-n}, \quad (4.10)$$

and both do not add to unity in general because there is still the possibility of having $\text{sgn}[X] = 0$. [...] is the ceiling function and, for $\text{sgn}[X] = \pm 1$, the coefficient C_n^k counts the possibilities of having n out of the k spins with a \pm sign. The probability of a single spin being ± 1 can be expressed in terms of magnetization as $p_{\pm} = (1 \pm m)/2$. Therefore, the moments of the sign function read

$$\langle \text{sgn}[X] \rangle = P[\text{sgn}[X] = +1] - P[\text{sgn}[X] = -1] \quad (4.11)$$

and

$$\langle \text{sgn}^2[X] \rangle = P[\text{sgn}[X] = +1] + P[\text{sgn}[X] = -1]. \quad (4.12)$$

For a given k and lattice topology, Equations (4.11) and (4.12) can be calculated, providing the value of σ . However, they become simpler in the regime of large connectivities. Note that each term of the binomial distribution approaches a normal distribution with mean kp_{\pm} and variance $kp_{+}p_{-}$, so that

$$\begin{aligned} \sum_{n=\lceil k/2 \rceil}^k C_n^k p_{\pm}^n p_{\mp}^{k-n} &\rightarrow \frac{1}{\sqrt{2\pi kp_{+}p_{-}}} \int_{k/2}^k e^{-\frac{(\ell - kp_{\pm})^2}{2kp_{+}p_{-}}} d\ell \\ &= \frac{1}{2}\sqrt{\pi} \left\{ \text{erf} \left[\frac{k(1-p_{\pm})}{\sqrt{2kp_{+}p_{-}}} \right] - \text{erf} \left[\frac{k(1/2-p_{\pm})}{\sqrt{2kp_{+}p_{-}}} \right] \right\}, \end{aligned} \quad (4.13)$$

where $\text{erf}(x) = 2\pi^{-1/2} \int_0^x e^{-t^2} dt$ denotes the error function. Since $\lim_{x \rightarrow \infty} \text{erf}(\pm x) = \pm 1$, in the limit of large connectivity $k \gg 1$ we have $\langle \text{sgn}^2[X] \rangle \rightarrow 1$, and for small m the expressions to

$$m = q\bar{g} \left[\text{erf} \left(\sqrt{\frac{k}{2}} m \right) \right], \quad (4.14)$$

and

$$\frac{\sigma}{N} = \frac{1}{2} \ln \frac{1 - q\bar{g}}{1 + q\bar{g}} \left[\frac{m^2}{q\bar{g}} - q\bar{g} \right]. \quad (4.15)$$

For continuous phase transition, we resort to the results from the logistic description, in which at vicinity of the critical point m behaves as $m \sim (q - q_c)^{1/2}$, and thus the entropy production rate per site behaves as

$$\frac{\sigma}{N} \sim \frac{1}{2} \ln \frac{1 + q\bar{g}}{1 - q\bar{g}} \left[\frac{q_c - q}{q\bar{g}} + q\bar{g} \right], \quad (4.16)$$

for $q < q_c$, and

$$\frac{\sigma}{N} = \frac{q\bar{g}}{2} \ln \frac{1 + q\bar{g}}{1 - q\bar{g}}, \quad (4.17)$$

for $q > q_c$. Hence the entropy production rate is continuous at the critical point q_c , with value $q_c \bar{g} \ln[(1 + q_c \bar{g})(1 - q_c \bar{g})]/2$. However it presents a kink detected by a discontinuity in its first derivative, which jumps from

$$\frac{\partial}{\partial q} \frac{\sigma}{N} = \frac{q_c \bar{g}^2}{1 - q_c^2 \bar{g}^2} + \frac{1 - q_c \bar{g}^2}{2q_c \bar{g}} \ln \frac{1 - q_c \bar{g}}{1 + q_c \bar{g}}, \quad (4.18)$$

when $q \rightarrow q_c^-$, to

$$\frac{\partial \sigma}{\partial q N} = \frac{q_c \bar{g}^2}{1 - q_c^2 \bar{g}^2} - \frac{\bar{g}}{2} \ln \frac{1 - q_c \bar{g}}{1 + q_c \bar{g}}, \quad (4.19)$$

when $q \rightarrow q_c^+$, whose discontinuity is associated with the critical exponent $\alpha_{mf} = 0$. The above results dissect, for a generic system with \mathbb{Z}_2 symmetry, the behavior of σ and its derivative at the criticality. Remarkably, having the classical exponents β_{mf} and γ_{mf} (evaluated from the variance of the order parameter [5]), we see that the hyperscaling relation $\alpha_{mf} + 2\beta_{mf} + \gamma_{mf} = 2$ is satisfied, reinforcing that the criticality is signed by the jump in the first derivative of σ/N , in close proximity to the specific heat discontinuity for equilibrium systems.

The above description of mean-field entropy production also correctly identifies the signatures of first-order phase transitions. According to Eq.(4.2), m jumps from $m^{(S)}(q_f)$ to 0 at $q = q_f$ and thereby from Eq. (4.15) the entropy production will jump from

$$\frac{1}{2} \left(q_f \bar{g} - \frac{m^{(S)}(q_f)^2}{q_f \bar{g}} \right) \ln \left[\frac{1 + q_f \bar{g}}{1 - q_f \bar{g}} \right], \quad (4.20)$$

to

$$\frac{q_f \bar{g}}{2} \ln \left[\frac{1 + q_f \bar{g}}{1 - q_f \bar{g}} \right]. \quad (4.21)$$

Also, m jumps from 0 to $m^{(S)}(q_b)$ at $q = q_b$, leading to a jump in σ/N from

$$\frac{q_b \bar{g}}{2} \ln \left[\frac{1 + q_b \bar{g}}{1 - q_b \bar{g}} \right], \quad (4.22)$$

to

$$\frac{1}{2} \left(q_b \bar{g} - \frac{m^{(S)}(q_b)^2}{q_b \bar{g}} \right) \ln \left[\frac{1 + q_b \bar{g}}{1 - q_b \bar{g}} \right]. \quad (4.23)$$

This bistable behavior in the entropy production rate not only distinguishes continuous and discontinuous phase transitions, but also properly locates the hysteretic loop.

4.2.2 Mean-field description - Majority vote model with inertia

To illustrate previous results, we study one of the simplest models presenting a non-equilibrium phase transition, the majority vote (MV) model. In its original version, the phase transition is continuous [127], additional features such as inertia and the lattice's topology can give rise to first-order phase transitions [I, 128].

The model is defined as follows: Each site i of an arbitrary lattice can assume \bar{q} possible

integer values, $s_i = \{0, 1, \dots, \bar{q} - 1\}$. The dynamics is ruled by the fraction of neighboring nodes in each state and by the inertia θ , that expresses the dependence on the local spin. With probability $1 - f$ (f being the misalignment parameter) the local spin s_i follows the majority neighborhood spin s'_i , and with complementary probability f the majority rule is not followed. For $\bar{q} = 2$ and $\theta = 0$, the majority vote becomes equivalent to the Ising model in contact with two heat reservoirs, one being a source of heat at infinite temperature, and the other a sink of heat at zero temperature [127].

Recent studies [I, 129, 130] revealed that large inertia shifts the phase transition to a first-order one for all values of \bar{q} . An order-disorder phase transition arises by increasing f , whose classification (continuous or first-order) depends on θ and the lattice connectivity k . For low \bar{q} ($\bar{q} < 4$) and $\theta = 0$ (inertialess regime), it is always continuous, but the increase of \bar{q} modifies the symmetry properties (\mathbb{Z}_2 and \mathbb{C}_{3v} for $\bar{q} = 2$ and 3, respectively), hence leading to distinct sets of critical exponents. The phase transition becomes discontinuous for larger connectivities k when θ increases.

The n -th moment of the order parameter $\langle m^n \rangle$ is calculated by the quantity

$$\langle m^n \rangle = \left\langle \left| \sum_{i=1}^N \exp(2\pi i s_i / \bar{q}) / N \right|^n \right\rangle, \quad (4.24)$$

with $\langle \bullet \rangle$ denoting the ensemble average. The $n = 1$ is a reliable order parameter since $m > 0$ in the ordered phase and zero in the disordered phase. The steady entropy production rate per site can be calculated from the entropy flux as

$$\frac{\sigma}{N} = \frac{1}{N} \left\langle \sum_{q'=1}^{\bar{q}-1} \sum_{i=1}^N w_i(\vec{s}) \ln \frac{w_i(\vec{s})}{w_i(\vec{s}^{(q')})} \right\rangle, \quad (4.25)$$

with $w_i(\vec{s})$ the transition rate of changing spin i to one of its $\bar{q} - 1$ other values given state $\vec{s} = \{s_1, \dots, s_N\}$, and $w_i(\vec{s}^{(q')})$ the transition rate of flipping back spin i given that it has another value $\vec{s}^{(j)} = \{\dots, s_{i-1}, q', s_{i+1}, \dots, s_N\}$.

For $\bar{q} = 2$, the above transition rate is more conveniently rewritten by taking the transformation $s_i \rightarrow 2s_i - 1 = \pm 1$, so the magnetization is $m = \langle \sigma_i \rangle$ and the transition rate $w_i(\vec{s})$

reads

$$w_i(\vec{s}) = \frac{1}{2}[1 - (1 - 2f)s_i \text{sgn}[X]] = \begin{cases} f & \text{if } s_i \text{sgn}[X] = 1 \\ 1 - f & \text{if } s_i \text{sgn}[X] = -1 \\ 1/2 & \text{if } s_i \text{sgn}[X] = 0 \end{cases} \quad (4.26)$$

where the first case $s_i \text{sgn}[X] = 1$ represents when the site has the same spin of its neighbours, the second $s_i \text{sgn}[X] = -1$ when the spin is the opposite, and the last case is arbitrary since there is no majority in the neighborhood.

Inertia θ is inserted in the system through the neighborhood dependence according to the following change in X :

$$X = (1 - \theta) \sum_{j=1}^k s_j/k + \theta s_i, \quad (4.27)$$

which represents the local-dependence on the site's spin in the decision of following or not following the majority. When $\theta = 0$ its own spin does not play a role. As $0 \leq \theta \leq 1/2$ increases, the more the site tends to follow its own spin, in contrast to the neighborhood's majority. Now for $\theta > 1/2$ the site's spin will always rule the value of $\text{sgn}[X]$. Thus the name inertia.

From Eq. (4.3), the steady-state expression for the majority vote's absolute magnetization m reads

$$m = (1 - 2f) \langle \text{sgn}[X] \rangle. \quad (4.28)$$

Due to the presence of inertia in Eq. (4.27), the local spin now contributes to $\text{sgn}[X]$. At the mean-field level we assumed that the probabilities each spin is independent, thus

$$\begin{aligned} m &= (1 - 2f) \left\{ P[X > 0, s_i = 1] + P[X > 0, s_i = -1] \right. \\ &\quad \left. - P[X < 0, s_i = 1] - P[X < 0, s_i = -1] \right\} \\ &= (1 - 2f) \left\{ P[X > 0 | s_i = 1] P[s_i = 1] + P[X > 0 | s_i = -1] P[s_i = -1] \right. \\ &\quad \left. - P[X < 0 | s_i = 1] P[s_i = 1] - P[X < 0 | s_i = -1] P[s_i = -1] \right\}, \quad (4.29) \end{aligned}$$

and the conditional probabilities read

$$P[X > 0 | s_i = 1] = \sum_{n=n_1}^k C_n^k p_+^n p_-^{k-n}, \quad P[X > 0 | s_i = -1] = \sum_{n=n_2}^k C_n^k p_+^n p_-^{k-n}, \quad (4.30)$$

and

$$P[X < 0 | s_i = 1] = \sum_{n=n_2}^k C_n^k p_-^n p_+^{k-n}, \quad P[X < 0 | s_i = -1] = \sum_{n=n_1}^k C_n^k p_-^n p_+^{k-n}, \quad (4.31)$$

with

$$n_1 := \left\lceil \frac{k(1-2\theta)}{2(1-\theta)} \right\rceil \quad \text{and} \quad n_2 := \left\lfloor \frac{k}{2(1-\theta)} \right\rfloor. \quad (4.32)$$

Equation (4.29) provides the evaluation of m for a given lattice topology with connectivity k . For large values of k it simplifies to the transcendental equation

$$\begin{aligned} & \frac{m}{(1-2f)} \left(2 - (1-2f) \left\{ \operatorname{erf} \left[\sqrt{\frac{k}{2}} \left(\frac{\theta}{1-\theta} + m \right) \right] + \operatorname{erf} \left[\sqrt{\frac{k}{2}} \left(\frac{\theta}{1-\theta} - m \right) \right] \right\} \right) \\ &= \operatorname{erf} \left[\sqrt{\frac{k}{2}} (1-m) \right] - \operatorname{erf} \left[\sqrt{\frac{k}{2}} (1+m) \right] \\ &+ \operatorname{erf} \left[\sqrt{\frac{k}{2}} \left(\frac{\theta}{1-\theta} + m \right) \right] - \operatorname{erf} \left[\sqrt{\frac{k}{2}} \left(\frac{\theta}{1-\theta} - m \right) \right], \end{aligned} \quad (4.33)$$

which goes to Eq. (4.14) at $\theta = 0$, as expected.

The equation above for the complete graph $k \rightarrow \infty$ goes to the transcendental expression

$$m = \frac{(1-2f)(1 + \operatorname{sgn}[m - \theta/(1-\theta)])}{2 - (1-2f)(1 - \operatorname{sgn}[m - \theta/(1-\theta)])}, \quad (4.34)$$

which, for positive values of magnetization (for negative values the analysis is analogous) has a solution

$$m = \begin{cases} 1-2f & \text{if } f < (1-2\theta)/2(1-\theta) \\ 0 & \text{if } f > (1-2\theta)/2(1-\theta) \end{cases} \quad (4.35)$$

which means that in the limit of infinite connectivity the phase transition is located at $f = (1-2\theta)/2(1-\theta)$. For $\theta = 0$ it is continuous and located at $f = 1/2$. Also, since the solution $m = 0$ always exists, the hysteretic branch reaches the axis. See Figure 4.2.

Now, we turn to the majority vote's entropy production. In order to evaluate σ/N from Eq. (4.25) we take the ratio between $w_i(\vec{s})$ and its reverse $w_i(\vec{s}^{(j)})$ given by

$$\frac{w_i(\vec{s})}{w_i(\vec{s}^{(j)})} = \frac{1 - (1-2f)s_i \operatorname{sgn}[\sum_{j=1}^k s_j + \frac{k\theta}{1-\theta}s_i]}{1 + (1-2f)s_i \operatorname{sgn}[\sum_{j=1}^k s_j - \frac{k\theta}{1-\theta}s_i]}. \quad (4.36)$$

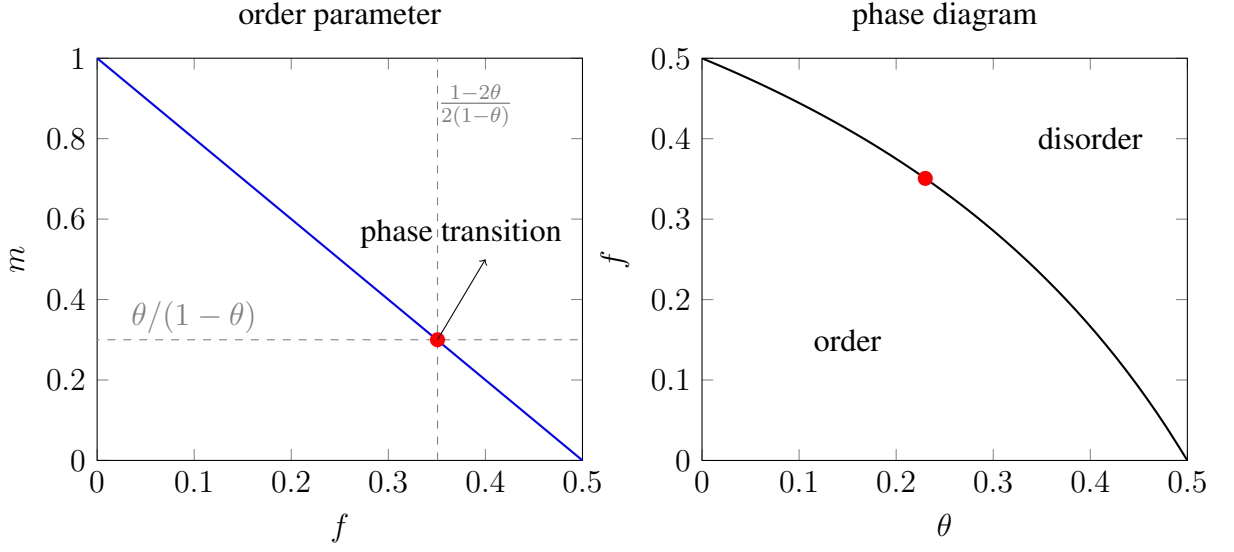


Figure 4.2: At the mean-field level, the limit of infinite connectivity $k \rightarrow \infty$ leads to a discontinuous phase transition when the magnetization goes below $\theta/(1 - \theta)$. In the left panel inertia has a value of $\theta = 0.23$, in the right panel the phase transition location is at $f = (1 - 2\theta)/2(1 - \theta)$.

Inspection of the above ratio reveals that only local configurations with $\left| \sum_{j=1}^k \sigma_j \right|$ greater than $k\theta/(1 - \theta)$ will contribute to σ/N , since only in these cases such a ratio is different from 1. It is reasonable since, if the site would always follow its own spin, there would be no interactions and each and every site would relax to its (trivial) equilibrium state.

Therefore, the neighborhood can be simplified to the subset of local configuration that contribute to the entropy production $X' \in X$, leading to the approximation $\ln[w_i(\vec{s})/w_i(\vec{s}^{(q')})] \approx s_i \text{sgn}(X') \ln[f/(1 - f)]$. The expression for the entropy production rate per site is then given by

$$\frac{\sigma}{N} = \frac{1}{2} \ln \frac{f}{1-f} [\langle s_i \text{sgn}[X'] \rangle - (1 - 2f) \langle \text{sgn}[X']^2 \rangle] \quad (4.37)$$

and notice that the entropy production vanishes for $f = 0$ and $f = 0.5$, since the model will be in equilibrium.

As previously performed, the expression of the mean-field of one site is obtained by replacing $\langle s_i \text{sgn}[X'] \rangle$ with $\langle s_i \rangle \langle \text{sgn}[X'] \rangle$, so that

$$\frac{\sigma}{N} = \frac{1}{2} \ln \frac{f}{1-f} [m \langle \text{sgn}[X'] \rangle - (1 - 2f) \langle \text{sgn}[X']^2 \rangle] = \frac{1 - 2f}{2} \ln \frac{1-f}{f} \text{Var} [\text{sgn}(X')], \quad (4.38)$$

which can be obtained following the same procedure used for the magnetization and is strictly non-negative. Using aforementioned procedures for $\langle \text{sgn}[X'] \rangle$ and $\langle \text{sgn}[X']^2 \rangle$, the mean-field

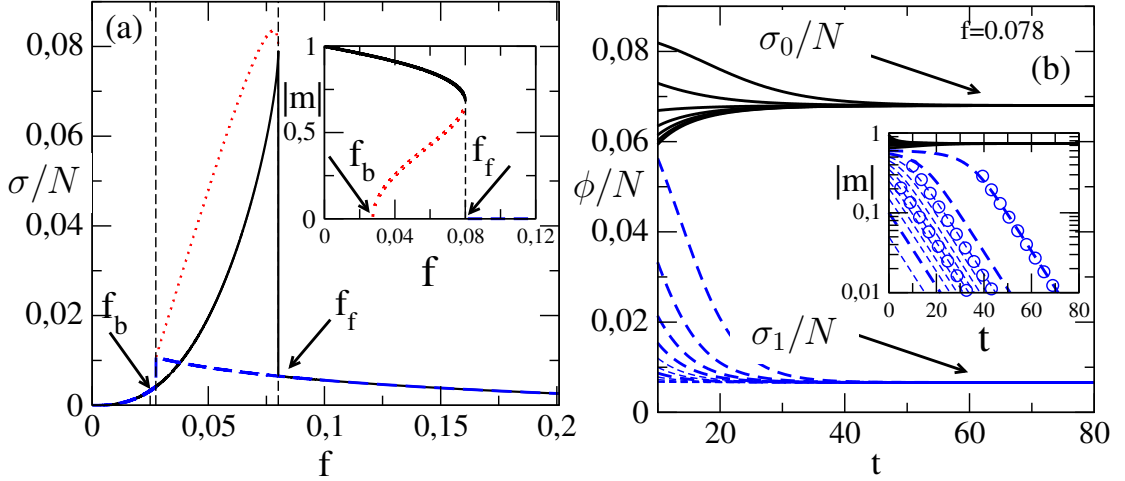


Figure 4.3: Panel (a) depicts the bistable behavior of entropy production rate per site σ/N and the order parameter $|m|$ (inset) for $\theta = 0.43$ and $k = 12$. Continuous black curves denote the stable solutions for $m_0 > m^{(U)}$, while blue dashed curves stand for $m_0 < m^{(U)}$. They coincide for $f > f_f$ and $f < f_b$, and are different inside the hysteresis $f_b < f < f_f$. Dotted curves correspond to the unstable solutions $m = m^{(U)}$, attained when $m_0 = m^{(U)}(f)$. Panel (b) shows the time evolution of entropy flux ϕ/N for distinct initial configurations and $f = 0.078$, solid black curves for $m_0 > m^{(U)}$ and dashed blue for $m_0 < m^{(U)}$. The inset shows the time evolution of $|m|$, where circles correspond to the analytical prediction $m \sim e^{a(f_b-f)t}$, valid for $m_0 \ll 1$.

steady entropy production in the limit of $k \rightarrow \infty$ behaves as

$$\frac{\sigma}{N} = \begin{cases} 0 & \text{if } f < (1 - 2\theta)/2(1 - \theta) \\ \frac{1-2f}{2} \ln \frac{1-f}{f} & \text{if } f > (1 - 2\theta)/2(1 - \theta) \end{cases} \quad (4.39)$$

In the inertialess case $\theta = 0$, the majority vote model in the complete graph $k \rightarrow \infty$ always has zero entropy production since $f < 0.5$, as already observed in [131]. However, the presence of inertia also moves such a system out of equilibrium in the disordered phase.

Figure 4.3 summarizes some of the results discussed so far for discontinuous transitions. Taking into account a neighborhood of $k = 12$ sites and distinct inertia values, the order parameter $|m|$ [see Inset of Fig. 4.3(a)] jumps at f_f and f_b . The time evolution of $|m|$ follows the theoretical prediction $m \sim e^{a(f_b-f)t}$ for $m_0 \ll 1$ [see the Inset of Fig. 4.3(b)]. Discontinuities are also presented in the entropy production at the same locations. Along the hysteretic branch, the entropy flux per site $\phi/N(t)$ converges to two well-defined values, σ_0/N and σ_1/N .

As stated above, the entropy production presents a kink at $f = f_c$ for continuous transitions, a value for which the derivative is discontinuous and locates the critical point f_c . For the inertialess case or even for low θ , the entropy production increases monotonically before f_c and

decreases afterward. This can be understood by inserting $q = 1 - 2f$ and $g[X] = \text{sgn}[X]$ into Equation (4.14),

$$m = (1 - 2f) \text{erf} \left(m \sqrt{\frac{k}{2}} \right), \quad (4.40)$$

and the entropy production rate per site is given by

$$\frac{\sigma}{N} = \frac{1}{2} \ln \frac{f}{1-f} \left[\frac{m^2}{1-2f} - (1-2f) \right]. \quad (4.41)$$

At the vicinity of the critical point, where m is expected to be small, the right-hand side of Equation (4.40) can be expanded in a Taylor series; hence,

$$m \sim (f_c - f)^{1/2}, \quad (4.42)$$

where we find $\beta_{\text{mf}} = 1/2$ as the mean-field critical exponent, and

$$f_c = \frac{1}{2} \left\{ 1 - \sqrt{\frac{\pi}{2k}} \right\} \quad (4.43)$$

is the critical point.

From Eq. (4.42), entropy production behaves as

$$\frac{\sigma}{N} \rightarrow \begin{cases} \frac{1-2f}{2} \ln \frac{1-f}{f} \left[1 - \frac{12}{k} \frac{f_c - f}{(1-2f)^2} \right] & f \rightarrow f_c^- \\ \frac{1-2f}{2} \ln \frac{1-f}{f} & f \rightarrow f_c^+ \end{cases} \quad (4.44)$$

and therefore σ is continuous at the criticality. Whereas its first derivative $\sigma' \equiv \partial\sigma/\partial f$ is discontinuous, with a jump of size

$$\Delta \left[\frac{\sigma}{N} \right]_{f=f_c} \sim \sqrt{\frac{1}{k}} \ln \frac{1 - \sqrt{\pi/2k}}{1 + \sqrt{\pi/2k}}, \quad (4.45)$$

hence consistent with the exponent $\alpha_{mf} = 0$. Importantly, the maximum of σ not necessarily corresponds to the critical point, ruling out its importance as a phase transition locator, even if it is suggestive for the inertialess case. Figure 4.3 illustrates above results for continuous phase transitions. The phase transition is located by a discontinuity in the first derivative.

Lastly, in Fig. 4.5 we plot the phase diagrams for $k = 12$ and $k = 20$ evaluated through by the entropy production analysis previously described. We see that both phase transition location

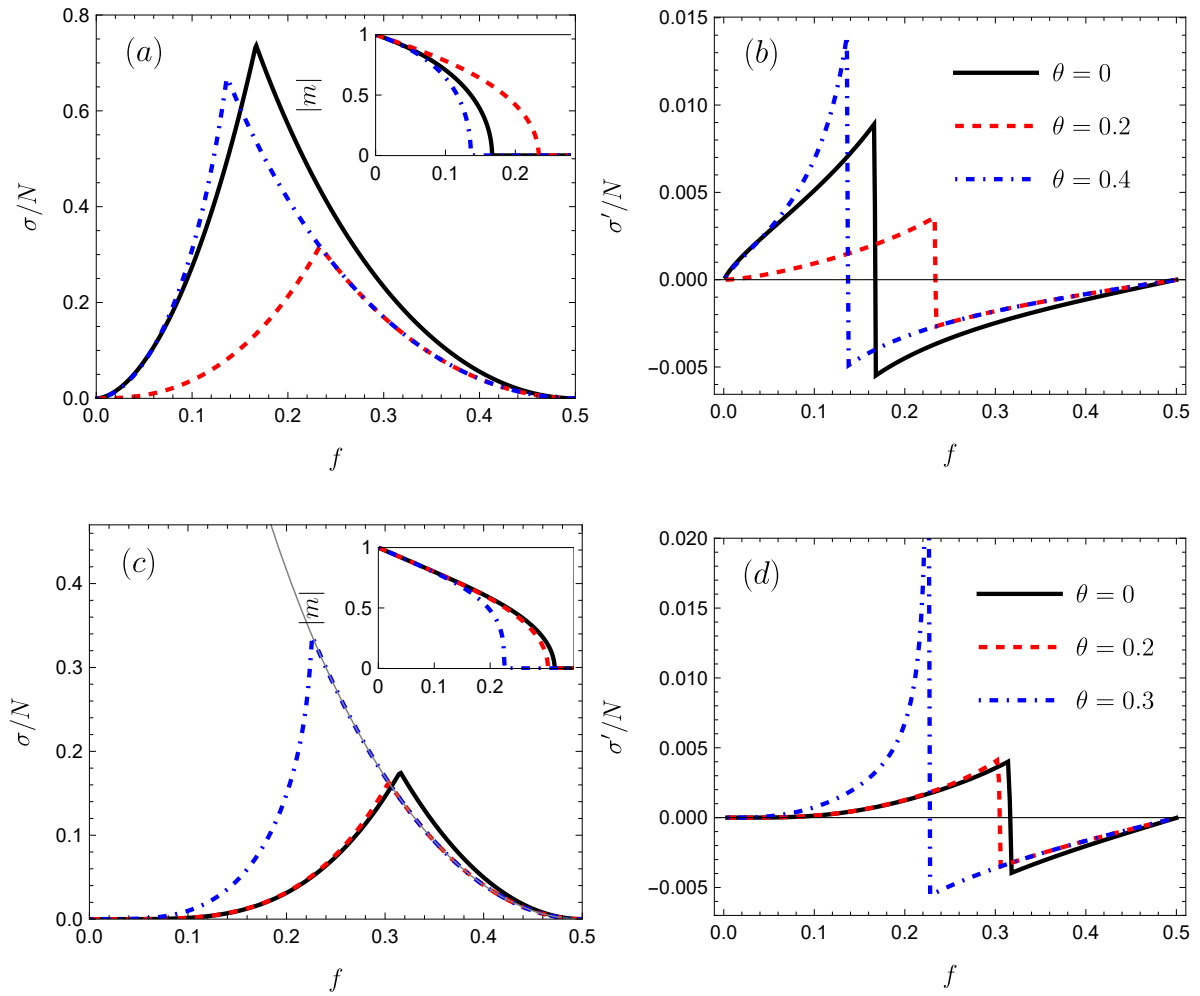


Figure 4.4: Left panels show entropy production in terms of the misalignment parameter and for different values of inertia, and the order parameter as insets. Right panels show entropy production's derivative $\sigma' \equiv \partial\sigma/\partial f$. Top panels are results for connectivity $k = 4$ and bottom panels for $k = 12$. The gray curve in panel (c) stands for the $k \rightarrow \infty$ behavior to the right of the critical point as described in Eq. (4.39).

and its classification are in full agreement with those obtained from order parameter analysis (see e.g. Fig. 1 in reference [129]).

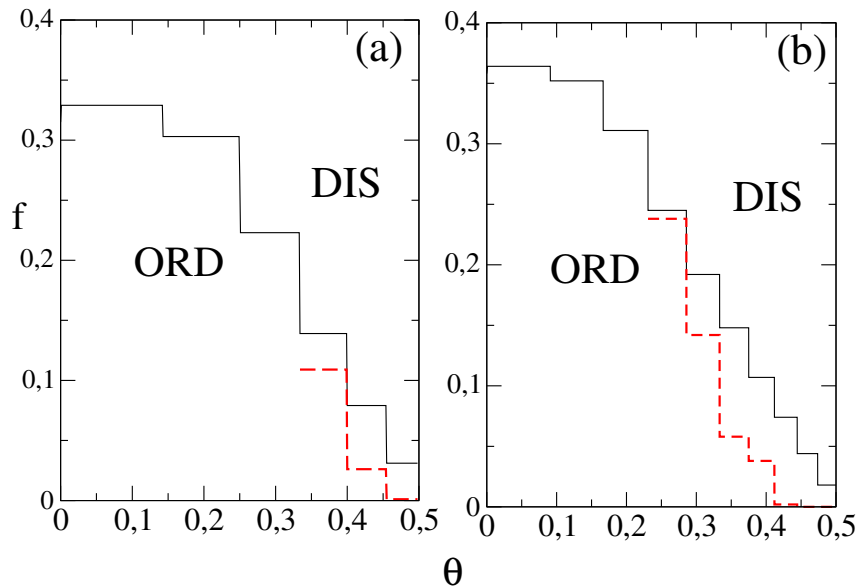


Figure 4.5: Panels (a) and (b) show the mean-field phase diagrams for $k = 12$ and $k = 20$ through analysis of entropy production. Black solid and red dashed lines correspond to the values of f_f and f_b , respectively. They coincide for continuous transitions but are different for discontinuous.

4.2.3 Beyond the mean-field theory

In addition to the mean-field theory, we present a general analytical description of the entropy production behavior in continuous and first-order phase transitions on regular lattices as well as complex networks. Verifying the theoretical predictions and building on them, numerical simulations for the majority vote model will be performed for distinct network topologies in the following section.

Discontinuous transitions in regular Lattices: Distinct works [I, 129, 130, 132] have attested that discontinuous phase transitions yield stark differences in regular and complex networks. In the first case, it emerges through sudden changes of $|m|$, its variance $\chi = N[\langle m^2 \rangle - |m|^2]$ and other quantities whose scaling behavior goes with the system volume N .

In the vicinity of q_0 the correlation length is finite for an arbitrary first-order phase transition, the probability distribution can be approximately written as a sum of two independent Gaussian distributions, from which one extracts a scaling behavior with the system volume [I, 132–134]. More specifically, the probability distribution is given by $P_N(m) = P_N^{(o)}(m) + P_N^{(d)}(m)$, where

$P_N^{(\alpha)}(m)$ is associated to the phase α (with order parameter m_α):

$$P_N^{(\alpha)}(m) = \frac{\sqrt{N}}{\sqrt{2\pi}} \frac{\exp[N\{\Delta q m - (m - m_\alpha)^2/(2\chi_\alpha)\}]}{[F'_o(\Delta q; N) + F'_d(\Delta q; N)]}. \quad (4.46)$$

The parameters χ_α and $\Delta q \equiv q_N - q_0$ correspond to the distribution width and the “distance” to the coexistence point q_0 , respectively.

Although in principle the assumption of two independent Gaussians cannot properly describe a “weak” discontinuous phase transition, in which an overlap between $P_N^{(o)}(m)$ and $P_N^{(d)}(m)$ is expected, its reliability has been verified in several examples of non-equilibrium phase transitions with distinct properties [132, 133], even in some cases with the presence of overlapping.

Despite the steady entropy production rate displaying a non-trivial dependence on the system features and on generic correlations of type $\langle s_i \rangle$, $\langle s_i s_{i+1} \rangle$, $\langle s_i s_{i+1} s_{i+2} \rangle$ and so on, Schnakenberg’s expression for σ depicts it as the ensemble average of a fluctuating quantity, enabling us to resort to previous ideas based on the central limit theorem. The generality of the distribution of order parameters for tackling phase coexistence [132] suggests the extension of a similar relationship for the steady entropy production. More concretely, we assume that at the steady state the fluctuating entropy production rate σ^f is distributed as $P_N(\sigma^f) = P_N^{(o)}(\sigma^f) + P_N^{(d)}(\sigma^f)$, where $P_N^{(\alpha)}(\sigma^f)$ is given by

$$P_N^{(\alpha)}(\sigma^f) = \frac{\sqrt{N}}{\sqrt{2\pi}} \frac{\exp[N\{\Delta q \sigma^f - (\sigma^f - \sigma_\alpha^f)^2/(2\bar{\chi}_\alpha)\}]}{[F_o(\Delta q; N) + F_d(\Delta q; N)]}, \quad (4.47)$$

and each Gaussian is centered at σ_α^f with width of the α peak being $\bar{\chi}_\alpha$. Given that $P_N(\sigma^f)$ is normalized, each term $F_{o(d)}$ then reads

$$F_\alpha(\Delta q; N) = \sqrt{\bar{\chi}_\alpha} \exp\{N\Delta q [\sigma_\alpha^f + \bar{\chi}_\alpha \Delta q/2]\} \quad (4.48)$$

for $\alpha = \{o, d\}$.

The steady entropy production is straightforwardly calculated as $\sigma = \int_{-\infty}^{\infty} \sigma^f P_N(\sigma^f) d\sigma^f$, which is read as

$$\sigma = \frac{\sum_\alpha (\sigma_\alpha^f + \bar{\chi}_\alpha \Delta q) F_\alpha(\Delta q; N)}{F_o(\Delta q; N) + F_d(\Delta q; N)}. \quad (4.49)$$

Near phase coexistence, in which Δq is expected to be small, the terms $\mathcal{O}(\Delta q)$ dominate over

$\mathcal{O}(\Delta q)^2$ and Eq. (4.49) can be approximately rewritten as

$$\sigma \approx \frac{\sqrt{\bar{\chi}_o} \sigma_o^f + \sqrt{\bar{\sigma}_d^f} \sigma_d^f \exp\{-N[(\sigma_o^f - \sigma_d^f)\Delta q]\}}{\sqrt{\bar{\chi}_o} + \sqrt{\bar{\chi}_d} \exp\{-N[(\sigma_o^f - \sigma_d^f)\Delta q]\}}. \quad (4.50)$$

Note that in the large volume limit $N \rightarrow \infty$, Equation (4.50) reproduces the jump from ϕ_o and ϕ_d when $\Delta q \rightarrow 0_-$ and $\Delta q \rightarrow 0_{-(+)}$, respectively. Remarkably, the curves for different values of N cross at the transition point $\Delta q = 0$, at

$$\sigma^* \approx \frac{\sqrt{\bar{\chi}_o} \sigma_o^f + \sqrt{\bar{\chi}_d} \sigma_d^f}{\sqrt{\bar{\chi}_o} + \sqrt{\bar{\chi}_d}}. \quad (4.51)$$

The crossing point clearly discerns continuous and discontinuous phase transitions and can be used as an indicator of the phase coexistence, as observed in Ref. [135] (Figs. 7 and 8) for a chemical reaction model.

Discontinuous transitions in complex networks: The mean-field descriptions is more powerful for describing complex networks rather than regular lattices; the presence of structure cannot be captured by this technique. The phase coexistence in complex networks is akin to the mean-field results [I, 129, 130, 136], whose behavior is generically characterized by the existence of a hysteretic loop and bistability.

The order parameter presents a spinodal line in which, along the hysteretic loop, the system will converge to one of the possible steady states depending on the initial configuration. In order to locate the ‘‘forward transition’’ point q_f , the system is initially placed in an ordered configuration and the control parameter q is increased by an amount δ , whose final state at q is used as the initial condition at $q + \delta$, until the order parameter discontinuity is observed. Conversely, the ‘‘backwards transition’’ point q_b is pinpointed by starting from the disordered phase and decreasing q until the order parameter jump takes place. Entropy production also captures these features, which can be viewed through a general argument for order-disorder phase transitions.

The order parameter behaves as $\langle s_i \rangle \sim N^{-1/2}$ in the disordered phase, and the mean-field behavior of the correlations is given by $\langle s_i s_{i+1} \cdots s_{i+n} \rangle \approx \langle s_i \rangle \langle s_{i+1} \rangle \cdots \langle s_{i+n} \rangle = N^{-n/2}$. Hence, in the thermodynamic limit, all correlations will vanish in the disordered phase and σ will depend solely on control parameters. Conversely, $\langle s_i s_{i+1} \cdots s_{i+n} \rangle$ presents a well-defined non-zero value in the ordered phase, and σ depends not only on the control parameters but also on correlations. Therefore, the jumps at q_f (from $m_1 \equiv m(q_f) \neq 0$ to 0) and q_b (from 0 to

$m_2 \equiv m(q_b) \neq 0$), commonly viewed in terms of order parameter, will also be present in the entropy production.

The presence of bistability implies that $\phi(t)$ will converge to one of the two well-defined values, since along the hysteretic branch the system behaves either as in the disordered or ordered phase, depending on the initial condition. Although this argument is valid for a generic order-disorder phase transition, it is expected to describe other types of phase transitions, provided the order parameter and correlations also present a hysteretic behavior. Thereby, both cases reveal that the entropy production behavior also embraces phase coexistence traits commonly treated in terms of the order parameter.

Continuous phase transitions: Albeit characterized by the vanishing of the order parameter $|m|$ and algebraic divergences of other quantities at the criticality, the behavior of quantities becomes rounded due to finite-size effects. According to the standard finite-size scaling, they behave as $|m| = N^{-\beta/\nu} \tilde{f}(N^{1/\nu}|\epsilon|)$, $\chi = N^{\gamma/\nu} \tilde{g}(N^{1/\nu}|\epsilon|)$ with \tilde{f} and \tilde{g} being scaling functions and $\epsilon = (q - q_c)/q_c$ the scaled distance to the critical point.

Typically, q_c is located by choosing a quantity that intersects for distinct system sizes. For order-disorder phase transitions, the Binder cumulant U_4 fulfills the above requirement [137], whose crossing value U_0^* depends on the lattice topology and the symmetry properties. Some papers [117, 138] have described similar scaling relations for entropy production. Close to the criticality, σ is continuous

$$\sigma - \sigma_c \sim (q_c - q)^{1-\alpha}, \quad (4.52)$$

and its first derivative $\sigma' \equiv \partial\sigma/\partial q$ diverges at $q = q_c$:

$$\sigma' \sim (q_c - q)^{-\alpha}. \quad (4.53)$$

Due to finite-size effects, it is reasonable to assume that σ' behaves as $\sigma' = N^{\alpha/\nu} \tilde{h}(N^{1/\nu}|\epsilon|)$, with \tilde{h} being an appropriate scaling function. From the exponents β , α and γ , we wish to check whether the hyperscaling relation $\alpha + 2\beta + \gamma = 2$, fulfilled in the mean-field theory approach, is also satisfied in different scenarios for continuous phase transitions.

4.2.4 Beyond mean-field - Majority vote model with inertia

Here, we go back to the majority vote model introduced in Section 4.2.2 and already analyzed on a theoretical basis, and perform a numerical analysis based on Monte Carlo simulations.

For a given network topology with fixed size N , misalignment parameter f , and inertia θ , a site i is chosen randomly. Its spin value s_i is updated ($s_i \rightarrow s'_i$) according to the transition rate

$$w_{s'_i} = (1 - \theta) \sum_{j=1}^k \delta(s'_i, s_j) / k + \theta \delta(s'_i, s_i), \quad (4.54)$$

where the sum runs over the k nearest neighbors of the site i . With probability $1 - f$, s_i changes to the majority neighborhood spin s'_i , and with complementary probability f the majority rule is not followed. A Monte Carlo step corresponds to repeating this procedure N times, that is, trial N of updating a randomly drawn spin. After repeating the above dynamics with a sufficient number of steps (in order of 10^6 Monte Carlo steps for the model studied), the system attains a stationary steady state that might or might not be in equilibrium.

Random-regular networks are complex networks in which every site has the same fixed number of neighbors k , while the connections are randomly distributed. They have been generated through a configuration model scheme [139]: For a system with N nodes and connectivity k , we first start with a set of Nk points, distributed in N groups, each of which contains exactly k points. Next, one chooses a random pairing of points between groups and then creates a network linking nodes i and j if there is a pair containing points in the i -th and j -th sets, until $Nk/2$ pairs are obtained. If the resulting network configuration presents a loop or duplicate links, the above process is restarted.

The increase of connectivity k in bidimensional topologies is achieved by extending the range of interaction neighborhood. For example, $k = 4, 8, 12$ and 20 include interactions between the first, first to second, first to third, and first to fourth next neighbors, respectively, as sketched in Fig. 4.6.

Discontinuous phase transitions: Figure 4.7 exemplifies these predictions for the majority vote model in bidimensional lattices with $k = 20$ and $\theta = 0.375$. The entropy production curves follow the theoretical predictions of the Eqs. (4.50) and (4.51) (continuous lines in panels (a) and (b)), whose intersection among curves occurs at $f_c = 0.05084(5)$, in excellent agreement with estimates obtained from standard techniques [132]. The alternative phase transition locators are the maximum of χ that leads to $f_c = 0.0509(1)$, the minimum of Binder's cumulant leading to $f = 0.0510(1)$, and the equal area of the order parameter distribution leading to $f_c 0.0509(1)$. Panel (d) shows the scaling of these indicator with the system size, all of them converge to the same value.

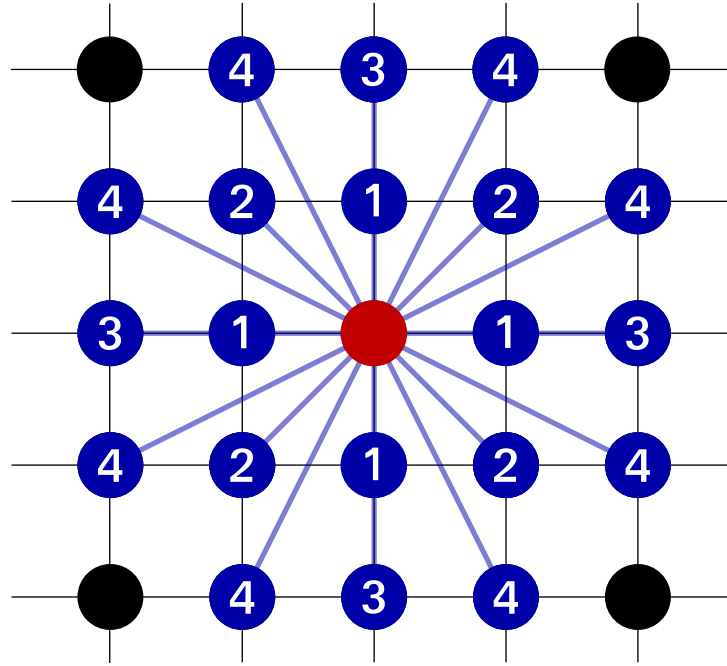


Figure 4.6: Local neighborhood for a bidimensional lattice. The central site in red is connected to its first (1), second (2), third (3) and fourth (4) next neighbors.

Under transformation $y = (f - f_0)N$ the entropy production collapses into a single curve [inset of Fig. 4.7 (c)], reinforcing the reliability of Eq. (4.50) for describing σ at the phase coexistence region. Out of the scaling regime ($f > f_0$ for large N), σ/N depends solely on the control parameters f and θ , as can be seen in the inset of panel (a). Discussed trademarks of entropy production in a phase transition will be verified by simulations for the Schlögl and a nonequilibrium version of the Potts model in Section 4.3.5.

Considering the case of complex structures, Fig. 4.8 depicts the main results for the majority vote model in a random-regular network with $k = 20, \theta = 0.3$ and $N = 10^4$. The entropy production reveals the existence of a hysteretic loop [panel (a)] located at the interval $f_b = 0.055 < f < f_f = 0.15$, in complete equivalence with the order parameter branch [panel (b)]. For higher inertia values (inset), the bistability extends over $0 \leq f \leq f_f$, both for magnetization and entropy production rate, similar to the limit of $k \rightarrow \infty$ discussed in Eq. (4.39).

As we observed, phase transitions can be located from the analyses of entropy production, therefore, phase diagrams can be raised. They are shown in Fig. 4.9 for both regular and complex networks, indicating the role of inertia in the phase transition order: Large enough inertia leads to discontinuous phase transitions, and the hysteretic region increases as θ grows. The hysteretic loop can be seen in panel (b) as the distance from forward (black lines and circles) and backward (red dashed lines and crosses) values.

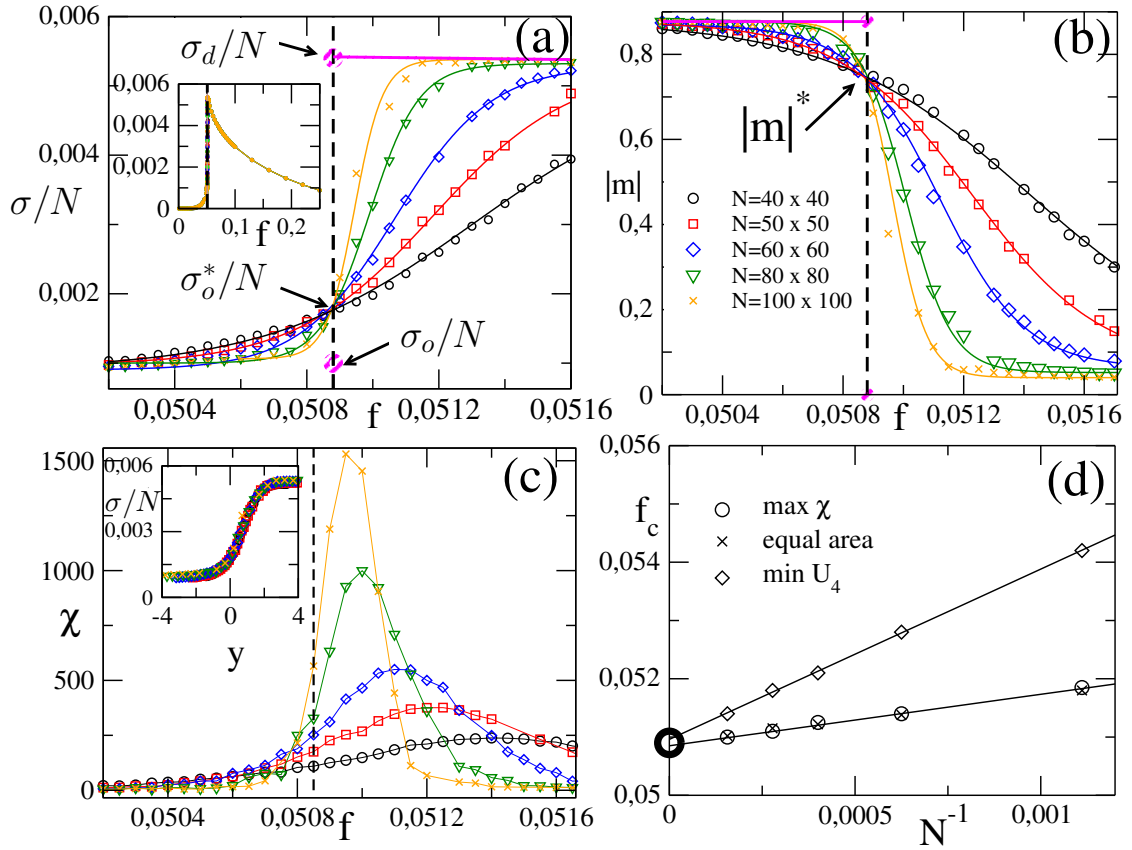


Figure 4.7: Majority vote model in a bidimensional lattice with $k = 20$ and $\theta = 0.375$. For distinct system sizes, the plots show relevant quantities in terms of the misalignment parameter at the phase coexistence vicinity: (a) entropy production rate per site, (b) order parameter, (c) variance. The dashed vertical lines indicate where the curves cross. The continuous lines in panels (a) and (b) correspond to the theoretical description in Eq. (4.50). Panel (d) shows the values of f obtained from different criteria, maximum of χ , equal area of order parameter distributions, and minimum of U_4 ; the open circle represents the value towards which the extrapolation of the lines hit the axis, i.e. the inferred value for $N \rightarrow \infty$ limit. Insets: (a) σ/N for more values of f , (b) σ/N under transformation $y = (f - f_0)N$.

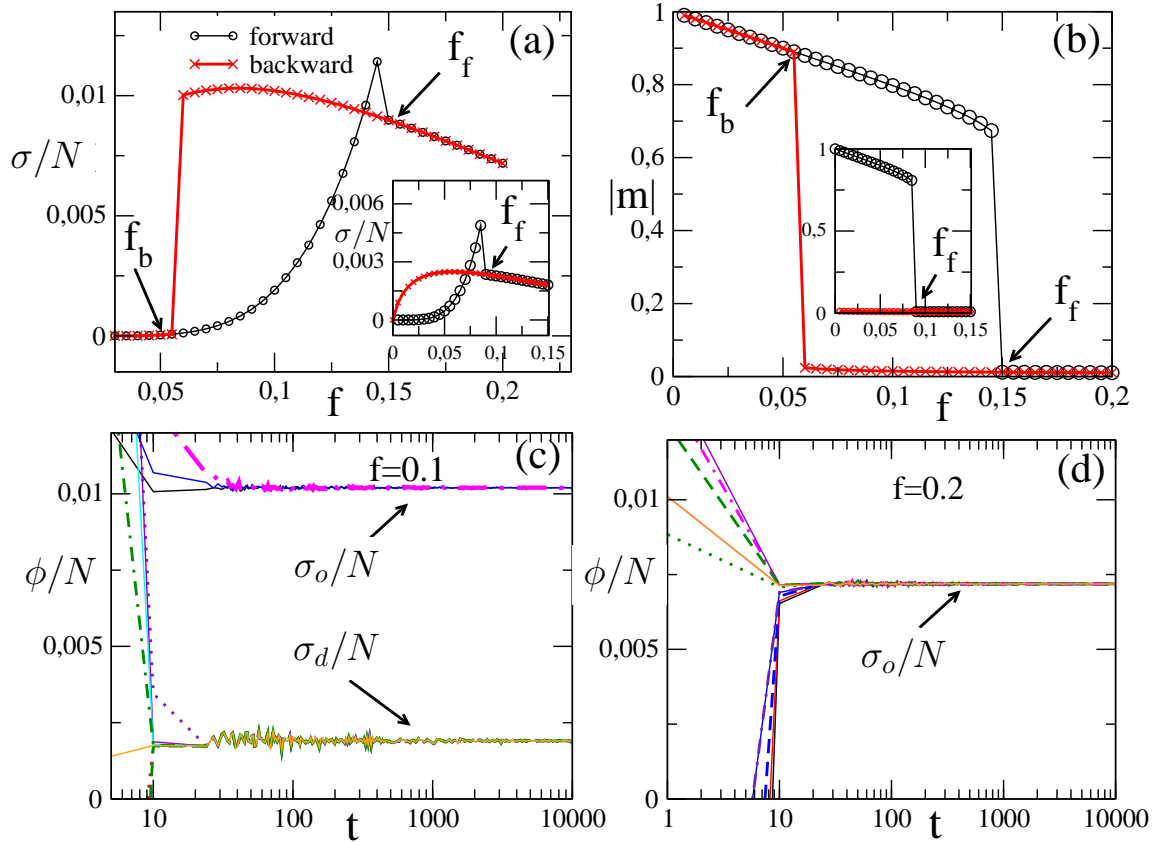


Figure 4.8: Panels (a) and (b) show the σ/N and $|m|$ in terms of f defined in a random-regular network with $k = 20$ and $N = 10^4$; the main panels have inertia $\theta = 0.3$ while the insets have $\theta = 0.375$. Black and red curves correspond to the forward and backward trajectories, respectively. The time evolution of $\phi(t)$ for distinct initial conditions m_0 for $f_b < f = 0.10 < f_f$ is shown in panel (c) and $f = 0.20 > f_f$ in (d).

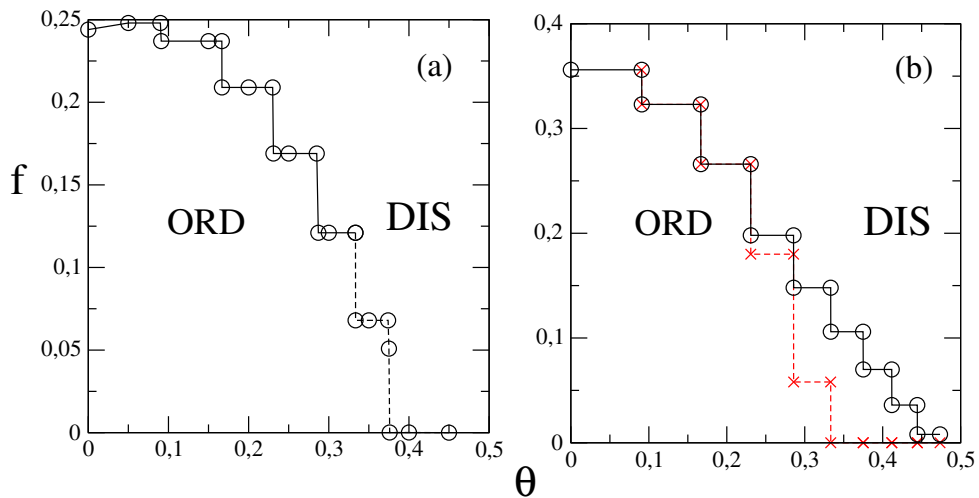


Figure 4.9: Panels (a) and (b) show the phase diagrams for $k = 20$ for regular and random-regular through the analysis of entropy production. ORD denotes the ordered phase while DIS the disordered. Continuous lines correspond to continuous phase transitions, and dashed lines to discontinuous. In panel (b), the red dashed lines stem from the backward trajectories.

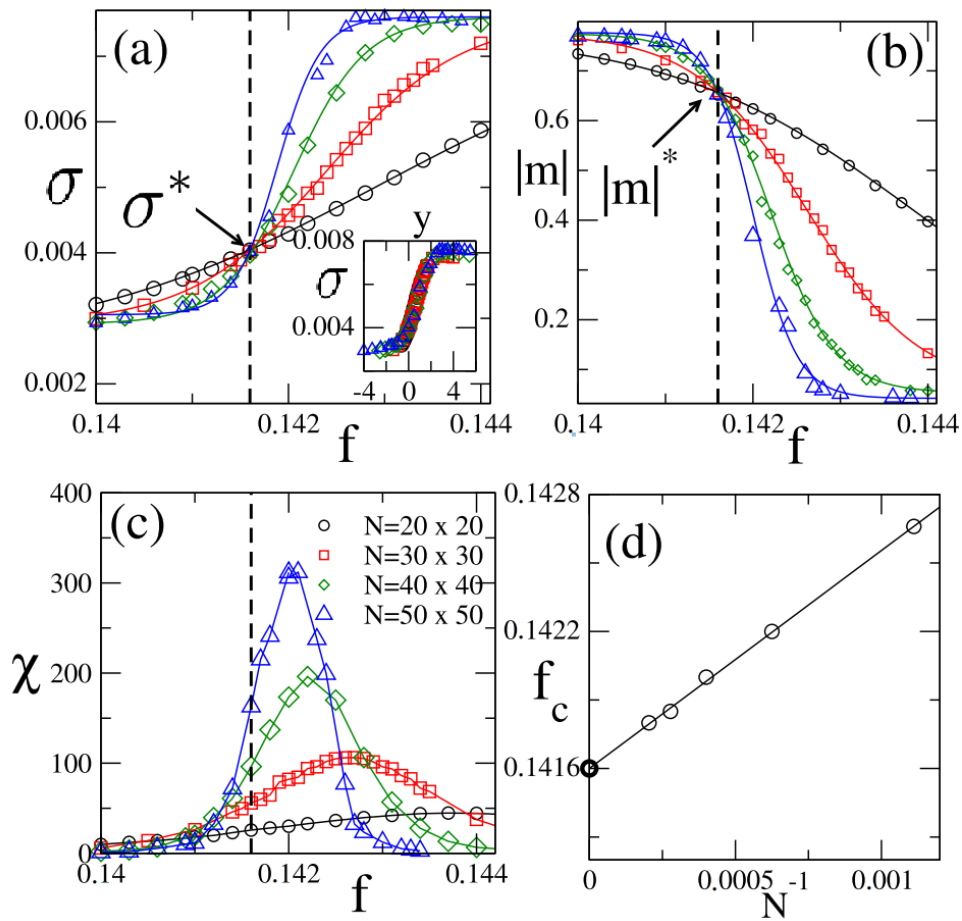


Figure 4.10: $\bar{q} = 3$ majority vote model in a regular lattice with $k = 20$ and $\theta = 0.32$. In similarity to Fig. 4.7, the panels respectively show entropy production rate (and its collapse under $y = (f - f_0)N$), order parameter, variance, and the critical point localization from the maximum of χ .

On the contrary, Figures 4.10 and 4.11 depict the main results for the bidimensional and random-regular structures for $\bar{q} = 3$, in which the symmetry C_{3v} leads to an entirely different critical behavior from the $\bar{q} = 2$ case. However, the phase coexistence behavior is analogous to the previous ones, including the existence of bistability (complex networks), crossing among curves at the transition point ($f_0 = 0.14160(5)$) and scaling with the system volume (regular structures). Thereby we reinforced the robustness of our findings at discontinuous phase transitions.

Continuous phase transitions: Previous results show that regardless of the value of inertia θ [I], the phase transition remains continuous in regular structures when $k < 20$, and the critical exponents are consistent with $\beta = 1/8$, $\gamma = 7/4$ and $1/\nu = 1$ [127]. Figure 4.12 illustrates continuous phase transition traits in terms of the entropy production.

Although σ is finite and continuous at the critical point [panel (a)], σ' increases without

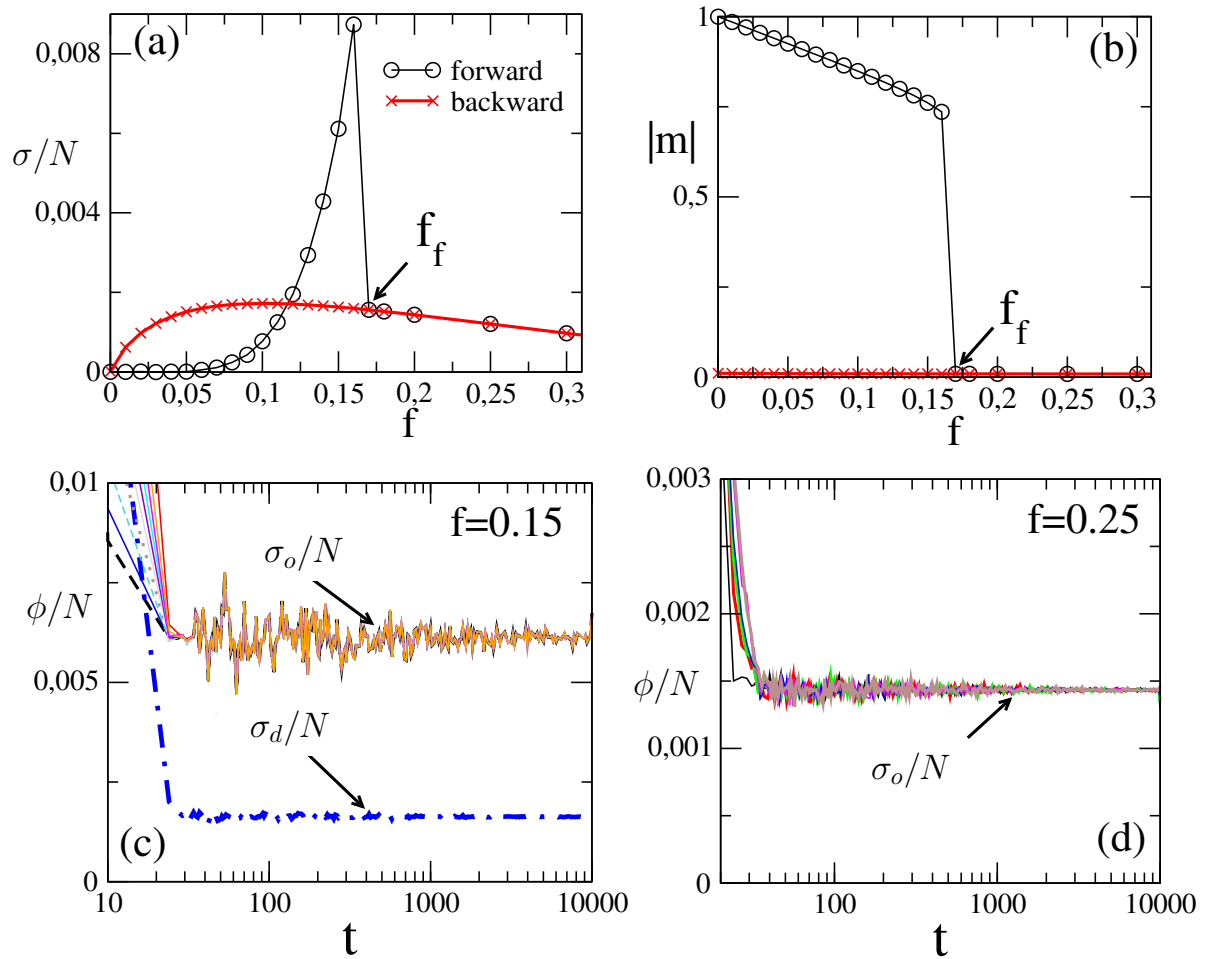


Figure 4.11: For the $\bar{q} = 3$ majority vote model in a random-regular complex network with $k = 20$ and $\theta = 0.35$, in similarity to Fig. 4.8, panels show entropy production rate, order parameter, entropy flux inside and outside the phase coexistence region, respectively.

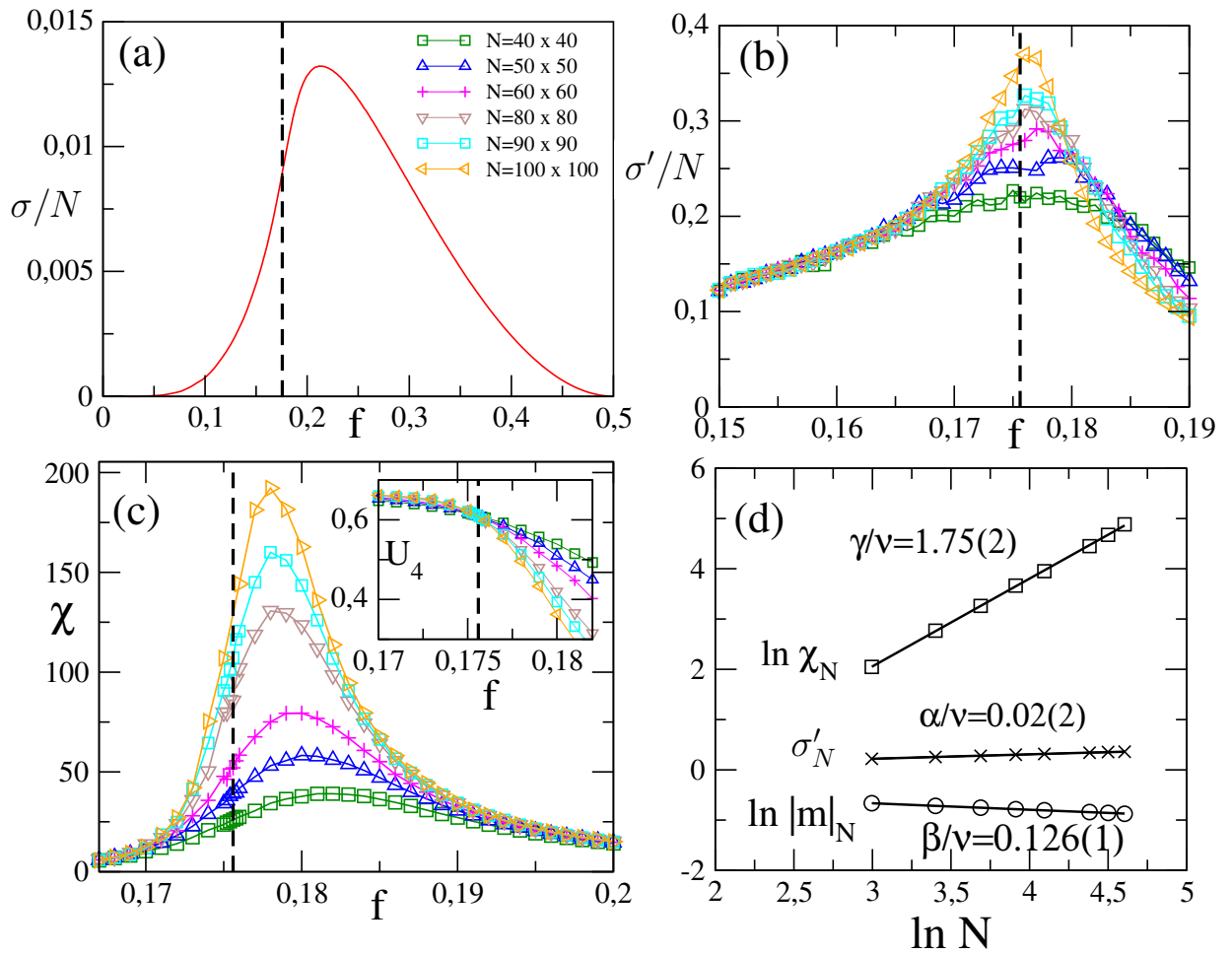


Figure 4.12: Regular lattice for interactions between the first to the third next neighbors, $k = 12$, and $\theta = 0.2$. Panels (a), (b) and (c) depict the entropy production, its derivative, and variance in terms of f for different system sizes. Inset: The same but for the Binder cumulant U_4 . Dashed vertical lines locate the critical point f_c evaluated through the crossing among U_4 curves. In (d), the scaling of $\ln \chi_N$, Π'_N , and $\ln |m|_N$ with $\ln N$ at $f = f_c$.

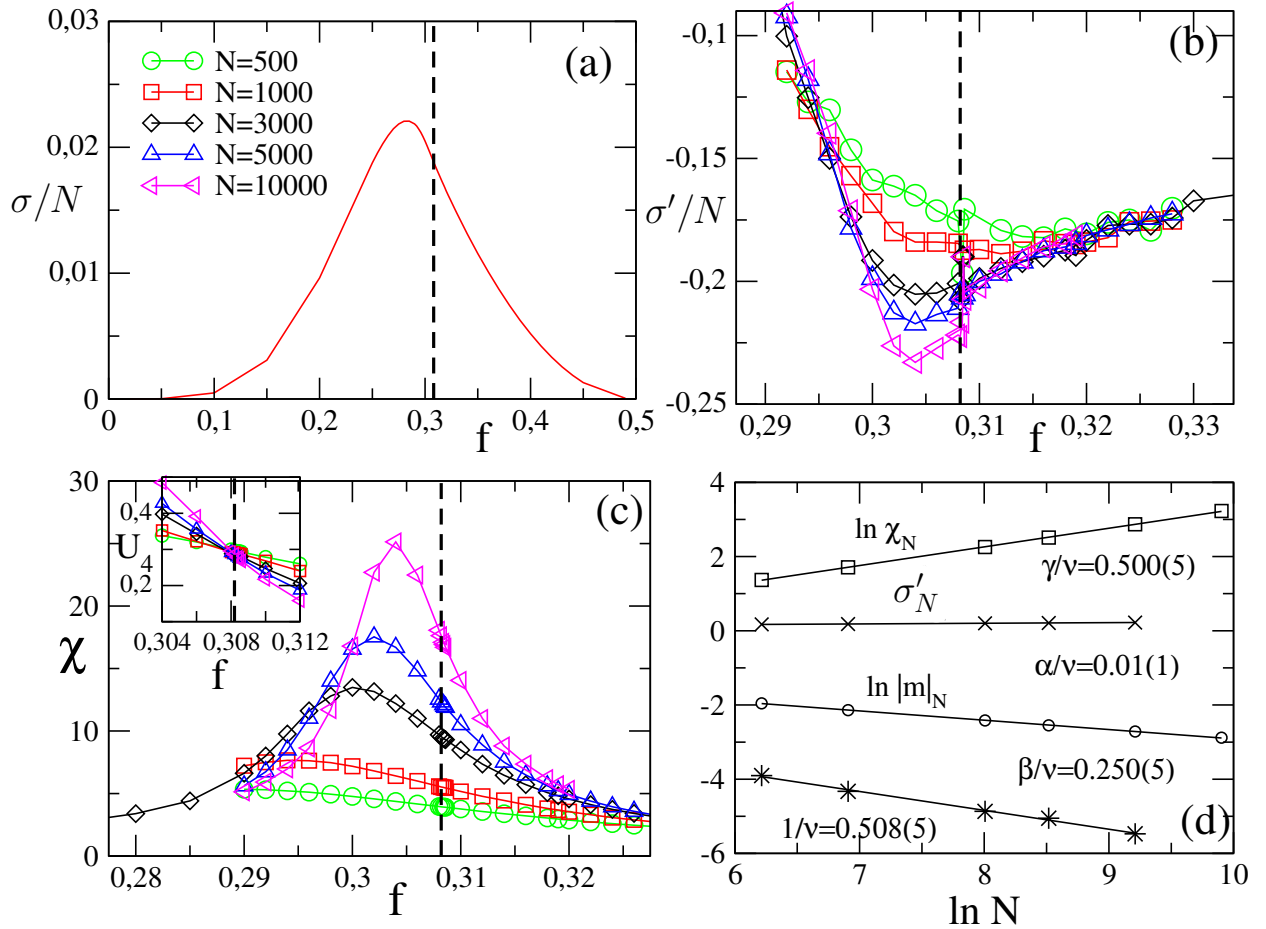


Figure 4.13: Random-regular network with $k = 12$ and $\theta = 0$. Panels (a)–(c) show the steady entropy production, its derivative and variance for distinct system sizes. Inset is the Binder cumulant. Panel (d) different scalings with the system size at $f = f_c$ and their respective exponent.

limits as $N \rightarrow \infty$ [panel (b)], eventually leading to a divergence. For finite systems, σ'_N evaluated at $f = f_c$ increases logarithmically with N , to which a critical exponent of $\alpha = 0$ is associated [panel (d)].

Figure 4.13 extends the analysis to random-regular structures. In that case, the critical behavior follows exponents $\beta/\nu = 1/4$, $\gamma/\nu = 1/2$ and $1/\nu = 1/2$ [140], rather different from mean-field values $\beta = 1/2$, $\gamma = 1$ and $1/\nu = 2$, and those from regular lattices observed in Fig. 4.12.

In similarity to the bidimensional case, $\sigma(f_c)$ is finite while $\sigma'_N(f_c)$ logarithmically increases with the system size, which is also consistent to a logarithmic divergence and exponent $\alpha = 0$. Such conclusions are reinforced by appealing to the hyperscaling relation $\alpha + 2\beta + \gamma = 2$. Having the values of β and γ , we re-obtain $\alpha = 0$ in both cases.

Lastly, the $\bar{q} = 3$ case is characterized in regular lattices by the critical exponents $\beta = 1/9$

and $\gamma = 13/9$. According to the hyperscaling relation, the exponent associated with the entropy production should be $\alpha = 1/3$. Recently, the value $\alpha = 0.32(2)$ has been obtained from numerical simulations in Ref. [141], in full accordance with our theoretical predictions.

4.3 Two-state coarse graining of phase transitions

The previous analysis provided a general description of the entropy production behavior along continuous and first-order phase transitions, now we address particularities of the latter. First-order phase transitions present a region of phase coexistence marked by a hysteresis, within which quantities such as the stochastic entropy production rate have a bimodal probability distribution. Moreover, the characteristic time of jumps between phases (viz. the metastability lifetime) increases exponentially with the system volume. Hence, different timescales emerge and their consequences on the statistics of integrated currents such as entropy production will be addressed [V].

The average entropy production rate has been found to be always finite around the transition point, with the first derivative either diverging, in continuous transitions [II, 60, 117, 118, 121, 125, 142], or presenting a jump in discontinuous ones [II, 118, 124]. These clear signatures suggest, in fact, that the average entropy production could even be used to classify the type of transition. Conversely, the behavior of higher order statistics, such as the variance, is much less understood. Currents fluctuate at the stochastic level; therefore, they are associated to probability distributions. Understanding the behavior of said distributions constitutes a major area of research, as they form the basis for extending the laws of thermodynamics towards the microscale, providing insights into non-trivial properties of non-equilibrium physics.

As stated previously, the crucial aspect of first-order transitions is that when the volume V is large, the transitions between coexisting phases become exponentially suppressed. The system will thus be governed by two very distinct timescales, one describing fast relaxation *within* each phase and another describing seldom transitions *between* the phases. The latter will be referred to as the metastability lifetime τ_m , and usually grows exponentially with V [143] (for continuous transitions these divergences are algebraic).

Cumulants of thermodynamic currents are usually assessed via numerical approaches, such as Monte Carlo simulations [II], or large deviation theory [122, 144–148]. In both cases, cumulants are computed from long-time sample averages, integrated over a large enough time win-

dow τ and relying on the system's ergodicity. Although the considered stochastic processes are indeed ergodic for finite-sized systems, estimating currents around a phase transition can lead to an apparent ergodicity breaking. Evaluating $J_\tau = \langle \mathcal{J}_\tau \rangle / \tau$ from an ensemble average will correctly sample every possible state. However, when $\langle \mathcal{J}_\tau \rangle$ is obtained from the long-time limit, there can be a sampling bias for large systems due to the discussed exponential metastability lifetime increase, the system will be stuck within the phase of the initial state for $\tau \ll \tau_m$, will produce a few jumps for τ in the order of τ_m , and will ultimately meet ergodicity for $\tau \gg \tau_m$. As a consequence, the order of the limits $\tau \rightarrow \infty$ and $V \rightarrow \infty$ becomes non-trivial [149]. Evidently, this necessary integration time can surpass the age of the universe, becoming unfeasible in experiments or simulations, thus the need to study the role of integration time τ throughout different timescales.

In this section, we approach this issue by introducing the idea of conditional currents: The value of integrated entropy production conditional to the system being in a given phase. We focus, in particular, on the diffusion coefficient (scaled variance). We formulate a finite-time large deviation theory, which neatly highlights the non-trivial interplay between τ and τ_m . This is then specialized to a minimal 2-state model, that is able to capture the key features of the problem and also provides useful predictions. These are then tested on two paradigmatic examples of discontinuous transitions: Schlögl's model of chemical kinetics, and a 12-states Potts model subject to two baths at different temperatures.

4.3.1 Large deviation theory

We consider a continuous-time discrete state space Markov process $X(t)$ that undergoes a discontinuous phase transition when the control parameter λ crosses a value λ_c . Its dynamics is ruled by the master equation

$$\frac{d}{dt} p_i(t) = \sum_j \{W_{ij} p_j - W_{ji} p_i\} := \sum_j \mathbf{W}_{ij} p_j, \quad (4.55)$$

where $W_{ij} \equiv W_{j \rightarrow i}$ denotes the transition rates from j to i , $\mathbf{W}_{ii} \equiv -\sum_{j \neq i} W_{ji}$, and we assume ergodicity. In the following, the non-equilibrium stationary distribution is denoted by p_i^∞ .

At the vicinity of the phase transition the coexistence of phases leads to a mixed sampling of phases when integrated currents are being measured. We consider the generic thermodynamic

²More details on the stochastic modelling can be found in Chapter 2

integrate current evaluated up to time τ to be

$$\mathcal{J}_\tau = \int_0^\tau dt \sum_{i,j} d_{ij} \delta_{X(t^-),i} \delta_{X(t^+),j}, \quad (4.56)$$

where δ_{ij} is the Kronecker delta, $X(t^\pm)$ is the state of the system immediately before and after a transition and d_{ij} is a time anti-symmetric function $d_{ij} = -d_{ji}$, which defines the current in question. Its average J_τ and diffusion coefficient (scaled variance) D_τ are defined as

$$J_\tau = \langle \mathcal{J}_\tau \rangle / \tau, \quad D_\tau = (\langle \mathcal{J}_\tau^2 \rangle - \langle \mathcal{J}_\tau \rangle^2) / (2\tau). \quad (4.57)$$

In the limit $\tau \rightarrow \infty$, such a current will behave according to a large deviation principle [146]. But due to the sensitive interplay between τ and τ_m , we will not assume $\tau \rightarrow \infty$, as is customary. Instead, we will analyze the behavior of \mathcal{J}_τ as a function of τ . More specifically, our interest is in the regime where τ is large compared to the ‘‘within-phase’’ relaxation timescales, but not necessarily larger than the metastability lifetime τ_m . It turns out that $J_\tau \equiv J$ is independent of τ , irrespective of whether τ is large or not [146]. Conversely, for D_τ , this will be the case iff $\tau \gg \tau_m$.

For a given control parameter λ tuning the phase coexistence, one can generically label the distinct phases as 0 (for $\lambda < \lambda_c$) and 1 (for $\lambda > \lambda_c$). To study the contributions of each of them, we establish a partition of the set of states Ω into two subsets, Ω_0 and Ω_1 , representing each phase. The criteria for doing so is model dependent, and will be discussed further below. We monitor the phases by defining an indicator random variable (henceforth called the *phase indicator*)

$$I_t \equiv I(X(t)) = \begin{cases} 0 & X(t) \in \Omega_0 \\ 1 & X(t) \in \Omega_1 \end{cases} \quad (4.58)$$

which specifies in which phase the system is at time t . The probability of finding the system in phase 1, in the stationary distribution, is then $q \equiv E(I_t) = \Pr(I_t = 1)$. For readability, we will also use the notation $q_1 = q$ and $q_0 = 1 - q$, when convenient.

The main feature we introduce in such a study is the notion of conditional currents, given which phase $\alpha = \{0, 1\}$ the system is in. Inserting the identity $1 = (1 - I_t) + I_t$ inside the

integral (4.56) allows us to define the current when the system is in phase 1 as

$$\mathcal{J}_{\tau|1} = \int_0^{\tau} dt I_{t+} \sum_{i,j} d_{ij} \delta_{X(t^-),i} \delta_{X(t^+),j}. \quad (4.59)$$

The current $\mathcal{J}_{\tau|0}$ is defined similarly, but with $1 - I_t$ instead. There is an ambiguity here as to whether we use I_{t-} or I_{t+} . But this only affects those jumps occurring at time t in which $I_{t-} = 0(1)$ and $I_{t+} = 1(0)$, which are extremely rare compared to all others. It is important to clarify, at this point, that while the current (4.59) is conditioned on which phase the system is in, the dynamics itself is unconditional; that is, the system is still allowed to transition freely between phases. One could also analyze the currents for a conditional dynamics, where a reflecting barrier is placed between the phases, trapping the system in one phase or another. The relation between these two scenarios will be discussed further.

From Eq. (4.59), the total current (4.56) is then recovered as

$$\mathcal{J}_{\tau} = \mathcal{J}_{\tau|0} + \mathcal{J}_{\tau|1}, \quad (4.60)$$

an identity which holds at the stochastic level.

The conditional first moments are defined as

$$\mu_{\alpha} = \frac{E(\mathcal{J}_{\tau|\alpha})}{\tau q_{\alpha}}, \quad (4.61)$$

where the factor of q_{α} in the denominator is placed to compensate for the varying times the system spends in each phase. The average current is thus decomposed as

$$J = (1 - q)\mu_0 + q\mu_1. \quad (4.62)$$

As with J , the conditional averages μ_i will be shown below to also be independent of τ .

Similarly, we define conditional diffusion coefficients

$$D_{\tau|\alpha} = \frac{E(\mathcal{J}_{\tau|\alpha}^2) - E(\mathcal{J}_{\tau|\alpha})^2}{2\tau q_{\alpha}}, \quad (4.63)$$

which represent the fluctuations of the system within each phase. From Eq. (4.60), we therefore

see that the diffusion coefficient D_τ in Eq. (4.57) is split in three terms

$$D_\tau = (1 - q)D_{\tau|0} + qD_{\tau|1} + C_\tau, \quad C_\tau := \frac{1}{\tau} \text{Cov}(\mathcal{J}_{\tau|0}, \mathcal{J}_{\tau|1}), \quad (4.64)$$

where $\text{Cov}(A, B) = \langle AB \rangle - \langle A \rangle \langle B \rangle$ is the covariance between conditional currents A and B , and is expected to be significant only in the vicinity of the transition point.

To shed light on the behaviour of conditional currents, we consider here a finite-time version of large deviation theory [9, 80, 150, 151], and then adapt results to the conditional case. Let $G_\tau(\eta) = \langle e^{\eta \mathcal{J}_\tau} \rangle^3$ denote the moment generating function associated to the current (4.56). Decomposing it as

$$G_\tau(\eta) = \sum_i E(e^{\eta \mathcal{J}_\tau} | X_\tau = i) p_i(\tau) = \sum_i G_i(\eta), \quad (4.65)$$

we find that the entries $G_i(\eta)$ will evolve according to equation

$$\frac{dG_i(\eta)}{d\tau} = \sum_j \mathbf{L}_{ij}(\eta) G_j(\eta), \quad (4.66)$$

where the tilted operator $\mathbf{L}(\eta)$ depends on both the transition matrix \mathbf{W} in Eq. (4.55), and the type of current in question, according to

$$\mathbf{L}(\eta)_{ij} = e^{\eta d_{ij}} \mathbf{W}_{ij}, \quad (4.67)$$

where, recall, $d_{ii} = 0$. To evaluate J and D_τ , we only require the series expansion of $\mathbf{L}(\eta)$, which we write as

$$\mathbf{L}(\eta) = \mathbf{W} + \eta \mathbf{L}_1 + \eta^2 \mathbf{L}_2, \quad (4.68)$$

for matrices $L_{1(2)}$ given by

$$(\mathbf{L}_1)_{ij} = W_{ij} d_{ij}, \quad (\mathbf{L}_2)_{ij} = W_{ij} d_{ij}^2 / 2. \quad (4.69)$$

³ η is a real-valued parameter that carries many names. Depending on the field's jargon, it can be referred to as tilting parameter, counting field, Lagrange parameter and even frequency, since by $\eta \rightarrow -\eta$ a Laplace transform emerges.

4.3.2 Finite-time large deviation theory

Now, we derive expressions for the first and second current moments from the large deviation theory. Unlike standard treatments, the main difference here is that we focus on finite integration times τ . The starting point is Eq. (4.66), describing the evolution of the entries $G_i(\eta)$ of the moment generating function. Treating it as a vector $|\mathbf{G}(\eta)\rangle$ and from its series expansion in powers of η , we have that

$$|\mathbf{G}(\eta)\rangle = |\mathbf{p}^\infty\rangle + \eta|\mathbf{g}_1\rangle + \eta^2|\mathbf{g}_2\rangle + \dots, \quad (4.70)$$

where $|\mathbf{p}^\infty\rangle$ is the steady-state of \mathbf{W} . Combining this with the series expansion of the tilted operator, $\mathbf{L}(\eta) = \mathbf{W} + \eta\mathbf{L}_1 + \eta^2\mathbf{L}_2$, and collecting terms of the same order in η , we have the following system of equations

$$\frac{d}{d\tau}|\mathbf{p}^\infty\rangle = \mathbf{W}|\mathbf{p}^\infty\rangle, \quad (4.71)$$

$$\frac{d}{d\tau}|\mathbf{g}_1\rangle = \mathbf{L}_1|\mathbf{p}^\infty\rangle + \mathbf{W}|\mathbf{g}_1\rangle, \quad (4.72)$$

$$\frac{d}{d\tau}|\mathbf{g}_2\rangle = \mathbf{L}_2|\mathbf{p}^\infty\rangle + \mathbf{L}_1|\mathbf{g}_1\rangle + \mathbf{W}|\mathbf{g}_2\rangle. \quad (4.73)$$

From these, the moments can be obtained from the property $\langle \mathcal{J}_\tau^n \rangle = [d^n G_\tau(\eta)/d\eta^n]_{\eta=0}$, the first and second moments are

$$E(\mathcal{J}_\tau) = \langle \mathbf{1}|\mathbf{g}_1\rangle, \quad E(\mathcal{J}_\tau^2) = 2\langle \mathbf{1}|\mathbf{g}_2\rangle, \quad (4.74)$$

Equation (4.71) is automatically satisfied. The solution of Eq. (4.72), with $|\mathbf{g}_1(\tau=0)\rangle = 0$, is given by

$$|\mathbf{g}_1(\tau)\rangle = \int_0^\tau d\tau' e^{\mathbf{W}(\tau-\tau')} \mathbf{L}_1|\mathbf{p}^\infty\rangle. \quad (4.75)$$

For concreteness, we assume that \mathbf{W} is diagonalizable. The eigenvalues are λ_i , right eigenvectors are $\mathbb{W}|\mathbf{x}_i\rangle = \lambda_i|\mathbf{x}_i\rangle$ and left eigenvectors are $\langle \mathbf{y}_i|\mathbb{W} = \langle \mathbf{y}_i|\lambda_i$. From the irreducibility of the network, the steady-state is unique, thus one eigenvalue must be zero, say $\lambda_0 = 0$. The corresponding eigenvectors are then $|\mathbf{x}_0\rangle = |\mathbf{p}\rangle$ and $\langle \mathbf{y}_0| = \langle \mathbf{1}|$. We can then write

$$e^{\mathbf{W}\tau} = |\mathbf{p}^\infty\rangle\langle \mathbf{1}| + \sum_{i \neq 0} e^{\lambda_i\tau} |\mathbf{x}_i\rangle\langle \mathbf{y}_i|. \quad (4.76)$$

The eigenvectors satisfy $\langle \mathbf{1} | \mathbf{p}^\infty \rangle = \langle \mathbf{y}_i | \mathbf{x}_i \rangle = 1$ and $\langle \mathbf{1} | \mathbf{x}_i \rangle = \langle \mathbf{y}_i | \mathbf{p} \rangle = 0$. Thus, plugging (4.76) in (4.75), we find

$$|\mathbf{g}_1(\tau)\rangle = |\mathbf{p}^\infty\rangle \langle \mathbf{1} | \mathbf{L}_1 | \mathbf{p}^\infty \rangle \tau + \sum_{i \neq 0} \frac{e^{\lambda_i \tau} - 1}{\lambda_i} |\mathbf{x}_i\rangle \langle \mathbf{y}_i | \mathbf{L}_1 | \mathbf{p}^\infty \rangle \quad (4.77)$$

and by taking the inner product $\langle \mathbf{1} | \mathbf{g}_1 \rangle$, it follows that the second term vanishes and we obtain the first moment for arbitrary values of τ given by

$$\langle \mathcal{J}_\tau \rangle = \langle \mathbf{1} | \mathbf{L}_1 | \mathbf{p}^\infty \rangle \tau \equiv J. \quad (4.78)$$

Turning now to the second moment, the solution of Eq. (4.73) reads

$$|\mathbf{g}_2(\tau)\rangle = \int_0^\tau d\tau' e^{\mathbf{W}(\tau-\tau')} (\mathbf{L}_2 | \mathbf{p}^\infty \rangle + \mathbf{L}_1 | \mathbf{g}_1(\tau') \rangle). \quad (4.79)$$

Since Eq. (4.74) depends only on $\langle \mathbf{1} | \mathbf{g}_2 \rangle$, Eq. (4.76) together with the fact that $\langle \mathbf{1} | \mathbf{x}_i \rangle = 0$ leads to the following expression

$$\langle \mathbf{1} | \mathbf{g}_2(\tau) \rangle = \int_0^\tau d\tau' \left\{ \langle \mathbf{1} | \mathbf{L}_2 | \mathbf{p}^\infty \rangle + \langle \mathbf{1} | \mathbf{L}_1 | \mathbf{g}_1(\tau') \rangle \right\}. \quad (4.80)$$

Notice that the inner product in the first term is time-independent. For the integration of the second term we use Eq. (4.77), leading to

$$\langle \mathbf{1} | \mathbf{g}_2(\tau) \rangle = \langle \mathbf{1} | \mathbf{L}_2 | \mathbf{p}^\infty \rangle \tau + \int_0^\tau d\tau' \int_0^{\tau'} d\tau'' \langle \mathbf{1} | \mathbf{L}_1 e^{\mathbf{W}(\tau'-\tau'')} \mathbf{L}_1 | \mathbf{p}^\infty \rangle. \quad (4.81)$$

From the above expression and the first moment squared, D_τ is given by

$$D_\tau = \langle \mathbf{1} | \mathbf{L}_2 | \mathbf{p}^\infty \rangle + \frac{1}{\tau} \int_0^\tau d\tau' \int_0^{\tau'} d\tau'' \langle \mathbf{1} | \mathbf{L}_1 e^{\mathbf{W}(\tau'-\tau'')} \mathbf{L}_1 | \mathbf{p}^\infty \rangle - \frac{J^2 \tau}{2}. \quad (4.82)$$

and by carrying out the integrals, we finally have that

$$D_\tau = \langle \mathbf{1} | \mathbf{L}_2 | \mathbf{p}^\infty \rangle + \sum_{i \neq 0} \langle \mathbf{1} | \mathbf{L}_1 | \mathbf{x}_i \rangle \langle \mathbf{y}_i | \mathbf{L}_1 | \mathbf{p}^\infty \rangle \left(\frac{e^{\lambda_i \tau} - 1 - \lambda_i \tau}{\lambda_i^2 \tau} \right). \quad (4.83)$$

This expression makes clear that D_τ will sensibly depend on the interplay between τ and all eigenvalues λ_i of \mathbf{W} . In the limit of integration times much larger than relaxation times $\tau \gg 1/|\lambda_i| \forall i$ the term $e^{\lambda_i \tau} - 1$ may be neglected, and the scaled variance simplifies to the widely used expression from large deviation theory

$$D_\tau = \langle \mathbf{1} | \mathbf{L}_2 | \mathbf{p}^\infty \rangle - \langle \mathbf{1} | \mathbf{L}_1 \mathbf{W}^+ \mathbf{L}_1 | \mathbf{p}^\infty \rangle, \quad (4.84)$$

where $\mathbf{W}^+ = \sum_{i \neq 0} \lambda_i |x_i\rangle \langle y_i|$ is the Moore-Penrose pseudoinverse of \mathbf{W} expressed in the singular value decomposition fashion.

Within the coexistence region, there will appear a clear separation of time scales in the eigenvalues λ_i . At least one eigenvalue will be very small, of the order $\lambda_i \sim -1/\tau_m$, while all others will be much larger (describing the within-phase dynamics). If τ is large compared to these time scales, but not with respect to τ_m , then the approximation taking Eq. (4.83) to (4.84) will not hold true. Since τ_m scales exponentially with volume, as we approach the thermodynamic limit $V \rightarrow \infty$, larger and larger values of τ must be considered. This is a direct illustration of the non-commutativity of the limits $\tau \rightarrow \infty$ and $V \rightarrow \infty$.

4.3.3 Conditional cumulants

Eqs. (4.78) and (4.82) also apply to the conditional currents (4.59). One simply has to modify accordingly the tilted operator $\mathbf{L}(\eta)$ or, equivalently, the matrices \mathbf{L}_1 and \mathbf{L}_2 in Eq. (4.69). For each conditional current $\mathcal{J}_{\tau|\alpha}$, we define a projection operator Π^α such that $\Pi_{ij}^\alpha = \delta_{i,j} \sum_{k \in \mathcal{S}_\alpha} \delta_{j,k}$; i.e., it projects onto the states \mathcal{S}_α associated with phase $\alpha = 0, 1$. The corresponding tilted operator will then be defined similarly, but with a current of the form $d_{ij}^\alpha = d_{ij} \Pi_{jj}^\alpha$, which means that one should instead use matrices $\mathbf{L}_1 \Pi^\alpha$ and $\mathbf{L}_2 \Pi^\alpha$.

Taking also into account the factor q_α in the denominator, Eq. (4.78) yields

$$\mu_\alpha = \frac{1}{q_\alpha} \langle \mathbf{1} | \mathbf{L}_1 \Pi^\alpha | \mathbf{p}^\infty \rangle. \quad (4.85)$$

Proceeding similarly to Eq. (4.82), we find

$$D_{\tau|\alpha} = \frac{\langle \mathbf{1} | \mathbf{L}_2 \Pi^\alpha | \mathbf{p}^\infty \rangle}{q_\alpha} + \frac{1}{\tau q_\alpha} \int_0^\tau d\tau' \int_0^{\tau'} d\tau'' \langle \mathbf{1} | \mathbf{L}_1 \Pi^\alpha e^{\mathbf{W}(\tau' - \tau'')} \mathbf{L}_1 \Pi^\alpha | \mathbf{p}^\infty \rangle - \frac{\mu_\alpha^2 q_\alpha \tau}{2}. \quad (4.86)$$

Lastly, to obtain the covariance in Eq. (4.64), we simply subtract the combination $(1 - q)D_{\tau|0} + qD_{\tau|1}$ from D_τ in Eq. (4.82). Recalling that $\Pi^0 + \Pi^1 = 1$, this then yields

$$C_\tau = \frac{1}{\tau} \int_0^\tau d\tau' \int_0^{\tau'} d\tau'' \langle \mathbf{1} | \mathbf{L}_1 \Pi^0 e^{\mathbf{W}(\tau' - \tau'')} \mathbf{L}_1 \Pi^1 | \mathbf{p}^\infty \rangle + \frac{1}{\tau} \int_0^\tau d\tau' \int_0^{\tau'} d\tau'' \langle \mathbf{1} | \mathbf{L}_1 \Pi^1 e^{\mathbf{W}(\tau' - \tau'')} \mathbf{L}_1 \Pi^0 | \mathbf{p}^\infty \rangle - q(1 - q)\mu_0\mu_1\tau. \quad (4.87)$$

Concerning the timescales of the discontinuous transition, we notice that all diffusion coefficients, D_τ , $D_{\tau|\alpha}$ and C_τ , are subject to a similar dependence, which is ultimately associated with the matrix $e^{\mathbf{W}(\tau - \tau')}$. Thus, we expect that all quantities should scale similarly with τ .

Up to this point, the conditioning is placed over the current. A system (presenting discontinuous phase transition) evolves following a usual master equation and the observables are conditioned to the phase. Alternatively, the dynamics can be conditioned to a phase by construction of the stochastic process. Let the transition matrix be given by

$$\mathbf{W} = \begin{pmatrix} \mathbf{W}_{00} & \mathbf{W}_{01} \\ \mathbf{W}_{10} & \mathbf{W}_{11} \end{pmatrix}, \quad (4.88)$$

referring to the two subsets \mathcal{S}_0 and \mathcal{S}_1 of each phase. A conditional *dynamics*, given phase α , is one governed by the restricted matrix $\mathbf{W}_{\alpha\alpha}$ (with appropriate adjustments at the boundaries to ensure that it remains a proper transition matrix).

We can similarly adapt Eqs. (4.78) and (4.82) to this case. Let $|\mathbf{p}_\alpha^\infty\rangle$ denote the steady-state of the intra-phase dynamics \mathbf{W}_α . For large system sizes, both coexisting phases will be well separated, which will be quite similar to $q_\alpha^{-1}\Pi^\alpha|\mathbf{p}^\infty\rangle$. Applying Eq. (4.78) will then yield exactly the same first moment μ_α in Eq. (4.85). Hence, *as far as the first moments are concerned, the distinction between conditional currents and conditional dynamics is thus irrelevant.*

However, for the diffusion coefficients, this is absolutely crucial. The reason is associated with the matrix exponential $e^{\mathbf{W}(\tau' - \tau'')}$ in Eq. (4.82). Conditioning on the dynamics would lead instead to a matrix $e^{\mathbf{W}_{\alpha\alpha}(\tau' - \tau'')}$. Since $\mathbf{W}_{\alpha\alpha}$ is essentially $\Pi^\alpha \mathbf{W} \Pi^\alpha$ (except for small modifications at the boundaries), we therefore see that the problem amounts to the difference between $\Pi^\alpha e^{\mathbf{W}(\tau' - \tau'')} \Pi^\alpha$ (conditioning on the currents) and $e^{\Pi^\alpha \mathbf{W}(\tau' - \tau'')} \Pi^\alpha$ (conditioning on the dynamics). The two objects are *drastically* different. The diffusion coefficients obtained by condi-

tioning the dynamics, which we shall henceforth refer to as $\gamma_{\tau|\alpha}$, will thus be fundamentally different from the diffusion coefficients $D_{\tau|\alpha}$ in Eq. (4.63).

An intuitive argument as to why this is the case goes as follows. Currents (4.59) are integrated over a certain time interval τ . Hence, its diffusion coefficient will depend on correlations between different instants of time, and these are dramatically affected by the long timescale τ_m introduced by the discontinuous transition. In fact, let us define $Z_t = \sum_{i,j} d_{ij} \delta_{X(t^-),i} \delta_{X(t^+),j}$, so that Eq. (4.59) can be written as

$$\mathcal{J}_{\tau|1} = \int_0^\tau dt I_t Z_t. \quad (4.89)$$

The corresponding second moment will thus be

$$\langle \mathcal{J}_{\tau|1}^2 \rangle = \int_0^\tau dt \int_0^\tau dt' \langle I_t I_{t'} Z_t Z_{t'} \rangle. \quad (4.90)$$

Therefore, it depends, among other things, on the correlations between I_t and $I_{t'}$, which decays very slowly around the transition point. For instance, in the simplest case where one can assume a Markovian 2-state evolution for I_t (as will in fact be considered further in Sect. 4.3.4), one has

$$C(t-t') = \text{Cov}(I_t, I_{t'}) = q(1-q)e^{-(t-t')/\tau_m}, \quad (4.91)$$

which will thus decay very slowly over time for large systems. This means that $D_{\tau|\alpha}$ in Eq. (4.63) will depend very sensibly on the interplay between τ and τ_m . In contrast, the diffusion coefficients γ_α , for the conditional dynamics, will not. And hence, even for moderately large τ , one expects it to be τ -independent.

4.3.4 Lumping of phases

Many discontinuous non-equilibrium transitions can be approximated, for large volumes V , by a 2-state model [143], where each state accounts for a distinct coexisting phase. All inter-phase degrees of freedom are lumped into a single state, viz. 0 and 1, and every possible jump between phases are reduced to transitions $0 \leftrightarrow 1$. That is, one essentially reduces the dynamics to the monitoring of the phase indicator I_t . In general, the dynamics of I_t will be non-Markovian, as this would represent a hidden Markov chain. Instead, a minimal model is one in which the

dynamics of I_t can be assumed to be Markovian, which is justified when V is sufficiently large. In this case, instead of the full master equation (4.55), we may restrict the dynamics to

$$\frac{d}{dt}q_i = \sum_{j=0,1} \mathbf{W}_{ij}q_j, \quad \mathbf{W} = \begin{pmatrix} -a & b \\ a & -b \end{pmatrix}. \quad (4.92)$$

Here, a and b respectively represent the rates for the system to jump between states $0 \rightarrow 1$ and $1 \rightarrow 0$ of the minimal model, that is, the rates at which phase transitions occur. The steady-state yields $q \equiv q_1 = E(I_t) = a/(a + b)$. Moreover, the metastability lifetime in this case reads $\tau_m = 1/(a + b)$. For large volumes, τ_m increases exponentially, as well as a and b decrease exponentially. Considering the same observation time window, phase transitions become more rare with system size, which is precisely the aim of the present study.

Finally, from Eq. (4.92) one can compute the two-time correlation function, which is given in Eq. (4.91). And since I_t can take on only two values, once $C(t - t')$ is known, we can reconstruct the full joint distribution $\Pr(I_t = i, I_{t'} = i')$ from the properties of the covariance, for arbitrary times t, t' , as

$$\Pr(I_t = i, I_{t'} = i') = \begin{cases} q^2 + C(t - t') & i = i' = 1, \\ (1 - q)^2 + C(t - t') & i = i' = 0, \\ q(1 - q) - C(t - t') & i \neq i'. \end{cases} \quad (4.93)$$

Close to λ_c , the transition rates a and b will usually behave, up to polynomial corrections, as

$$a \sim e^{-V(c_0 - c_a \Delta \lambda)}, \quad b \sim e^{-V(c_0 + c_b \Delta \lambda)}, \quad (4.94)$$

where $c_0, c_a, c_b > 0$ are constants and $\Delta \lambda = \lambda - \lambda_c$. Note how the rates are indeed exponentially decreasing with V . Transitions hence become rare when V is large. From (4.94) we also get $\tau_m \sim e^{c_0 V}$, which is the aforementioned exponential dependence. Finally,

$$q = (1 + e^{-cV \Delta \lambda})^{-1}, \quad (4.95)$$

where $c = c_a + c_b > 0$; hence q changes abruptly from 0 to 1 as λ crosses λ_c , as illustrated in Fig. 4.14(a).

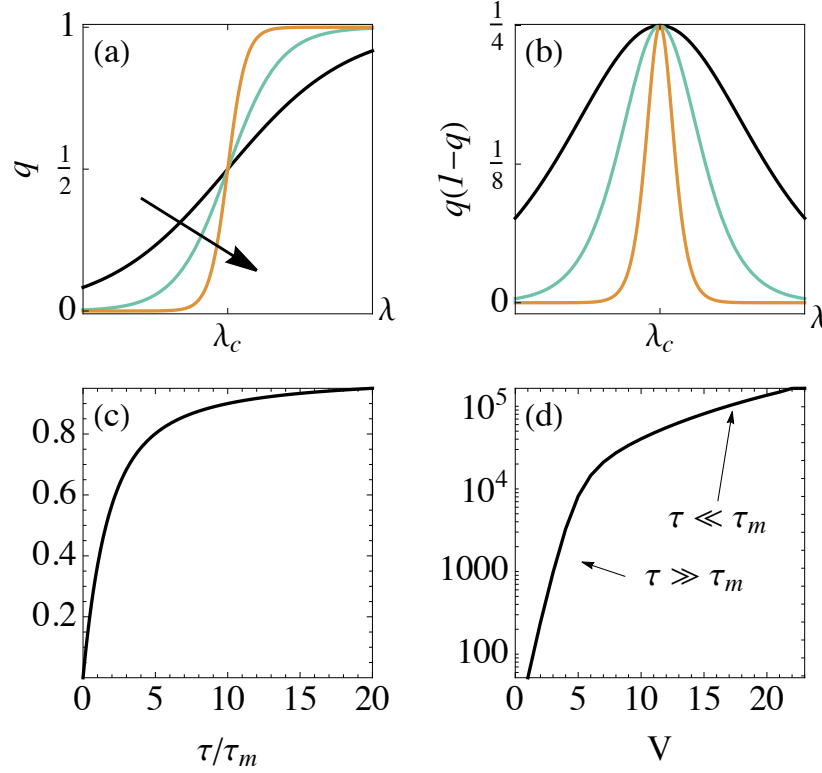


Figure 4.14: Predictions of the minimal model of discontinuous transitions. (a) The probability $q = (1 + e^{-cV\Delta\lambda})^{-1}$ of finding the system in phase 1, for increasing volumes (depicted by the arrow). (b) $q(1 - q)$, which is non-negligible only in the vicinity of the transition point. (c) The quantity $(e^{-\tau/\tau_m} - 1 + \tau/\tau_m)/(\tau/\tau_m)$ appearing in Eq. (4.99). It tends to unity when $\tau \gg \tau_m$. (d) Prototypical behavior of the diffusion coefficient (4.99) as a function of volume, for a fixed τ . When V is such that $\tau \gg \tau_m$, the diffusion coefficient grows exponentially with V . But for a fixed τ , as V is increased, one must eventually cross the point $\tau \sim \tau_m$, after which the scaling becomes at most polynomial (due to the possible dependences of μ_i, D_i on V). Parameters: $c_0 = c_a = c_b = \lambda_c = 1, \mu_0 = V/2, \mu_1 = 2V, \gamma_0 = \gamma_1 = V$.

Since conditional averages are weakly dependent on $\Delta\lambda$, from $J = (1 - q)\mu_0 + q\mu_1$ we see that the average current is given by

$$J = \frac{\mu_0 e^{-cV\Delta\lambda} + \mu_1}{1 + e^{-cV\Delta\lambda}}, \quad (4.96)$$

that also changes abruptly around λ_c , interpolating from μ_0 to μ_1 . It is worth mentioning that this relation is similar to Eq. (4.50), obtained from a Gaussian approach.

Unconditional diffusion coefficient: From the two-state model, the cumulants of a current,

up to order λ^2 , can be obtained from the tilted operator [152]

$$\mathbf{L}(\lambda) = \begin{pmatrix} -a + \lambda\mu_0 + \lambda^2\gamma_0 & b \\ a & -b + \lambda\mu_1 + \lambda^2\gamma_1 \end{pmatrix} \quad (4.97)$$

$$:= \mathbf{W} + \lambda\mathbf{L}_1 + \lambda^2\mathbf{L}_2. \quad (4.98)$$

where γ_i are the diffusion coefficients conditioned on the dynamics, not the currents.

Using Eq. (4.99) we can obtain the diffusion coefficient D_τ , using the two-state transition matrix \mathbf{W} we find that its stationary state is $|\mathbf{p}\rangle = (1 - q, q)$, the non-zero eigenvalue is $\lambda_1 = -1/\tau_m$, and its right and left eigenvectors are given by $|\mathbf{x}_1\rangle = (-1, 1)$ and $|\mathbf{y}_1\rangle = (-q, 1 - q)$. Hence, using the explicit forms of \mathbf{L}_1 and \mathbf{L}_2 in Eq. (4.98), we get

$$D_\tau = \gamma + q(1 - q)(\mu_1 - \mu_0)^2 \tau_m f(\tau/\tau_m), \quad (4.99)$$

where $\gamma \equiv (1 - q)\gamma_0 + q\gamma_1$ is independent of τ and

$$f(t) \equiv (e^{-t} - 1 + t)/t. \quad (4.100)$$

The interesting part is the last term in Eq. (4.99). First, it depends on $q(1 - q)$, which is non-negligible only in the vicinity of the transition point (Fig. 4.14(b)). Second, it depends on the interplay between τ and τ_m through the function f , which is shown in Fig. 4.14(c).

When $\tau \ll \tau_m$ we get $f(\tau/\tau_m) \simeq \tau/2\tau_m$, so that Eq. (4.99) can be approximated to

$$D_\tau \simeq \gamma + q(1 - q)(\mu_1 - \mu_0)^2 \tau/2, \quad \tau \ll \tau_m, \quad (4.101)$$

which is thus *linear* in τ . Conversely, when $\tau \gg \tau_m$, we get

$$D_\tau \simeq \gamma + q(1 - q)(\mu_1 - \mu_0)^2 \tau_m, \quad \tau \gg \tau_m, \quad (4.102)$$

which is independent of τ , *but linear in τ_m* . Hence, when V is large, this will become exponentially dominant. As a consequence, the large volume diffusion coefficient will actually become independent of the γ_i , and will instead be governed essentially by the mismatch in *conditional averages* $(\mu_1 - \mu_0)^2$, in agreement with previous studies on Schlögl's model [122]. In other words, the fluctuations in integrated current at large volumes are governed by the distance

between the phases rather than by their own fluctuations.

This offers another explicit illustration of the order of limits issue, which we depict graphically in Fig. 4.14(d): For a given τ , as we increase V the diffusion coefficient will at first increase exponentially according to Eq. (4.102). But if τ is fixed, then a point will always be reached around which $\tau \sim \tau_m$. And beyond this point, the scaling will be given by Eq. (4.101), which is at most polynomial in V (due to a potential polynomial volume dependence of μ_i, γ_i).

Even though these results were developed for a 2-level model, they are still expected to hold for a broad class of discontinuous transitions. The reason is that, as discussed in Ref. [153], the eigenvalues and eigenvectors of the two-level transition matrix (4.92) are connected to some of the eigenvalues and eigenvectors of the full matrix \mathbf{W} in Eq. (4.55). But, in addition, the full \mathbf{W} will also have several other eigenvalues associated to the within-phase dynamics. Thus, the step from Eq. (4.83) to (4.99) only assumes that τ is much larger than all other λ_i , so that within-phase terms can be neglected.

Conditional diffusion coefficients: We can also use this minimal model to relate the diffusion coefficients $D_{\tau|i}$ in Eq. (4.63) to the parameters μ_i, γ_i . To do so, we use Eq. (4.86) with \mathbf{W} now replaced by the two-state matrix \mathcal{W} in Eq. (4.92). As a result, we find

$$D_{\tau|1} = \gamma_1 + \mu_1^2(1 - q)\tau_m f(\tau/\tau_m), \quad (4.103)$$

$$D_{\tau|0} = \gamma_0 + \mu_0^2 q \tau_m f(\tau/\tau_m), \quad (4.104)$$

$$C_\tau = -2q(1 - q)\mu_0\mu_1\tau_m f(\tau/\tau_m), \quad (4.105)$$

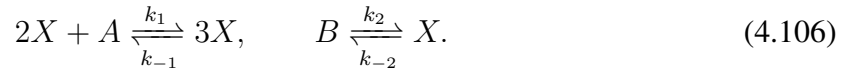
which can be combined together in the form (4.64), to yield Eq. (4.99). All conditional quantities are thus found to scale similarly with τ , according to the function f in Eq. (4.100). This allows us to conclude that even the conditional diffusion coefficients will be dominated by jumps between phases, and will be negligibly affected by the internal fluctuations within each phase. We find this result both relevant and non-trivial.

It is also interesting to notice how the sign of the covariance (4.105) depends only on the signs of μ_0 and μ_1 . A positively correlated covariance means that fluctuations above (below) average in one phase tend to lead to fluctuations above (below) the average in the other; and vice-versa for $C < 0$. We see in Eq. (4.105) that the covariance will be negative whenever μ_0, μ_1 have the same sign.

4.3.5 Schlögl's model

In this Section we verify previous results in a model with a nonequilibrium discontinuous phase transition, the “second Schlögl model” [154]. It represents an ideal laboratory for testing our main prescriptions as it presents an exact solution, and was recently analyzed in Ref. [122].

The model describes a system with 3 chemical species, A , B and X , supporting two types of chemical reactions:



Here $k_{\pm 1}$, $k_{\pm 2}$ are kinetic constants that account, respectively, for catalytic, spontaneous creation and spontaneous annihilation of X . The concentrations of A and B are fixed at a and b due to the presence of chemostats. The dynamics of $p_n(t) = P(X(t) = n)$, for $n = 0, 1, 2, \dots$, is then described by the master equation [143, 153]

$$\dot{p}_n = f_{n-1}p_{n-1} + g_{n+1}p_{n+1} - (f_n + g_n)p_n, \quad (4.107)$$

where

$$f_n := \frac{ak_1n(n-1)}{V} + bk_2V, \quad (4.108)$$

$$g_n := \frac{k_{-1}n(n-1)(n-2)}{V^2} + k_{-2}n. \quad (4.109)$$

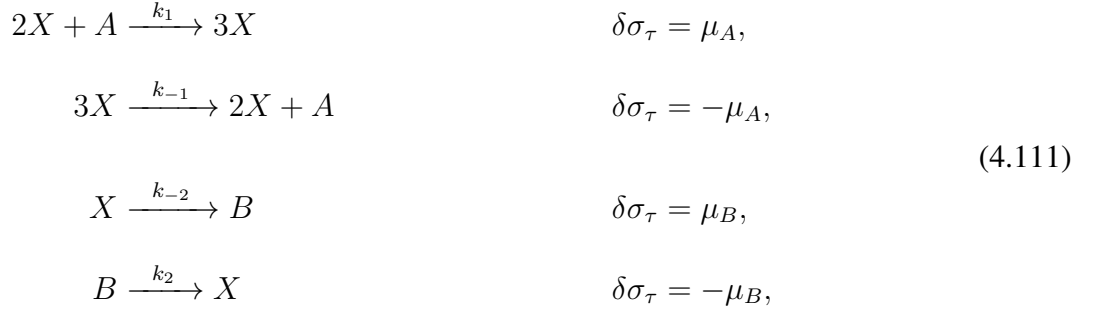
The concentration $x(t) = X(t)/V$ presents a bistable behavior for large V [153], which is determined by the roots of the differential equation governing the deterministic behavior of x for large volumes

$$\frac{dx}{dt} = ak_1x^2 + bk_2 - k_{-1}x^3 - k_{-2}x = 0. \quad (4.110)$$

The bistable region is defined as the interval in the control parameters for which this equation has three real roots, x_0, x^*, x_1 . The first and last represent stable states for the most likely density within each phase, whereas x^* is unstable and serves as the phase separator. Hence, we define the phase-indicator in the Schlögl's model as a random variable I_t such that $I_t = 1$ when $X(t) > Vx^*$ and 0 otherwise.

For concreteness, we choose as thermodynamic current the entropy production $\mathcal{J}_\tau = \sigma_\tau$. Whenever there is a transition, the net current (4.56) changes by an increment $\delta\sigma_\tau$ defined

according to the following rules:



where $\mu_A = \ln ak_1/k_{-1}$ and $\mu_B = \ln k_{-2}/bk_2$.

The model was simulated using the Gillespie algorithm. We fix $ak_1 = k_{-2} = 1$, $bk_2 = 0.2$, and take as control parameter the chemical potential gradient $\Delta\mu = \mu_B - \mu_A = \ln [(k_{-2}ak_1)/(k_{-1}bk_2)]$. For these parameters, the phase coexistence point in the thermodynamic limit occurs at $\Delta\mu_0 \sim 3.047$ [122]. Figs. 4.15(a) and (b) present a basic characterization of the steady-state. First, in Fig. 4.15(a) we show the numerically computed metastability timescale τ_m , as a function of the volume V , confirming the exponential dependence with V . This is obtained by collecting the mean first passage time $T_{x_i \rightarrow x^*}$ for the system to go from each stable point $x_{0(1)}$ to the unstable point, x^* . The rates a and b in Eq. (4.92) are then given by $a = (2T_{x_0 \rightarrow x^*})^{-1}$ and $b = (2T_{x_1 \rightarrow x^*})^{-1}$ [155], from which we determine $\tau_m = 1/(a + b)$. Second, Fig. 4.15(b) characterizes the probability q of finding the system in phase 1, as a function of $\Delta\mu - \Delta\mu_0$, for different values of V , where markers are simulation data and the curves are a fit of $q = (1 + e^{-cV(\Delta\mu - \Delta\mu_0)})^{-1}$; both agree very well for large volumes and/or small $\Delta\mu - \Delta\mu_0$. This is expected, since Schlögl's model is known to have a well defined 2-state limit [143, 153] when V is large.

Sample stochastic trajectories of the current \mathcal{J}_τ [Eq. (4.56)] as a function of τ are shown in Fig. 4.15(c), for fixed $\Delta\mu = 3.35$ and $V = 10$. Red and blue curves represent the situations where the system start in phases 1 and 0 respectively. For short τ the curves tend to remain well separated, so that \mathcal{J}_τ behaves as either $\mathcal{J}_{\tau|1}$ or $\mathcal{J}_{\tau|0}$. The corresponding statistics of \mathcal{J}_τ , shown in the inset, would thus be a prototypical bimodal distribution. Conversely, when $\tau \gg \tau_m \sim 40$, transitions between the phases begin to occur, which cause the corresponding distribution to change to unimodal.

The conditional mean current and diffusion coefficients are shown in Fig. 4.15(d)-(g). For concreteness, we focus on the special point $q = 1/2$; i.e., where the two phases are equally

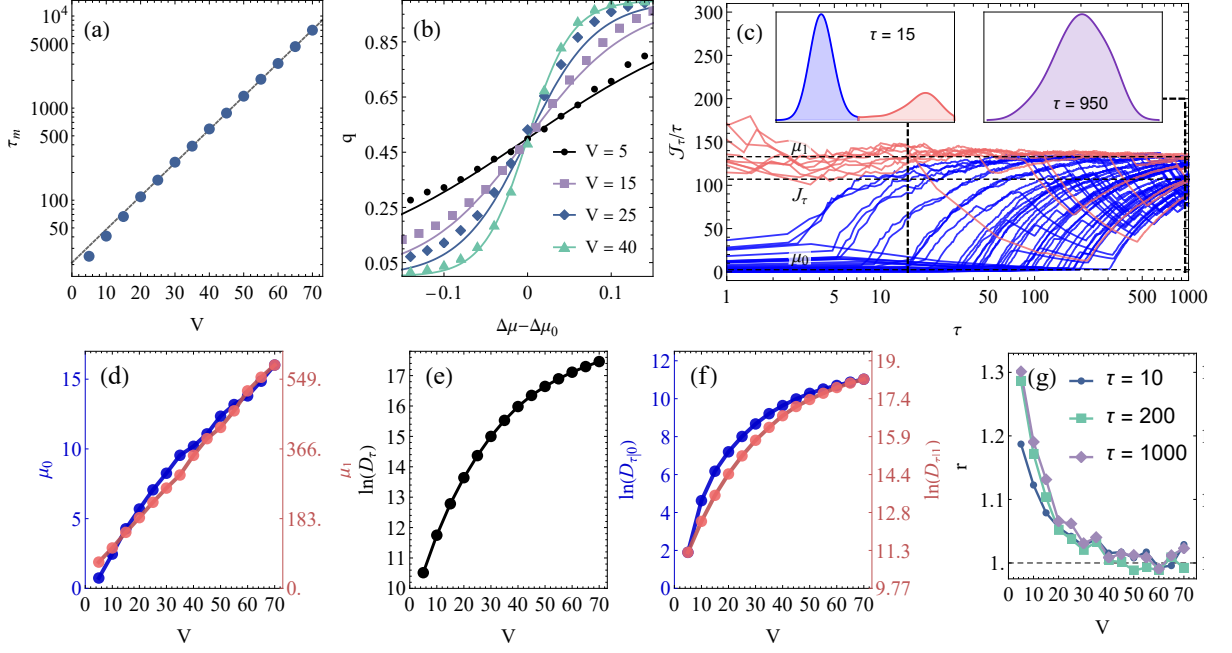


Figure 4.15: Conditional currents for Schlögl's model, computed using the Gillespie algorithm. (a) τ_m vs. V . (b) q vs. $\Delta\mu - \Delta\mu_0$ for different values of V . Solid lines are a fit of $q = (1 + e^{-cV(\Delta\mu - \Delta\mu_0)})^{-1}$. (c) Stochastic trajectories of \mathcal{J}_τ/τ vs. τ , starting either in phase 1 (red) or phase 0 (blue). The insets show the corresponding histograms at different times τ . (d)-(g) Mean and diffusion coefficient as a function of V , with $\tau = 10^3$ and $\Delta\mu$ fixed by setting $q = 1/2$. (d) Conditional means $\mu_{0(1)}$ [Eq. (4.61)]. (e) Diffusion coefficient D_τ [Eq. (4.57)]. (f) Conditional diffusion coefficients $D_{\tau|i}$ [Eq. (4.63)]. (g) The ratio r in Eq. (4.112), as a function of V , for different values of τ . Other parameters: $a = k_1 = k_2 = k_{-2} = 1$ and $b = 0.2$.

likely. As this depends on V , for each volume we first fix $\Delta\mu$ as the point where $q = 1/2$. This reduces the free parameters to V and τ only. The conditional averages $\mu_{0(1)}$ as a function of the volume are shown in Fig. 4.15(a). They are both found to be extensive in V , as expected; moreover, the activity in phase 1 is generally much larger, causing $\mu_1 \gg \mu_0$.

Conversely, the diffusion coefficient D_τ (Fig. 4.15(e)) and their conditional counterparts $D_{\tau|i}$ (Fig. 4.15(f)) are both exponential in V , in line with previous studies [122]. For large volumes, these are also well described by the third term in Eq. (4.99) (or (4.103)-(4.104)). We confirm this by plotting in Fig. 4.15(g) the ratio

$$r = \frac{D_\tau}{q(1-q)(\mu_1 - \mu_0)^2 \tau_m f(\tau/\tau_m)}, \quad (4.112)$$

where all quantities in the rhs are computed independently from the simulations. One can also consider similar definitions for $r_{0(1)}$. Since the γ_i are at most polynomial in V , if this ratio tends to $r \rightarrow 1$ when V is large, it serves as a confirmation that, for large V , the model effectively

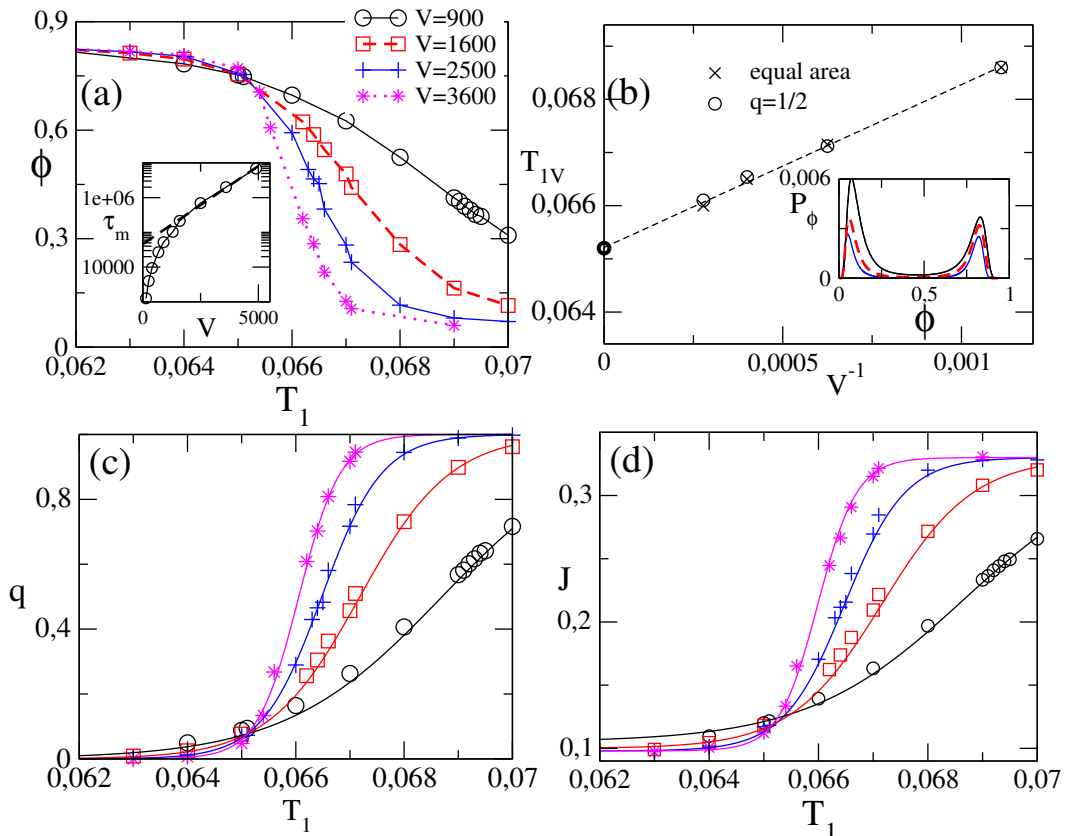


Figure 4.16: Characterization of the 12-state Potts model in contact with two thermal baths of temperatures T_1 and $T_1 + \Delta T$ (with fixed $\Delta T = 0.9$). (a) Order parameter ϕ vs. T_1 for different volumes V . Inset: metastability lifetime τ_m vs. V . (b) Finite-size analysis of the transition point T_{1V} vs. V^{-1} , yielding the asymptotic value $T_{01} = 0.0651(1)$. Inset: distribution of ϕ at T_{1V} , for different volumes. (c) Phase probability q vs. T_1 , again for different volumes. The continuous lines are fits of $q = [1 + Qe^{-Vc(T_1 - T_{10})}]^{-1}$. (d) Average entropy production rate as current J [Eq. (4.57)], which closely follows the behavior of q .

behaves as the 2-state minimal model of Sec. 4.3.4. As is clear in Fig. 4.15(g), this is indeed the case.

The results verified here in the Schlögl model were also verified in a version of the Potts model, the 12-state Potts model connected to two baths at different temperatures [V]. It is defined on a regular lattice and exhibits a nonequilibrium phase transition under a different mechanism. Despite the absence of an exact solution, all main features about the phase transition and statistics about entropy production fluctuations are present, see Figs. 4.16 and 4.17.

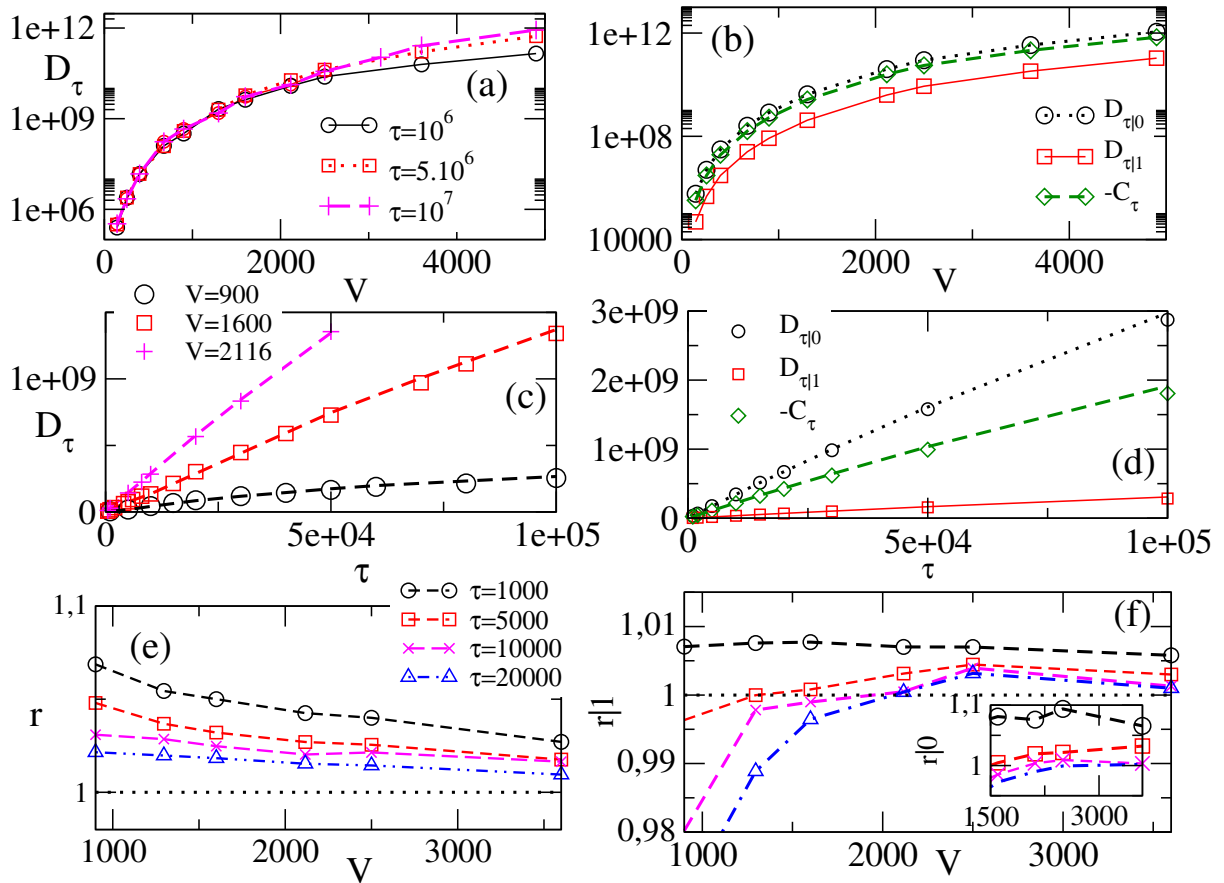


Figure 4.17: Unconditional and conditional diffusion coefficients for the 12-state Potts model. (a) D_τ vs. V for different values of τ . (b) $\tau|i$ and C_τ vs. V with $\tau = 5 \times 10^6$. (c) D_τ vs. τ for different V . (d) $D_{\tau|i}$ and C_τ vs. τ for $V = 1600$. Continuous lines in (c) and (d) are the theoretical predictions from Eq. (4.99). (e) The ratio (4.112) between D_τ and the predictions of the minimal model, Eq. (4.99), which tends to unity for large volumes. Curves are for different values of τ . (f) Same, but for $r|0$ (main plot) and $r|1$ (inset). In all curves, for each V , we fix T_1 as the value T_{1V} for which $q = 1/2$. Other details are as in Fig. 4.16.

4.4 Chapter's summary

This chapter discussed how nonequilibrium phase transitions can be typified by proper entropy production signatures, as well as a detailed study of its statistics at the phase coexistence region, in particular the interplay between metastability lifetime and integration time windows.

The importance of this study lies in the fact that nonequilibrium phase transitions are not understood as well as their equilibrium counterparts, in which case methods based on free energies are well established and documented. Here, we explore how to characterize these transitions without losing track of the intrinsic irreversibility.

The description of both continuous and discontinuous phase transitions can be carried out in terms of entropy production, a property particular to nonequilibrium phenomena. Using a mean-field description of systems with \mathbb{Z}_2 symmetry, Gaussian approximations and numerical simulations of complex and regular structures, we showed that the phase transition can be located and its possible to classify if the transition is first-order or continuous. Furthermore, the hysteresis can be located (first-order) and critical exponents can be obtained (continuous).

For continuous phase transitions, the set of critical exponents that comprise universality classes is a major area of investigation. The critical exponent α is related to the specific heat, a quantity that can only be defined in equilibrium. Since it is related to the variation of heat and inspired by Clausius heat theorem, we obtained this exponent from the derivative of entropy production rate and observed that the hyperscaling relation is satisfied. This result suggests further research on the nonequilibrium critical exponents obtained from entropy production, in particular beyond the considered \mathbb{Z}_2 class of systems and/or mean-field.

In the case of first-order transitions, the phase coexistence gives rise to an apparent ergodicity breaking close to the transition for large systems. The statistics of thermodynamic currents becomes greatly affected by the integration time window and poses a problem in characterizing phase transitions, which are known to occur in the very limit of large systems.

To account for the currents in each of the coexisting phases, we introduce the idea of conditional statistics by exploring the currents conditioned to a given phase and also the currents over conditioned dynamics. From a finite-time version of large deviation theory, we obtained general relations for the unconditional and conditional cumulants of a generic current, which can be entropy production itself. We also proposed a minimal model that captures all essential features of the problem.

The behaviors obtained were verified with numerical simulations of physical systems: iner-

tial majority-vote, Schlögl's second model, and Potts models.

Chapter 5

Heat engines

Heat engines leveraged the development of equilibrium thermodynamics in the 19th century. Recent developments enable scaling down heat engines to the mesoscopic level, where the fluctuations and the net energy fluxes share the same order of magnitude. In addition to engineered devices that convert heat into useful work, many processes in nature are described as stochastic heat engines, notably many biophysical motors [104, 106, 156]. The environment-induced fluctuations are key to exploring the main features of heat engines and how to manipulate them. Hence, accounting for randomness is needed, and the results of stochastic thermodynamics have been widely applied to a plethora of small heat engines [157–176]. Inquiries into entropy production lead to conclusions about the efficiency and power of motors [VII, 152, 170, 177].

The two most important figures of merit of a heat engine are power and efficiency, which are regarded as fluctuating quantities in stochastic thermodynamics. The famous Carnot efficiency upper limit now bounds the average efficiency, $\langle \eta \rangle \leq \eta_C = 1 - T_C/T_H$, with T_C and T_H being the cold and hot reservoir temperatures. This bound, which dates back to 1824 [178], represents the efficiency of a perfectly reversible engine that can be achieved in the quasistatic regime. Out of equilibrium, dissipation represents the loss of useful energy to the environment, and thus the interest in its quantification. A perfectly efficient engine working reversibly operates very slowly. If we imagine periodic operation of the machine, it translates into a diverging period τ , which is clearly unfeasible and, even further, a vanishing power (useful energy per unit of time). Since the role of time is closely connected to the interplay between power and efficiency, it can be explored by tuning the total period of operation or the intervals involved in the protocol.

This chapter deals with above points by considering two types of nonequilibrium mesoscopic engines: those composed of two-level systems and Brownian particles. In the first part,

we study a two-level system (viz. quantum dot) that alternately interacts with two reservoirs, constituting a collisional sequential heat engine [IV]¹. Collisional models, e.g. a system interacting sequentially and repeatedly with distinct environments instead of a continuous interaction with all reservoirs, have been considered a suitable description of engineered reservoirs [179]. In particular, we mention the case of quantum systems, in which the reservoir is conveniently represented as a sequential collection of uncorrelated particles [180]. Additionally, the collisional approach provides a realistic description of systems interacting with small fractions of the environment or even those evolving under the influence of distinct drivings [181, 182]. In particular, many aspects of a stochastic pump in which a single-level quantum dot is connected sequentially and periodically to different reservoirs have recently been discussed [183–186], here we focus on the fraction of interaction time [IV].

We introduce the idea of adjusting the interaction time asymmetry to optimize engine performance. Despite the simplicity of the system, it presents the regimes of heat engine, refrigerator, heater, and accelerator, highlighting the importance of searching for optimized protocols [159, 169, 186, 187]. As a first finding, asymmetric interaction times play an important role in enhancing power output. Also, as an extra advantage, efficiencies become somewhat greater than the endoreversible Curzon-Ahlborn efficiency $\eta_{CA} = 1 - \sqrt{T_C/T_H}$ [163, 188, 189].

In the second part, we present another class of engines composed of a pair of interacting Brownian engines. Brownian particles are often at the core of small-scale heat engines [158, 190–198]. Most of them are based on single-particle engines; significant theoretical [157, 159, 173, 179, 199–205] and experimental [158, 206, 207] results have recently been carried out. Distinct questions can be raised about the interaction and driving forces contribution to the engine's performance. The protocol has many degrees of freedom that can be optimized to meet different goals [IV, 159, 167, 168, 188]. Understanding the role of interaction can provide a bottom-up perspective for the emergence of collective effects in many-body engines [124, 208, 209].

A first relevant characteristic of the considered model is that each Brownian particle evolves under the action of a time-dependent force, which is arguably the simplest way to take Brownian particles out of equilibrium [191, 192], and systems with time-dependent driving have been shown to outperform steady-state systems [41, 210, 211]. Secondly, the system presents an interaction between particles modeled by a potential that depends on both positions. Fluxes

¹A generalization of such a model for an arbitrary number of reservoirs was explored in Ref. [III] to compare different thermodynamic uncertainty relations for systems with periodic driving.

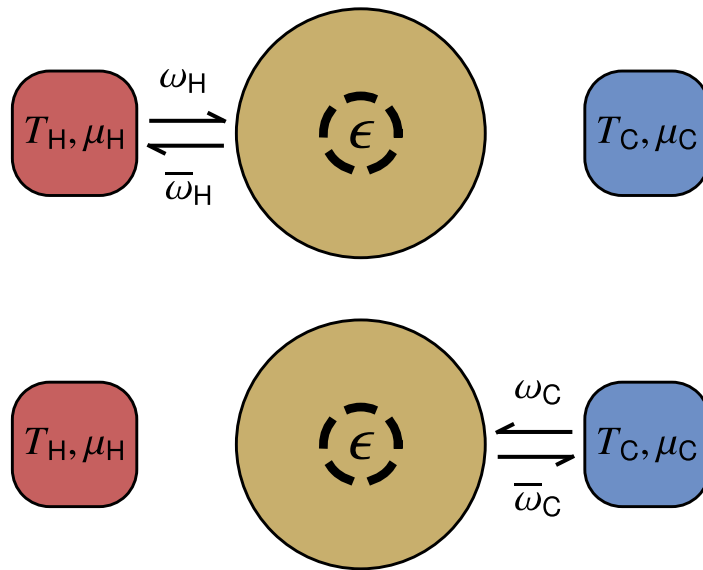


Figure 5.1: Sketch of a quantum dot periodically and sequentially placed in contact with a hot (during a time τ_H) and a cold (during a time $\tau - \tau_H$) reservoir. When in contact with a reservoir, the quantum dot receives a particle with rate ω_i and donates a particle with rate $\bar{\omega}_i$ (i being H for the hot reservoir and C for the cold one). When the quantum dot is occupied, its energy increases by ϵ .

are established through interaction, in contrast to single-particle descriptions. Other works involving interacting particles are restricted to time-independent driving [198, 212].

5.1 Asymmetric interaction in a collisional model

5.1.1 Collisional two-level system

The present model [cf. Fig. 5.1] consists of a two-level system, namely the quantum dot, that has energy ϵ when occupied by an electron and zero when empty. It is placed in contact with a hot equilibrium reservoir (H) for the interval τ_H , with which it can exchange a particle. The interaction with the hot reservoir ceases and the system is instantaneously placed in contact with a cold reservoir (C), this interaction lasts for an interval $\tau - \tau_H$ and at its end the contact is broken and the period finishes. In realistic scenarios the instantaneous reservoir swap is achieved by having distinct timescales for the interactions and the switchings.

When the system is empty and in contact with the hot reservoir, it can receive a particle with rate ω_H , whereas if it is filled, it can pass the particle with rate $\bar{\omega}_H$; analogously for the cold reservoir. Since the reservoirs are assumed to be in thermal equilibrium, the occupation

probability of the quantum dot evolves toward an equilibrium value $p_i^{\text{eq}} \equiv \omega_i/(\omega_i + \bar{\omega}_i)$ when in contact with a unique reservoir $i \in \{\text{H}, \text{C}\}$. The connection between microscopic transition rates and intensive macroscopic thermodynamic quantities follows the Fermi-Dirac distribution $p_i^{\text{eq}} = [e^{(\epsilon - \mu_i)/T_i} + 1]^{-1}$, where μ_i the chemical potential, T_i the temperature and the Boltzmann constant is set to 1. Note that this is consistent with the local detailed balance condition $\omega_i/\bar{\omega}_i = e^{-(\epsilon - \mu_i)/T_i}$, ensuring thermodynamic consistency and connection with macroscopic quantities. Therefore, the temperature of each reservoir is given by

$$T_i = \frac{\mu_i - \epsilon}{\log \omega_i/\bar{\omega}_i}. \quad (5.1)$$

The ratio of the transition rates $\omega_i/\bar{\omega}_i$ carries an important physical meaning, it quantifies the willingness of the reservoir to concede a particle to the quantum dot, with equilibrium regime being reached for $\omega_{\text{H}}/\bar{\omega}_{\text{H}} = \omega_{\text{C}}/\bar{\omega}_{\text{C}}$.

Since the system is ergodic, and provided that the reservoirs do not share the same temperature and potential, it will evolve toward a periodic non-equilibrium steady-state that is not preserved under time-reversal $t \rightarrow \tau - t$, exhibiting its irreversible character. In contrast, if both reservoirs are equivalent, the quantum dot will reach an equilibrium steady-state as a system in contact with a single reservoir would. Interestingly, when the relation $\omega_{\text{H}}/\bar{\omega}_{\text{H}} = \omega_{\text{C}}/\bar{\omega}_{\text{C}}$ is satisfied, the occupation probability will be time-independent and the state might be named pseudo-equilibrium, since the difference in chemical potential and temperature compensate.

We start the analysis in a hybrid manner: During the interaction with the i -th reservoir, the evolution has continuous-time and its transition matrix is given by

$$\mathbf{W}_i \equiv \begin{pmatrix} -\omega_i & \bar{\omega}_i \\ \omega_i & -\bar{\omega}_i \end{pmatrix}. \quad (5.2)$$

Let $p_i(t)$ be the occupation probability at time t , and index i states that the system is in contact with reservoir i at time t . The master equation therefore has piecewise time-dependent rates,

$$\frac{d}{dt} \begin{pmatrix} 1 - p_i(t) \\ p_i(t) \end{pmatrix} = (\mathbf{W}_{\text{H}}\delta_{i,\text{H}} + \mathbf{W}_{\text{C}}\delta_{i,\text{C}}) \begin{pmatrix} 1 - p_i(t) \\ p_i(t) \end{pmatrix}, \quad (5.3)$$

which is simplified to an expression

$$\frac{d}{dt}p_i(t) = \omega_i - (\omega_i + \bar{\omega}_i)p_i(t) \quad (5.4)$$

that highlights that at each interaction the equilibrium state is given by $\omega_i/(\omega_i + \bar{\omega}_i)$.

This is a system of two differential equations and can be solved by noticing that $p_i(t)$ has to be continuous, therefore at the non-equilibrium steady state it follows that $p_H(\tau_H) = p_C(\tau_H)$, and $p_H(0) = p_C(\tau)$ takes into account that the system has to return to the initial state after a cycle, consisting of the boundary conditions. Under those conditions, the exact solution is given by

$$p_H(t) = \frac{\omega_H}{\omega_H + \bar{\omega}_H} - \frac{e^{-(\omega_H + \bar{\omega}_H)t} [1 - e^{-(\omega_C + \bar{\omega}_C)(\tau - \tau_H)}]}{1 - e^{-(\omega_H + \bar{\omega}_H)\tau_H - (\omega_C + \bar{\omega}_C)(\tau - \tau_H)}} \frac{\omega_H \bar{\omega}_C - \bar{\omega}_H \omega_C}{(\omega_H + \bar{\omega}_H)(\omega_C + \bar{\omega}_C)}, \quad t = [0, \tau_H] \pmod{\tau} \quad (5.5)$$

and

$$p_C(t) = \frac{\omega_C}{\omega_C + \bar{\omega}_C} - \frac{e^{-(\omega_C + \bar{\omega}_C)(t - \tau_H)} [1 - e^{-(\omega_H + \bar{\omega}_H)\tau_H}]}{1 - e^{-(\omega_H + \bar{\omega}_H)\tau_H - (\omega_C + \bar{\omega}_C)(\tau - \tau_H)}} \frac{\bar{\omega}_H \omega_C - \omega_H \bar{\omega}_C}{(\omega_H + \bar{\omega}_H)(\omega_C + \bar{\omega}_C)}, \quad t = [\tau_H, \tau] \pmod{\tau}. \quad (5.6)$$

The net particle flux per unit of time is given by the change in occupation probability during an interaction, given by $\bar{J}_H := [p_H(\tau_H) - p_H(0)]/\tau_H$ for the hot reservoir and $\bar{J}_C := [p_C(\tau) - p_C(\tau - \tau_H)]/(\tau - \tau_H)$ for the cold one². At the stochastic level these fluxes J_i can be regarded as the number of particles exchanged with the i -th reservoir, taking into account their directions, over the total time in which reservoir and quantum dot interacted along the trajectory.

Since no electron accumulation in the quantum dot is possible, all particles leaving a given reservoir must enter the other one, such that $\bar{J}_H + \bar{J}_C = 0$, and the fluxes read

$$\bar{J}_H = -\bar{J}_C = \frac{1}{\tau} \frac{(1 - e^{-(\omega_H + \bar{\omega}_H)\tau_H})(1 - e^{-(\omega_C + \bar{\omega}_C)(\tau - \tau_H)})}{1 - e^{-(\omega_H + \bar{\omega}_H)\tau_H - (\omega_C + \bar{\omega}_C)(\tau - \tau_H)}} \frac{\omega_H \bar{\omega}_C - \bar{\omega}_H \omega_C}{(\omega_H + \bar{\omega}_H)(\omega_C + \bar{\omega}_C)}. \quad (5.7)$$

Since transition rates and time intervals are always positive, the factor with exponentials on the right-hand side is always positive and can reach zero in specific limits. The sign of the rightmost factor, and therefore the sign of the fluxes, depends on how both reservoirs differ through Eq. (5.1).

We pause to make a few comments: (i) such results recover the findings from Refs. [III,

²Notice that both fluxes point from the reservoir to the quantum dot. In thermodynamics, it is fundamental to keep track of the fluxes' directions to understand the meaning of energy flows and characterize devices.

183] for symmetric interaction times ($\tau_H = \tau/2$); (ii) the hot reservoir is “more willing” to concede particles than the cold reservoir when $\omega_H/\bar{\omega}_H > \omega_C/\bar{\omega}_C$, implying that $\bar{J}_H > 0$ and $\bar{J}_C < 0$, which is consistent with a flux from hot to cold; (iii) the period τ only provides a time scale for the model and will be henceforth treated as $\tau = 1$, this property becomes evident if fluxes, transition rates, and interaction times are scaled by a given factor, which would not change Eqs. (5.5)-(5.7); (iv) the present system can operate as a heat engine, refrigerator, heater or accelerator, provided the parameters ω_i and $\bar{\omega}_i$ (or equivalently, ϵ , μ_i and T_i) are conveniently adjusted.

5.1.2 The role of asymmetric switching

Once obtained the probability distribution in Eqs. (5.5) and (5.6), we can establish the connection between stochastic dynamics and thermodynamics by identifying the energetic fluxes as in Chapter 2. Per period, the net heat flowing from a reservoir to the quantum dot is $\bar{Q}_i \equiv (\epsilon - \mu_i)\bar{J}_i$, and the net chemical work related to particle transport is $\bar{W}_i^{\text{chem}} \equiv \mu_i\bar{J}_i$, where $i = \{C, H\}$. By definition, these quantities are identified preserving the first law $\bar{Q}_C + \bar{Q}_H + \bar{W}_C^{\text{chem}} + \bar{W}_H^{\text{chem}} = 0$.

We set the output power to the chemical work performed by the quantum dot $\bar{P} := -(\bar{W}_H^{\text{chem}} + \bar{W}_C^{\text{chem}})$. Since efficiency is typically a measure of “what you get and what you give”, corresponding to the ratio between power and input heat. In the heat engine regime, the net efficiency is given by

$$\bar{\eta} := \frac{\bar{P}}{\bar{Q}_H} = 1 - \frac{\mu_C - \epsilon}{\mu_H - \epsilon} = 1 - \frac{T_C \ln \omega_C/\bar{\omega}_C}{T_H \ln \omega_H/\bar{\omega}_H} \leq 1 - \frac{T_C}{T_H}. \quad (5.8)$$

Notice that it can be obtained only in terms of the macroscopic parameters in the first equality, or in terms of the transition rates specified by the following conditions at the heat engine regime:

$$\frac{\omega_C}{\bar{\omega}_C} < \frac{\omega_H}{\bar{\omega}_H} < 1, \quad \text{and} \quad \mu_H < \mu_C < \epsilon \quad (5.9)$$

are met, ensuring $T_H > T_C$ and the positiveness of both temperatures, the power output, and the heat extracted from the hot reservoir.

We pause again to make some comments: (i) the condition for an equilibrium steady state $\omega_H/\bar{\omega}_H = \omega_C/\bar{\omega}_C$ leads to Carnot efficiency; (ii) the heat engine regime also implies that heat flows from the quantum dot to the cold reservoir, $\bar{Q}_C < 0$; (iii) since efficiency does not depend on τ_H and τ , η , it is independent of the protocol. In contrast, the power output \bar{P} depends on

both τ_H and τ , so we have the freedom to choose time intervals that enhance the power with no losses to the net efficiency.

In order to exploit distinct possibilities of optimizing the engine performance, the next sections will be devoted to power maximization with respect to the protocol asymmetry and its complete maximization (also taking into account the reservoir properties). Since the extracted power increases monotonically with the ratio between temperatures, the analysis will be carried out for finite fixed ratios T_C/T_H .

Best protocol: A relevant timescale, the characteristic time t_{char} is the typical relaxation time towards the equilibrium state. Since there are two equilibrium states (associated with each thermal reservoirs), it is defined as the largest between characteristic times $t_{\text{char}}^H \equiv 1/(\omega_H + \bar{\omega}_H)$ and $t_{\text{char}}^C \equiv 1/(\omega_C + \bar{\omega}_C)$. By considering such timescale, Fig. 5.2 depicts the interplay between power output, period, characteristic time, and the fraction of time spent in contact with the hot reservoir τ_H/τ .

In all cases, the chemical potentials and the energy are fixed, providing $\eta = 1/3$ for the chosen parameters. A common trait of all panels is that the power output (and also the heat extracted) vanishes for τ_H/τ near 1 or 0. This is expected since the quantum dot would be “virtually” in contact with a single reservoir and reach equilibrium, and hence the net fluxes vanish. It should be noted that the value of τ_H for which the power is maximized barely changes with the ratio τ/t_{char} , but it is extremely dependent on the other parameters of the model. Furthermore, for a constant value of τ/t_{char} , the power output can be noticeably different, being very sensitive to τ_H/τ , and the best choice of τ_H/τ is roughly independent of τ/t_{char} . The unique value of τ_H that maximizes the \bar{P} for a given value of τ and the other parameters can be numerically obtained from the transcendental equation

$$\frac{(\omega_H + \bar{\omega}_H) e^{-(\omega_H + \bar{\omega}_H)\tau_H} [1 - e^{-(\omega_C + \bar{\omega}_C)(\tau - \tau_H)}]^2}{(\omega_C + \bar{\omega}_C) e^{-(\omega_C + \bar{\omega}_C)(\tau - \tau_H)} [1 - e^{-(\omega_H + \bar{\omega}_H)\tau_H}]^2} = 1, \quad (5.10)$$

whose values were used in Fig. 5.2 to obtain the white dashed lines.

In order to obtain a qualitative insight about the best value of τ_H/τ , we observe that the quantum dot needs to interact with a reservoir during a period comparable to its characteristic time so its state is effectively affected. Therefore, characteristic times provide a notion for how long a good engine will interact with each reservoir—e.g. if $t_{\text{char}}^H \ll t_{\text{char}}^C$ the hot reservoir needs to interact very briefly compared to the cold one, so we can expect that a good protocol will present a small τ_H/τ . Hence, it is reasonable that good performance protocols will present interaction

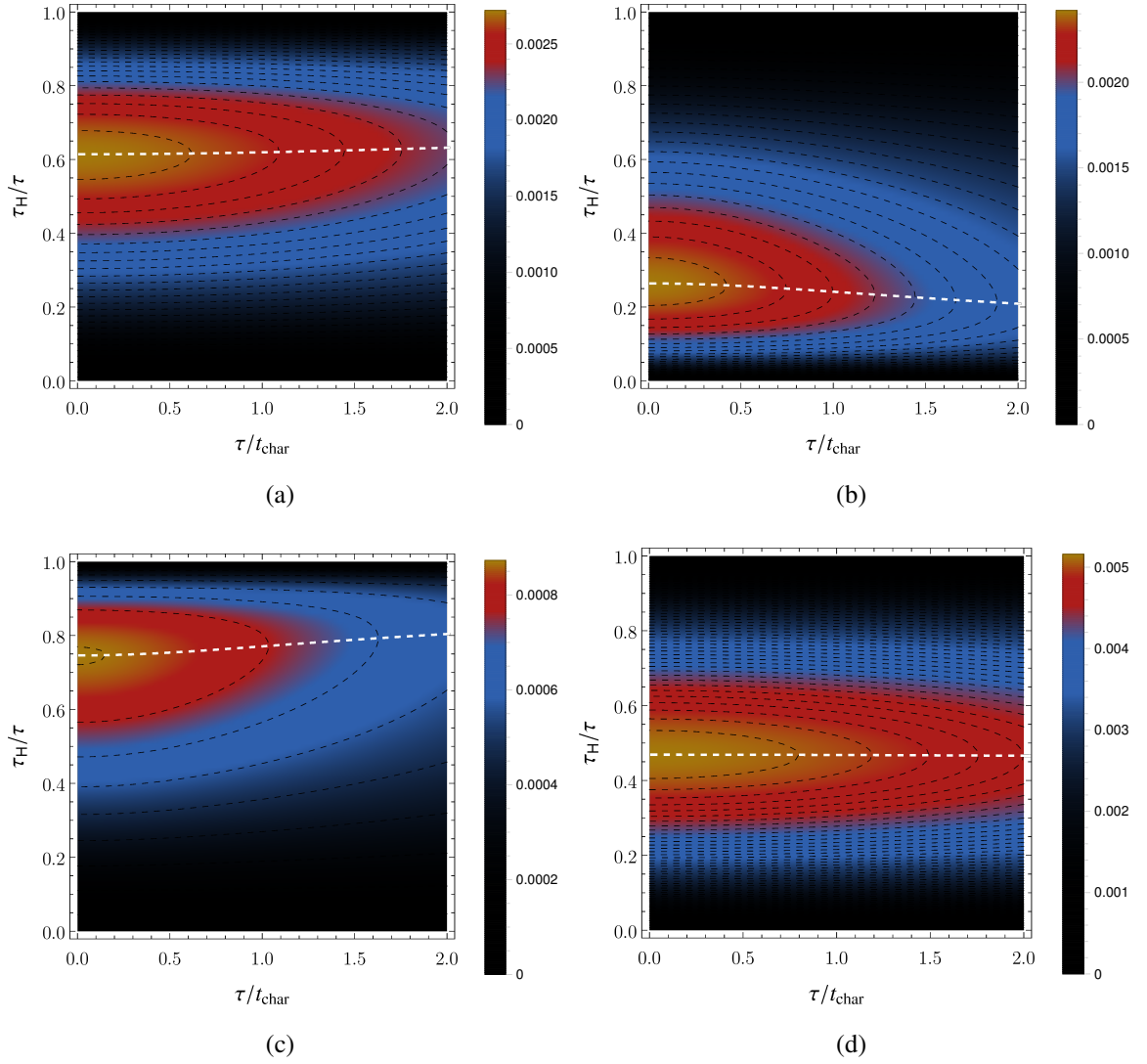


Figure 5.2: Power outputs in terms of τ/t_{char} and τ_{H}/τ , for distinct control parameters. Each dashed black curve represents an increment of 10^{-4} in the value of the power, the white dashed curve represents the values of τ_{H}/τ that maximize the power for each value of τ/t_{char} . For all panels, we set $\mu_{\text{H}} = 0.4$ and $\mu_{\text{C}} = 0.6$ and energy $\epsilon = 1$. The remaining parameters are (a) $T_{\text{H}} = 0.4$, $T_{\text{C}} = 0.1$, $\omega_{\text{H}} = 0.04$, $\bar{\omega}_{\text{H}} = 0.18$, $\omega_{\text{C}} = 0.01$ and $\bar{\omega}_{\text{C}} = 0.55$; (b) $T_{\text{H}} = 2.0$, $T_{\text{C}} = 0.5$, $\omega_{\text{H}} = 0.64$, $\bar{\omega}_{\text{H}} = 0.86$, $\omega_{\text{C}} = 0.06$ and $\bar{\omega}_{\text{C}} = 0.13$; (c) $T_{\text{H}} = 3.5$, $T_{\text{C}} = 1.2$, $\omega_{\text{H}} = 0.09$, $\bar{\omega}_{\text{H}} = 0.11$, $\omega_{\text{C}} = 0.71$ and $\bar{\omega}_{\text{C}} = 0.99$; (d) $T_{\text{H}} = 0.4$, $T_{\text{C}} = 0.1$, $\omega_{\text{H}} = 0.13$, $\bar{\omega}_{\text{H}} = 0.58$, $\omega_{\text{C}} = 0.01$ and $\bar{\omega}_{\text{C}} = 0.55$.

times around the characteristic times of each reservoir. This is exemplified in Fig. 5.2, where $t_{\text{char}}^{\text{H}}/(t_{\text{char}}^{\text{H}} + t_{\text{char}}^{\text{C}})$ gives approximately 0.7, 0.1, 0.9 and 0.4 for panels *a*, *b*, *c* and *d*, respectively, in fair agreement with the best value of τ_{H}/τ observed in the plots. Since the efficiency is protocol independent, as a rule of thumb we should choose very small values of τ , in agreement with [213, 214], and maximize the power output with respect to τ_{H} . Although small, we recall that the period τ should be sufficiently larger than the time required to switch the interaction of

the quantum dot from one reservoir to another, similar to the symmetric case [183, 185].

An interesting question that may be raised about this best protocol procedure is: How much do we gain by tuning τ_H instead of just letting the quantum dot be half the period in contact with each reservoir (symmetric case)? In order to answer such a question, Fig. 5.3 depicts the density plots of the ratio between power output for τ_H to the power output for the symmetric case $\bar{P}(\tau_H)/\bar{P}(\tau/2)$ as a function of both τ_H/τ and T_C/T_H . As the temperature changes (with fixed $\bar{\omega}_i$, ϵ and μ_i), t_{char} also changes due to Eq. (5.1). Hence, comparisons between Figs. 5.2 and 5.3 should take this change into account.

Here, we used the same values of chemical potentials and energy as in Fig. 5.2. As can be seen, by properly tuning τ_H one can increase the power output by more than 25% [Figs. 5.3(a) and 5.3(e)] compared to the symmetric case. However, in order for the tuning to be more effective, the transition rates $\bar{\omega}_H$ and $\bar{\omega}_C$ must be distinct, adding an asymmetry to the system. Figs. 5.3(c) and 5.3(d) reveal that the ratio $\bar{P}(\tau_H)/\bar{P}(\tau/2)$ is less than or equal to 1 for $\bar{\omega}_H = \bar{\omega}_C$. Finally, by comparing Fig. 5.3(a) with Fig. 5.3(b), and Fig. 5.3(e) with Fig. 5.3(f), we notice that the tuning of τ_H can increase the power output for $\bar{\omega}_H$ greater or smaller than $\bar{\omega}_C$, leading to τ_H smaller or larger than $\tau/2$, respectively. For $\bar{\omega}_H > \bar{\omega}_C$ the region of greater enhancement corresponds to the high efficiencies and power outputs (small T_C/T_H).

Complete maximization of power: In addition to optimization in terms of the protocol (τ and τ_H) the chemical potentials and temperatures can be properly chosen to enhance the heat engine, which will be done by optimizing the transition rates.

Figure 5.4 depicts the behavior of the resulting values for τ_H/τ , $\omega_H/\bar{\omega}_H$ and $\omega_C/\bar{\omega}_C$ when power is maximized in terms of protocol and transition rates. Values of $\bar{\omega}_H$ and $\bar{\omega}_C$ are chosen over a square grid with values ranging from 0.1 to 2 with steps of 0.05, for each of these values we obtain the maximizing τ_H , ω_H and ω_C . The results are displayed as the minimum, mean, and maximum values, as three curves from bottom to top.

Although the resulting $\omega_H/\bar{\omega}_H$ and $\omega_C/\bar{\omega}_C$ vary slightly with rates $\bar{\omega}_H$ and $\bar{\omega}_C$, an opposite trend is verified for τ_H , which is very sensitive to the choice of transition rates. This suggests that a good choice of time protocol is the most relevant parameter for power maximization. This finding is reinforced by examining the behavior of maximized values of power in Fig. 5.5. Continuous lines represent minimum, mean, and maximum values of optimal power when only τ_H is tuned (best protocol) and the rates are fixed at “reliable” but non-maximized choices, while dashed lines refer to complete maximization. The curves show no significant difference

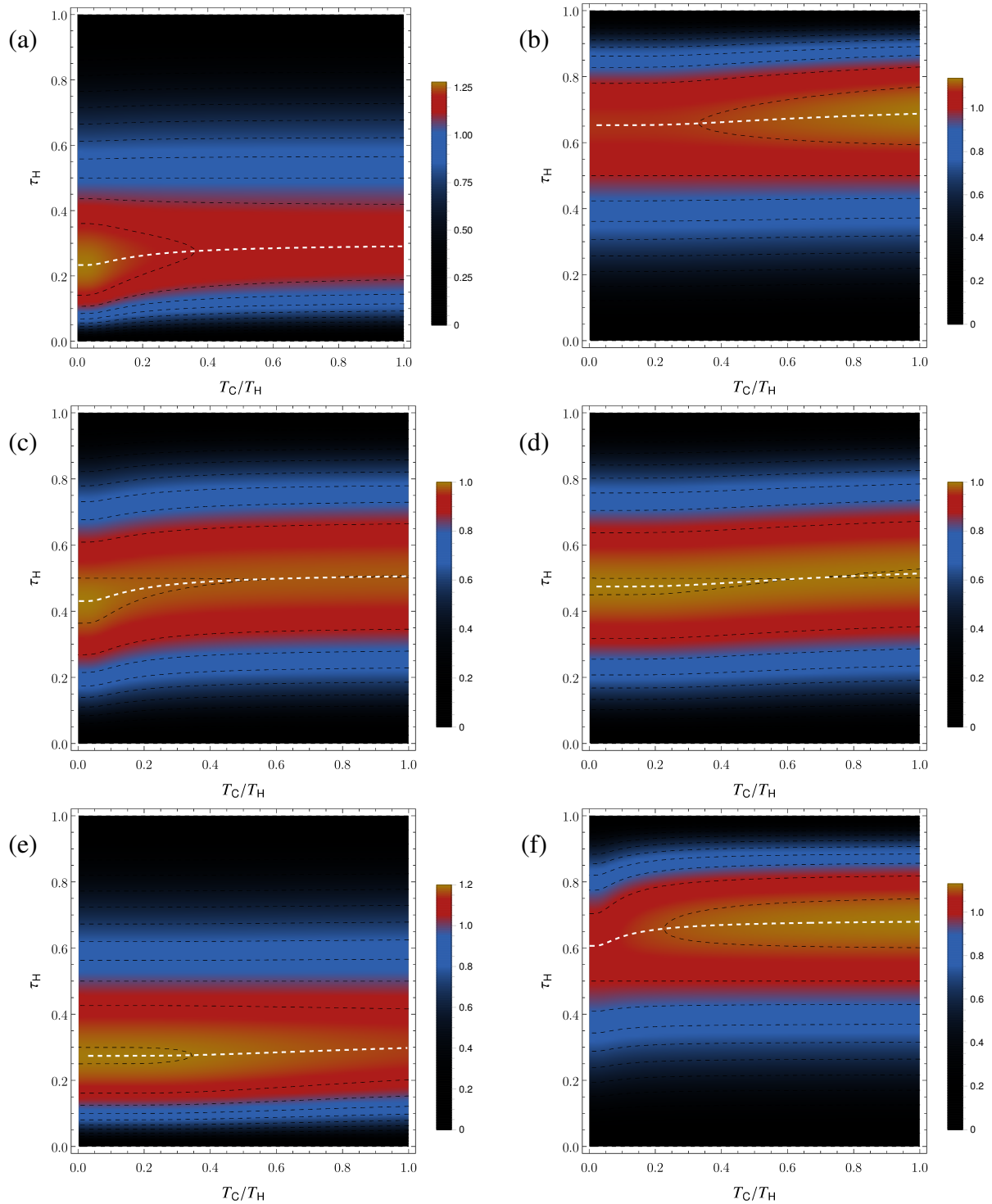


Figure 5.3: Density plots of the power as a function of τ_H and T_C/T_H divided by the symmetric case power. Each dashed black curve represents an increment of 0.1 in the value of the power and the white dashed curve represents the value of τ_H that maximizes the power for each value of T_C/T_H . For all panels, we set $\tau = 1$, $\mu_H = 0.4$, $\mu_C = 0.6$ and $\epsilon = 1$. The remaining parameters are (a) $T_H = 2.0$, $\bar{\omega}_H = 0.86$ and $\bar{\omega}_C = 0.14$; (b) $T_H = 0.4$, $\bar{\omega}_H = 0.16$ and $\bar{\omega}_C = 0.69$; (c) $T_H = 2.0$, $\bar{\omega}_H = 0.5$ and $\bar{\omega}_C = 0.5$; (d) $T_H = 0.4$, $\bar{\omega}_H = 0.5$ and $\bar{\omega}_C = 0.5$; (e) $T_H = 0.3$, $\bar{\omega}_H = 0.86$ and $\bar{\omega}_C = 0.14$; (f) $T_H = 3.0$, $\bar{\omega}_H = 0.16$ and $\bar{\omega}_C = 0.69$.

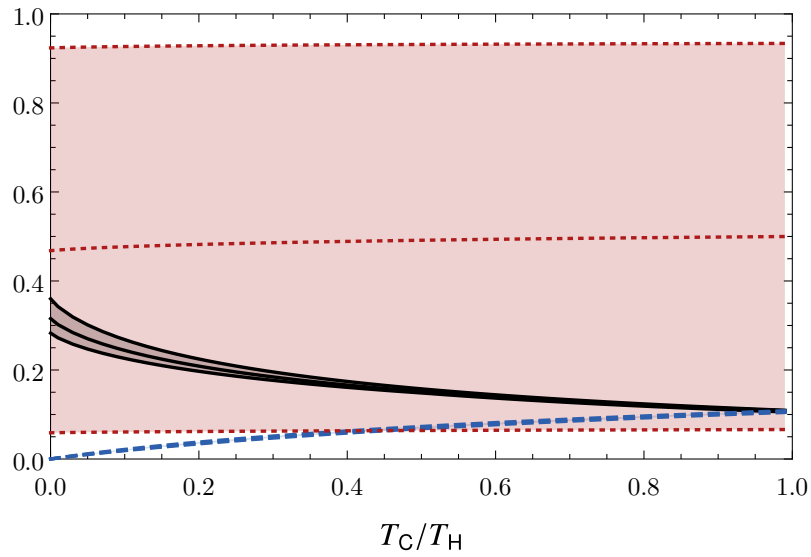


Figure 5.4: Values of τ_H/τ (red dotted), $\omega_H/\bar{\omega}_H$ (black continuous) and $\omega_C/\bar{\omega}_C$ (blue dashed) after the maximization of power for fixed temperatures and $\tau = 1$. The maximum, mean and minimum value for each quantity is presented for different values of $\bar{\omega}_H$ and $\bar{\omega}_C$, more details in the text.

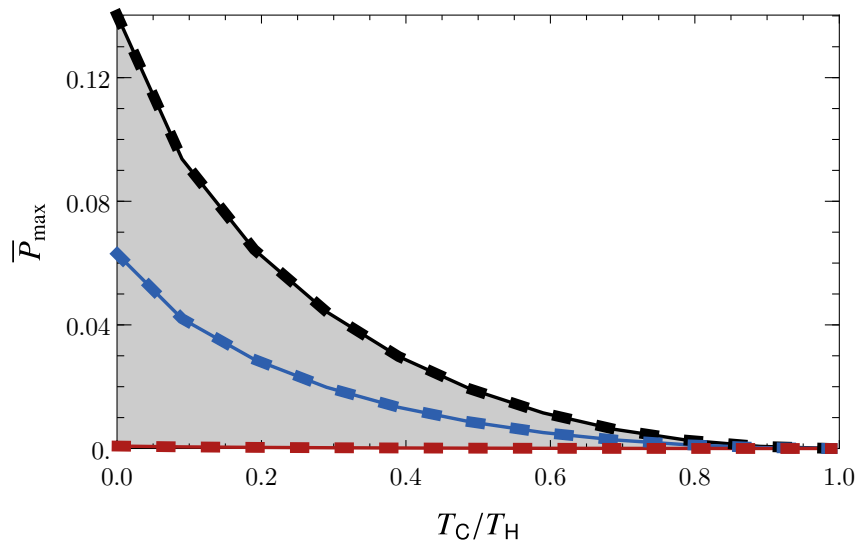


Figure 5.5: Maximum power output \bar{P}_{\max} versus T_C/T_H for $\tau = 1$ and the same grid used in Fig. 5.4, where maximum (black), mean (blue) and minimum (red) values of maximum power are displayed. Continuous lines account for the maximization in terms of τ_H only, while dashed lines represent the maximization in terms of τ_H , $\omega_H/\bar{\omega}_H$ and $\omega_C/\bar{\omega}_C$.

between them.

Lastly, the efficiency at maximal power η_{MP} is compared to the well-established Curzon-Ahlborn efficiency and Carnot in Figs. 5.6 and 5.7, respectively, for different temperatures. Similarly to Figs. 5.4 and 5.5, the optimization is carried out for all values of $\bar{\omega}_H$ and $\bar{\omega}_C$ over a

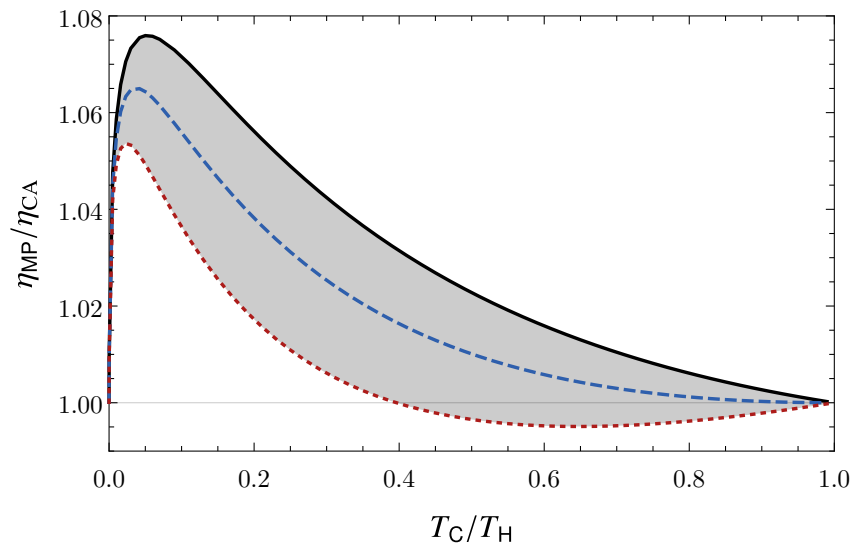


Figure 5.6: Ratio between the efficiency at maximum power η_{MP} and the Curzon-Ahlborn efficiency η_{CA} versus T_C/T_H for $\epsilon = 1$ and $\tau = 1$. The lines represent their loci of maximum (black continuous), mean (blue dashed) and minimum (red dotted) values obtained for the same grid used in Fig. 5.4.

grid.

Except for some specific choices of $\bar{\omega}_H$ and $\bar{\omega}_C$ in a small range of T_C/T_H between 0.4 and 1, the maximization provides an efficiency slightly higher than the Curzon-Ahlborn value. As is the case for Carnot and Curzon-Ahlborn efficiencies, Eqs. (5.1) and (5.8) show that η_{MP} depends only on the temperature ratio and not on the specific value of T_H . When $T_C/T_H \rightarrow 0$ and 1, all efficiencies collapse at the asymptotic values 1 and 0, respectively.

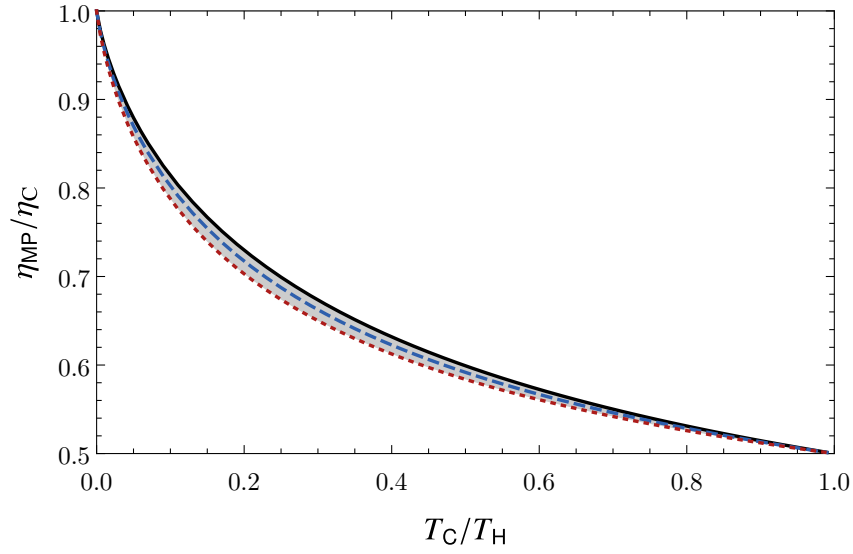


Figure 5.7: Ratio between efficiency at maximum power η_{MP} and Carnot η_{C} versus $T_{\text{C}}/T_{\text{H}}$ for $\epsilon = 1$ and $\tau = 1$. The lines represent their locci of maximum (black continuous), mean (blue dashed) and minimum (red dotted) values obtained for the same grid used in Fig. 5.4.

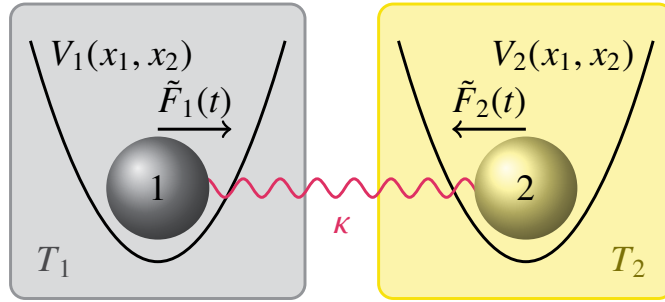


Figure 5.8: Scheme of the two-particle Brownian engine. Each particle is subject to a temperature T_i , potential V_i and time-dependent external force \tilde{F}_i . The particles are coupled by a harmonic interaction with stiffness κ .

5.2 Interacting Brownian engine

5.2.1 Dynamic and thermodynamic description

In this Section we consider another route for studying the efficiency of thermal engines composed of Brownian particles. Previous works, both theoretical and experimental, focused on single-particle engines. Here, we consider an engine composed of two interacting Brownian particles [VI]. In particular, we explore the interplay between driving amplitude, frequency, and interaction between particles in the machine's operation.

The model is composed of two interacting underdamped Brownian particles $i = \{1, 2\}$ with equal mass m , each subject to a distinct time-dependent external force $\tilde{F}_i(t)$, in contact with

a thermal bath of temperature T_i at all times, and coupled to a potential that depends on both positions $V_i(x_1, x_2)$, as illustrated in Fig. 5.8. Their positions and velocities, x_i and v_i , evolve in time according to the following set of Langevin equations:

$$\frac{dv_1}{dt} = \frac{1}{m} F_1^*(x_1, x_2) + \frac{1}{m} \tilde{F}_1(t) - \gamma v_1 + \zeta_1, \quad (5.11)$$

$$\frac{dv_2}{dt} = \frac{1}{m} F_2^*(x_1, x_2) + \frac{1}{m} \tilde{F}_2(t) - \gamma v_2 + \zeta_2, \quad (5.12)$$

and

$$\frac{dx_1}{dt} = v_1, \quad \frac{dx_2}{dt} = v_2, \quad (5.13)$$

where γ is the friction parameter. There are eight forces that act on the system: Two forces $F_i^*(x_1, x_2)$, related to the harmonic potentials and the interaction between particles, two external driving components $\tilde{F}_i(t)$, dissipative friction forces $-\gamma v_i$, and stochastic forces $\zeta_i(t)$. The first forces can be described as derivatives of a potential V_i given by $F_i^*(x_1, x_2) = -\partial V_i / \partial x_i$, whereas the stochastic forces are white noise due to the environment: $\langle \zeta_i(t) \rangle = 0$ and $\langle \zeta_i(t) \zeta_j(t') \rangle = 2\gamma k_B T_i \delta_{ij} \delta(t - t') / m$. The above set of Langevin equations is associated with the probability distribution $P(x_1, x_2, v_1, v_2, t)$, whose time evolution is governed by the respective Fokker-Planck-Kramers equation:

$$\frac{\partial P}{\partial t} = - \sum_{i=1}^2 \left(v_i \frac{\partial P}{\partial x_i} + [F_i^* + \tilde{F}_i(t)] \frac{\partial P}{\partial v_i} + \frac{\partial J_i}{\partial v_i} \right), \quad (5.14)$$

where

$$J_i = -\gamma v_i P - \frac{\gamma T_i}{m} \frac{\partial P}{\partial v_i}. \quad (5.15)$$

is interpreted as a ‘‘flux current’’ of a continuity equation, and the equilibrium condition is met by $J_i = 0$, as in Section 2.

If the temperatures of both particles are equal and the external forces are absent, the probability distribution converges to the Gibbs equilibrium distribution at large times, $P^{\text{eq}}(x_1, x_2, v_1, v_2) \propto e^{-E/T}$, where E is the total energy of the system.

The time evolution of a generic average $\langle x_i^n v_j^m \rangle$ can be obtained from the Fokker-Planck-Kramers equation (5.14) for suited boundary conditions. We assume the reasonable condition that $P(x_1, x_2, v_1, v_2, t)$ and its derivatives vanish when x_i or v_i approaches to $\pm\infty$, which paves the way for integration by parts. More specifically, we are interested in obtaining expressions

for thermodynamic quantities, such as the heat exchanged between particles and their reservoirs, and the work performed by each external force on its particle. Their expressions can be obtained from the time evolution of the mean energy $\langle E \rangle$, together with the Fokker-Planck-Kramers equation, and being consistent to the first law of thermodynamics [8, 59]:

$$\frac{d\langle E \rangle}{dt} = - \sum_{i=1}^2 (\dot{W}_i + \dot{Q}_i), \quad (5.16)$$

where \dot{W}_i is the rate of work done on particle i due to the external force $\tilde{F}_i(t)$,

$$\dot{W}_i = -m\tilde{F}_i(t) \langle v_i \rangle, \quad (5.17)$$

and \dot{Q}_i is the rate of heat delivered to reservoir i . An expression for the heat can be derived from the above two equations:

$$\dot{Q}_i = \gamma (m \langle v_i^2 \rangle - T_i). \quad (5.18)$$

Similarly, the time evolution of the entropy of the system $S = -\langle \ln P(x_1, x_2, v_1, v_2) \rangle$ (once again $k_B = 1$) is the difference between the entropy production rate σ and entropy flux rate ϕ from the system to the thermal reservoirs given by

$$\sigma = \frac{m}{\gamma} \sum_{i=1}^2 \frac{1}{T_i} \int \frac{J_i^2}{P} dx_1 dx_2 dv_1 dv_2, \quad (5.19)$$

and

$$\phi = - \sum_{i=1}^2 \frac{m}{T_i} \int v_i J_i dx_1 dx_2 dv_1 dv_2, \quad (5.20)$$

respectively. Note that $\sigma \geq 0$, whereas ϕ can be conveniently rewritten in terms of the ratio between \dot{Q}_i and temperature T_i :

$$\phi = \sum_i \gamma \left(\frac{m \langle v_i^2 \rangle}{T_i} - 1 \right) = \sum_{i=1}^2 \frac{\dot{Q}_i}{T_i}. \quad (5.21)$$

5.2.2 Harmonic potentials and periodic driving

Having obtained the evolution of positions and velocities, and their connections to relevant thermodynamic quantities for the study of engines, we turn the calculation of thermodynamic quantities. We consider that the potential is the combination of an harmonic trap and interaction

between particles,

$$V_i = \frac{k_i}{2}x_i^2 + \frac{\kappa}{2}(x_i - x_j)^2, \quad (5.22)$$

with associate forces given by

$$F_i^* = -kx_i - \kappa(x_i - x_j). \quad (5.23)$$

We also consider external forces $\tilde{F}_1(t)$ and $\tilde{F}_2(t)$ as the work sources 1 and 2, with same frequency ω , distinct amplitudes and distinct phases, characterized by a lag δ , in similarity to Refs. [173, 192, 215, 216]. Hence, the external forces are given by

$$\tilde{F}_1(t) = X_1 \cos(\omega t), \quad \tilde{F}_2(t, \delta) = X_2 \cos[\omega(t - \delta)]. \quad (5.24)$$

From Eq. (5.16) and due to the fact that $\langle E \rangle$ is a state function, the work per period in the nonequilibrium steady state is obtained by the integration over a period:

$$\bar{W}_i = -\frac{\omega}{2\pi} \int_0^{2\pi/\omega} \tilde{F}_i(t) dt \quad (5.25)$$

and the heat exchanged per period is

$$\bar{Q}_i = \bar{\kappa}(T_j, T_i) + \gamma \frac{\omega\gamma}{2\pi} \int_0^{2\pi/\omega} \langle v_i \rangle^2(t) dt, \quad (5.26)$$

where T_j is the temperature of particle $j \neq i$, $\bar{\kappa} = \gamma\kappa^2/[2\kappa^2 + 2\gamma^2(\kappa + k)]$ is the thermal conduction [8, 217], and we used the covariance $\text{cov}(v_i, v_i) = \langle v_i^2 \rangle - \langle v_i \rangle^2$ obtained from the Fokker-Planck-Kramers equation.

The heat and work can be related to the second law of thermodynamics as follows: In the nonequilibrium steady state the entropy production over a cycle is promptly obtained from Eq. (5.21) and can be related to the average work and heat according to

$$\bar{\sigma} = \frac{4T^2}{4T^2 - \Delta T^2} \left[-\frac{1}{T}(\bar{W}_1 + \bar{W}_2) + (\bar{Q}_1 - \bar{Q}_2) \frac{\Delta T}{2T^2} \right], \quad (5.27)$$

where $T = (T_1 + T_2)/2$ and $\Delta T = T_2 - T_1$. The steady-state entropy production per period can also be viewed as sum of two components: $\bar{\sigma} = \Phi_T + \bar{\Phi}_f$, where the former, Φ_T , is the flux

of entropy due to the temperature difference

$$\Phi_T = \frac{4\bar{\kappa}\Delta T^2}{4T^2 - \Delta T^2}, \quad (5.28)$$

and the latter due to external forces

$$\bar{\Phi}_f = \tilde{L}_{11}X_1^2 + (\tilde{L}_{12} + \tilde{L}_{21})X_1X_2 + \tilde{L}_{22}X_2^2. \quad (5.29)$$

Above expressions might suggest that we are working on the linear regime (close to equilibrium), but they are exact. In order to relate them with thermodynamic fluxes and forces, we are going to perform the analysis of a small temperature difference ΔT between thermal baths. By introducing the thermodynamic forces $f_1 = X_1/T$, $f_2 = X_2/T$ and $f_T = \Delta T/T^2$, $\bar{\sigma}$ is given by

$$\bar{\sigma} \approx J_1f_1 + J_2f_2 + J_Tf_T, \quad (5.30)$$

where flux i ($i = 1, 2$ or T) is associate with force f_i and given by the following expressions $\bar{W}_1 = -TJ_1f_1$, $\bar{W}_2 = -TJ_2f_2$ and $\bar{Q}_1 - \bar{Q}_2 = 2J_Tf_T$. From them, it follows that fluxes assume bilinear forms $J_1 = L_{11}f_1 + L_{12}f_2$, $J_2 = L_{21}f_1 + L_{22}f_2$, and $J_T = L_{TT}f_T$. In this linear stochastic thermodynamics approach, one can identify the Onsager coefficients:

$$L_{11} = L_{22} = \left(\frac{T\gamma\omega^2}{2}\right) \frac{\gamma^2\omega^2 + (\omega^2 - (k + \kappa))^2 + \kappa^2}{[\gamma^2\omega^2 + (\omega^2 - k)^2][\gamma^2\omega^2 + (\omega^2 - (k + 2\kappa))^2]}, \quad (5.31)$$

$$L_{12} = \left(\frac{T\kappa\omega}{2}\right) \frac{2\gamma\omega(\kappa + k - \omega^2)\cos(\delta\omega) - [\gamma^2\omega^2 - (\omega^2 - (k + \kappa))^2 + \kappa^2]\sin(\delta\omega)}{[\gamma^2\omega^2 + (\omega^2 - k)^2][\gamma^2\omega^2 + (\omega^2 - (k + 2\kappa))^2]}, \quad (5.32)$$

$$L_{21} = \left(\frac{T\kappa\omega}{2}\right) \frac{2\gamma\omega(\kappa + k - \omega^2)\cos(\delta\omega) + [\gamma^2\omega^2 - (\omega^2 - (k + \kappa))^2 + \kappa^2]\sin(\delta\omega)}{[\gamma^2\omega^2 + (\omega^2 - k)^2][\gamma^2\omega^2 + (\omega^2 - (k + 2\kappa))^2]}, \quad (5.33)$$

and

$$L_{TT} = \bar{\kappa}T^2. \quad (5.34)$$

All other Onsager coefficients are zero, revealing that there is no coupling between f_T and f_1 or f_T and f_2 . Hence, heat cannot be converted into work and vice-versa, while work can be exchanged between both work sources. Thus we explore the present engine as a work-to-work converter in later sections.

We pause to make some comments: (i) for $\Delta T = 0$, expressions for L_{ij} 's ($i = 1$ and 2)

are exact and valid for arbitrary large values of f_i 's; (ii) one can verify that $L_{11} = L_{22} \geq 0$ and $(L_{12} + L_{21})^2 \leq 4L_{11}L_{22}$ in agreement with the second law of thermodynamics; (iii) The non-diagonal Onsager coefficients L_{12} and L_{21} are not the same, except for the lag-less case $\delta = 0$; (iv) in the regime of low and large frequencies, all coefficients behave as ω^2 and $1/\omega^2$ (diagonal) and $1/\omega^4$ (non-diagonal for $\delta = 0$), respectively; (v) the non-diagonal coefficients vanish for sufficiently weak interactions while the diagonal is finite, consistently with a quasi-decoupling between particles. Conversely, when the coupling parameter is very strong, $\kappa \rightarrow \infty$, all coefficients remain finite and coincide with those for a single Brownian particle in a harmonic potential subjected to both external forces [192]; (vi) for large ΔT , Eq. (5.18) states that the heat exchanged with thermal bath i has two contributions: The first, coming from external forces, has the form $A_i f_i^2 + B_i f_i f_j + C_i f_j^2$ (with coefficients A_i, B_i and C_i listed in Ref. [VI]) and it is strictly non-negative. Hence, coefficients satisfy $A_i \geq 0$ and $C_i \geq 0$ and $B_i^2 - 4A_i C_i \leq 0$. The second term, coming from the difference of temperatures, can be positive or negative depending on the sign of $T_j - T_i$. In the absence of external forces, the entropy production reduces to Eq. (5.28); (vii) expressions for coefficients \tilde{L}_{ij} 's appearing in Eq. (5.29) are exact and hold beyond linear regime listed (large forces and/or large difference of temperatures) between thermal baths; (viii) the interplay between both terms can change the direction of the heat flowing per cycle, implying that the coupling parameter can change the regime of operation of the engine, from heater to heat engine and vice-versa, as κ is increased and decreased. Similar findings have also been observed for two coupled double-quantum-dots [218] and coupled spins [219].

5.2.3 Efficiency as a work-to-work converter

By considering for instance particle $i = 2$ as the work source, the heat engine regime satisfies $\mathcal{P} = \overline{\dot{W}}_1 \geq 0$ so, according to Eq (5.18), the system will receive heat when $T_1 \gg T_2$ or $T_2 \gg T_1$, respectively consistent with $\overline{\dot{Q}}_1 < 0$ or $\overline{\dot{Q}}_2 < 0$. Conversely, when the difference of temperatures between thermal baths is small and/or when forces f_1/f_2 are large, both particles do not necessarily receive heat from the thermal bath and only input work can be converted into output work. Such class of engines is known as work-to-work converters.

Since $\overline{\dot{Q}}_1$ and $\overline{\dot{Q}}_2$ are non-negative for equal temperatures, consistently with the system

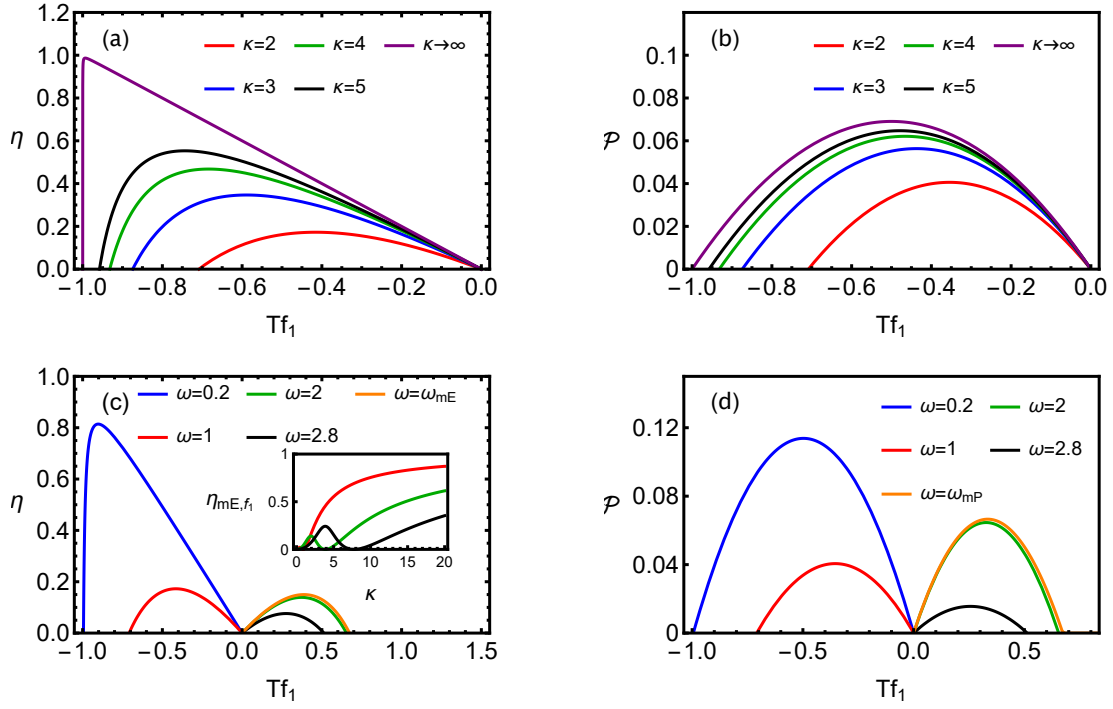


Figure 5.9: For the work-to-work regime, panels (a) and (b) depict the efficiency η and power output \mathcal{P} versus strength force $X_1 = Tf_1$ for distinct interaction parameters κ and $\omega = 1$. In (c) and (d), the same but for distinct values of ω and $\kappa = 2$. Inset: Maximum efficiency η_{mE,f_1} versus κ for distinct ω 's. In all cases, we set $X_2 = Tf_2 = 1$, $T = 0.3$, $\delta = 0$ and $k = 0.1$.

dumping heat into the thermal baths, Eq. (5.36) reduces to the ratio between work sources:

$$\eta \equiv -\frac{\mathcal{P}}{\overline{\dot{W}}_2} = -\frac{L_{11}f_1^2 + L_{12}f_1f_2}{L_{21}f_2f_1 + L_{22}f_2^2}, \quad (5.35)$$

where the second term in the right-hand side of Eq. (5.35) was re-expressed in terms of Onsager coefficients and thermodynamic forces.

Figure 5.9 depicts, for $\delta = 0$, the main features of the efficiency and power output by analyzing the influence of interaction κ and frequency ω . We find that stronger interaction between particles improves substantially the machine performance. Properly tuning κ not only changes the operation regime, from heater to a work-to-work converter (engine), but also increases the power, efficiency and the range of operation [e.g. the possible values of f_1 within the same engine regime, cf. panels (a) and (b)].

Unlike the engine, in the heater operation mode (often called dud engine), work is extracted from both work sources ($\overline{\dot{W}}_1$ and $\overline{\dot{W}}_2 > 0$). For sufficiently strong interactions, maximum efficiencies increase towards the ideal limit $\eta_{mE,f_1} \rightarrow 1$ achieved as $\kappa \rightarrow \infty$ (inset). There are two range of output forces for the engine operation: In the first, for $k + \kappa > \omega^2$, f_1 has

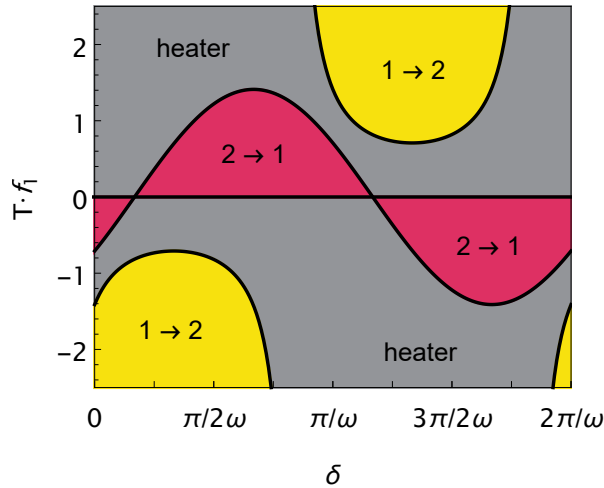


Figure 5.10: Operation modes diagram of $X_1 = T f_1$ versus δ for the work-to-work converter. Symbols $1 \rightarrow 2$ and $2 \rightarrow 1$ correspond to the engine and in which there is, respectively, conversion from $\overline{W}_1 < 0$ into $\overline{W}_2 > 0$ and $\overline{W}_1 > 0$ into $\overline{W}_2 > 0$. The word “heater” corresponds to the dud regime. Parameters: $X_2 = T f_2 = \gamma = \omega = 1$, $k = 0.1$, $T = 0.3$ and $\kappa = 2$.

opposite direction to f_2 [panels (c) and (d)]. The increase of frequency in such a case reduces the machine efficiency until it vanishes for $\omega^2 = k + \kappa$. Conversely, f_1 has the same direction to f_2 when $k + \kappa < \omega^2$, with optimal frequencies ω_{mE} and ω_{mP} ensuring maximum efficiency and power. The maximum efficiency frequency is given by $\omega_{mE} = \sqrt{k + \kappa + \sqrt{k + \kappa + \kappa^2}}$, with efficiency and power given by Eq. (5.35). Whenever ω_{mE} is independent on the ratio f_2/f_1 , ω_{mP} depends on them.

Finally, the engine behaves very inefficiently for $\omega \gg 1$. This can be understood by the fact that the system presents some inertia, quantified by a relaxation timescale, and does not properly respond to abrupt changes when the frequency is too large.

Next, we examine the influence of a phase difference between harmonic forces. Figure 5.10 represents an operation mode diagram, showing that the existence of a lag between driving forces not only controls the power and efficiency, but can also guide the operation modes of the machine. In other words, depending on the value of δ , the work is extracted from the work source 1 and dumped into 2, $\eta = -\overline{W}_2/\overline{W}_1$, or vice-versa, $\eta = -\overline{W}_1/\overline{W}_2$, or work can be extracted from both work sources and released as heat. For some values of forces, the three regimes can be achieved by solely changing the lag. Such changes of conversion in the operation mode share some similarities with some theoretical models for kinesin in which the range chemical potentials and mechanical forces can rule the energy conversion (chemical into mechanical and vice-versa) [220].

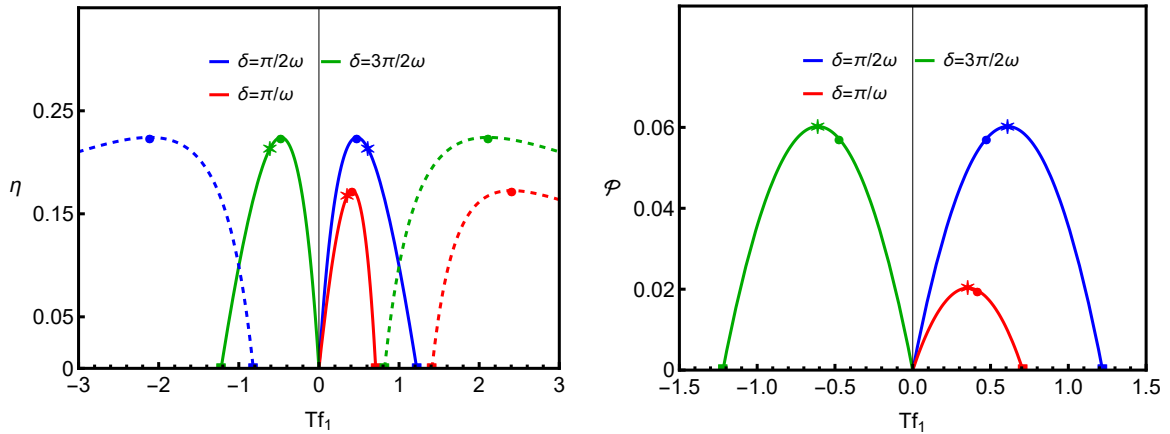


Figure 5.11: For the same parameters of Fig. 5.10, the efficiency η (left) and power output \mathcal{P} (right) versus $X_1 = Tf_1$ for distinct phase differences δ . Dashed and continuous lines correspond to the conversion from \overline{W}_1 into \overline{W}_2 and vice-versa, respectively. Circles and stars denote the maximum efficiency and maximum power, respectively.

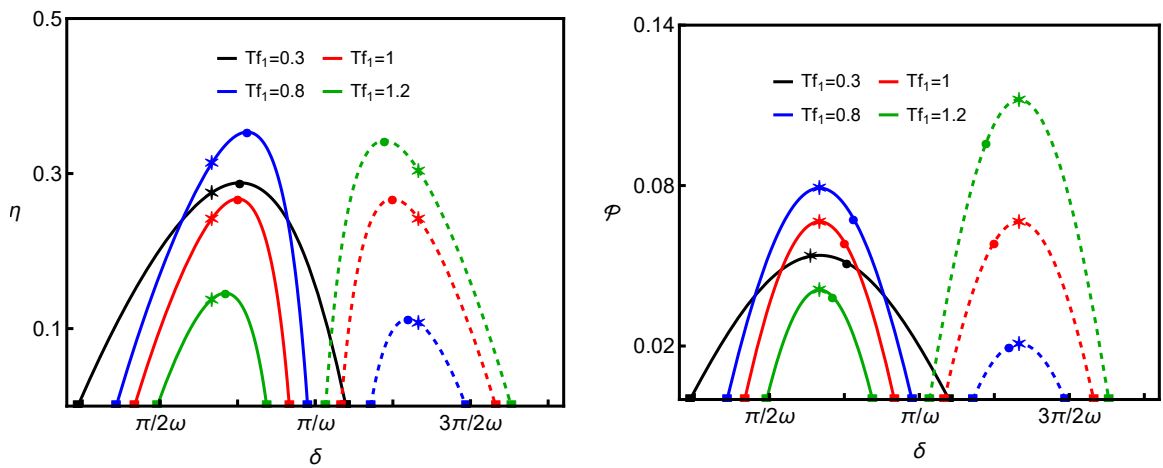


Figure 5.12: For the same parameters from Fig. 5.10, the efficiency η (left) and power output \mathcal{P} (right) versus phase difference δ for distinct $X_1 = Tf_1$'s. Continuous and dashed lines correspond to the conversion from \overline{W}_2 into \overline{W}_1 and vice-versa, respectively. Circles and stars denote the maximum efficiency and maximum power, respectively.

Figures 5.11 and 5.12 show efficiency and power for fixed values of X_1 and δ , slices of Fig. 5.10. We can see that, for the parameters involved, choosing values of force and lag drastically change both efficiency and power, however, the efficiency is still far from the regime of perfect work-to-work conversion $\eta = 1$. In general, maximum power and maximum efficiency are attained at close values.

Different strategies to optimize the heat engine are discussed in Ref. [VI]. Therein, the authors discuss the consequences of maximizing efficiency and power in terms of output force,

interaction, lag, and all of them simultaneously.

5.2.4 Different temperatures

In this section, we derive general findings for the case of each particle placed in contact with a distinct thermal bath. We shall restrict our analysis to $k + \kappa > \omega^2$. Although the power output \mathcal{P} is the same as before, the efficiency may change due to the emergence of heat flow and therefore its maximization will occur, in general, for distinct output forces and phase differences when compared with the work-to-work converter. The efficiency η of such a case then reads:

$$\eta = -\frac{\mathcal{P}}{\overline{\dot{W}}_2 + \overline{\dot{Q}}_i}. \quad (5.36)$$

Contrasting with the work-to-work converter, in which particles only dump heat to the reservoirs [and therefore heat is not considered in Eq. (5.35)], the temperature difference may be responsible for some heat flow between reservoirs through the system. The difference in temperature affects the velocity fluctuations but it does not change its average $\langle v_i \rangle$, therefore the output power \mathcal{P} is unaffected by ΔT . Thus, the efficiency will always decrease as the temperature gap increases.

The discussed regime in which the system receives heat from one reservoir is achieved when the parameters satisfy specific conditions, the threshold values separating regimes are denoted f_h and δ_h . For a reservoir i that provides heat, they can be obtained from $\overline{\dot{Q}}_i(f_h, \delta) = 0$ for some fixed δ , or analogously for δ_h and fixed f . For small temperature differences, the range of possible parameters fulfilling $\overline{\dot{Q}}_i < 0$ is small. However, large temperature differences yield heat fluxes with ease.

Despite that all calculations are exact, expressions for efficiency and their maximizations become involved since they also depend on coefficients A_i , B_i , and C_i . To obtain some insight about its behavior in the presence of heat flux, let us perform an analysis for $\Delta T \ll 1$ and $\Delta T \gg 1$. In the former limit, η is approximately given by $\eta \approx -(\overline{\dot{W}}_1/\overline{\dot{W}}_2)(1 - \overline{\dot{Q}}_i/\overline{\dot{W}}_2)$. In terms of Onsager coefficients,

$$\eta \approx -\frac{L_{11}f_1^2 + L_{12}f_1f_2}{L_{22}f_2^2 + L_{12}f_2f_1} \left(1 + \frac{\overline{\dot{Q}}_i}{T(L_{22}f_2^2 + L_{21}f_2f_1)} \right), \quad (5.37)$$

where the input heat $\overline{\dot{Q}}_i < 0$ evidently decreases the efficiency.

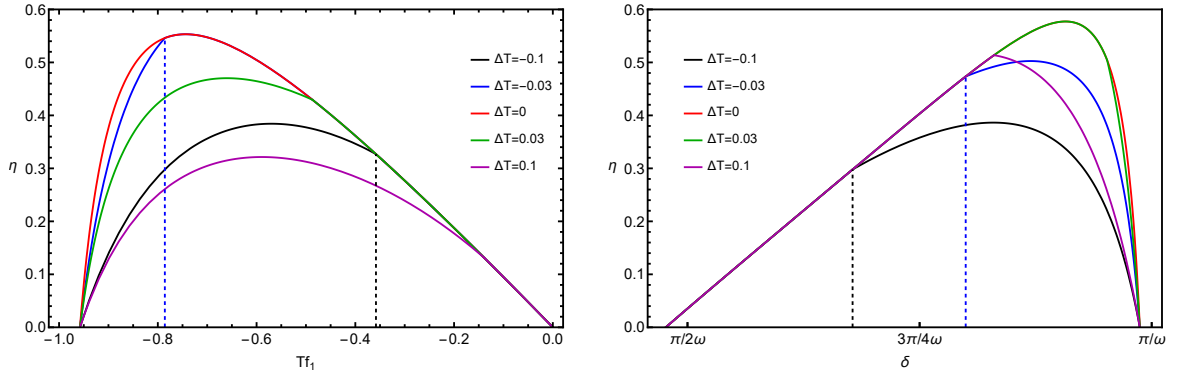


Figure 5.13: For distinct temperature differences, left and right panels depict the efficiency versus Tf_1 (for $\delta = 0$) and versus δ (for $Tf_1 = 1$), respectively. The vertical lines denote the values of f_h and δ_h in which heat stalls. The red curves show the work-to-work efficiency. Parameters: $T = 0.3 + \Delta T/2$, $\omega = 1$, $k = 0.1$, $\kappa = 5$ and $Tf_2 = 1$.

For the limit of a large temperature difference $\Delta T \gg 1$, the efficiency is approximately given by

$$\eta \approx -\frac{T}{\bar{\kappa}\Delta T} (L_{12}f_1f_2 + L_{11}f_1^2), \quad (5.38)$$

revealing that η decreases asymptotically as ΔT^{-1} . Recalling that the terms in parentheses do not depend on temperature, $\eta \ll 1$, with maximum values η_{mE} and $\eta_{mE,\delta}$.

To illustrate above findings, Fig. 5.13 exemplifies the efficiency for distinct and small $\Delta T = T_2 - T_1$ for fixed $\delta = 0$ and $f_1 = 1$. When there is a temperature difference, $\Delta T \neq 0$, the efficiency is always lower than in the $\Delta T = 0$ work-to-work regime. The heat influx \bar{Q}_i stalls for parameters f_h and δ_h , shown by vertical dashed lines, causing an efficiency collapse between different regimes. As stated previously, the power \mathcal{P} is the same as in Fig. 5.9(b) for $\kappa = 5$. Since \bar{Q}_1 and \bar{Q}_2 exhibit distinct dependencies of f_1 and δ , the amount of heat received will be different when $\Delta T > 0$ or < 0 .

5.3 Chapter summary

In Section 5.1 we explored how asymmetric protocols are important to enhance an engine's performance. Considering a stochastic pump composed of a quantum dot alternately colliding with two reservoirs, we observed that proper optimization of the power output can lead to a gain greater than 25% when compared to the symmetric case.

Fine-tuning the time protocol is suggested to be more relevant for the optimization than other parameters involved. Moreover, adjusting the protocol should be easier than independently

tuning the pair temperature and chemical potential. In fact, the choice of a “good” (instead of optimal) engine together with optimized time provides a reliable recipe for obtaining an almost optimal engine in terms of power output, whose associated efficiencies are usually somewhat larger than the Curzon-Ahlborn one, but much larger than the symmetric case efficiency.

Adding the role of interaction in heat engines, Section 5.1 explored the behavior of a two-particle Brownian engine with time-dependent driving forces. The time symmetry between both forces is broken with the introduction of a lag parameter δ , which plays a role in the regime of operation and performance.

We focused on the work-to-work conversion and observed that the intensity of interactions increases both power and efficiency. The frequency of driving oscillation and input force introduce non-trivial effects on the regime of operation, and a temperature difference preserves output power while decreasing efficiency. It is also worth noting that in the case of infinitely strong coupling, $\kappa \rightarrow \infty$, our results reduce to those of a single particle with two external forces [192]; and, at constant temperature, our system can be mapped onto a general Ornstein-Uhlenbeck process [221].

“And all this science I don’t understand it’s just my job five days a week”

Elton John in *Rocket Man*

Chapter 6

Conclusions and Discussions

Throughout this thesis, we have studied phase transitions, stochastic thermodynamics, heat engines, and the interplay between them. In particular, we have explored how the passage of time is amenable to thermodynamic analysis and its role across all the aforementioned fields.

We have shown that nonequilibrium phase transitions can be characterized by stochastic thermodynamics quantities, displaying similarities to the well-established study of equilibrium transitions [II]. For periodic driving systems, we have shown that the thermodynamic uncertainty relations are generally loose and with no clear favored bound [III]. Lastly, we have explored fluctuations, performance, and the role of distinct ingredients, such as interaction, in heat engines [IV, VI].

Transition-based coarse-graining: Under the sole assumption of Markovian underlying dynamics, we built on first-passage time problems to develop a framework for the study of systems where partial information stems from a few visible transitions [VII]. From analytical expressions, we have shown how to generate the transition statistics. On the other hand, we have shown how the collected statistics convey information about the internal (thermo)dynamics. With such a framework, it is possible to make predictions, fit models, test candidate models, and infer topology and thermodynamic quantities through the (in)equalities presented.

Entropy production can be lower bounded by visible entropy production, which can be split into two distinct contributions: A contribution from sequences of transitions and one from inter-transition times, hence establishing the physicality of such terms. This lower bound can be cast in the form of an efficiency upper bound for molecular motors in terms of its displacement.

Through equations for conditional probabilities of transitions, we connect continuous-time Markov chains to respective discrete-time Markov chains. A fluctuation relation can be re-

covered by analyzing transition statistics when the observer keeps track of an internal notion of time, the total number of transitions [VIII]. Finally, an algorithm for the evaluation of Kullback-Leibler divergence was implemented and made open-source, which is relevant for evaluating the visible entropy production and comparing general time-series across disciplines.

These results were verified and illustrated with the Gillespie simulations of arbitrary networks, and experimentally-validated biophysical models of dynein and kinesin. A minimal model for template-directed polymerization reveals that the statistics of transitions can probe the presence of disorder.

Phase transitions: We have shown how entropy production can be used as a tool to characterize nonequilibrium phase transitions in similarity to order parameters in equilibrium transitions, while keeping track of the distance to equilibrium [II]. It can be used to detect the location of the phase transition, whether continuous or first-order, critical exponents, and the region of phase coexistence. These results were verified in the inertial majority vote model [I].

For first-order phase transitions, we studied the fluctuation of integrated currents through a finite-time version of large deviation theory [V]. Both the statistics of currents conditioned to a phase and a two-state model coarse-graining reveal how integration times turn the bimodal distribution into unimodal, details of how the variance scales non-trivially with the volume and how intra-phase variances contribution to the current fluctuations become negligible for large systems. These results were numerically verified in the second Schlögl's model and a 12-states Potts model.

Heat engines: Tuning the interaction time of sequential engines is a powerful route for the performance optimization and conveniently accessible in the form of a protocol rather than a change of temperatures or energies. In a model of interacting Brownian engines, we observed how lag can change the regime of operation, and interaction strength enhances both efficiency and power.

Comparing TURs in an exact periodically driven system: The usefulness of any bound is closely related to its tightness. Therefore, we quantitatively explored how loose thermodynamic uncertainty relations can be for the purpose of inferring entropy production in [III]. For systems under time-periodic driving, the original thermodynamic uncertainty relation does not hold [210, 211, 222]. However, we applied distinct extensions of the thermodynamic uncertainty relation valid for time-periodic systems [38–43] to an exactly solvable model of a collisional heat engine. We observed that, far from equilibrium, all inequalities are orders of magnitude loose

in most regimes, and some increase indefinitely. This fact raises the need for more specialized bounds and inference schemes, such as *hyperaccurate* currents [223, 224] and the use of information from waiting times [VII, 28, 29, 87].

Future perspectives: Apart from potential applications of such findings to numerous systems of interest, many of which are already cited in the introductory Chapter 1, many possibilities are open for developing the provided theoretical tools. The conditions related to tightness of entropy production and efficiency bounds can be explored; transition statistics is a promising tool for probing disorder and could be established as such if more detailed analyses are performed; the behavior of entropy production can be explored for more symmetry classes; fluctuations at the phase coexistence region can be explored for quantities such as work by using time-dependent rates [225, 226]; optimization of heat engines can be combined with previously known methods (see e.g. Refs. [IV, 159, 167, 168, 188]); modulation of excited level can be included in the engines to introduce an additional possibility to extract work.

Promising research also arises from the combination of the three major themes presented in this thesis. The transition-based coarse-graining framework can be connected to phase transitions to study systems where the inter-phase dynamics is hidden, while phase transitions are visible, not restricted to only two phases. Transition-based coarse-graining can also be applied to heat engines for the study of fluctuating efficiency [157, 227] and multi-terminal machines [228]. Finally, heat engines can be composed of many interacting bodies that go through a phase transition or operate at the criticality/coexistence, which will lead to consequences in engine performance [124, 209, 229–231].

References

- [1] Herbert B Callen. *Thermodynamics and an Introduction to Thermostatistics*. 1998.
- [2] Ludwig von Bertalanffy. “Ètude thermodynamique des phénomènes irréversibles”. In: *Nature* 163.4141 (1949), pp. 384–384.
- [3] Terrell L Hill. *Free energy transduction and biochemical cycle kinetics*. Courier Corporation, 2013.
- [4] Daniel T Gillespie and L Petzold. “Numerical simulation for biochemical kinetics”. In: *Systems Modelling in Cellular Biology* (2006), pp. 331–354.
- [5] Tânia Tomé and Mário J De Oliveira. *Stochastic dynamics and irreversibility*. Springer, 2015.
- [6] Ken Sekimoto. “Langevin Equation and Thermodynamics”. In: *Progress of Theoretical Physics Supplement* 130 (Jan. 1998), pp. 17–27.
- [7] Tânia Tomé. “Entropy production in nonequilibrium systems described by a Fokker-Planck equation”. In: *Brazilian journal of physics* 36 (2006), pp. 1285–1289.
- [8] Tânia Tomé and Mário J. de Oliveira. “Entropy production in irreversible systems described by a Fokker-Planck equation”. In: *Phys. Rev. E* 82 (2 Aug. 2010), p. 021120.
- [9] Joel L Lebowitz and Herbert Spohn. “A Gallavotti–Cohen-type symmetry in the large deviation functional for stochastic dynamics”. In: *Journal of Statistical Physics* 95.1 (1999), pp. 333–365.
- [10] J. Schnakenberg. “Network theory of microscopic and macroscopic behavior of master equation systems”. In: *Rev. Mod. Phys.* 48 (4 Oct. 1976), pp. 571–585.
- [11] Massimiliano Esposito. “Stochastic thermodynamics under coarse graining”. In: *Physical Review E* 85.4 (2012), p. 041125.

- [12] Denis J. Evans, E. G. D. Cohen, and G. P. Morriss. “Probability of second law violations in shearing steady states”. In: *Phys. Rev. Lett.* 71 (15 Oct. 1993), pp. 2401–2404.
- [13] Gavin E Crooks. “Nonequilibrium measurements of free energy differences for microscopically reversible Markovian systems”. In: *Journal of Statistical Physics* 90.5 (1998), pp. 1481–1487.
- [14] Gavin E. Crooks. “Entropy production fluctuation theorem and the nonequilibrium work relation for free energy differences”. In: *Phys. Rev. E* 60 (3 Sept. 1999), pp. 2721–2726.
- [15] C. Jarzynski. “Nonequilibrium Equality for Free Energy Differences”. In: *Phys. Rev. Lett.* 78 (14 Apr. 1997), pp. 2690–2693.
- [16] Delphine Collin et al. “Verification of the Crooks fluctuation theorem and recovery of RNA folding free energies”. In: *Nature* 437.7056 (2005), pp. 231–234.
- [17] S. Ciliberto. “Experiments in Stochastic Thermodynamics: Short History and Perspectives”. In: *Phys. Rev. X* 7 (2 June 2017), p. 021051.
- [18] C. Van den Broeck and M. Esposito. “Ensemble and trajectory thermodynamics: A brief introduction”. In: *Physica A: Statistical Mechanics and its Applications* 418 (2015). Proceedings of the 13th International Summer School on Fundamental Problems in Statistical Physics, pp. 6–16.
- [19] Édgar Roldán and Juan M. R. Parrondo. “Entropy production and Kullback-Leibler divergence between stationary trajectories of discrete systems”. In: *Phys. Rev. E* 85 (3 Mar. 2012), p. 031129.
- [20] J M R Parrondo, C Van den Broeck, and R Kawai. “Entropy production and the arrow of time”. In: *New Journal of Physics* 11.7 (July 2009), p. 073008.
- [21] Christopher Jarzynski and Daniel K. Wójcik. “Classical and Quantum Fluctuation Theorems for Heat Exchange”. In: *Phys. Rev. Lett.* 92 (23 June 2004), p. 230602.
- [22] Udo Seifert. “Stochastic thermodynamics, fluctuation theorems and molecular machines”. In: *Reports on Progress in Physics* 75.12 (Nov. 2012), p. 126001.
- [23] Nobel Prize Outreach. *The Nobel Prize in Chemistry*. 1977.
- [24] Ilya Prigogine. “Time, structure, and fluctuations”. In: *Science* 201.4358 (1978), pp. 777–785.

- [25] Andre C Barato and Udo Seifert. “Thermodynamic uncertainty relation for biomolecular processes”. In: *Physical review letters* 114.15 (2015), p. 158101.
- [26] Todd R Gingrich et al. “Dissipation bounds all steady-state current fluctuations”. In: *Physical review letters* 116.12 (2016), p. 120601.
- [27] Gianmaria Falasco and Massimiliano Esposito. “Dissipation-Time Uncertainty Relation”. In: *Phys. Rev. Lett.* 125 (12 Sept. 2020), p. 120604.
- [28] Ignacio A Martínez et al. “Inferring broken detailed balance in the absence of observable currents”. In: *Nature communications* 10.1 (2019), pp. 1–10.
- [29] Dominic J. Skinner and Jörn Dunkel. “Estimating Entropy Production from Waiting Time Distributions”. In: *Phys. Rev. Lett.* 127 (19 Nov. 2021), p. 198101.
- [30] Édgar Roldán and Juan MR Parrondo. “Estimating dissipation from single stationary trajectories”. In: *Physical review letters* 105.15 (2010), p. 150607.
- [31] Patrick P. Potts and Peter Samuelsson. “Thermodynamic uncertainty relations including measurement and feedback”. In: *Phys. Rev. E* 100 (5 Nov. 2019), p. 052137.
- [32] André M. Timpanaro et al. “Thermodynamic Uncertainty Relations from Exchange Fluctuation Theorems”. In: *Phys. Rev. Lett.* 123 (9 Aug. 2019), p. 090604.
- [33] Andre C Barato and Udo Seifert. “Universal bound on the Fano factor in enzyme kinetics”. In: *The Journal of Physical Chemistry B* 119.22 (2015), pp. 6555–6561.
- [34] Patrick Pietzonka, Andre C Barato, and Udo Seifert. “Universal bound on the efficiency of molecular motors”. In: *Journal of Statistical Mechanics: Theory and Experiment* 2016.12 (2016), p. 124004.
- [35] Udo Seifert. “Stochastic thermodynamics: From principles to the cost of precision”. In: *Physica A: Statistical Mechanics and its Applications* 504 (2018), pp. 176–191.
- [36] K Proesmans, L Peliti, and D Lacoste. *A case study of thermodynamic bounds for chemical kinetics Chemical Kinetics Beyond the Textbook*. 2018.
- [37] Jordan M Horowitz and Todd R Gingrich. “Thermodynamic uncertainty relations constrain non-equilibrium fluctuations”. In: *Nature Physics* (2019), pp. 1–6.
- [38] Karel Proesmans and Christian Van den Broeck. “Discrete-time thermodynamic uncertainty relation”. In: *EPL (Europhysics Letters)* 119.2 (2017), p. 20001.

- [39] Andre C Barato et al. “Bounds on current fluctuations in periodically driven systems”. In: *New Journal of Physics* 20.10 (2018), p. 103023.
- [40] Timur Koyuk, Udo Seifert, and Patrick Pietzonka. “A generalization of the thermodynamic uncertainty relation to periodically driven systems”. In: *Journal of Physics A: Mathematical and Theoretical* (2018).
- [41] Karel Proesmans and Jordan M Horowitz. “Hysteretic thermodynamic uncertainty relation for systems with broken time-reversal symmetry”. In: *J. Stat. Mech.: Theory and Experiment* 2019.5 (2019), p. 054005.
- [42] AC Barato et al. “A unifying picture of generalized thermodynamic uncertainty relations”. In: *Journal of Statistical Mechanics: Theory and Experiment* 2019.8 (2019), p. 084017.
- [43] Timur Koyuk and Udo Seifert. “Operationally accessible bounds on fluctuations and entropy production in periodically driven systems”. In: *Physical Review Letters* 122.23 (2019), p. 230601.
- [44] F Schlögl. “On stability of steady states”. In: *Zeitschrift für Physik A Hadrons and nuclei* 243.4 (1971), pp. 303–310.
- [45] Ekaterina A. Korobkova et al. “Hidden Stochastic Nature of a Single Bacterial Motor”. In: *Phys. Rev. Lett.* 96 (5 Feb. 2006), p. 058105.
- [46] Roop Mallik et al. “Cytoplasmic dynein functions as a gear in response to load”. In: *Nature* 427.6975 (2004), pp. 649–652.
- [47] Ronald D Vale, Thomas S Reese, and Michael P Sheetz. “Identification of a novel force-generating protein, kinesin, involved in microtubule-based motility”. In: *Cell* 42.1 (1985), pp. 39–50.
- [48] Masayoshi Nishiyama, Hideo Higuchi, and Toshio Yanagida. “Chemomechanical coupling of the forward and backward steps of single kinesin molecules”. In: *Nature Cell Biology* 4.10 (2002), pp. 790–797.
- [49] Nicolaas Godfried Van Kampen. *Stochastic processes in physics and chemistry*. Vol. 1. Elsevier, 1992.
- [50] Abraham Tamir. *Applications of Markov chains in chemical engineering*. Elsevier, 1998.

- [51] David F Anderson and Thomas G Kurtz. “Continuous time Markov chain models for chemical reaction networks”. In: *Design and analysis of biomolecular circuits*. Springer, 2011, pp. 3–42.
- [52] Francesco Avanzini et al. “Nonequilibrium thermodynamics of non-ideal chemical reaction networks”. In: *The Journal of Chemical Physics* 154.9 (Mar. 2021), p. 094114.
- [53] Linda JS Allen. *An introduction to stochastic processes with applications to biology*. CRC press, 2010.
- [54] Anatoly B. Kolomeisky and Michael E. Fisher. “Molecular Motors: A Theorist’s Perspective”. In: *Annual Review of Physical Chemistry* 58.1 (May 2007), pp. 675–695.
- [55] Debashish Chowdhury. “Modeling Stochastic Kinetics of Molecular Machines at Multiple Levels: From Molecules to Modules”. In: *Biophysical Journal* 104.11 (June 2013), pp. 2331–2341.
- [56] David H Wolpert. “The stochastic thermodynamics of computation”. In: *Journal of Physics A: Mathematical and Theoretical* 52.19 (2019), p. 193001.
- [57] Hao Ge and Hong Qian. “Physical origins of entropy production, free energy dissipation, and their mathematical representations”. In: *Phys. Rev. E* 81 (5 May 2010), p. 051133.
- [58] Massimiliano Esposito and Christian Van den Broeck. “Three faces of the second law. I. Master equation formulation”. In: *Phys. Rev. E* 82 (1 July 2010), p. 011143.
- [59] Christian Van den Broeck and Massimiliano Esposito. “Three faces of the second law. II. Fokker-Planck formulation”. In: *Phys. Rev. E* 82 (1 July 2010), p. 011144.
- [60] Tânia Tomé and Mário J. de Oliveira. “Entropy production in irreversible systems described by a Fokker-Planck equation”. In: *Phys. Rev. E* 82 (2 Aug. 2010), p. 021120.
- [61] Jannik Ehrich. “Tightest bound on hidden entropy production from partially observed dynamics”. In: *Journal of Statistical Mechanics: Theory and Experiment* 2021.8 (2021), p. 083214.
- [62] Stefano Bo and Antonio Celani. “Multiple-scale stochastic processes: decimation, averaging and beyond”. In: *Physics reports* 670 (2017), pp. 1–59.
- [63] Gianluca Teza and Attilio L. Stella. “Exact Coarse Graining Preserves Entropy Production out of Equilibrium”. In: *Phys. Rev. Lett.* 125 (11 Sept. 2020), p. 110601.

- [64] Lucas Lacasa et al. “Multiplex Decomposition of Non-Markovian Dynamics and the Hidden Layer Reconstruction Problem”. In: *Phys. Rev. X* 8 (3 Aug. 2018), p. 031038.
- [65] Simone Pigolotti and Angelo Vulpiani. “Coarse graining of master equations with fast and slow states”. In: *The Journal of Chemical Physics* 128.15 (2008), p. 154114.
- [66] Saar Rahav and Christopher Jarzynski. “Fluctuation relations and coarse-graining”. In: *Journal of Statistical Mechanics: Theory and Experiment* 2007.09 (Sept. 2007), P09012–P09012.
- [67] Carlos Drummond de Andrade. “Claro enigma”. In: *São Paulo: Companhia das Letras* (2012).
- [68] Ken Sekimoto. “Derivation of the First Passage Time Distribution for Markovian Process on Discrete Network”. In: (2021).
- [69] Arnab Pal, Shlomi Reuveni, and Saar Rahav. “Thermodynamic uncertainty relation for first-passage times on Markov chains”. In: *Phys. Rev. Research* 3 (3 Aug. 2021), p. L032034.
- [70] Terrell L Hill. “Interrelations between random walks on diagrams (graphs) with and without cycles”. In: *Proceedings of the National Academy of Sciences* 85.9 (1988), pp. 2879–2883.
- [71] Mamata Sahoo and Stefan Klumpp. “Backtracking dynamics of RNA polymerase: pausing and error correction”. In: *Journal of Physics: Condensed Matter* 25.37 (2013), p. 374104.
- [72] Sidney Redner. *A guide to first-passage processes*. Cambridge university press, 2001.
- [73] Yann R Chemla, Jeffrey R Moffitt, and Carlos Bustamante. “Exact solutions for kinetic models of macromolecular dynamics”. In: *The Journal of Physical Chemistry B* 112.19 (2008), pp. 6025–6044.
- [74] Matteo Polettini. “Fisher information of Markovian decay modes”. In: *The European Physical Journal B* 87.9 (2014), pp. 1–9.
- [75] Christian Maes. “Frenesy: Time-symmetric dynamical activity in nonequilibria”. In: *Physics Reports* 850 (2020). Frenesy: time-symmetric dynamical activity in nonequilibria, pp. 1–33.

- [76] J. P. Garrahan et al. “Dynamical First-Order Phase Transition in Kinetically Constrained Models of Glasses”. In: *Phys. Rev. Lett.* 98 (19 May 2007), p. 195702.
- [77] Marco Baiesi, Christian Maes, and Bram Wynants. “Nonequilibrium linear response for Markov dynamics, I: jump processes and overdamped diffusions”. In: *Journal of statistical physics* 137.5 (2009), pp. 1094–1116.
- [78] Édgar Roldán and Pierpaolo Vivo. “Exact distributions of currents and frenesy for Markov bridges”. In: *Phys. Rev. E* 100 (4 Oct. 2019), p. 042108.
- [79] Christian Maes and Karel Netočný. “Nonequilibrium corrections to gradient flow”. In: *Chaos: An Interdisciplinary Journal of Nonlinear Science* 29.7 (2019), p. 073109.
- [80] Hugo Touchette. “The large deviation approach to statistical mechanics”. In: *Physics Reports* 478.1-3 (2009), pp. 1–69.
- [81] Juan P. Garrahan. “Simple bounds on fluctuations and uncertainty relations for first-passage times of counting observables”. In: *Phys. Rev. E* 95 (3 Mar. 2017), p. 032134.
- [82] Matteo Polettini and Massimiliano Esposito. “Effective fluctuation and response theory”. In: *Journal of Statistical Physics* 176.1 (2019), pp. 94–168.
- [83] Naoto Shiraishi and Takahiro Sagawa. “Fluctuation theorem for partially masked nonequilibrium dynamics”. In: *Phys. Rev. E* 91 (1 Jan. 2015), p. 012130.
- [84] Thomas M. Cover and Joy A. Thomas. *Elements of Information Theory 2nd Edition (Wiley Series in Telecommunications and Signal Processing)*. Wiley-Interscience, July 2006.
- [85] A. Gomez-Marin, J. M. R. Parrondo, and C. Van den Broeck. “Lower bounds on dissipation upon coarse graining”. In: *Phys. Rev. E* 78 (1 July 2008), p. 011107.
- [86] Yuhai Tu. “The nonequilibrium mechanism for ultrasensitivity in a biological switch: Sensing by Maxwell’s demons”. In: *Proceedings of the National Academy of Sciences* 105.33 (2008), pp. 11737–11741.
- [87] Jann van der Meer, Benjamin Ertel, and Udo Seifert. “Thermodynamic Inference in Partially Accessible Markov Networks: A Unifying Perspective from Transition-Based Waiting Time Distributions”. In: *Phys. Rev. X* 12 (3 Aug. 2022), p. 031025.
- [88] Alexander Kraskov, Harald Stögbauer, and Peter Grassberger. “Estimating mutual information”. In: *Phys. Rev. E* 69 (6 June 2004), p. 066138.

- [89] Juan A Bonachela, Haye Hinrichsen, and Miguel A Muñoz. “Entropy estimates of small data sets”. In: *Journal of Physics A: Mathematical and Theoretical* 41.20 (Apr. 2008), p. 202001.
- [90] Fernando Perez-Cruz. “Kullback-Leibler divergence estimation of continuous distributions”. In: *2008 IEEE International Symposium on Information Theory*. 2008, pp. 1666–1670.
- [91] Pedro E. Harunari and Ariel Yssou. *Kullback-Leibler divergence estimation algorithm and inter-transition times application*. https://github.com/pedroharunari/KLD_estimation. 2022.
- [92] Hong Qian and X Sunney Xie. “Generalized Haldane equation and fluctuation theorem in the steady-state cycle kinetics of single enzymes”. In: *Physical Review E* 74.1 (2006), p. 010902.
- [93] Hao Ge. “Waiting cycle times and generalized Haldane equality in the steady-state cycle kinetics of single enzymes”. In: *The Journal of Physical Chemistry B* 112.1 (2008), pp. 61–70.
- [94] Izaak Neri, Édgar Roldán, and Frank Jülicher. “Statistics of Infima and Stopping Times of Entropy Production and Applications to Active Molecular Processes”. In: *Phys. Rev. X* 7 (1 Feb. 2017), p. 011019.
- [95] Matteo Polettini and Massimiliano Esposito. “Transient fluctuation theorems for the currents and initial equilibrium ensembles”. In: *Journal of Statistical Mechanics: Theory and Experiment* 2014.10 (2014), P10033.
- [96] José A. Morin et al. “Mechano-chemical kinetics of DNA replication: identification of the translocation step of a replicative DNA polymerase”. In: *Nucleic Acids Research* 43.7 (Mar. 2015), pp. 3643–3652.
- [97] Sander Verbrugge, Lukas C. Kapitein, and Erwin J.G. Peterman. “Kinesin Moving through the Spotlight: Single-Motor Fluorescence Microscopy with Submillisecond Time Resolution”. In: *Biophysical Journal* 92.7 (Apr. 2007), pp. 2536–2545.
- [98] Xinghua Shi and Taekjip Ha. “Single-Molecule FRET: Technique and Applications to the Studies of Molecular Machines”. In: *Molecular Machines in Biology*. Ed. by Joachim Frank. Cambridge University Press, 2011, pp. 4–19.

- [99] Jin-Der Wen et al. “Following translation by single ribosomes one codon at a time”. In: *Nature* 452.7187 (Mar. 2008), pp. 598–603.
- [100] Carlos J. Bustamante et al. “Optical tweezers in single-molecule biophysics”. In: *Nature Reviews Methods Primers* 1.1 (Mar. 2021).
- [101] John T. Canty et al. “Structure and Mechanics of Dynein Motors”. In: *Annual Review of Biophysics* 50.1 (May 2021), pp. 549–574.
- [102] Jonathon Howard and RL Clark. “Mechanics of motor proteins and the cytoskeleton”. In: *Appl. Mech. Rev.* 55.2 (2002), B39–B39.
- [103] Andreja Šarlah and Andrej Vilfan. “The winch model can explain both coordinated and uncoordinated stepping of cytoplasmic dynein”. In: *Biophysical journal* 107.3 (2014), pp. 662–671.
- [104] Wonseok Hwang and Changbong Hyeon. “Energetic Costs, Precision, and Transport Efficiency of Molecular Motors”. In: *The Journal of Physical Chemistry Letters* 9.3 (2018). PMID: 29329502, pp. 513–520.
- [105] Carlos Bustamante, Jan Liphardt, and Felix Ritort. “The Nonequilibrium Thermodynamics of Small Systems”. In: *Physics Today* 58.7 (July 2005), pp. 43–48.
- [106] Steffen Liepelt and Reinhard Lipowsky. “Kinesin’s Network of Chemomechanical Motor Cycles”. In: *Phys. Rev. Lett.* 98 (25 June 2007), p. 258102.
- [107] Nick J Carter and RA Cross. “Mechanics of the kinesin step”. In: *Nature* 435.7040 (2005), pp. 308–312.
- [108] Pierre Gaspard. “Template-Directed Copolymerization, Random Walks along Disordered Tracks, and Fractals”. In: *Phys. Rev. Lett.* 117 (23 Nov. 2016), p. 238101.
- [109] Sophia Rudorf and Reinhard Lipowsky. “Protein Synthesis in *E. coli*: Dependence of Codon-Specific Elongation on tRNA Concentration and Codon Usage”. In: *PLOS ONE* 10.8 (Aug. 2015). Ed. by Hans-Joachim Wieden, e0134994.
- [110] Yariv Kafri, David K. Lubensky, and David R. Nelson. “Dynamics of molecular motors with finite processivity on heterogeneous tracks”. In: *Phys. Rev. E* 71 (4 Apr. 2005), p. 041906.
- [111] Thomas Harms and Reinhard Lipowsky. “Driven Ratchets with Disordered Tracks”. In: *Phys. Rev. Lett.* 79 (15 Oct. 1997), pp. 2895–2898.

- [112] Julia M Yeomans. *Statistical mechanics of phase transitions*. Clarendon Press, 1992.
- [113] Elay Shech. “What is the paradox of phase transitions?” In: *Philosophy of Science* 80.5 (2013), pp. 1170–1181.
- [114] Joaquin Marro and Ronald Dickman. “Nonequilibrium phase transitions in lattice models”. In: *Nonequilibrium Phase Transitions in Lattice Models* (2005).
- [115] P. W. Anderson. “More Is Different”. In: *Science* 177.4047 (1972), pp. 393–396.
- [116] Leo P Kadanoff. “More is the same; phase transitions and mean field theories”. In: *Journal of Statistical Physics* 137.5 (2009), pp. 777–797.
- [117] Leonardo Crochik and Tânia Tomé. “Entropy production in the majority-vote model”. In: *Phys. Rev. E* 72 (5 Nov. 2005), p. 057103.
- [118] Yirui Zhang and Andre C Barato. “Critical behavior of entropy production and learning rate: Ising model with an oscillating field”. In: *Journal of Statistical Mechanics: Theory and Experiment* 2016.11 (2016), p. 113207.
- [119] Andre Cardoso Barato and Haye Hinrichsen. “Entropy production of a bound nonequilibrium interface”. In: *Journal of Physics A: Mathematical and Theoretical* 45.11 (2012), p. 115005.
- [120] Benjamin Andrae et al. “Entropy Production of Cyclic Population Dynamics”. In: *Phys. Rev. Lett.* 104 (21 May 2010), p. 218102.
- [121] Bruno O. Goes, Carlos E. Fiore, and Gabriel T. Landi. “Quantum features of entropy production in driven-dissipative transitions”. In: *Phys. Rev. Research* 2 (1 Feb. 2020), p. 013136.
- [122] Basile Nguyen and Udo Seifert. “Exponential volume dependence of entropy-current fluctuations at first-order phase transitions in chemical reaction networks”. In: *Phys. Rev. E* 102 (2 Aug. 2020), p. 022101.
- [123] Thomas Martynec, Sabine HL Klapp, and Sarah AM Loos. “Entropy production at criticality in a nonequilibrium Potts model”. In: *New Journal of Physics* 22.9 (2020), p. 093069.
- [124] Tim Herpich, Juzar Thingna, and Massimiliano Esposito. “Collective Power: Minimal Model for Thermodynamics of Nonequilibrium Phase Transitions”. In: *Phys. Rev. X* 8 (3 Sept. 2018), p. 031056.

- [125] Tim Herpich and Massimiliano Esposito. “Universality in driven Potts models”. In: *Phys. Rev. E* 99 (2 Feb. 2019), p. 022135.
- [126] Ronald Dickman. “Phase coexistence far from equilibrium”. In: *New Journal of Physics* 18.4 (2016), p. 043034.
- [127] Mario J de Oliveira. “Isotropic majority-vote model on a square lattice”. In: *Journal of Statistical Physics* 66.1-2 (1992), pp. 273–281.
- [128] Hanshuang Chen et al. “Critical noise of majority-vote model on complex networks”. In: *Phys. Rev. E* 91 (2 Feb. 2015), p. 022816.
- [129] Hanshuang Chen et al. “First-order phase transition in a majority-vote model with inertia”. In: *Physical Review E* 95.4 (2017), p. 042304.
- [130] Pedro E Harunari, MM de Oliveira, and CE Fiore. “Partial inertia induces additional phase transition in the majority vote model”. In: *Physical Review E* 96.4 (2017), p. 042305.
- [131] Agata Fronczak and Piotr Fronczak. “Exact solution of the isotropic majority-vote model on complete graphs”. In: *Phys. Rev. E* 96 (1 July 2017), p. 012304.
- [132] Marcelo M de Oliveira, MGE da Luz, and Carlos E Fiore. “Finite-size scaling for discontinuous nonequilibrium phase transitions”. In: *Physical Review E* 97.6 (2018), p. 060101.
- [133] MM de Oliveira, MGE da Luz, and CE Fiore. “Generic finite size scaling for discontinuous nonequilibrium phase transitions into absorbing states”. In: *Physical Review E* 92.6 (2015), p. 062126.
- [134] Murty S. S. Challa, D. P. Landau, and K. Binder. “Finite-size effects at temperature-driven first-order transitions”. In: *Phys. Rev. B* 34 (3 Aug. 1986), pp. 1841–1852.
- [135] Miguel Pineda and Michail Stamatakis. “Non-Equilibrium Thermodynamics and Stochastic Dynamics of a Bistable Catalytic Surface Reaction”. In: *Entropy* 20.11 (2018).
- [136] Jesús Gómez-Gardeñes et al. “Explosive Synchronization Transitions in Scale-Free Networks”. In: *Phys. Rev. Lett.* 106 (12 Mar. 2011), p. 128701.
- [137] Kurt Binder. “Finite size scaling analysis of Ising model block distribution functions”. In: *Zeitschrift für Physik B Condensed Matter* 43.2 (1981), pp. 119–140.
- [138] Tânia Tomé and Mário J. de Oliveira. “Entropy Production in Nonequilibrium Systems at Stationary States”. In: *Phys. Rev. Lett.* 108 (2 Jan. 2012), p. 020601.

- [139] Béla Bollobás. “The Isoperimetric Number of Random Regular Graphs”. In: *European Journal of Combinatorics* 9.3 (1988), pp. 241–244.
- [140] Luiz F. C. Pereira and F. G. Brady Moreira. “Majority-vote model on random graphs”. In: *Phys. Rev. E* 71 (1 Jan. 2005), p. 016123.
- [141] Oscar A Barbosa and Tânia Tomé. “The critical behavior of the entropy production in irreversible models with C_{3v} symmetry”. In: *Journal of Physics A: Mathematical and Theoretical* 52.38 (Aug. 2019), p. 385002.
- [142] Pyoung Seop Shim, Hyun Myung Chun, and Jae Dong Noh. “Macroscopic time-reversal symmetry breaking at a nonequilibrium phase transition”. In: *Physical Review E* 93 (2016), p. 012113.
- [143] Peter Hänggi et al. “Bistable systems: Master equation versus Fokker-Planck modeling”. In: *Physical Review A* 29.1 (Jan. 1984), pp. 371–378.
- [144] L. Levitov and G. Lesovik. “Charge distribution in quantum shot noise”. In: *JETP letters* 58.3 (1993), pp. 230–235.
- [145] C. Flindt et al. “Universal oscillations in counting statistics”. In: *Proceedings of the National Academy of Sciences* 106.25 (June 2009), pp. 10116–10119.
- [146] Hugo Touchette. “The large deviation approach to statistical mechanics”. In: *Physics Reports* 478.1-3 (2009), pp. 1–69.
- [147] Massimiliano Esposito, U Harbola, and S Mukamel. “Nonequilibrium fluctuations, fluctuation theorems, and counting statistics in quantum systems”. In: *Reviews of Modern Physics* 81.4 (Dec. 2009), pp. 1665–1702.
- [148] Zbigniew Koza. “General technique of calculating the drift velocity and diffusion coefficient in arbitrary periodic systems”. In: *Journal of Physics A: Mathematical and General* 32.44 (Nov. 1999), pp. 7637–7651.
- [149] F Baras, M Malek Mansour, and J. E. Pearson. “Microscopic simulation of chemical bistability in homogeneous systems”. In: *The Journal of Chemical Physics* 105.18 (Nov. 1996), pp. 8257–8261.
- [150] Massimiliano Esposito, Upendra Harbola, and Shaul Mukamel. “Entropy fluctuation theorems in driven open systems: Application to electron counting statistics”. In: *Phys. Rev. E* 76 (3 Sept. 2007), p. 031132.

- [151] A. Imparato and L. Peliti. “The distribution function of entropy flow in stochastic systems”. In: 2007.02 (Feb. 2007), pp. L02001–L02001.
- [152] Patrick Pietzonka, Kevin Kleinbeck, and Udo Seifert. “Extreme fluctuations of active Brownian motion”. In: *New Journal of Physics* 18.5 (2016), p. 052001.
- [153] Melissa Vellela and Hong Qian. “Stochastic dynamics and non-equilibrium thermodynamics of a bistable chemical system: The Schlögl model revisited”. In: *Journal of the Royal Society Interface* 6.39 (2009), pp. 925–940.
- [154] F. Schlögl. “Chemical reaction models for non-equilibrium phase transitions”. In: *Zeitschrift für Physik* 253.2 (Apr. 1972), pp. 147–161.
- [155] Daniel T. Gillespie. “On the calculation of mean first passage times for simple random walks”. In: *The Journal of Chemical Physics* 74.9 (May 1981), pp. 5295–5299.
- [156] Frank Jülicher, Armand Ajdari, and Jacques Prost. “Modeling molecular motors”. In: *Rev. Mod. Phys.* 69 (4 Oct. 1997), pp. 1269–1282.
- [157] Gatién Verley et al. “The unlikely Carnot efficiency”. In: *Nature communications* 5.1 (2014), pp. 1–5.
- [158] Ignacio A. Martínez et al. “Brownian carnot engine”. In: *Nature Physics* 12.1 (2016), p. 67.
- [159] Tim Schmiedl and Udo Seifert. “Efficiency at maximum power: An analytically solvable model for stochastic heat engines”. In: *Europhysics Letters* 81.2 (2007), p. 20003.
- [160] Udo Seifert. “Stochastic thermodynamics, fluctuation theorems and molecular machines”. In: *Reports on Progress in Physics* 75.12 (2012), p. 126001.
- [161] Massimiliano Esposito, Katja Lindenberg, and Christian Van den Broeck. “Universality of efficiency at maximum power”. In: *Physical Review Letters* 102.13 (2009), p. 130602.
- [162] Bart Cleuren, Bob Rutten, and Christian Van den Broeck. “Universality of efficiency at maximum power”. In: *The European Physical Journal Special Topics* 224.5 (2015), pp. 879–889.
- [163] Christian Van den Broeck. “Thermodynamic efficiency at maximum power”. In: *Physical Review Letters* 95.19 (2005), p. 190602.

- [164] Massimiliano Esposito et al. “Quantum-dot Carnot engine at maximum power”. In: *Physical Review E* 81.4 (2010), p. 041106.
- [165] Udo Seifert. “Efficiency of autonomous soft nanomachines at maximum power”. In: *Physical Review Letters* 106.2 (2011), p. 020601.
- [166] Yuki Izumida and Koji Okuda. “Efficiency at maximum power of minimally nonlinear irreversible heat engines”. In: *Europhysics Letters* 97.1 (2012), p. 10004.
- [167] N. Golubeva and A. Imparato. “Efficiency at Maximum Power of Interacting Molecular Machines”. In: *Phys. Rev. Lett.* 109 (19 Nov. 2012), p. 190602.
- [168] Viktor Holubec. “An exactly solvable model of a stochastic heat engine: optimization of power, power fluctuations and efficiency”. In: *Journal of Statistical Mechanics: Theory and Experiment* 2014.5 (2014), P05022.
- [169] Michael Bauer, Kay Brandner, and Udo Seifert. “Optimal performance of periodically driven, stochastic heat engines under limited control”. In: *Physical Review E* 93.4 (2016), p. 042112.
- [170] Karel Proesmans, Bart Cleuren, and Christian Van den Broeck. “Power-efficiency-dissipation relations in linear thermodynamics”. In: *Physical Review Letters* 116.22 (2016), p. 220601.
- [171] ZC Tu. “Efficiency at maximum power of Feynman’s ratchet as a heat engine”. In: *Journal of Physics A: Mathematical and Theoretical* 41.31 (2008), p. 312003.
- [172] S Ciliberto. “Experiments in stochastic thermodynamics: Short history and perspectives”. In: *Physical Review X* 7.2 (2017), p. 021051.
- [173] Bruno AN Akasaki, Mário J de Oliveira, and Carlos E Fiore. “Entropy production and heat transport in harmonic chains under time-dependent periodic drivings”. In: *Physical Review E* 101.1 (2020), p. 012132.
- [174] Ignacio A Martínez et al. “Colloidal heat engines: a review”. In: *Soft matter* 13.1 (2017), pp. 22–36.
- [175] HED Scovil and EO Schulz-DuBois. “Three-level masers as heat engines”. In: *Physical Review Letters* 2.6 (1959), p. 262.
- [176] Martin Josefsson et al. “A quantum-dot heat engine operating close to the thermodynamic efficiency limits”. In: *Nature Nanotechnology* 13.10 (2018), p. 920.

- [177] Patrick Pietzonka and Udo Seifert. “Universal trade-off between power, efficiency, and constancy in steady-state heat engines”. In: *Physical Review Letters* 120.19 (2018), p. 190602.
- [178] Sadi Carnot. “Réflexions sur la puissance motrice du feu et sur les machines propres à développer cette puissance”. In: *Annales scientifiques de l’École Normale Supérieure*. Vol. 1. 1872, pp. 393–457.
- [179] Angel L. L. Stable et al. “Thermodynamics of collisional models for Brownian particles: General properties and efficiency”. In: *Physical Review Research* 2 (4 Oct. 2020), p. 043016.
- [180] Franklin LS Rodrigues et al. “Thermodynamics of weakly coherent collisional models”. In: *Physical Review Letters* 123.14 (2019), p. 140601.
- [181] Juan MR Parrondo, Jordan M Horowitz, and Takahiro Sagawa. “Thermodynamics of information”. In: *Nature Physics* 11.2 (2015), pp. 131–139.
- [182] Philipp Strasberg et al. “Quantum and information thermodynamics: a unifying framework based on repeated interactions”. In: *Physical Review X* 7.2 (2017), p. 021003.
- [183] Alexandre Rosas, Christian Van den Broeck, and Katja Lindenberg. “Stochastic thermodynamics for a periodically driven single-particle pump”. In: *Physical Review E* 96 (5 Nov. 2017), p. 052135.
- [184] Rosas, Alexandre and Van den Broeck, Christian and Lindenberg, Katja. “Three-stage stochastic pump: Another type of Onsager-Casimir symmetry and results far from equilibrium”. In: *Physical Review E* 97.6 (June 2018).
- [185] Sang Hoon Lee, Jaegon Um, and Hyunggyu Park. “Nonuniversality of heat-engine efficiency at maximum power”. In: *Physical Review E* 98 (5 Nov. 2018), p. 052137.
- [186] Vasco Cavina et al. “Maximum power heat engines and refrigerators in the fast-driving regime”. In: *arXiv preprint arXiv:2010.00586* (2020).
- [187] Saikat Mondal, Sourav Bhattacharjee, and Amit Dutta. “Exploring the role of asymmetric-pulse modulation in quantum thermal machines and quantum thermometry”. In: *Physical Review E* 102.2 (2020), p. 022140.
- [188] FL Curzon and B Ahlborn. “Efficiency of a Carnot engine at maximum power output”. In: *American Journal of Physics* 43.1 (1975), pp. 22–24.

- [189] I I Novikov. “The efficiency of atomic power stations (a review)”. In: *Journal of Nuclear Energy (1954)* 7.1-2 (1958), pp. 125–128.
- [190] Sudeesh Krishnamurthy et al. “A micrometre-sized heat engine operating between bacterial reservoirs”. In: *Nat. Phys* 12.12 (2016), pp. 1134–1138.
- [191] Valentin Blickle and Clemens Bechinger. “Realization of a micrometre-sized stochastic heat engine”. In: *Nat. Phys* 8.2 (2012), pp. 143–146.
- [192] Karel Proesmans et al. “Brownian Duet: A Novel Tale of Thermodynamic Efficiency”. In: *Phys. Rev. X* 6 (4 Oct. 2016), p. 041010.
- [193] Pedro A Quinto-Su. “A microscopic steam engine implemented in an optical tweezer”. In: *Nat. Commun.* 5.1 (2014), p. 5889.
- [194] Philip H Jones, Onofrio M Maragò, and Giovanni Volpe. *Optical Tweezers: Principles and Applications*. Cambridge University Press, 2015.
- [195] John AC Albay et al. “Optical tweezers as a mathematically driven spatio-temporal potential generator”. In: *Opt. Express* 26.23 (Nov. 2018), pp. 29906–29915.
- [196] Avinash Kumar and John Bechhoefer. “Nanoscale virtual potentials using optical tweezers”. In: *Appl. Phys. Lett.* 113.18 (2018), p. 183702.
- [197] Govind Paneru and Hyuk Kyu Pak. “Colloidal engines for innovative tests of information thermodynamics”. In: *Adv. Phys.: X* 5.1 (2020), p. 1823880.
- [198] Junang Li et al. “Quantifying dissipation using fluctuating currents”. In: *Nat. Commun.* 10.1 (2019), p. 1666.
- [199] Karel Proesmans et al. “Efficiency of single-particle engines”. In: *Phys. Rev. E* 92 (3 Sept. 2015), p. 032105.
- [200] Shubhashis Rana et al. “Single-particle stochastic heat engine”. In: *Phys. Rev. E* 90 (4 Oct. 2014), p. 042146.
- [201] J. Hoppenau, M. Niemann, and A. Engel. “Carnot process with a single particle”. In: *Phys. Rev. E* 87 (6 June 2013), p. 062127.
- [202] Z. C. Tu. “Stochastic heat engine with the consideration of inertial effects and shortcuts to adiabaticity”. In: *Phys. Rev. E* 89 (5 May 2014), p. 052148.

- [203] Petr Chvosta et al. “Energetics and performance of a microscopic heat engine based on exact calculations of work and heat distributions”. In: *J. Stat. Mech.* 2010.03 (2010), P03002.
- [204] A. Imparato et al. “Work and heat probability distribution of an optically driven Brownian particle: Theory and experiments”. In: *Phys. Rev. E* 76 (5 Nov. 2007), p. 050101.
- [205] Carlos A Plata et al. “Building an irreversible Carnot-like heat engine with an overdamped harmonic oscillator”. In: *J. Stat. Mech.* 2020.9 (2020), p. 093207.
- [206] John AC Albay et al. “Shift a laser beam back and forth to exchange heat and work in thermodynamics”. In: *Sci Rep* 11.1 (2021), p. 4394.
- [207] Yonggun Jun, Mom čilo Gavrilov, and John Bechhoefer. “High-Precision Test of Landauer’s Principle in a Feedback Trap”. In: *Phys. Rev. Lett.* 113 (19 Nov. 2014), p. 190601.
- [208] Hadrien Vroylandt, Massimiliano Esposito, and Gatien Verley. “Collective effects enhancing power and efficiency”. In: *EPL (Europhysics Letters)* 120.3 (Nov. 2017), p. 30009.
- [209] Hadrien Vroylandt, Massimiliano Esposito, and Gatien Verley. “Efficiency Fluctuations of Stochastic Machines Undergoing a Phase Transition”. In: *Phys. Rev. Lett.* 124 (25 June 2020), p. 250603.
- [210] Andre C. Barato and Udo Seifert. “Cost and Precision of Brownian Clocks”. In: *Phys. Rev. X* 6 (4 Dec. 2016), p. 041053.
- [211] Viktor Holubec and Artem Ryabov. “Cycling Tames Power Fluctuations near Optimum Efficiency”. In: *Phys. Rev. Lett.* 121 (12 Sept. 2018), p. 120601.
- [212] Jong-Min Park, Hyun-Myung Chun, and Jae Dong Noh. “Efficiency at maximum power and efficiency fluctuations in a linear Brownian heat-engine model”. In: *Phys. Rev. E* 94 (1 July 2016), p. 012127.
- [213] Paolo Andrea Erdman et al. “Maximum power and corresponding efficiency for two-level heat engines and refrigerators: optimality of fast cycles”. In: *New Journal of Physics* 21.10 (2019), p. 103049.
- [214] Victor Mukherjee, Abraham G Kofman, and Gershon Kurizki. “Anti-Zeno quantum advantage in fast-driven heat machines”. In: *Communications Physics* 3.1 (2020), pp. 1–12.

- [215] Karel Proesmans and Christian Van den Broeck. “The underdamped Brownian duet and stochastic linear irreversible thermodynamics”. In: *Chaos* 27.10 (2017), p. 104601.
- [216] Carlos E. Fiore and Mário J. de Oliveira. “Entropy production and heat capacity of systems under time-dependent oscillating temperature”. In: *Phys. Rev. E* 99 (5 May 2019), p. 052131.
- [217] W. A. M. Morgado and D. O. Soares-Pinto. “Exact time-averaged thermal conductance for small systems: Comparison between direct calculation and Green-Kubo formalism”. In: *Phys. Rev. E* 79 (5 May 2009), p. 051116.
- [218] Jefferson Luan Diniz de Oliveira, Moisés Rojas, and Cleverson Filgueiras. “Two coupled double quantum-dot systems as a working substance for heat machines”. In: *Phys. Rev. E* 104 (1 July 2021), p. 014149.
- [219] Xiao-Li Huang et al. “Quantum Stirling heat engine and refrigerator with single and coupled spin systems”. In: *Eur. Phys. J. D* 68.2 (2014), pp. 1–8.
- [220] S. Liepelt and R. Lipowsky. “Operation modes of the molecular motor kinesin”. In: *Phys. Rev. E* 79 (1 Jan. 2009), p. 011917.
- [221] Ying Tang et al. “Work relations connecting nonequilibrium steady states without detailed balance”. In: *Phys. Rev. E* 91.4 (2015), p. 042108.
- [222] Somrita Ray and Andre C Barato. “Dispersion of the time spent in a state: general expression for unicyclic model and dissipation-less precision”. In: *Journal of Physics A: Mathematical and Theoretical* 50.35 (2017), p. 355001.
- [223] Daniel Maria Busiello and Simone Pigolotti. “Hyperaccurate currents in stochastic thermodynamics”. In: *Physical Review E* 100.6 (2019), p. 060102.
- [224] Daniel Maria Busiello and Carlos Fiore. “Hyperaccurate bounds in discrete-state Markovian systems”. In: *arXiv preprint arXiv:2205.00294* (2022).
- [225] Gatien Verley, Christian Van den Broeck, and Massimiliano Esposito. “Modulated two-level system: Exact work statistics”. In: *Physical Review E* 88.3 (Sept. 2013), p. 032137.
- [226] Lorenzo Bertini et al. “Level 2.5 Large Deviations for Continuous-Time Markov Chains with Time Periodic Rates”. In: *Annales Henri Poincaré* 19.10 (Oct. 2018), pp. 3197–3238.

- [227] M. Polettni, G. Verley, and M. Esposito. “Efficiency Statistics at All Times: Carnot Limit at Finite Power”. In: *Phys. Rev. Lett.* 114 (5 Feb. 2015), p. 050601.
- [228] Kay Brandner and Udo Seifert. “Multi-terminal thermoelectric transport in a magnetic field: bounds on Onsager coefficients and efficiency”. In: *New Journal of Physics* 15.10 (2013), p. 105003.
- [229] Viktor Holubec and Artem Ryabov. “Work and power fluctuations in a critical heat engine”. In: *Phys. Rev. E* 96 (3 Sept. 2017), p. 030102.
- [230] Michele Campisi and Rosario Fazio. “The power of a critical heat engine”. In: *Nature communications* 7.1 (2016), pp. 1–5.
- [231] Leonardo da Silva Souza et al. “Collective effects on the performance and stability of quantum heat engines”. In: *Phys. Rev. E* 106 (1 July 2022), p. 014143.

Appendix

Front page of the papers

SCIENTIFIC REPORTS

OPEN

Fundamental ingredients for discontinuous phase transitions in the inertial majority vote model

Jesus M. Encinas¹, Pedro E. Harunari¹, M. M. de Oliveira² & Carlos E. Fiore¹

Received: 9 February 2018

Accepted: 27 April 2018

Published online: 19 June 2018

Discontinuous transitions have received considerable interest due to the uncovering that many phenomena such as catastrophic changes, epidemic outbreaks and synchronization present a behavior signed by abrupt (macroscopic) changes (instead of smooth ones) as a tuning parameter is changed. However, in different cases there are still scarce microscopic models reproducing such above trademarks. With these ideas in mind, we investigate the key ingredients underpinning the discontinuous transition in one of the simplest systems with up-down Z_2 symmetry recently ascertained in [Phys. Rev. E 95, 042304 (2017)]. Such system, in the presence of an extra ingredient—the inertia—has its continuous transition being switched to a discontinuous one in complex networks. We scrutinize the role of three central ingredients: inertia, system degree, and the lattice topology. Our analysis has been carried out for regular lattices and random regular networks with different node degrees (interacting neighborhood) through mean-field theory (MFT) treatment and numerical simulations. Our findings reveal that not only the inertia but also the connectivity constitute essential elements for shifting the phase transition. Astoundingly, they also manifest in low-dimensional regular topologies, exposing a scaling behavior entirely different than those from the complex networks case. Therefore, our findings put on firmer bases the essential issues for the manifestation of discontinuous transitions in such relevant class of systems with Z_2 symmetry.


Spontaneous breaking symmetry manifests in a countless sort of systems besides the classical ferromagnetic-paramagnetic phase transition^{1,2}. For example, fishes moving in ordered schools, as a strategy of protecting themselves against predators, can suddenly reverse the direction of their motion due to the emergence of some external factor, such as water turbulence, or opacity³. Also, some species of Asian fireflies start (at night) emitting unsynchronized flashes of light but, some time later, the whole swarm is flashing in a coherent way⁴. In social systems as well, order-disorder transitions describe the spontaneous formation of a common language, culture or the emergence of consensus⁵.

Systems with Z_2 (“up-down”) symmetry constitute ubiquitous models of spontaneous breaking symmetry, and their phase transitions and universality classes have been an active topic of research during the last decades^{1,2,6}. Nonetheless, several transitions between the distinct regimes do not follow smooth behaviors^{7–9}, but instead, they manifest through abrupt shifts. These *discontinuous* (nonequilibrium) transitions have received much less attention than the critical transitions and a complete understanding of their essential aspects is still lacking. In some system classes, essential mechanisms for their occurrence¹⁰, competition with distinct dynamics^{11,12}, phenomenological finite-size theory¹³ and others^{14–17} have been pinpointed.

Heuristically, the occurrence of a continuous transition in systems with Z_2 symmetry is described (at a mean field level) by the logistic equation $\frac{d}{dt}m = am - bm^3$, that exhibit the steady solutions $m = 0$ and $m = \pm\sqrt{a/b}$. The first solution is stable for negative values of the tuning parameter a , while the second is stable for positive values of a . For the description of abrupt shifts, on the other hand, one requires the inclusion of an additional term $+cm^2$, where $c > 0$ ensures finite values of m . In such case, the jump of m yields at $a = \frac{b^2}{4c}$, reading $\pm\sqrt{b/2c}$. Despite portrayed under the simple above logistic equation, there are scarce (nonequilibrium) *microscopic* models forecasting discontinuous transitions¹⁸.

¹Instituto de Física, Universidade de São Paulo, Caixa Postal 66318 05315-970, São Paulo, São Paulo, Brazil.

²Departamento de Física e Matemática, CAP, Universidade Federal de São João del Rei, Ouro Branco, MG, 36420-000, Brazil. Correspondence and requests for materials should be addressed to C.E.F. (email: fiore@if.usp.br)

Entropy production as a tool for characterizing nonequilibrium phase transitionsC. E. Fernández Noa, Pedro E. Harunari, M. J. de Oliveira, and C. E. Fiole
Instituto de Física da Universidade de São Paulo, 05314-970 São Paulo, Brazil (Received 21 November 2018; published 3 July 2019)

Nonequilibrium phase transitions can be typified in a similar way to equilibrium systems, for instance, by the use of the order parameter. However, this characterization hides the irreversible character of the dynamics as well as its influence on the phase transition properties. Entropy production has been revealed to be an important concept for filling this gap since it vanishes identically for equilibrium systems and is positive for the nonequilibrium case. Based on distinct and general arguments, the characterization of phase transitions in terms of the entropy production is presented. Analysis for discontinuous and continuous phase transitions has been undertaken by taking regular and complex topologies within the framework of mean-field theory (MFT) and beyond the MFT. A general description of entropy production portraits for Z_2 (“up-down”) symmetry systems under the MFT is presented. Our main result is that a given phase transition, whether continuous or discontinuous has a specific entropy production hallmark. Our predictions are exemplified by an icon system, perhaps the simplest nonequilibrium model presenting an order-disorder phase transition and spontaneous symmetry breaking: the majority vote model. Our work paves the way to a systematic description and classification of nonequilibrium phase transitions through a key indicator of system irreversibility.

DOI: [10.1103/PhysRevE.100.012104](https://doi.org/10.1103/PhysRevE.100.012104)**I. INTRODUCTION**

Thermodynamics states that while certain quantities including the energy are ruled by a conservation law, the entropy is not conserved. In the general case of a system coupled with an environment, the time variation of entropy dS/dt has two contributions: the flux to the reservoir Φ and the entropy production rate Π [1,2], that is,

$$\frac{dS}{dt} = \Pi(t) - \Phi(t). \quad (1)$$

Since in the steady state the time variation of S vanishes, $dS/dt = 0$, $\Pi = \Phi$ and all entropy produced must be delivered to the environment.

The entropy production has been the subject of considerable interest in physics [3–7], population dynamics [8], biological systems [9], experimental verification [10], and others. A microscopic definition of entropy production, in the realm of systems described by a master equation, is given by the Schnakenberg expression [11]:

$$\Pi(t) = \frac{k_B}{2} \sum_{ij} \{W_{ji}P_i(t) - W_{ij}P_j(t)\} \ln \frac{W_{ji}P_i(t)}{W_{ij}P_j(t)}, \quad (2)$$

where W_{ji} is the transition rate from the state i to state j with associated probability $P_i(t)$ at the time t , and W_{ij} denotes the reverse transition rate. Equation (2) implies that $\Pi(t)$ is always nonnegative because $(x - y) \ln(x/y) \geq 0$, vanishing when the detailed balance $W_{ij}P_j - W_{ji}P_i = 0$ is fulfilled. Thus, it distinguishes equilibrium from nonequilibrium systems. Defining the nonequilibrium entropy by $S(t) = -k_B \sum_i P_i(t) \ln P_i(t)$, a microscopic relation for the flux $\Phi(t)$

is obtained:

$$\Phi(t) = k_B \sum_{ij} W_{ij} \ln \frac{W_{ij}}{W_{ji}} P_j(t). \quad (3)$$

Equation (3) constitutes an alternative (and advantageous) formula for evaluating the steady entropy production, since it corresponds to an average that can be evaluated from the transition rates and it will be the subject of analysis in the present paper.

Despite the recent advances of stochastic thermodynamics, a fundamental question is whether entropy production can be utilized as a reliable tool for typifying nonequilibrium phase transitions. Different studies have been undertaken in this direction [4,7,8,12–18]. Some of them [4,7,8,18] indicate that continuous phase transitions can be identified by a divergence of the first derivative of Π whose associated exponent plays an analogous role to the specific heat. Other features, such as stochastic thermodynamics of many-particle systems at phase transitions to a synchronized regime have also been investigated [14,16,17]. Despite such a progress, a theoretical description of the entropy production at phase transition regimes, mainly in the context of discontinuous phase transition, has not been satisfactorily established yet.

In this paper we present a characterization of phase transitions in terms of the entropy production. Our study embraces the analysis of continuous and discontinuous phase transitions within the framework of mean-field theory (MFT) and beyond MFT. It is based on general considerations about the probability distribution related to the phase coexistence. The description of continuous phase transition takes into account the extension of finite-size scaling ideas and hyperscaling relations to nonequilibrium systems. A general description of entropy production for Z_2 (“up-down”) symmetry systems in the realm of MFT is presented. Our main result is that a given

Exact statistics and thermodynamic uncertainty relations for a periodically driven electron pump

Pedro E. Harunari¹, Carlos E. Fiore¹ and Karel Proesmans^{2,3}

¹ Institute of Physics of São Paulo University, Rua do Matão, 1371, 05508-090 São Paulo, SP, Brazil

² Simon Fraser University, 8888 University Drive, Burnaby, British Columbia, Canada

³ Hasselt University, B-3590 Diepenbeek, Belgium

E-mail: pedro.harunari@usp.br

Abstract. We introduce a model for a periodically driven electron pump that sequentially interacts with an arbitrary number of heat and particle reservoirs. Exact expressions for the thermodynamic fluxes, such as entropy production and particle flows are derived arbitrarily far from equilibrium. We use the present model to perform a comparative study of thermodynamic uncertainty relations that are valid for systems with time-periodic driving.

Maximal power for heat engines: Role of asymmetric interaction timesPedro E. Harunari,^{1,*} Fernando S. Filho^{1,†} Carlos E. Fiore^{1,‡} and Alexandre Rosas^{2,§}¹Instituto de Física da Universidade de São Paulo, 05508-090 São Paulo, SP, Brazil²Departamento de Física, CCEN, Universidade Federal da Paraíba, Caixa Postal 5008, 58059-900 João Pessoa, Brazil

(Received 18 December 2020; revised 2 March 2021; accepted 4 May 2021; published 9 June 2021)

The performance of endoreversible thermal machines operating at finite power constitutes one of the main challenges of nonequilibrium classical and quantum thermodynamics, engineering, and others. We introduce the idea of adjusting the interaction time asymmetry in order to optimize the engine performance. We consider one of the simplest thermal machines, composed of a quantum dot interacting sequentially with two different reservoirs of heat and particles. Distinct optimization protocols are analyzed in the framework of stochastic thermodynamics. Results reveal that asymmetric interaction times play a fundamental role in enhancing the power output and that maximizations can provide an increase of more than 25% compared with the symmetric case. As an extra advantage, efficiencies at maximum power are slightly greater than the endoreversible Curzon-Ahlborn efficiency for a broad range of reservoir temperatures.

DOI: [10.1103/PhysRevResearch.3.023194](https://doi.org/10.1103/PhysRevResearch.3.023194)**I. INTRODUCTION**

The efficiency of any heat engine is bounded by Carnot efficiency $\eta_C = 1 - T_C/T_H$, with T_C and T_H being the cold and hot reservoir temperatures. It constitutes one of the main results of thermodynamics and is one of the distinct formulations of the second law. Such an ideal limit was introduced by Carnot in 1824 [1,2] and consists of a reversible machine composed by two isothermal and two adiabatic quasistatic strokes. Although it is a universal upper bound valid for all engines, irrespective of their designs, compositions, or nature, whether classical [3,4] or quantum [5,6], such an (ideal) limit is impractical, not only due to imperfections in the machine construction, which increases the dissipation, but also because its achievement would demand the machine to operate in a fully reversible way during infinitely large times, implying its operation at a null power (finite work divided by infinite time).

Thus it is usually desirable to build thermal machines to be as efficient as possible operating at finite power outputs. One of the main findings for endoreversible thermal machines is the Curzon and Ahlborn efficiency [7], in which the efficiency at maximum power is given by $\eta_{CA} = 1 - \sqrt{T_C/T_H}$. Such a remarkable finding has also been derived in several distinct works (see, e.g., Refs. [8,9]), and despite not possessing the same universal status as the Carnot efficiency, it provides a

powerful guide as to the operation of nonequilibrium engines under more realistic situations and sheds light on the construction and performance of small-scale engines (nanoscopic devices) working in a maximum power regime from the tools of stochastic thermodynamics [3,4,9–24]. In this context, single-level quantum dots have been proposed as prototype machines, whose simplicity allows detailed investigation of their performances at maximum power [25–27].

Collisional models, e.g., a system interacting sequentially and repeatedly with distinct environments (instead of continuous interaction with all the reservoirs), have been considered as a suitable description of engineered reservoirs [28]. Among the distinct situations for that, we mention the case of quantum systems, in which the reservoir is conveniently represented as a sequential collection of uncorrelated particles [29,30]. Additionally, the collisional approach attempts to provide realistic systems interacting only with small fractions of the environment or even those evolving under the influence of distinct drivings over each member [31,32]. Particularly, many aspects of a stochastic pump in which a single-level quantum dot (QD) is connected sequentially and periodically to different reservoirs have been discussed lately for symmetric interaction times [33–35].

In this paper, we introduce the idea of adjusting the interaction time asymmetry in order to optimize the engine performance. The present approach is rather different from some findings [10,19,36,37] exactly because we explore this adjustment of the interaction time; that is, the interaction time is the focus of our study. Despite the simplicity of the system, its large applicability and richness allow its usage as heat engine, refrigerator, heater, or accelerator, hence highlighting the importance of searching for optimized protocols. As a main finding, under suited situations, asymmetric interaction times play an important role in the enhancement of power output. Also, as an extra advantage, efficiencies become somewhat greater than the endoreversible Curzon-Ahlborn efficiency.


*pedroharunari@gmail.com

†fernando.francisco.filhof@gmail.com

‡fiore@if.usp.br

§arosas@fisica.ufpb.br

Published by the American Physical Society under the terms of the [Creative Commons Attribution 4.0 International license](https://creativecommons.org/licenses/by/4.0/). Further distribution of this work must maintain attribution to the author(s) and the published article's title, journal citation, and DOI.

PHYSICAL REVIEW E **104**, 064123 (2021)**Current fluctuations in nonequilibrium discontinuous phase transitions**C. E. Fiore,^{1,*} Pedro E. Harunari^{1,2,†} C. E. Fernández Noa^{1,‡} and Gabriel T. Landi^{1,‡}¹*Instituto de Física da Universidade de São Paulo, 05314-970 São Paulo, Brazil*²*Complex Systems and Statistical Mechanics, Physics and Materials Science Research Unit, University of Luxembourg, Luxembourg L-1511, G.D. Luxembourg* (Received 7 September 2021; accepted 29 November 2021; published 17 December 2021)

Discontinuous phase transitions out of equilibrium can be characterized by the behavior of macroscopic stochastic currents. But while much is known about the average current, the situation is much less understood for higher statistics. In this paper, we address the consequences of the diverging metastability lifetime—a hallmark of discontinuous transitions—in the fluctuations of arbitrary thermodynamic currents, including the entropy production. In particular, we center our discussion on the *conditional* statistics, given which phase the system is in. We highlight the interplay between integration window and metastability lifetime, which is not manifested in the average current, but strongly influences the fluctuations. We introduce conditional currents and find, among other predictions, their connection to average and scaled variance through a finite-time version of large deviation theory and a minimal model. Our results are then further verified in two paradigmatic models of discontinuous transitions: Schlögl's model of chemical reactions, and a 12-state Potts model subject to two baths at different temperatures.

DOI: [10.1103/PhysRevE.104.064123](https://doi.org/10.1103/PhysRevE.104.064123)**I. INTRODUCTION**

In microscopic systems, currents of heat, work, and entropy production must be treated as random variables, which fluctuate over different runs of an experiment [1,2]. This represents a paradigm shift in thermodynamics, and has already led to fundamental advancements in the field, such as fluctuation theorems [3–8] and, more recently, the discovery of thermodynamic uncertainty relations [9–13]. It also entails practical consequences, e.g., in the design of Brownian engines [14–17], molecular motors [18–21], information-driven devices [22,23], and bacterial baths [24]. In these systems, both the output power [13,25] and the efficiency [26–29] may fluctuate significantly, leading to possible violations of macroscopic predictions, such as the Carnot limit [14].

A scenario of particular interest is that of nonequilibrium steady states (NESSs), which occur when a system is placed in contact with multiple reservoirs at different temperatures T_i and/or chemical potentials μ_i . NESSs are characterized by finite currents of energy and matter, and thus also a finite entropy production rate σ_i [1,30–33]. At the stochastic level, these become fluctuating quantities, associated to a probability distribution. Understanding the behavior of said distributions constitutes a major area of research, as they form the basis for extending the laws of the thermodynamics towards the microscale, providing insights in nontrivial properties of nonequilibrium physics. Of particular interest is their behavior across nonequilibrium phase transitions [34]. Most of our understanding, however, is centered on the

average current. For instance, the average entropy production rate has been found to be always finite around the transition point, with the first derivative either diverging, in continuous transitions [35–41], or presenting a jump in discontinuous ones [38,39,42]. These clear signatures suggest, in fact, that the average entropy production could even be used to classify the type of transition. Conversely, the behavior of higher order statistics, such as the variance, is much less understood.

Cumulants of thermodynamic currents are usually assessed via numerical approaches, such as Monte Carlo simulations [39], or large deviation theory (LDT) [7,43–47]. In both cases, cumulants are computed from long-time sample averages, integrated over a time window τ . Ultimately, one is interested in taking $\tau \rightarrow \infty$, at least in principle. But in systems presenting discontinuous transitions this can become an issue, since the phase coexistence is characterized by states with very long metastability lifetimes τ_m . In fact, τ_m increases exponentially with the system volume V , which is a consequence of the discontinuous nature of the transition (for continuous transitions these divergences are algebraic). As a consequence, the order of the limits $\tau \rightarrow \infty$ and $V \rightarrow \infty$ becomes nontrivial [48].

In this paper we approach this issue by introducing the idea of conditional currents, given which phase the system is in. We focus, in particular, on the diffusion coefficient (scaled variance). We formulate a finite-time large deviation theory, which neatly highlights the nontrivial interplay between τ and τ_m . This is then specialized to a minimal two-state model, that is able to capture the key features of the problem and also provides useful predictions. These are then tested on two paradigmatic examples of discontinuous transitions: Schlögl's model of chemical kinetics, and a 12-state Potts model subject to two baths at different temperatures.




This paper is organized as follows: Section II presents the main concepts and assumptions considered. The conditional

*fiorecarlos.cf@gmail.com

†pedroharunari@gmail.com

‡gtlandi@gmail.com

Obtaining efficient thermal engines from interacting Brownian particles under time-periodic drivings

Iago N. Mamede ¹, Pedro E. Harunari,^{1,2} Bruno A. N. Akasaki ¹, Karel Proesmans,^{2,3,4} and C. E. Fiore ¹

¹*Instituto de Física da Universidade de São Paulo, 05314-970 São Paulo, Brazil*

²*Complex Systems and Statistical Mechanics, Physics and Materials Science Research Unit, University of Luxembourg, L-1511 Luxembourg, Luxembourg*

³*Hasselt University, B-3590 Diepenbeek, Belgium*

⁴*Niels Bohr Institute, University of Copenhagen, Blegdamsvej 17, Copenhagen, Denmark*



(Received 18 October 2021; accepted 18 January 2022; published 4 February 2022)

We introduce an alternative route for obtaining reliable cyclic engines, based on two interacting Brownian particles under time-periodic drivings which can be used as a work-to-work converter or a heat engine. Exact expressions for the thermodynamic fluxes, such as power and heat, are obtained using the framework of stochastic thermodynamic. We then use these exact expression to optimize the driving protocols with respect to output forces, their phase difference. For the work-to-work engine, they are solely expressed in terms of Onsager coefficients and their derivatives, whereas nonlinear effects start to play a role since the particles are at different temperatures. Our results suggest that stronger coupling generally leads to better performance, but careful design is needed to optimize the external forces.

DOI: [10.1103/PhysRevE.105.024106](https://doi.org/10.1103/PhysRevE.105.024106)

I. INTRODUCTION

Small-scale engines operating out of equilibrium have received significantly increasing attention in the last years, especially because several processes in nature (mechanical, biological, chemical and others) are related to some kind of energy conversion (e.g., mechanical into chemical and vice versa) [1–3]. The constant fluctuating flow of energy constitutes a fundamental feature fueling the operation of nonequilibrium engines which is well described by the framework of stochastic thermodynamics [1].

Entropy production plays a fundamental role in nonequilibrium thermodynamics. It satisfies fluctuation theorems [4,5], general bounds also known as thermodynamic uncertainty relations (TURs) [6–13] and general trade-offs between power, efficiency, and dissipation [14,15]. Here we look at a case study of a cyclic heat engine in which the nonequilibrium features are due to distinct thermal reservoirs and time-dependent external forces. We focus on systems with time-dependent driving for two reasons: first, time-dependent driving is arguably the simplest way to drive Brownian particles out of equilibrium [16,17] and second, systems with time-dependent driving have been shown to outperform steady-state systems [18–20].

Brownian particles are often at the core of nanoscaled heat engines [16,17,21–28]. Most of them are based on single-particle engines and have been studied for theoretical [29–38] and experimental [21,39,40] settings. On the other hand, the number of studies on the thermodynamic properties of interacting chains of particles are limited and often constrained to time-independent driving [28,41]. The scarcity of results [42], together the richness of such system, raises distinct and

relevant questions about the interaction contribution to the performance, the interplay between interaction and driving forces, and choice of protocol optimization. The last is a field in itself with many recent works focusing on the optimization of distinct engines in terms of efficiency and/or power [32,43–46].

In this work we conciliate above issues by introducing an interacting version of the underdamped Brownian duet [47], in which each particle is subject to a distinct thermal bath and driving force. The existence of distinct parameters (interaction between particles, strength of forces, phase difference, and frequency) provides several routes for tackling optimization that will be analyzed using the framework of stochastic thermodynamics. In order to exploit the role of distinct parameters, analysis will be considered for the (simplest) system composed of two Brownian particles. Two different situations will be addressed. Initially, we consider the case in which the thermal baths have the same temperature (interacting particle work-to-work converter) [17], in which maximizations are solely expressed in terms of Onsager coefficients and their derivatives. We then advance beyond the work-to-work converter by including a temperature difference between thermal baths and general predictions are obtained for distinct set of temperatures.

Distinct types of optimization will be introduced and analyzed: maximization of output power and efficiency with respect to the output forces, phase difference between external forces, and both of them. We obtain expressions for efficiency, power, and the optimization parameters in both regimes of maximum efficiency and maximum power. Results reveal that the coupling parameter is found to monotonically enhance both efficiency and/or power, highlighting the importance of

What to learn from a few visible transitions' statistics?

Pedro E. Harunari,^{1,2,*} Annweshia Dutta,^{3,4} Matteo Polettini,² and Édgar Roldán^{3,†}

¹*Instituto de Física da Universidade de São Paulo, 05314-970 São Paulo, Brazil*

²*Complex Systems and Statistical Mechanics, Department of Physics and Materials Science, University of Luxembourg, L-1511 Luxembourg, Luxembourg*

³*ICTP – The Abdus Salam International Centre for Theoretical Physics, Strada Costiera 11, 34151 Trieste, Italy*

⁴*Department of Physics, Indian Institute of Science Education and Research, Tirupati 517507, India*

(Dated: August 18, 2022)

Interpreting partial information collected from systems subject to noise is a key problem across scientific disciplines. Theoretical frameworks often focus on the dynamics of variables that result from coarse-graining the internal states of a physical system. However, most experimental apparatuses can only detect a partial set of transitions, while internal states of the physical system are blurred or inaccessible. Here, we consider an observer who records a time series of occurrences of one or several transitions performed by a system, under the assumption that its underlying dynamics is Markovian. We pose the question of how one can use the transitions' information to make inferences of dynamical, thermodynamical, and biochemical properties. First, elaborating on first-passage time techniques, we derive analytical expressions for the probabilities of consecutive transitions and for the time elapsed between them, which we call *inter-transition times*. Second, we derive a lower bound for the entropy production rate that equals to the sum of two non-negative contributions, one due to the statistics of transitions and a second due to the statistics of inter-transition times. We also show that when only one current is measured, our estimate still detects irreversibility even in the absence of net currents in the transition time series. Third, we verify our results with numerical simulations using unbiased estimates of entropy production, which we make available as an open-source toolbox. We illustrate the developed framework in experimentally-validated biophysical models of kinesin and dynein molecular motors, and in a minimal model for template-directed polymerization. Our numerical results reveal that while entropy production is entailed in the statistics of two successive transitions of the same type (i.e. repeated transitions), the statistics of two different successive transitions (i.e. alternated transitions) can probe the existence of an underlying disorder in the motion of a molecular motor. Taken all together, our results highlight the power of inference from transition statistics ranging from thermodynamic quantities to network-topology properties of Markov processes.

Keywords: stochastic thermodynamics, biophysics, inference, first-passage times

I. INTRODUCTION

Model systems in physics [1], chemistry [2–4], biology [5–7], and computation [8] are routinely described by Markov processes, which are also amenable to thermodynamic analysis [9–13]. This approach thrives when there is full knowledge of the system's internal state, but in most practical applications experimental apparatuses access few degrees of freedom or have a finite resolution, thus only partial information is available. One example is the rotation of flagella in a bacterial motor [14]: observation of orientation switches in the direction of the bacteria's flagella suggests the existence of internal states that are hidden from the observer.

The problem of measuring partial information, or of coarse-graining degrees of freedom, is usually framed in terms of the internal state of a system [15–20]. However, in most practical applications, an external observer only measures “footprints” of one or several transitions, rather than the internal state itself, as sketched in Fig. 1(a).

These footprints may be due to physical degrees of freedom satisfying microscopic reversibility, in which case it is possible to talk about their energetic and entropic balance, as sketched in Fig. 1(b) where the observer can detect the emission and absorption of a photon γ , or the production or consumption of a chemical species X . Finally, Fig. 1(c) sketches the motion of a molecular motor (e.g. a kinesin) along a periodic track (e.g. microtubule). The motor undergoes structural changes followed by a translocation step associated to the consumption of some resources (e.g. adenosine triphosphate). The only visible transitions are in this case the forward and backward steps along the track. As explained below, this situation is customary in experiments where the motion of a microscopic bead attached to the motor can be used to detect spatial displacements along the track while conformational changes and chemical fuel consumption remain undetectable to the experimenter [21].

Significant developments in single-molecule experimental techniques with biological systems at cellular and sub-cellular level have been reported over the last few decades [22]. For example, the motion of biomolecular machines involved in cellular transport such as kinesin [23], dynein [24, 25] and myosin [26] has been resolved at the sub-nanometer resolution. Examples

* pedroharunari@gmail.com

† edgar@ictp.it

The beat of a current

Pedro E. Harunari,¹ Alberto Garilli,² and Matteo Polettini^{2,*}

¹*Instituto de Física da Universidade de São Paulo, 05314-970 São Paulo, Brazil*

²*Department of Physics and Materials Science, University of Luxembourg,
Campus Limpertsberg, 162a avenue de la Faïencerie, L-1511 Luxembourg (G. D. Luxembourg)*
(Dated: May 11, 2022)

The fluctuation relation, milestone of thermodynamics based on Markov processes, is only established when a set of fundamental currents can be measured and all transitions are reversible. Here we prove that it also holds for systems with hidden transitions (possibly irreversible) if observations are carried “at their own beat”, that is, by stopping the experiment after a given number of visible transitions rather than after the elapse of an external clock time. This suggests that thermodynamics may be best described by Markov processes in the space of transitions, rather than states.

PACS numbers: 05.70.Ln, 02.50.Ey

Consider the “symbolism of atomic measurements”, as Schwinger called quantum mechanics [1]: transitions in the energy spectrum of atoms were then only visible through spectral lines, i.e. the emission of photons. Or else, consider a chemical reactor fed by the in- and out-take of some controlled species: while flows can be monitored, the abundance of the reactants is only accessible by scanning with devices that involve internal degrees of freedom – e.g. magnetic, vibrational, electronic (NMR, UV/Vis and infrared [2–5] spectroscopy). Yet again, consider myosins carrying cargoes on actin filaments: their motion can be monitored via imaging techniques, but not their ATP-ADP metabolic cycle [6–8].

The physics of open systems is a discourse about transitions and transformations. However, our modern understanding based on continuous-time Markov chains (CTMC) is tightly bound to notions of the system’s internal state. Take the fluctuation relation (FR), the most encompassing result about nonequilibrium systems, stating that for currents c cumulated up to some stopping time τ the log-ratio of their positive to negative probabilities is linear

$$\log \frac{p_r(c)}{p_r(-c)} = f \cdot c. \quad (1)$$

The above relation holds at times $\tau = t$ beaten by an external clock (upon a proper choice of initial distribution [9], or asymptotically) only if the observer has access to (fundamentally) all currents and forces in the system’s state space, up to boundary contributions. Instead, it does not generally hold if some of the currents are not visible.

The main result of this manuscript is that a local current $c = n_\uparrow - n_\downarrow$, that is the number of times a certain transition denoted \uparrow occurs minus that of the opposite transition \downarrow , obeys the FR when it is counted “at its own beat”, namely the number of times $\tau \equiv n = n_\uparrow + n_\downarrow$ that either \uparrow or \downarrow are performed, regardless of what happens within the system in the meanwhile. The second main contribution is the introduction of the formalism

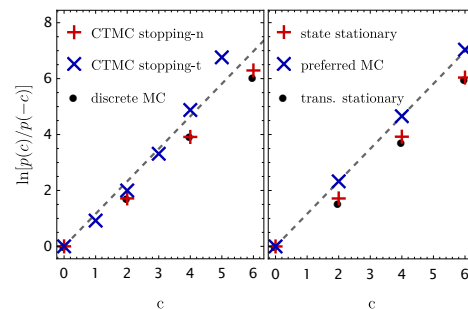


FIG. 1: Plots of $\log p_r(+c)/p_r(-c)$, $c \geq 0$ for different stopping times and processes, for the four-state system in Eq. (2), current along $1 \leftrightarrow 2$, a suitable choice of rates, equal number of samples⁷. *Left*: Sampling from the stationary distribution, comparison of CTMC at clock time t , at stopping time the total number of visible transitions n , and of transition-space Markov chain at discrete clock time n . *Right*: CTMC at stopping time n sampled from different initial distributions: transition-space stationary, state-space stationary, preferential distribution, showing that this latter lie on the line with slope $f^0 c$ (dashed line).

of Markov chains in the space of transitions, rather than states, which we prove to correctly describe the statistics of observables at total number of visible transitions.

This latter claim is sustained by the left panel of Fig. 1, comparing $\log p_r(c)/p_r(-c)$ in different simple numerical experiments with a CTMC at fixed- t and at fixed- n , and with the transition Markov chain: the latter two are equivalent. Here the FR, which holds asymptotically, is not observed due to the low number of transitions n . The right-hand panel shows that it is instead recovered in terms of an effective force f^0 [10], provided the initial state is sampled from a preferred initial distribution.

The Letter is self-contained, but in the Supplementary Material (marked with numbered superscripts⁸) we give derivations and details.